Laboratory Formation and Analysis of the Materials Comprising Interstellar Dust

by

Alan Douglas Scott

A thesis
presented to the University of Waterloo
in fulfillment of the
thesis requirement for the degree of
Doctor of Philosophy
in
Physics

Waterloo, Ontario, Canada, 1997

© Alan Scott 1997

National Library of Canada
Acquisitions and Bibliographic Services
395 Wellington Street
Ottawa ON K1A 0N4
Canada

Bibliothèque nationale du Canada
Acquisitions et services bibliographiques
395, rue Wellington
Ottawa ON K1A 0N4
Canada

Your file Votre référence

Our file Notre référence

The author has granted a non-exclusive licence allowing the National Library of Canada to reproduce, loan, distribute or sell copies of this thesis in microform, paper or electronic formats.

The author retains ownership of the copyright in this thesis. Neither the thesis nor substantial extracts from it may be printed or otherwise reproduced without the author's permission.

L'auteur a accordé une licence non exclusive permettant à la Bibliothèque nationale du Canada de reproduire, prêter, distribuer ou vendre des copies de cette thèse sous la forme de microfiche/film, de reproduction sur papier ou sur format électronique.

L'auteur conserve la propriété du droit d'auteur qui protège cette thèse. Ni la thèse ni des extraits substantiels de celle-ci ne doivent être imprimés ou autrement reproduits sans son autorisation.

0-612-22236-5

Canada

The University of Waterloo requires the signatures of all persons using or photocopying this thesis. Please sign below, and give address and date.

Laboratory Formation and Analysis of the

Materials Comprising Interstellar Dust

Abstract:

The optical properties of interstellar dust analogs are investigated. Thin, solid, amorphous films are deposited on a substrate through excimer laser ablation. This process is analogous to the vapour deposition of atoms and ions which is thought to occur in stellar outflows and the interstellar medium (ISM).

Refractive indices are calculated for typical polymeric hydrogenated amorphous carbon (HAC) films. Thickness dependent void structure is shown to influence the resultant density of the substance. Refractive indices are also determined for amorphous magnesium silicates in both the pyroxene ($MgSiO_3$) and olivine (Mg_2SiO_4) composites. A plausible dust grain model is constructed which successfully reproduces the major features of the diffuse interstellar extinction.

The effects of thermal annealing and dehydrogenation of HAC are investigated. The resulting graphitized HAC is shown to exhibit a spectral signature which is commonly associated with gas phase polycyclic aromatic hydrocarbons (PAHs). Thermal emission from HAC is observed for the first time and is shown to be an excellent match to various anomalous unidentified infrared (UIR) emitters. The emission from HAC closely resembles those rare sources labelled Type B UIR emitters in recent works by Geballe (1996) and Tokunaga (1996).

Near threshold laser ionization mass spectroscopy (LIMS) of HAC is shown to produce large ionized molecular clusters including fullerenes. The astrophysical implications of these results are discussed.

Acknowledgements

I would like to acknowledge all of those whose companionship, knowledge and support were invaluable in the allowing me to reach this stage with a small portion of my wits intact. Firstly, my supervisor Dr. Walt Duley for his knowledgeable direction and intuitive grasp of the subject. Thanks go out to the rest of my supervisory committee, Dr. A. Anderson, Dr. G. Harris, and Dr. N. Westwood for their informative comments and discussion.

For fruitful discussions and excellent theoretical work which helped things fit into place nicely, I would like to thank the rest of the Duley astrophysics group-- Sanjeev Seahra, and Geoffry Dadswell.

I am indebted to the following people who provided me with copies of their data: Dr. T. Geballe, Dr. Y. Pendleton, Dr. D. Cesarsky, and Dr. D. Furton for his HAC samples.

For companionship and forbearance with my day to day work I thank the Lasboys of P140, (soon to be Dr.) Mark "What Thesis?" Olfert, Dr. Hamid "The Peacock" Jahani, Dr. Grant "TG" Kinsman, George "I Don't Golf Anymore" Pinho, Serena "Doppler Girl" Schleuter, Hong-Ping Gu, Dr. Rob Meuller, and Joey "Muscle-boy" Soldo. Special thanks go out to all the past and present members of the CPBGA--Koy-man, Mark, Shoe, Scarfey, and all the rest-- who have made Friday afternoons a tradition throughout the years.

Special thanks must go out to my patient, loving wife, Janice, and my whole family without whose support I would probably still be picking apples instead of blowing things up with lasers.

This work was supported by OGS, & NSERC.

Table of Contents

1. INTRODUCTION **1**

2. THEORY **10**

2.1 Interstellar Grain Formation and Destruction 10

2.2 Carbonaceous Grain chemistry 12

2.3 HAC Grains interacting with the interstellar environment 18

2.4 Ultraviolet extinction in carbon grains 25

2.5 Carbon in Interstellar Infrared Spectra 37

3. EXPERIMENTAL SYSTEM **50**

3.1 UV Spectrometer with In-Situ Sample Preparation 50

3.2 FTIR Spectroscopy 55

3.3 Data Reduction for Emission Spectra 60

3.4 Thickness Measurement 61

3.5 Laser Ionization Mass Spectroscopy (LIMS) 63

4. RESULTS **68**

4.1 HAC Thin Films 68

4.2 HAC Refractive Indices 96

4.3 Optical Constants of Amorphous Silicates 109

4.4 IR Spectra and Annealing of HAC 114

4.5 LIMS of HAC 131

5. DISCUSSION OF ASTROPHYSICAL IMPLICATIONS **143**

5.1 The Role of HAC 143

5.1.1 HAC Absorption *150*

5.1.2 HAC Physical Structure *151*

5.1.3 HAC Emission *153*

5.1.4 Breakdown products of HAC *164*

5.2 THE ROLE OF SILICATES 168

5.3 EXTINCTION MODELLING 174

6. CONCLUSIONS **181**

7. CRITICAL PERSPECTIVE AND FUTURE WORK **185**

8. APPENDIX I **187**

8.1 8052 BASED MONOCHROMATOR CONTROLLER 187

9. REFERENCES **200**

10. GLOSSARY OF ACRONYMS **212**

11. INDEX **213**

List of Tables

Table 1 Measured depletions towards ζOph (Snow & Witt 1996) 5

Table 2 Physical properties of HAC films 72

Table 3 Allowed diffraction maxima for diamond and graphite. 90

Table 4 Diffraction maxima for dense region in figure 28. 93

Table 5 Diffraction maxima for dense region in figure 29. 93

Table 6 Comparison between spectral features seen in emission from HAC and those in absorption spectra. 121

Table 7 Identification of observed IR modes in carbonaceous films with contributions from nitrogen and oxygen 125

Table 8 Parameters for interstellar dust extinction model. 180

List of Illustrations

Figure 1 Average Interstellar Extinction (Whittet 1992) ____ 7

Figure 2 Two different crystalline forms of carbon: a) Crystal structure of diamond: each atom is located at the center of a regular tetrahedron, with four equidistant nearest-neighbour atoms at the four corners. b) Crystal structure of graphite, showing two-dimensional hexagonal arrays with strong bonds between atoms in each plane and much weaker bonds between planes. (Sears et al. 1986) ____ 13

Figure 3 π-state spectra of (a) ethylene, (b) planar rings with N = 5-8, (c) three fused sixfold rings, and four fused sixfold rings, (d) single graphite layer, and (e) layer containing two fivefold and two sixfold rings. Plotted in units of β, *the π interaction between two π states, ≈-2.9eV (Robertson & O'Reilly 1986).* ____ 15

Figure 4 Schematic of a HAC solid a) Section through a HAC grain of protographitic material loosely bonded through polymeric material to form a larger particle (Duley & Williams 1988); b) Schematic diagram illustrating types of carbon atom bonding in HAC; sp^1 (circled dots), sp^2 (filled circles), sp^3 (circled crosses) and hydrogen atoms (open circles). Double dots indicate bonding to other atoms (not shown) or rare dangling bonds (Jones et al. 1990). ____ 17

Figure 5 Schematic of a HAC surface illustrating likely breakage points which could result in the release of large molecules. ____ 19

Figure 6 Important reactions concerning the fragmentation and decomposition of HAC grains. ____ 22

Figure 7 The effect of particle shape on the lowest order surface mode resonance as calculated in the Rayleigh approximation for ellipsoids. The heavy line is a plot of the function $\varepsilon_1/\varepsilon_m = -(1/L_j-1)$, where $4\pi L_j$ is known as a depolarization factor. Solid arrows next to the various shapes designate the orientation of the electric field vector with respect to the particle axes (Gilra 1972). ____ 28

Figure 8 Mie scattering calculations illustrating the size dependence of the graphitic plasmon resonance. ____ 32

Figure 9 Mie scattering calculation illustrating the extinction from benzene spheres embedded in polyethylene. 35

Figure 10 Infrared absorption towards the galactic center sources GC IRS6E and GC IRS7 (Pendleton et al. 1994). ____ 38

Figure 11 Infrared emission towards the Orion Bar, illustrating the aromatic C=C and CH vibrations typical of UIR emitting regions (Roche 1988). 39

Figure 12 Comparison of infrared emission from IRAS 04296+3429 to absorption from semi-anthracite coal (Guillois et al. 1996). 44

Figure 13 Graph illustrating the relationship between size and 3.4μm/3.3μm flux ratio for planetary nebulae (Magazzù & Strazzulla 1990). 46

Figure 14 Observations of UIR emitters HD 44179 (The Red Rectangle) and NGC 7027 illustrating variations in 3.3μm peak width (Tokunaga et al. 1988). 48

Figure 15 Block diagram of UV spectrometer with in-situ sample deposition. 51

Figure 16 Block diagram of IR emission chamber. 57

Figure 17 FTIR contaminant spectrum (solid line) compared to IRAS 05341+0852 emission (circles) (Joblin et al. 1996). 58

Figure 18 Block diagram of time of flight spectrometer for LIMS experiment. 64

Figure 19 Model fits (Dadswell & Duley 1997b) to HAC absorption spectra. Solid and dashed lines show spectra of 2 different HAC films for each deposition temperature a) 297K: b) 77K, showing spectral differences under similar deposition conditions. Circles and triangles show a range of similar hydrogen and aromatic fractions. 70

Figure 20 Curves of equal compressive stress of i-carbon layers deposited on glass substrates in units of 10^9 Pa as functions of the bias voltage U_B and the ethylene pressure $p_{C_2H_4}$ (Enke 1981). 73

Figure 21 Stress relief patterns in thin HAC films. Upper: Nir (1984); Lower: Present study. 74

Figure 22 Cracking patterns in thin HAC films. Upper: Nir (1984); Lower: Present study. 75

Figure 23 Energy and thickness dependent structures illustrated on chemically etched Germanium films (Swab et al. 1980). Upper: Film surfaces RF deposited at increasing gas pressure: Lower: Analysis of dendritic and void structures in a single film at different magnifications, showing similar clustering features at each scale (Macleod 1982). 78

Figure 24 SEM of HAC surfaces deposited at 77K (a) before and (b) after exposure of film to UV radiation. 79

Figure 25 SEM of HAC surfaces deposited: (a) at 300K; (b) at 77K. 80

Figure 26 SEM of HAC surfaces after UV photo-processing: (a) deposited at 300K; (b) deposited at 77K. 81

Figure 27 Electron diffraction image of amorphous low hydrogen content HAC film. 86

Figure 28 TEM image of enhanced density area on low hydrogen content HAC film magnified 30,000x. 87

Figure 29 TEM image of enhanced density area on low hydrogen content HAC film magnified 13,000x. 88

Figure 30 Electron diffraction image of enhanced density area from figure 28. 91

Figure 31 Electron diffraction image of enhanced density area from figure 29. 92

Figure 32 Schematic diagram of light impinging normally on an absorbing film deposited upon a transparent substrate. 98

Figure 33 SEM of HAC film cross sections deposited at 300K: (a) as deposited; (b) photo-processed with UV radiation. 99

Figure 34 Cross sections of HAC films deposited at 77K. 100

Figure 35 Cross sections of HAC films deposited at 77K after UV photo-processing. 101

Figure 36 Measured indices of refraction n and k for HAC films deposited at 77K. 103

Figure 37 Measured indices of refraction n and k for HAC films deposited at 300K. 104

Figure 38 Effects of UV photo-processing on aliphatic CH stretching feature in HAC films deposited at 77K. 106

Figure 39 Effects of UV photo-processing on aliphatic CH stretching feature in HAC films deposited at 300K. 107

Figure 40 Electron dispersive x-ray analysis study illustrating the retention of parent crystal stoichiometry during excimer laser ablative thin film deposition of amorphous silicates. 111

Figure 41 Measured indices of refraction n and k for amorphous enstatite. 112

Figure 42 Measured indices of refraction n and k for amorphous forsterite. 113

Figure 43 (a) IR absorption spectrum of HAC, as deposited (bottom); heated to 700K (middle); and heated to 800K (top). Spectral range 3.1-4.0μm., zero shifted for clarity; (b) Same as (a), but for spectral range of 5.0-14μm 115

Figure 44 STM images of carbonaceous surfaces. (a) HAC as deposited; (b) HAC after annealing in vacuum to 800K; (c) graphite; (d) annealed HAC at higher magnification. Note ordered graphitic structures in upper right quadrant of (d). ____ *117*

Figure 45 IR emission from HAC at various annealing temperatures (in vacuum) from 573-773K in the spectral range of 3-15μm, zero shifted for clarity. ____ *119*

Figure 46 IR emission from HAC at various annealing temperatures (in vacuum) from 573-723K in the spectral range of 3.1-3.8μm. ____ *122*

Figure 47 IR absorption spectra of HAC after annealing to various temperatures (in air) from 300K (top) to 600K (bottom) in the spectral range of 3700-600cm^{-1}. ____ *124*

Figure 48 IR emission from HAC annealed in an oxygen atmosphere to 483, 673 and 773K. ____ *128*

Figure 49 IR emission from nitrogenated HAC annealed in vacuum to 523 and 773K. ____ *129*

Figure 50 IR emission from N-HAC at 483K and annealed in oxygen to 623 and 773K. ____ *130*

Figure 51 LIMS of HAC on copper at 0.13 J/cm^2. Successive shots on one location showing effects of photoprocessing and ablation (a) 5th shot; (b) 10th shot; (c) 18th shot; (d) 24th shot ____ *133*

Figure 52 LIMS of HAC on aluminum at 0.20 J/cm^2 (a) 1st shot; (b) 2nd shot; (c) 3rd shot ____ *134*

Figure 53 LIMS of graphite at 10^{12} W·m^{-2} and 532nm wavelength showing characteristic fullerene peaks (Leddingham & Singhal 1992). ____ *136*

Figure 54 LIMS of HAC on copper (a) 1st shot at 0.09 J/cm^2; (b) shots 3-8 at 0.09 J/cm^2 ____ *138*

Figure 55 LIMS of HAC on aluminum (a) 1st shot at 0.20 J/cm^2; (b) 2nd shot at 0.20 J/cm^2 ____ *139*

Figure 56 IR absorption spectrum of HAC deposited at 77K compared to astronomical observations of GC IRS6E and the Murchison Meteorite (Pendleton et al. 1994) ____ *144*

Figure 57 Various fits to the 3.4μm interstellar absorption feature (Pendleton 1994) ____ *145*

Figure 58 3μm emission region for the three basic types of UIR source (Tokunaga 1996). ____ *147*

Figure 59 Mid-IR emission region for type A and type B UIR source (Tokunaga 1996). ____ *148*

Figure 60 Comparison of IRAS emission spectra to IR absorption spectrum of polymeric HAC (lower solid curve) and partially annealed HAC (upper solid curve) ____ *152*

Figure 61 Comparison of type A UIR emission spectrum (NGC 7023) to emission from HAC annealed to 773K 154

Figure 62 3.1 - 3.8μm emission from HAC annealed to 773K, coal tar (de Muizon et al. 1990), and IRAS 21282+5050 (type A UIR emitter)(de Muizon et al. 1990) 155

Figure 63 Comparison of normalized 3.1 - 3.8μm HAC emission to various astronomical sources. HAC emission at 673 & 773K vs. IRAS 04296+3429 (Upper); HAC emission at 773K vs. CRL 2688 (Lower) (Geballe & van der Veen 1990; Geballe et al. 1992) 157

Figure 64 Comparison between thermal emission of IRAS 05341+0852 (circles) (Joblin et al. 1996) and that from a two component HAC dust mixture (solid line). Component (a) is the 650K emission from HAC which was deposited at 77K. Component (b) is the 800K emission from HAC which was deposited at 300K and subsequently annealed to ~850K. 158

Figure 65 7 - 13μm emission comparisons: a) IRAS 22272+5435 vs. polymeric HAC (calculated at 260K); b) IRAS 04296+3429 vs. partially annealed HAC (calc. at 380K); c) IRAS 07134+1006 vs. partially annealed HAC (calc. at 220K); d) IRAS 21282+5050 vs. admixture of polymeric and annealed HAC (calc. at 540K). Temperatures used for calculations are generally higher than those estimated from observed 10/18μm flux ratios. (Justtanont et al. 1996) 160

Figure 66 IR emission from energetic regions in M17 compared to emission from HAC at 573 and 773K (Cesarsky et al. 1996a; 1996b). 163

Figure 67 Values of the absorption coefficient k measured for amorphous forsterite and enstatite films compared to that from astronomical silicate (Draine & Lee 1984) 169

Figure 68 Mie calculations showing normalized absorption from spherical grains of amorphous enstatite. 170

Figure 69 Mie calculations showing normalized absorption from spherical grains of amorphous forsterite. 171

Figure 70 Absorption efficiency of Rayleigh sized amorphous forsterite and enstatite spheres compared to the silicate absorption feature towards Mira star U Tel (Dorschner et al 1995) and an average feature from several protostars (Pégourié & Papoular 1985). 173

Figure 71 Interstellar extinction model of Mathis & Whiffen (1989). The calculated (filled circles) and observed (solid line) values of A(λ)/A(V) for the grain model. The extinction for the composite grains alone (without the small graphite particles) is shown in the dotted line. ____ *175*

Figure 72 Characteristics of various grain populations used in the extinction model. ____ *177*

Figure 73 Model extinction curves (a) for the UV spectral region compared to the average interstellar extinction; (b) for the IR spectral region with inset of 3.4μm CH feature from HAC mantles. ____ *179*

Figure 74 Box diagram of monochromator controller unit. ____ *188*

Figure 75 Decoder circuit for VUV monochromator encoder wheel. ____ *189*

Figure 76 Circuit schematic showing wavelength counter and motor control. ____ *190*

Figure 77 Schematic of relay circuit controlling monochromator motors. ____ *191*

Figure 78 Circuit schematic showing photon counter interface and DMA addressing. ____ *193*

Figure 79 DMA timing diagram. ____ *194*

1. INTRODUCTION

Peering into the depths of space, astronomers this century have discovered dark obscuring splotches marring the bedazzling spectacle of the heavens. A nebulous haze enshrouds the stellar nurseries whilst glowing circlets of ethereal matter encompass the dying embers of ancient stars like cosmic funeral wreaths. Ashes to ashes, dust to dust. It is in these clouds of gas, dust and soot that stars, solar systems and civilizations are born. Upon its death, a star returns its outer layers to the interstellar medium which gave it birth--each cloud a tenuous structure where a single gram of matter may be spread out over more than a million cubic kilometers. Occupying vast volumes of space these seemingly insubstantial agglomerations account for 10% of the known mass in our galaxy.

Interstellar dust was first recognized in the 1920's in the photographic studies of E.E. Barnard and the analytic work of Max Wolf. Trumpler (1930) proved the existence of general interstellar extinction. He was able to relate the structure of open star clusters to their linear dimensions, and thus extrapolate their distance from the sun. When comparing these distances to those found using spectral types and apparent magnitudes, he found a discrepancy: the apparent magnitudes gave results indicating systematically larger distances than those obtained using the apparent diameter model. This problem could be resolved only by assuming that the observed cluster light was affected by a colour excess of about 0.3 magnitudes per kiloparsec (kpc). Colour excess is an astronomical term which refers to the difference between an object's intrinsic colour and its apparent colour and is defined by:

$$E_{B-V} = (B-V) - (B-V)_0 \qquad 1$$

Here, B is apparent magnitude in the blue spectral region, V is apparent magnitude in the visual region, and B-V is defined as the colour of the star. $(B-V)_o$ is the colour the star

would have in the absence of dust. Magnitudes are the relative inverted logarithmic units used to denote the brightness of a star. The smaller the magnitude, the brighter the star appears. The apparent magnitude is related to the flux observed from the Earth's surface. These ancient units were already in use around the time of Hipparchus (190-125 B.C.). The logarithmic nature of the scale reflects the eye's physiological response to optical stimuli. A constant change in apparent brightness reflects a logarithmic change in measured intensity. This sort of logarithmic response is similar to the body's auditory response as illustrated in the logarithmic decibel scale used to denote the intensity of sounds. The modern magnitude scale is due to Oxford astronomer N.G. Pogson (?-1891). If one denotes the ratio of the observed fluxes between two stars as S_1/S_2, then their difference in magnitude ($m_1 - m_2$) is:

$$m_1 - m_2 = -2.5 \log \frac{S_1}{S_2} \qquad 2$$

In practice, all stars are compared with a set of standard stars which have defined absolute values of magnitude. Sirius, the brightest star in the sky next to the sun (V = -26.78), has an apparent visual magnitude V = -1.45.

Another piece of evidence which supports the existence of interstellar dust is the phenomenon of elemental depletions in the gas phase. By measuring the equivalent width, W_v, of identifiable interstellar absorption lines in the spectra of stars, one can derive the gas phase column densities of elements. Equivalent width is defined as the width of a line removing the same energy from the spectrum as the line observed, but which absorbs all radiation over that width. Column density, N_X, is defined as the number of particles per unit area in the projection of a column of arbitrary length, L, onto a flat plane perpendicular to the line of sight:

$$N_X(cm^{-2}) = n_X(cm^{-3}) \times L(cm) \qquad 3$$

where n_X is the actual space density of the substance X.

For an unsaturated absorption line corresponding to a known transition with oscillator strength f, the column density of a substance can be calculated as follows:

$$N_X = \left(\frac{4\varepsilon_o m_e c}{e^2}\right)\frac{W_v}{f} \qquad 4$$

This quantity is most often specified relative to the column density of hydrogen and is useful for observational measurements.

Finally, the logarithmic depletion can be calculated by comparing interstellar column densities with solar column densities:

$$D_x = \log\left[\frac{N_x}{N_H}\right] - \log\left[\frac{N_x}{N_H}\right]_\odot \qquad 5$$

where N_X is the observed column density of element X and N_H is the observed column density of hydrogen. The subscript $\odot$ refers to solar values. Until very recently, all depletions were measured with respect to the Sun's elemental composition. Surveys of elemental compositions in F and G main sequence stars have shown that the solar system has elevated metallic abundances when compared to other stars in our galactic neighbourhood (Edvardsson et al. 1993; Tomkin et al. 1995; Sofia et al. 1997). For this reason a second depletion measure relative to a local average composition, $D_{X(stars)}$, may be derived as a more accurate

representation of the fraction of an element present in the gas phase. When comparing interstellar depletions to stellar, terrestrial or nebular abundances, we see that some elements are significantly depleted in the interstellar medium. These elements then can be hypothesized as the components of interstellar matter. Table 1 shows some representative depletions taken from Snow and Witt (1996) towards the moderately reddened star ζOph which is often used as a standard for depletion studies.

Dust can also be observed through absorption and emission in the infrared. Much of the infrared emission from dust is due to heating caused by the absorption of energetic photons. This thermal radiation is particularly intense surrounding energetic HII regions (where hydrogen is found in ionized HII form due to high ultraviolet flux) powered by O and B-type stars. In the core of these HII regions near to the star, the dust is swept away by radiation pressure. These regions have a hot, dusty halo where the heating is caused by absorption of UV continuum and Lyman α photons arising from inside the cloud.

It is easy to see then, why the optical properties of this dust are so very important in the fields of astronomy and astrophysics. Dust is a ubiquitous component of the interstellar medium and stars often appear reddened due to the scattering properties of interstellar dust grains. By comparing the spectra of obscured stars to those of unreddened stars of the same spectral type we can discover the wavelength dependence of the interstellar extinction (see figure 1). By averaging the extinction curves along various sightlines one can derive an average interstellar extinction curve (Savage & Mathis 1979). The major components of the interstellar extinction are quite uniform in most of the areas observed, although there are significant deviations from the mean along individual sightlines (Mathis 1990). From this information it is possible to make some deductions as to the size and composition of this interstellar matter. For instance, the fact that the extinction rises in the far ultraviolet regime indicates the existence of a distribution of small particles with ~0.05μm radius. The λ^{-1} extinction in the visible regime tells of another distribution of larger particles having ~0.1μm radius. From the observed

Table 1 Measured depletions towards ζOph (Snow & Witt 1996)

Atom	$D_{X(sun)}$	$D_{X(stars)}$
C	-0.47	-0.20
N	-0.16	+0.07
O	-0.41	-0.14
Mg	-0.81	-0.63
Si	-1.31	-1.03
S	+0.23	+0.35
Ca	-3.66	-3.50
Ti	-2.59	-2.38
Cr	-2.11	-1.95
Fe	-2.39	-2.15
Ni	-2.52	-2.32

polarization of star light we can deduce that some of the interstellar particles are elongated and aligned. One can observe known gas phase atomic absorption and emission bands that are associated, not with the stars themselves, but with actual interstellar clouds of material. These bands are related by Doppler shifts which are grouped at distinct radial velocities different from the background star. This information leads us to conclude that the material is often condensed in cloud-like structures. From these associated interstellar absorption and emission features we can further elucidate the structure and composition of the dust particles and associated gas.

Several important spectral features, some as yet unidentified, are associated with interstellar solids. A successful interstellar dust model must be able to account for the existence and observed properties of each feature.

The strong extinction feature which is observed at 217.5nm is ubiquitous in the interstellar medium with very little change in central wavelength from one region to another (Draine 1989). The width and strength of the band are somewhat variable depending on environment (Mathis 1990), and the carrier seems to be destroyed in energetic HII regions (Jenniskens & Greenberg 1993). It is commonly assumed that this feature arises from small particles (~0.005μm) of graphite (Gilra 1972; Savage & Mathis 1979; Hecht 1986), but the origin of small effectively mono-sized crystalline particles of graphite is an unsolved problem (Czyzak & Santiago 1973; Czyzak et al. 1982; Sorrell 1990). Observations by Witt et al. (1992) and Lillie & Witt (1976) suggest that this feature is caused purely by absorption without scattering which would argue against the possibility of a graphitic origin (see section 2.4). Such problems have caused researchers to postulate alternate origins for the 217.5nm feature. These alternate sources include hydroxyl ions in silicates (Duley et al. 1989b), charge

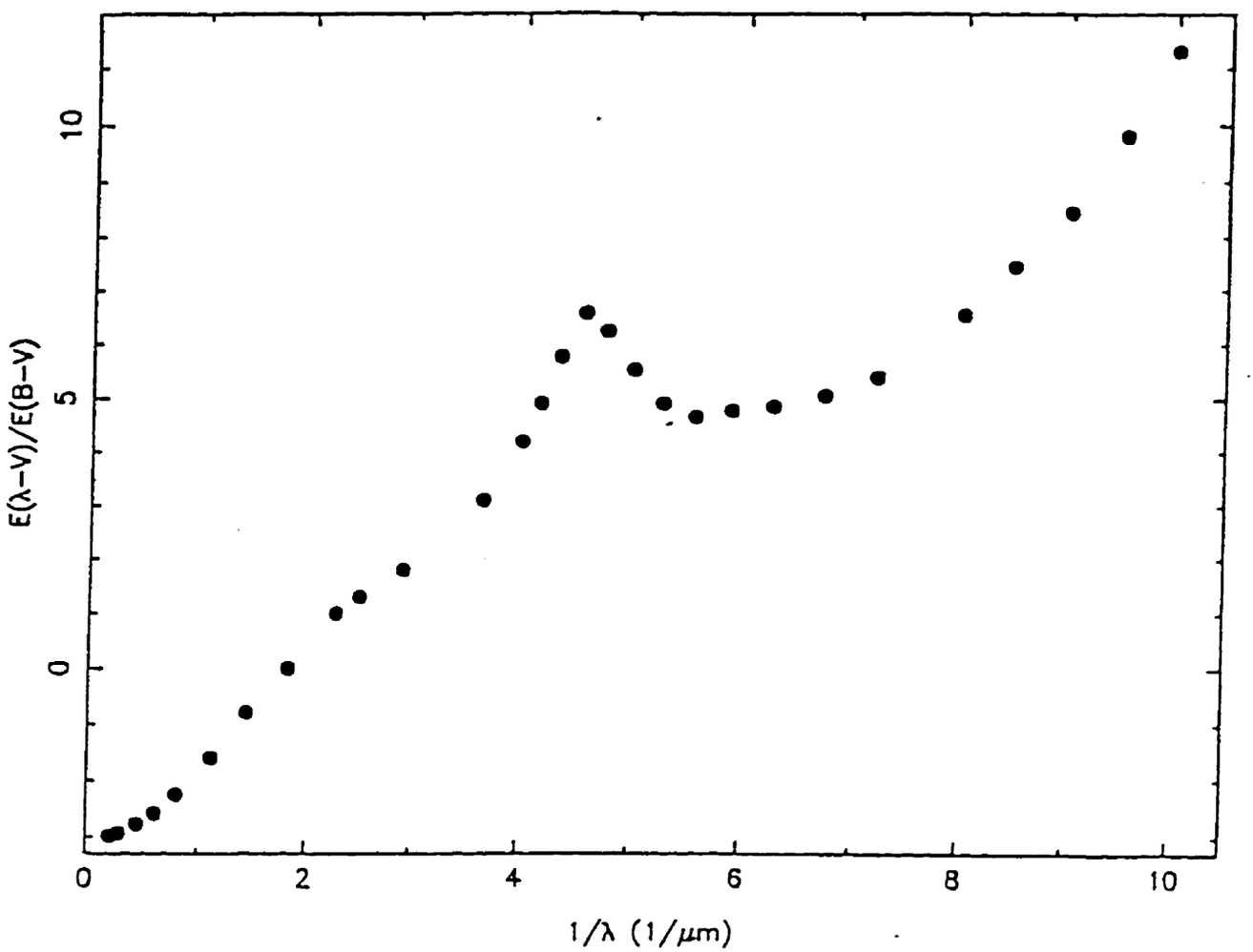


Figure 1 Average Interstellar Extinction (Whittet 1992)

transfer (Carnochan 1987), and amorphous carbon particles (Colangeli et al. 1986).

A strong interstellar absorption feature is typically observed at ~9.7μm in most quiescent regions of the ISM and is associated with a vibrational excitation in silicate dust (Penman 1976; Forrest et al. 1979; Willner et al. 1982; Olnon & Raimond 1986; Whittet et al. 1988). The large width and smoothness of this feature are reproduced by amorphous magnesium silicates (Day 1979, 1981; Dorschner & Henning 1986), while the observation of linear polarization in these IR bands indicates that silicate grains are elongated and aligned (Aitken et al. 1989).

Silicate grains with a range of sizes are an important component of all grain models and are postulated to contribute significantly to extinction at all wavelengths due to a combination of absorption and scattering (Greenberg 1989; Mathis 1989; Williams 1989). Large (0.1-0.2μm) silicate grains are suggested as the source of polarization at wavelengths in the visible and near-UV, while a population of much smaller (0.01μm) grains is required to produce the rapid rise in far UV extinction seen in many interstellar spectra. A recent discussion of the effect of small silicate particles on polarization in the far-UV (Kim & Martin 1995a; 1995b) has concluded that an excess of very small aligned silicate particles may be required to fit polarization observations in the region $\lambda^{-1} > 6\mu m^{-1}$ unless the optical constants of the silicate material are quite different from that customarily used for "astronomical silicate" (Draine & Lee 1984) which are based on crystalline olivine. There have been a number of laboratory measurements of refractive indices for silicates with compositions similar to those expected for interstellar dust (Huffman 1970; Huffman & Stapp 1971; Krätschmer & Huffman 1979; Jager et al. 1994; Dorschner et al. 1995), but until now no experimental data have been reported for amorphous silicates over a spectral range which includes both the 9.7μm infrared band and fundamental edge absorption at wavelengths shorter than 170nm.

A group of emission bands, situated in the near-IR at wavelengths of 3.3, 6.2, 7.7, 8.6, and 11.3μm, is commonly referred to as the unidentified infrared (UIR) bands (Gillet et al. 1973). These bands are strongest in energetic nebulae and areas with strong UV flux, but they

have also been recently observed by the ISO satellite in other galaxies (Boulade et al. 1996; Metcalfe et al. 1996) and at low levels in the diffuse interstellar medium (Mattila et al. 1996). Duley & Williams (1981) originally identified these bands with aromatic hydrocarbons. Sellgren (1984), observing the UIRs in reflection nebulae, first noticed the non-thermal nature of the emitting source. Since then, many have argued for a gas phase molecular origin for these structures in the form of polycylic aromatic hydrocarbons (PAHs) (Léger & Puget 1984; Allamandola et al. 1985; Allamandola et al. 1989; Sellgren 1989; Joblin et al. 1992; Lee & Wdowiak 1993; Robinson et al. 1997; Pauzat et al. 1997). Although many authors have been convinced of this identification, some problems remain to be addressed more thoroughly. Production mechanisms of large PAHs cannot easily account for the necessary column densities (Mendoza-Gómez et al. 1995). High-resolution laboratory data show extra PAH bands which are not observed in space as well as significant mismatches between emission bands of common PAHs and the UIR bands (Léger & Puget 1984; Wdowiak 1986; Sakata et al. 1990; Donn et al. 1989; Leach 1987; 1995; Cook et al. 1996).

This work will explore the spectral properties of silicate and carbonaceous materials which have been proposed as major components of interstellar dust. Processes such as annealing and interstellar shocks which could significantly affect the physical properties of interstellar dust will be simulated. A link between these processes and the formation of large molecules in the ISM is inferred. The results of this analysis will be discussed in light of current theories, and the astrophysical implications of these results will be presented.

2. THEORY

2.1 Interstellar Grain Formation and Destruction

Thermodynamic calculations (Frenklach & Feigelson 1989; Egan & Leung 1995) and observations of IR continuum emission (Williams et al. 1987; Woodsworth et al. 1990) show that the extended circumstellar envelopes of cool giant stars are a major source of interstellar dust particles. These huge stellar objects have converted much of their nuclear fuel to heavier elements. Their extended, tenuous envelopes can expand into space, enriching the surrounding interstellar medium, and eventually forming nebulous clouds of material. These stars are often classified according to composition as oxygen-rich M or carbon rich C-giants.

As these hot gases expand and cool, they reach temperatures at which the condensation of solids is possible. The particles formed collide and grow into the cores of dust particles. Thermodynamic calculations combined with the chemical constituents of the outflows can be used to predict the composition of the resultant particles. In oxygen rich sources, the cores of these interstellar dust particles should consist of magnesium and iron silicates (probably enstatite $MgSiO_3$, ferrosilicate $FeSiO_3$, forsterite Mg_2SiO_4, or fayalite Fe_2SiO_4) (Gilman 1969; Saxena & Ericksson 1983). These silicates would be refractory enough to withstand the heat in their regions of formation, whereas carbon based particles would be destroyed (Duley & Williams 1986). Elemental analysis of meteorites lends supporting evidence to this analysis as magnesium, silicon, oxygen and iron amount to more than 90% of all meteoritic elements (Suess 1964). Thermodynamic theory predicts that in a cooling atmosphere, solid Mg_2SiO_4 (forsterite) forms before solid $MgSiO_3$ (enstatite). Over time, through reaction with the interstellar gas, most of the silicate dust will be transformed into an enstatite stoichiometry (Grossman 1972; Larimer 1979).

As these cores migrate outward from the star, they cool and this allows condensation of carbon onto the surface of the grains (Duley 1985). The majority of this outer mantle is

most likely polymeric hydrogenated amorphous carbon (Jones et al. 1990). In carbon rich outflows it is likely that SiC, and hydrogenated amorphous carbon (HAC) grains will form on their own. An 11.3μm emission band seen in most carbon stars has been assigned to SiC. However, attempts to observe this feature in interstellar absorption have failed (Whittet et al. 1990). Several features attributable to HAC have been observed in carbonaceous outflows and planetary nebulae. A strong 7.7μm emission feature seen in these objects is commonly attributed to a C-C skeletal vibration in aromatic carbon compounds (Cohen et al. 1989). Extended red emission (ERE), a broad emission band centered in the red region of the visible spectrum, is seen in dusty regions throughout the galaxy and is most easily visible in the "Red Rectangle" in Orion. This feature has been identified as bandgap emission in semiconducting HAC (Duley 1985; Witt & Boroson 1990; Furton & Witt 1993).

Other sources of interstellar dust include expanding supernova remnants (Dwek et. al 1983, Dwek & Scalo 1980) and condensation in cold molecular clouds (Draine 1990; 1994). Recently, the rate of grain growth in interstellar clouds and the diffuse ISM has been shown to dominate the various stellar mechanisms of formation (Draine 1990; Jones et al. 1994). This suggests that the dust will have a much broader range of composition than has been previously assumed. Instead of being mostly homogeneous layered structures governed by condensation temperature in a stellar outflow, the structure will be a composite mixture governed by random collisions. In the coldest regions of molecular clouds it is known that molecular ices will form on solid grain cores (Whittet 1992). The interstellar depletion of various elements shows a distinct correlation with the condensation temperature (Whittet 1992).

Interstellar dust grains are also destroyed by various processes, leading to the assumption that they maintain a dynamic equilibrium at the observed space density. These destruction mechanisms include star formation, supernova shock-waves, erosion by sputtering and collisions, and dissociation in energetic regions. Sometimes only part of the grain is destroyed. Depending on the energy deposited by the various mechanisms, volatile outer mantles may be released into the gas phase leaving a more refractory core which can be

chemically altered over time by weak shocks and collisions (see Jones et al. 1994; Dorschner and Henning 1995 and references therein).

2.2 Carbonaceous Grain chemistry

Carbon is one of the most common elements in the universe and is the basis for all of life on this planet. This is because of its amazingly complex and strongly diverse chemistry. It is therefore not surprising that carbon is a very important element in the composition of interstellar particles. To understand the structure of interstellar dust it is necessary to learn about how carbon bonds with itself and with other atoms to form larger particles.

There has been much study of the structure and properties of amorphous carbon (a-C) and hydrogenated amorphous carbon (HAC). An atom of carbon has valency of four and can bond in three basic configurations depending on the orbital hybridization it undergoes. Sp^3 hybridization allows the atom to form a tetrahedral bonding configuration consisting of four single σ bonds while sp^2 hybridization gives the atom a planar trigonal orbital structure consisting of three single σ bonds and a double π bond. Sp^1 hybridization results in a linear chain with two σ bonds and two π bonds.

The sp^3 carbon configuration occurs in crystalline diamond. Tetragonally bonded carbon atoms can be termed either diamond-like or polymeric depending on the density and hydrogen content of the substance. A crystalline sp^2 carbon matrix occurs in graphite and is thermodynamically favoured over diamond. Graphite actually consists of non-interlaced planes of covalently bonded six atom aromatic carbon rings. The crystal structures of graphite and diamond are illustrated in figure 2. An aromatic ring is one in which the π bonds alternate in such a way as to create a resonantly enhanced bonding stability in which the π electrons are delocalized throughout the molecule.

Amorphous carbon in the interstellar medium is probably deposited onto silicate cores in polymeric form with a large atom fraction of hydrogen (Jones et al. 1990). This carbon will

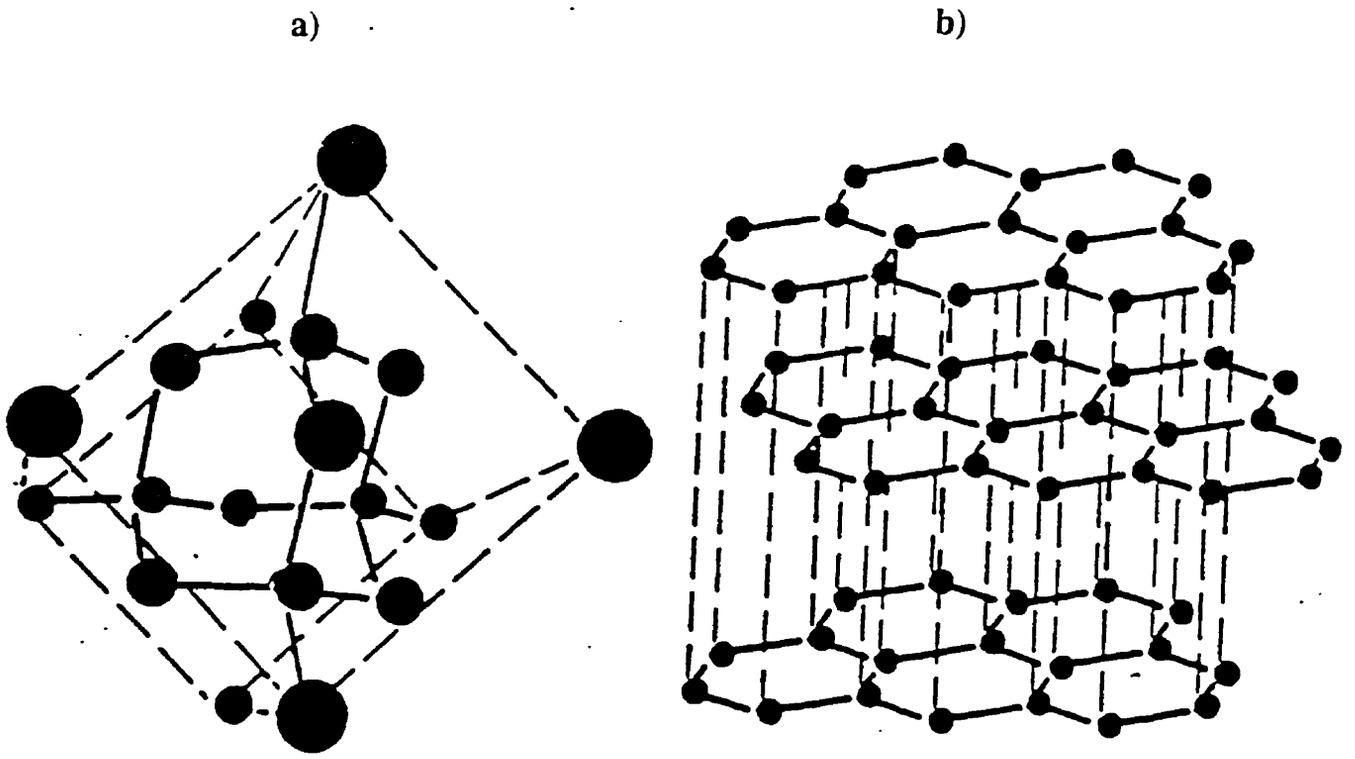


Figure 2 Two different crystalline forms of carbon: a) Crystal structure of diamond; each atom is located at the center of a regular tetrahedron, with four equidistant nearest-neighbour atoms at the four corners. b) Crystal structure of graphite, showing two-dimensional hexagonal arrays with strong bonds between atoms in each plane and much weaker bonds between planes. (Sears et al. 1986)

consist mainly of sp^2 and sp^3 bonded regions. It has been proposed by Robertson & O'Reilly (1986) that in a-C films the sp^2 carbons will preferentially form in planar structures consisting of rings with six carbons each, creating a de-localized electron structure. This is due to the fact that their aligned π bonds have a lower energy than if they were at a non-zero angle to each other. Indeed, the interaction energy between neighbouring π orbitals varies with the dihedral angle as a cosine. The carbon will then be in a lower energy state by forming clusters of aligned π bonds rather than having them distributed throughout the structure. Tight-binding molecular dynamics simulations support the existence of graphitic clusters in a-C (Wang et al. 1993).

The resulting amorphous material has a small band gap (~1eV) and is therefore a semiconductor. The importance of the π states is that they are only weakly bonding, and will thus form both the valence and conduction bands of the semiconductor. Therefore one can basically ignore the σ bond substructure of the film and concentrate on the π bonded areas when analyzing the band gap (Robertson & O'Reilly 1986). It is important to note that the π states in the carbon are only half filled. In this case any π bonded cluster with a gap in its spectrum at the Fermi energy would tend to lower the total electron energy per atom, thus stabilizing the structure. One can assume, to a first approximation, that the graphitic clusters behave as the analogous organic molecules of the same size (Salem 1966). Of those molecules consisting of 5-8 membered rings, six membered benzene is the most stable, having all of its occupied states well away from the Fermi energy. This is shown graphically in figure 3 taken from Robertson & O'Reilly (1986).

The energy of the band gap correlates with the size of these graphitic clusters--the more rings in the clusters, the smaller the band gap. Robertson & O'Reilly (1986) found that for compact (as opposed to linear) clusters:

$$E_g = \frac{5.6}{(M)^{\frac{1}{2}}} eV \qquad 6$$

where M is the number of aromatic rings in a cluster. For most a-C and HAC films the optical

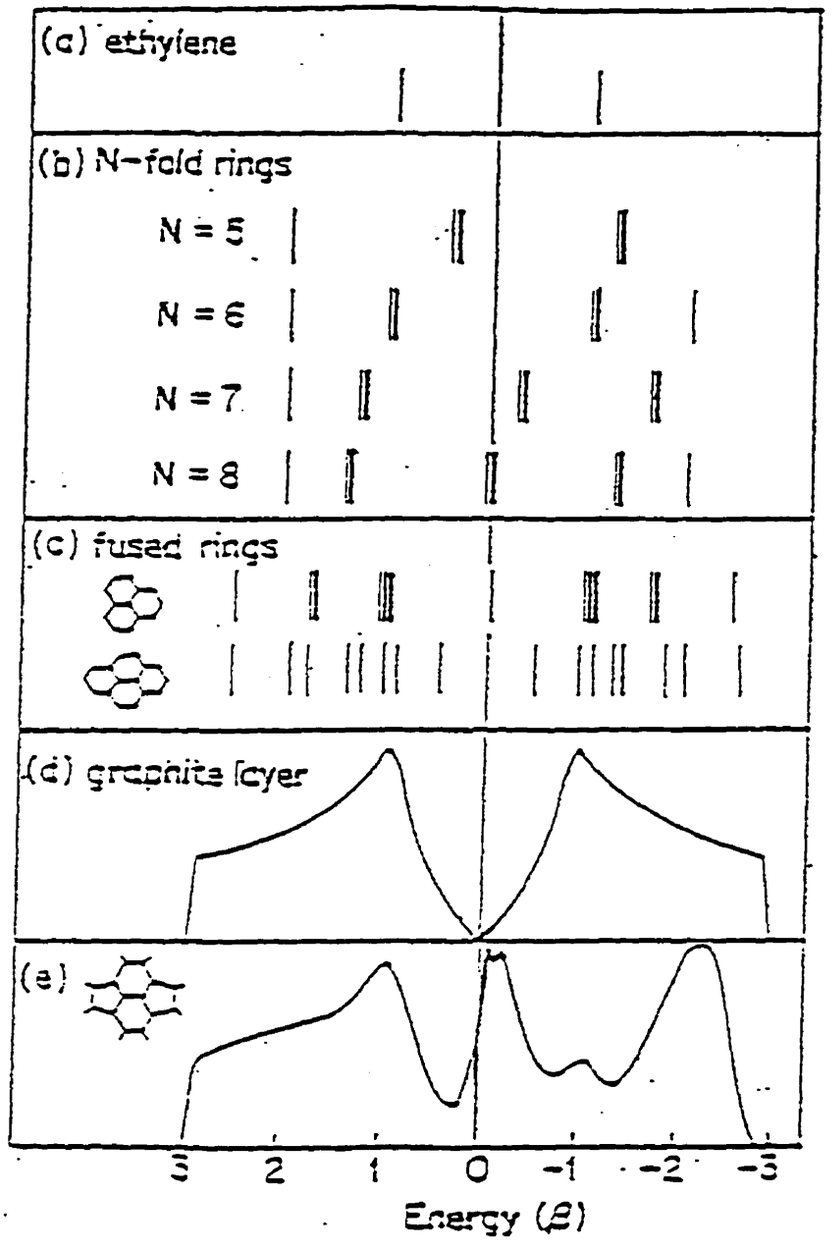
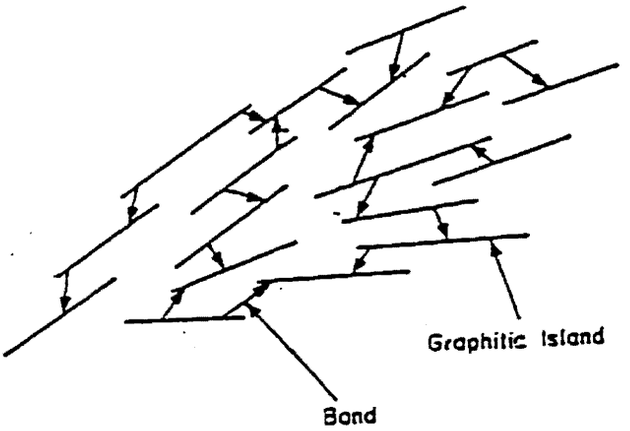


Figure 3 π-state spectra of (a) ethylene, (b) planar rings with N = 5-8, (c) three fused sixfold rings, and four fused sixfold rings, (d) single graphite layer, and (e) layer containing two fivefold and two sixfold rings. Plotted in units of β, the π interaction between two π states, =-2.9eV (Robertson & O'Reilly 1986).

absorption edge is quite broad which implies that there is a large distribution of cluster sizes present. As a consequence, these edge states are controlled not by clusters of average size but by the 1-5% of larger or less compact clusters. Amorphous carbon is estimated to be ~95% sp^2 bonded with an optical gap of 0.4-0.7eV (Robertson & O'Reilly 1986). This would correspond to 15-20Å islands each containing 34-60 rings. In the limiting case of total sp^2 hybridization, the material becomes crystalline graphite which has zero band gap.

The size of these crystalline islands varies with film deposition conditions. The addition of hydrogen will shift the cluster size to the small end of the distribution. Hydrogen does not bond preferentially to either form of carbon, but its inclusion will make it harder for the carbons to form extensive graphitic areas (Robertson & O'Reilly 1986: Angus et al. 1986). This means that HAC films have a larger band gap than a-C films and HAC films containing 30-60% hydrogen show band gaps in the 1.5-2.7eV range. A typical film with a band gap of about 2eV will still contain a considerable proportion (30-40%) of sp^2 sites. An optical gap of this size would require strong clustering of the few planar sites. It is estimated that clusters of four or more fused aromatic rings would be necessary (Robertson & O'Reilly 1986). There is also evidence from the dielectric function that the predominant $\pi \rightarrow \pi^*$ transition is at 5.3eV as in benzene, which would indicate that the predominant graphitic cluster consists of a single six membered ring (Fink et al. 1984). Figure 4 illustrates the internal physical and chemical structure of a HAC solid. It should be mentioned that Efstathiadis et al. (1996) dispute the existence of aromatic structures in HAC, calculating that entropic disorder tends to eliminate aromatic groups in favour of isolated olefinic (sp^2) bonds and non-aromatic rings.

a)



b)

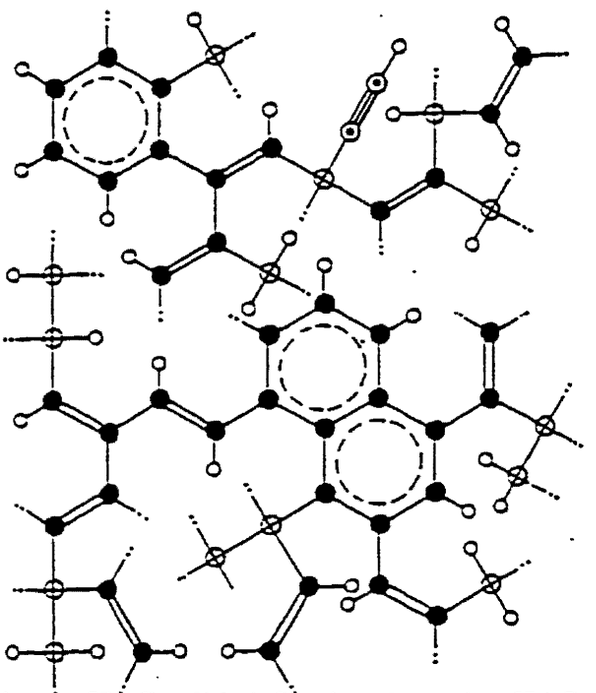


Figure 4 . Schematic of a HAC solid a) Section through a HAC grain of protographitic material loosely bonded through polymeric material to form a larger particle (Duley & Williams 1988); b) Schematic diagram illustrating types of carbon atom bonding in HAC; sp^1 (circled dots), sp^2 (filled circles), sp^3 (circled crosses) and hydrogen atoms (open circles). Double dots indicate bonding to other atoms (not shown) or rare dangling bonds (Jones et al. 1990).

2.3 HAC Grains interacting with the interstellar environment

The destruction of carbonaceous grains may have a large impact on the carbon chemistry of the interstellar medium. Due to the structure of HAC, its break-up can contribute large, stable PAH molecules directly to the gas phase in observable quantities. HAC solids consist largely of compact groupings of six membered aromatic carbon rings loosely interconnected by a hydrocarbon skeleton (Robertson & O'Reilly 1986). If the outer layers of grains consist of HAC, then there are several ways in which complex carbonaceous compounds could be returned to the interstellar gas phase in significant quantities. Fragmentation of HAC is likely to occur in the sp^3 hybridized carbon-carbon (C-C) single bonds which have a smaller dissociation energy than both the C=C double bonds and the aromatically stabilized areas which are analogous to free polycyclic aromatic hydrocarbons (PAHs). Figure 5 shows a schematic representation of the HAC surface showing likely points of fragmentation. Any process that can deposit enough energy onto the grain mantle to break a C-C bond is a candidate for the formation of large gas phase molecules.

Thermal energy can break a C-C bond. The average dissociation energy for a C=C double bond is 6.72eV, and for C-C single bonds it ranges from 3.61 to 3.91eV depending on the hybridization states of the individual carbon atoms (Efstathiadis et al. 1995; Akkerman et al. 1996). The temperatures corresponding to these energies are not commonly encountered under quiescent interstellar conditions. The typical binding energy for an atom in a refractory grain is approximately 5eV (Whittet 1992 p.234), requiring a temperature in excess of 10^5 K for efficient thermal sputtering. Direct thermal dissociation of HAC mantles is unimportant under equilibrium interstellar conditions since the temperatures of the clouds where dust is

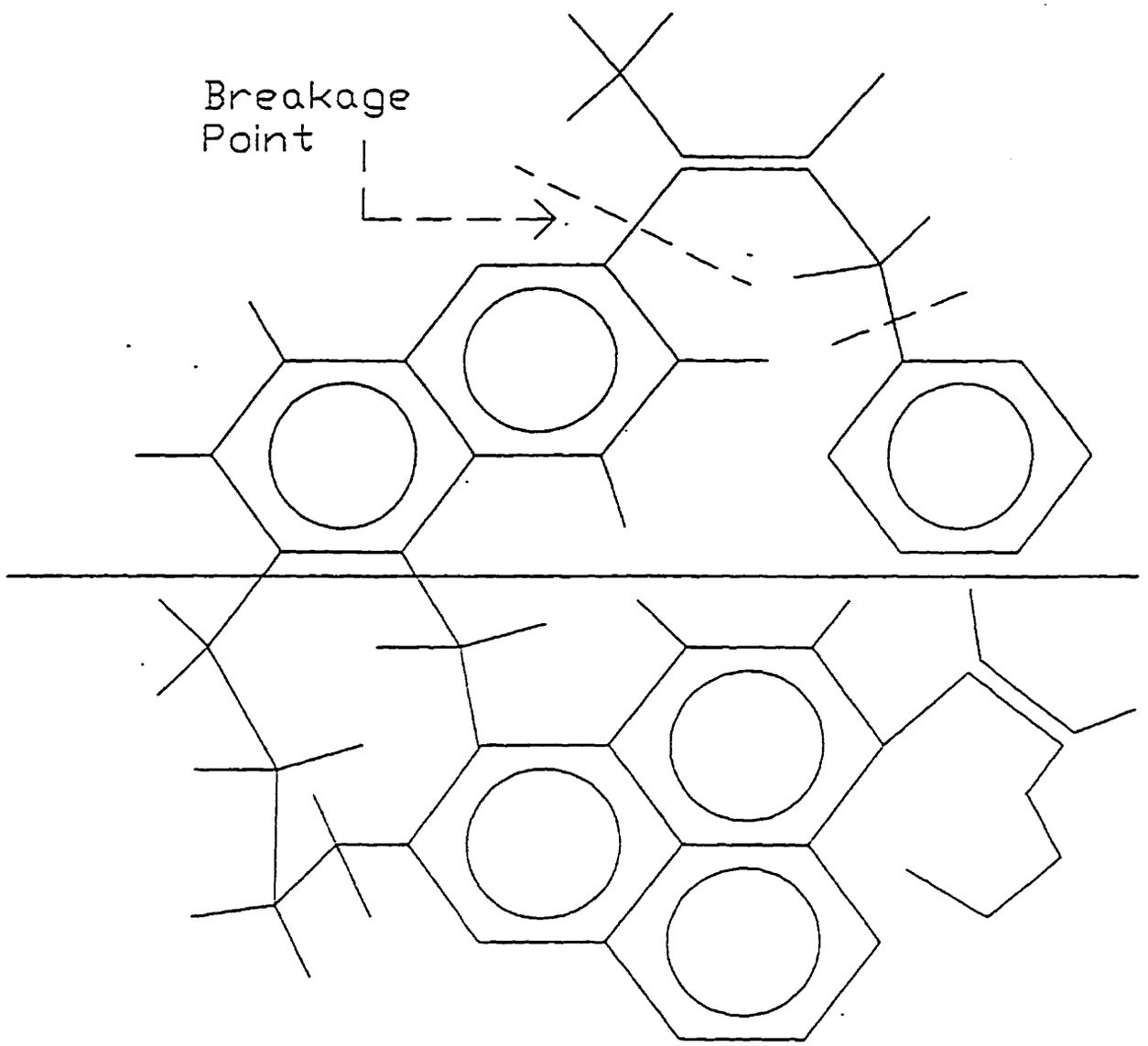


Figure 5 Schematic of a HAC grain surface illustrating likely breakage points which could result in the release of large molecules.

concentrated rarely exceed 100K (Duley & Williams 1984). Interstellar shocks with velocities $\cong$50 km·s^{-1} should supply the necessary energy for dust destruction (Seab 1988 p.303). When temperatures top ~10^3K (Rye 1977, Hsu 1988) the skeletal structure is chemically attacked by bonded and adsorbed hydrogen. The observed result of HAC heating is dehydrogenation and an increase in the graphitic character of the grain. A temperature of ~925K is necessary to drive off all hydrogen and create a pure sp^2 bonding structure (Smith 1984). These extreme temperatures might be reached in energetic regions of the interstellar medium. Dissociation regions and other areas observed in IR emission exhibit a range of grain temperatures, with grains closest to the central star being destroyed by the intense UV radiation. Thermal spiking can occur in very small grains or perhaps in localized areas of larger grains. This is a direct result of minimizing the available modes for equipartitioning of the photon energy. This effect might occur in the loosely interbonded graphitic islands of HAC solids upon absorption of a photon (Duley & Williams 1988; Duley et al. 1993). The saturated sp^3 regions which connect these PAH-like structures might act to thermally isolate them from each other, thus amplifying the thermal effects of locally absorbed photons. This possibility has been disputed, leaving the hotspot mechanism in need of experimental verification (Boutin et al. 1995). Superthermal grain-grain collisions which can occur during shocks would also create a sudden temperature increase which might fragment the mantle or even vaporize the entire grain.

Direct electronic excitation from a strongly bonding molecular orbital to a partially antibonding orbital can result in a large change in interatomic force. These might result in C-C dissociation on a time scale of one vibration but a radiationless transition can redistribute the electronic energy to vibrational modes thus halting the reaction. The timescales of these

processes are comparable ($\sim 10^{-14}$ s). Buch (1989) obtains a photodissociation rate of $\sim 10^{-9}$ s^{-1} for the weaker carbon-hydrogen (CH) bonds in an average interstellar radiation field.

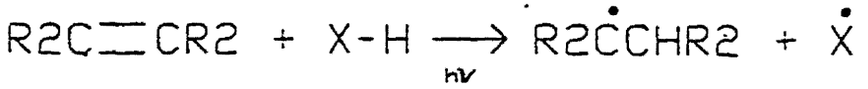
Chemical erosion of C-C bonds can also cause fragmentation. Impurities in the HAC solid can introduce molecular orbitals which are weakly bonding or partially antibonding. These bonds will have a smaller activation energy for dissociation than skeletal carbons. Figure 6 shows a few important chemical reactions.

The other important way that dust grains can affect interstellar chemistry is through desorption of weakly bonded molecular species. Surface catalyzed reactions which require the dissipation of energy are not likely to occur at an appreciable rate in the gas phase. In dark clouds, gas phase atomic depletions are enhanced due to freezing out onto the surface of dust grains at a temperature of approximately 10K (Duley et al. 1989a). Most molecules, upon colliding with the grain, will stick. The dust grain can then absorb excess energy (kinetic or chemical) as heat, and then re-emit in the infra-red. This process allows chemical reactions to occur which would otherwise require a three-body interaction. For example, the formation of H_2 molecules by radiative association is not efficient enough in the gas phase to maintain the observed column densities. Most interstellar hydrogen molecules are produced on the surface of dust grains (Duley & Williams 1984; Pirronello et al. 1997a; 1997b). Dust grains are therefore a very important component in interstellar chemistry.

To correctly characterize the surface of interstellar grains would help in determining the reaction rates of all surface catalyzed reactions. The density and strength of surface adsorption sites are the most important parameters for chemical modelling. From this information it is possible to determine the mobility of surface adsorbed species as well as their time of residence on the grain and their sticking probability after collision.

Example of rehydrogenation of HAC grain:

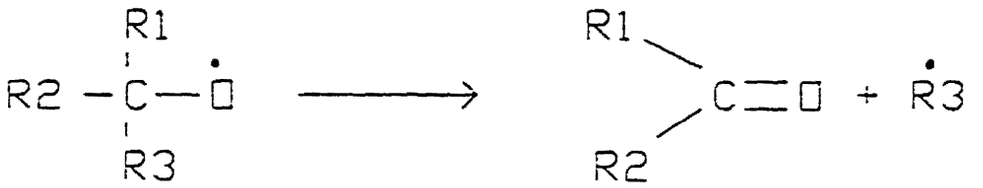
Radical Formation by Hydrogen Abstraction:



This reaction shows how hydrogen can attack the skeleton of a HAC grain and form highly reactive free radicals as well.

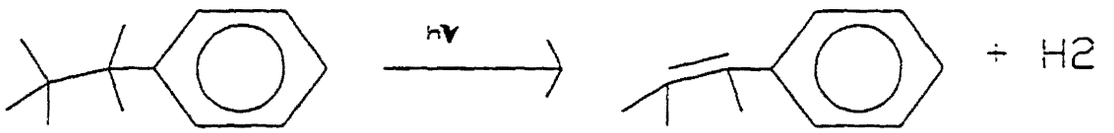
Example of HAC fragmentation:

Cleavage of C-C bond due to presence of oxygen:



This reaction proceeds by freeing the most stable free radical of R1, R2, or R3 from the carbon skeletal structure, producing a ketone.

Example of Dehydrogenation of HAC grain:



This reaction is a possible pathway for the graphitization of HAC grains upon photoprocessing. As the carbon skeleton becomes more graphitic, more stable aromatic rings will form.

Figure 6 Important reactions concerning the fragmentation and decomposition of HAC grains.

Surface catalysis will likely result in the creation of larger and more complex molecules than those formed in the gas phase. Bonding of these molecular groups to the carbon surface will be characterized by bond energies of ~0.5-1.0eV (Vidal-Madjar et al. 1975). This is significantly less than intramolecular bond energies. Therefore, energetic interactions involving dust from dark clouds is likely to remove these large groups from the dust grain surface in preference to the stronger covalent bonds in the HAC substrate.

Duley & Williams (1984) calculate that the column density of large carbon-chain molecules present in diffuse clouds is significant, and that gas phase reactions are unable to form substantial abundances of large ~10 atom molecules in the time available. Their grain fragmentation model predicts column densities ($\sim 10^{11}$ cm^{-2}) for polyynes which are comparable to those observed via rotational transitions towards Cas A, a strong continuum source in the Orion arm partially obscured by diffuse clouds which cause ~5 magnitudes of visual extinction (Bell et al. 1981). Presently, with our improved knowledge of the chemical structure of HAC surfaces we can infer that shocked grains will also be a source of gas phase PAHs (Scott & Duley 1996b; Scott et al. 1997b; Taylor & Williams 1993).

In general, any mechanism which can cause thermal spiking in a dust grain with kT~ adsorption energy is likely to contribute to the gas phase concentrations of large molecules. Included in these mechanisms are excitation of vibrational modes in the grains by:

i) radiationless transitions after photon/cosmic ray absorption.

ii) absorption of energy due to collisions with other interstellar particles.

iii) absorption of energy from surface chemical reactions.

This last mechanism is very interesting in that it can become self-sustaining. One common obstacle in the formation of large molecules on dust grains is the activation energy of

a reaction. Even if the reaction is exothermic, a large activation barrier will inhibit reaction at low temperatures. If the grain temperature is increased by any of the preceding mechanisms, this activation barrier might be overcome. This will in turn release more energy to the grain which might catalyze further reactions in a cascade effect. It is thought that heating of the dust above a critical temperature of about 27K can trigger chemical reactions between ultraviolet-generated radicals. This might result in explosion and dissipation of the entire mantle (Allen & Robinson 1975; d'Hendecort et. al 1982). The resulting gas phase species will depend on the composition of this amorphous layer. Brown et al. (1988) show that the concentration of these radicals may, however, be negligible.

As shown, there are several mechanisms available to break HAC skeletal bonds. As a direct consequence of these mechanisms and the known structure of HAC, there will be a release of large molecules into the gas phase. Most of these large molecules have a limited lifetime in the diffuse interstellar medium (~ 300 yrs.) due to photodissociation (Duley & Williams 1984a: Duley & Williams 1986), chemical sputtering (Allain et al. 1996; Barlow 1978), and dissociative recombination (Millar 1992). Therefore, equilibrium concentrations are expected to be rather low. Based on the mechanisms illustrated, rates of desorption are expected to increase in shocked areas or regions of high photon flux, resulting in an appreciable concentration of large molecules. HAC fragmentation will also be accelerated in these areas. Fragmentation should be able to produce large PAHs, and long chain hydrocarbons due only to the pre-existing arrangement of carbonaceous skeletal bonds in amorphous carbons. Rates of these reactions, however, remain uncertain. Recent observations of emitting nebulae show bands which can be attributed to a mixture of large PAH molecules (see section 2.5).

2.4 Ultraviolet extinction in carbon grains

In the ultraviolet spectral region, the most interesting and significant feature must be the 217.5nm extinction band. Theoretically there are a number of ways to model this band. The historical viewpoint is that this feature is caused by a plasmon resonance in small crystalline graphite particles (Gilra 1972, Mathis et. al 1977, etc.). Mie theory predicts that, for particles in vacuum, at wavelengths where the real part of the complex index of refraction, $\varepsilon_1 \leq -2$, a bulk electron resonance will cause an increase in scattering and absorption.

To determine the response of a particle to an external field one must calculate the induced dipole moment, $\vec{p}$, which is expressed as the product of a polarizability tensor α_{ij} with the applied field $\vec{E}_o$, or as the integral of the polarization per unit volume, $\vec{P}(r)$, over the whole particle (see van de Hulst 1957 for derivation). For simplicity, assume that the applied field is parallel to a major axis of the particle, thus diagonalizing α. In this case:

$$\vec{p} \equiv \alpha_j \vec{E}_o = \int \vec{P} dV \qquad 7$$

Maxwell's equations relate the polarization to the electric field at any point:

$$\vec{P} = (\varepsilon - \varepsilon_m)\frac{\vec{E}}{4\pi} \qquad 8$$

where ε_m is the dielectric constant of the medium ($=1$ *in vacuum*), and ε is the complex dielectric constant of the particle defined as:

$$\varepsilon \equiv \varepsilon_1 - i\varepsilon_2 \qquad 9$$

In general, for an ellipsoidal particle, the induced field, $\vec{E}_i$, is not parallel to the applied field, $\vec{E}_o$. The effect of the particle's polarization on the internal field is expressed generally as:

$$E_{1j} = E_{0j} - 4\pi L_j P_j \qquad 10$$

where the subscript j denotes the three major cartesian axes of the particle.

The depolarization factors, $4\pi L_j$, depend on the geometry and axis ratios of the particle. They will be found later by applying Maxwell's equations as boundary conditions.

The polarizability tensor for a particle small compared to the wavelength of light can then be derived from equations 7-10:

$$\alpha_j = \frac{V}{4\pi} \cdot \frac{\varepsilon - \varepsilon_m}{L_j(\varepsilon - \varepsilon_m) + \varepsilon_m} \qquad 11$$

where V is the volume of the particle.

The depolarization factors are expressed for an ellipsoidal particle with semi-axes l_j as follows:

$$L_j = \int_0^\infty \frac{l_j l_k l_l \cdot ds}{2\left(s + l_j^2\right)^{\frac{1}{2}}\left(s + l_k^2\right)^{\frac{1}{2}}\left(s + l_l^2\right)^{\frac{1}{2}}} \qquad 12$$

with the normalization:

$$\sum_j L_j = 1 \qquad 13$$

As well, the scattering and absorption cross sections depend on the polarizability α of the particle:

$$C_{sca}^{j} = \frac{8\pi}{3}\left(\frac{2\pi}{\lambda}\right)^{4}\left|\alpha_{j}\right|^{2} \qquad 14$$

$$C_{abs}^{j} = 4\pi\left(\frac{2\pi}{\lambda}\right)\mathrm{Im}\left(\alpha_{j}\right) \qquad 15$$

Therefore, by substituting equation 11 into equations 14 and 15, we see that:

$$C_{sca}^{j} = \frac{8\pi^{3}}{3}\frac{V^{2}}{\lambda^{4}}\frac{\left(\varepsilon_{1}-\varepsilon_{m}\right)^{2}+\varepsilon_{2}^{2}}{\left\{L_{j}\varepsilon_{1}+\varepsilon_{m}\left(1-L_{j}\right)\right\}^{2}+\left(L_{j}\varepsilon_{2}\right)^{2}} \qquad 16$$

$$C_{abs}^{j} = \frac{2\pi}{\lambda}V\frac{\varepsilon_{m}\varepsilon_{2}}{\left\{L_{j}\varepsilon_{1}+\varepsilon_{m}\left(1-L_{j}\right)\right\}^{2}+\left(L_{j}\varepsilon_{2}\right)^{2}} \qquad 17$$

One can then see that in vacuum a resonance maximum will occur in the scattering and absorption cross sections of a spherical particle (L_j = 1/3) for ε_1=-2. This situation usually occurs in the vicinity of an absorption peak. For other particle shapes the resonance wavelength will shift according to the depolarization factors as shown in figure 7. As spherical

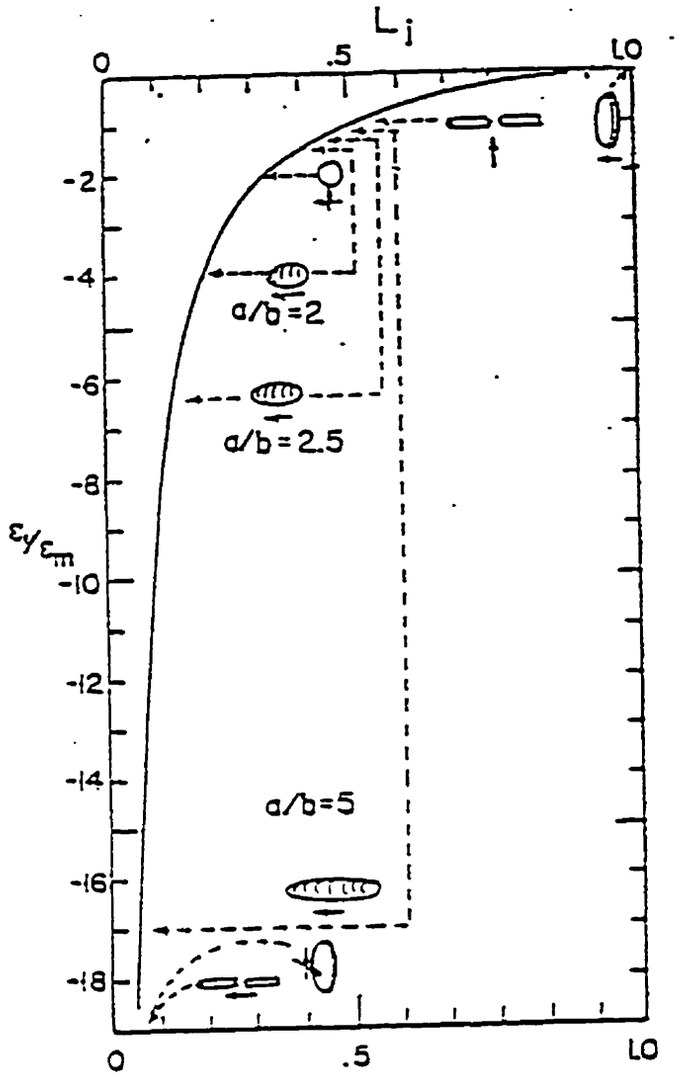


Figure 7 The effect of particle shape on the lowest order surface mode resonanace as calculated in the Rayleigh approximation for ellipsoids. The heavy line is a plot of the function $\varepsilon_l/\varepsilon_m = -(1/L_j-1)$, where $4\pi L_j$ is known as a depolarization factor. Solid arrows next to the various shapes designate the orientation of the electric field vector with respect to the particle axes (Gilra 1972).

particles get larger and begin to depart from the Rayleigh regime, the value of ε_1 where the resonance occurs shifts from the small particle value of -2. This shift is given to second order in the size parameter x by:

$$\varepsilon_1 = -2 - \frac{12}{5}x^2 \qquad 18$$

where $\varepsilon_m = 1$. and $x = \frac{2\pi a}{\lambda}$.

The wavelength at which peak extinction occurs will depend on the size and shape of the particle. For such large scale electron resonances, the existence of bulk crystallinity would seem to be important as well. This peak has never been observed experimentally in the spectrum of crystalline graphite particles (Draine 1989), leading to the conclusion that a true graphite plasmon resonance will be damped out in practical situations. Sorrel (1990) examines the main contributions to plasmon damping in carbonaceous solids.

An alternate theory which avoids the problem of graphite formation in space supposes that a significant part of the interstellar extinction occurs in partially graphitized HAC dust (Sorrel 1990; Jones et al. 1990). The short wavelength extinction is due mostly to sp^3 bonded polymeric carbon while the extinction towards the visible is due to sp^2 bonded graphitic carbon. This spectral region includes the 217.5nm absorption feature. This feature might arise in a-C but would be due to a $\pi \rightarrow \pi^*$ electronic transition in the de-localized electronic structure of the graphitized islands. This strong absorption band would not be an $-\varepsilon_1 = 2$ type resonance due to the absence of long range order and crystallinity.

Amorphous carbon has been found to exhibit a $\pi \rightarrow \pi^*$ absorption feature upon annealing and this absorption intensifies with increasing temperature (Fink et al. 1984). It is known that heating of a-C/HAC to 900K will cause the band gap to approach zero (Dischler et al. 1983a; Smith 1984; Fink et al. 1984). Heating above 1300K causes the diffraction pattern

to exhibit the strong and sharp peaks characteristic of graphite (Fink et al. 1984). This graphitization is accompanied by an increase in absorption near 240nm (Grigorivici et al. 1972). In addition to heat-induced graphitization, photo-darkening has also been shown to occur. Laboratory data show that a-C and HAC can be partially graphitized by exposure to UV radiation (Iida et al. 1984; Jenniskens et al. 1992). This is accompanied by a decrease in bandgap energy and (in the case of HAC) by a loss of hydrogen. Duley & Pinho (1993) have shown that the band gap energy of a HAC sample can change from 2eV to 0.6eV on exposure to 160nm UV radiation in vacuum. Iida et al. (1984) show a bandgap narrowing of 0.14eV in response to 365nm irradiation. Jenniskens et al. (1992) show the effects of UV processing on an amorphous organic residue similar to HAC. The measured bandgap decreases linearly with the log of the UV flux.

A Tauc plot is used to establish the band gap of the material from the knowledge of the spectral dependence of its measured absorption. Plotting $\sqrt{(\alpha tE)}$ vs. E, where $e^{-\alpha t}$ represents the ratio of transmitted over incident intensity, and E is the energy of the photon, often results in a straight line over a range of energies. The details of the relationship between the absorption coefficient, α, and the photon energy in the vicinity of a band gap are described by Tauc (1973). By extrapolating this line to the E axis ($\alpha tE=0$), one can determine the band gap energy for the semiconductor material being studied. Experimentally we find the optical absorption by measuring the ratio of incident to transmitted intensity at a given wavelength. We would expect that the band gap would decrease as graphitization and sp^2 clustering increase (Robertson & O'Reilly 1986; Akkerman et al. 1996).

It has been demonstrated that structural changes can be induced in amorphous materials due to localized heating by individual photons or energetic particles (e.g. Malinovsky 1987; Compagnini et al. 1990). When an ultraviolet photon is absorbed by a graphitic island, there will be a localized temperature increase which could cause chemical rearrangements. The temperature excursion ΔT for aromatic groups of various size in response to absorption of a photon can be roughly approximated by the classical formula:

$$\Delta T = \frac{h\nu}{k(3N-6)} \qquad 19$$

where N is the number of atoms in the aromatic group, hν is photon energy and k is the Boltzmann constant. It is apparent that smaller groups can have larger temperature excursions resulting in more chemical restructuring. This restructuring might result in growth of the graphitic islands, causing the band gap to diminish in size. If there exists a threshold temperature below which no further restructuring will occur, then one can infer that there will be a critical group size for a given radiation field. Therefore, with enough photo-processing, one might expect that the size distribution of graphitic islands would peak at this critical size. Iida et al. (1984) show that photo-induced bandgap narrowing of HAC films saturates after several hours at a value which is dependent on the energy of the photon.

The extinction due to light passing through such a substance can be modelled using Mie scattering theory. Refractive indices have been obtained for a-C (Duley 1984), but this carbon did not exhibit the 217.5nm absorption peak. We assume that this particular film did not contain the expected interstellar size distribution of graphitic islands. The indices calculated from reflection and refraction measurements are not due to a homogeneous bulk medium, but are merely effective refractive indices which take into account the scattering from the graphitic islands as well as absorption. Therefore these indices do not characterize a-C in general, but rather represent one specific micro-crystalline size distribution.

A realistic model for the extinction due to a-C or HAC would be a substance consisting of a substrate material with certain refractive indices, within which is embedded a variable distribution of small particles--the actual distribution being the only free variable of the model. For simplicity, assume that the micro-crystalline particles are spherical, although in reality they would be planar. The substrate material could be represented by diamond, polyethylene, or some hydrocarbon which would mimic the sp^3 regions of the HAC. At first inspection one would suspect that the indices of refraction for graphite should be used for the

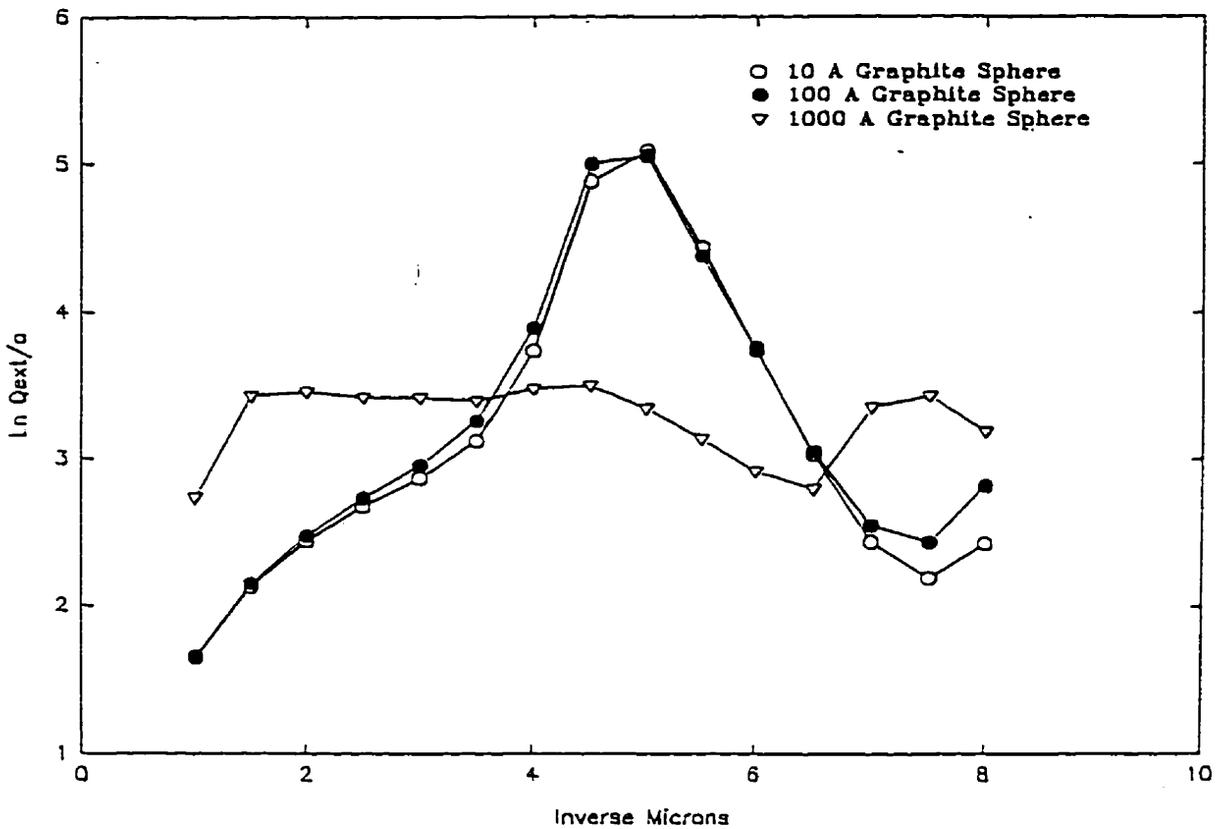


Figure 8 Mie scattering calculations illustrating the size dependence of the graphitic plasmon resonance.

compact sp^2 regions. Assuming sp^2 bonded graphitic spheres of <10nm radius, their scattering is not overly sensitive to the size distribution and consistently shows a peak in the range of 200-220nm which can remain visible for polyethylene coatings up to ~10 times the size of the graphitic particle. See figure 8 for the calculated extinction spectra from graphite spheres of different sizes. For our model to work, different distributions of sp^2 region sizes <10nm in radius must reproduce all observed spectra of a-Cs (e.g. Duley 1984 with no 220nm peak) as well as the astrophysical spectrum showing enhanced absorption at 217.5nm. Using the indices for graphite would give a definite absorption feature for all reasonable size distributions and so would not reproduce all a-C spectra. In reality, graphite is made up of planar sheets which should be modelled as thin disks instead of spheres. Gilra (1972) finds that in the more realistic case of disks the extinction peak occurs around 278nm which is even worse for an interstellar model. Research into the production of fullerenes, however, has shown that these planar sheets will begin to curl up into the third dimension as graphitization progresses (Kroto & McKay 1988), possibly shifting the resonance back towards the spherical value. The reason that the graphitic size distributions do not work as a model is that the indices of refraction used are those for bulk graphite. Very small trigonally bonded carbon subunits will have indices of refraction which differ from the bulk value due to electron path length restriction and quantum and edge effects (Huffman 1977; Cherchneff et al. 1991). A good approximation may be to model the graphitic island using the properties of the analogous organic PAH molecule of the same size (Duley & Williams 1981). If we examine the absorption from solids consisting of these PAH molecules, we see that the absorption is located in different spectral areas for different molecular sizes, and moves to longer wavelengths for the larger molecular species (Platt 1956; Clar 1972; Birks 1970). This makes sense intuitively, as the electrons in the π orbitals of these PAHs are de-localized throughout the molecule. Simple quantum mechanics then suggests that the smaller the localized area the larger the spacing between energy levels. If the distribution of sizes is not strongly peaked, the absorption will be spread out throughout the UV region, while a peaked size distribution will yield a sharp spectral absorption. The

calculated scattering due to 1Å spheres, having the indices of refraction of benzene, embedded in larger sized spheres of polyethylene are shown in figure 9 (the polyethylene represents the polymeric regions of the HAC). Therefore, to successfully model amorphous carbon using Mie scattering one needs a size distribution of sp^2 bonded regions using the indices of compact six atom ring structures like benzene, naphthalene, anthracene, etc. (McKenzie et al. 1983), as well as some linear chains and smaller numbers of odd numbered ring molecules. This distribution would be weighted towards the compact six membered ring structures for energetic reasons as explained previously. If this theory is correct, then a-C produced in the laboratory would have a relatively smooth distribution of cluster sizes ranging up to about 10nm since it does not display an extinction peak in the UV region (Duley 1984). The theory presented here predicts that UV photo-processed a-C will have a modified cluster size distribution peaked at a size which is dependent upon the average photon-energy. This then would produce an absorption peak at an associated wavelength which, for the correct conditions, will be centered at 217.5nm.

Recent theoretical work has acknowledged the likelihood that pure crystalline graphite will not form under standard interstellar conditions (Hecht 1986; Sorrel 1990). The formation of crystalline graphite usually requires a high temperature substrate so that the carbon atoms will be mobile on the surface, overcoming a strong activation barrier to reach the graphitic ground state. Cho et al. (1992) show how an increase in substrate temperature results in an increase in the number and degree of crystallinity of graphite microcrystallites with short-range order of 20-40Å. As well, the presence of atomic hydrogen during the deposition process tends to favour an sp^3 bonding configuration in the resulting material (Angus et al. 1986 p.106). The low temperature hydrogen rich interstellar environment is therefore thought to result in high hydrogen content polymeric HAC solids as one of the main components of interstellar dust (Jones et al. 1990). UV photoprocessed, dehydrogenated HAC has been suggested as the carrier of the 217.5nm band. Small a-C particles (Colangeli et al. 1986; Blanco et al. 1991; Schnaiter et al. 1996) and thermally annealed HAC particles (Mennella et al. 1995) exhibit a

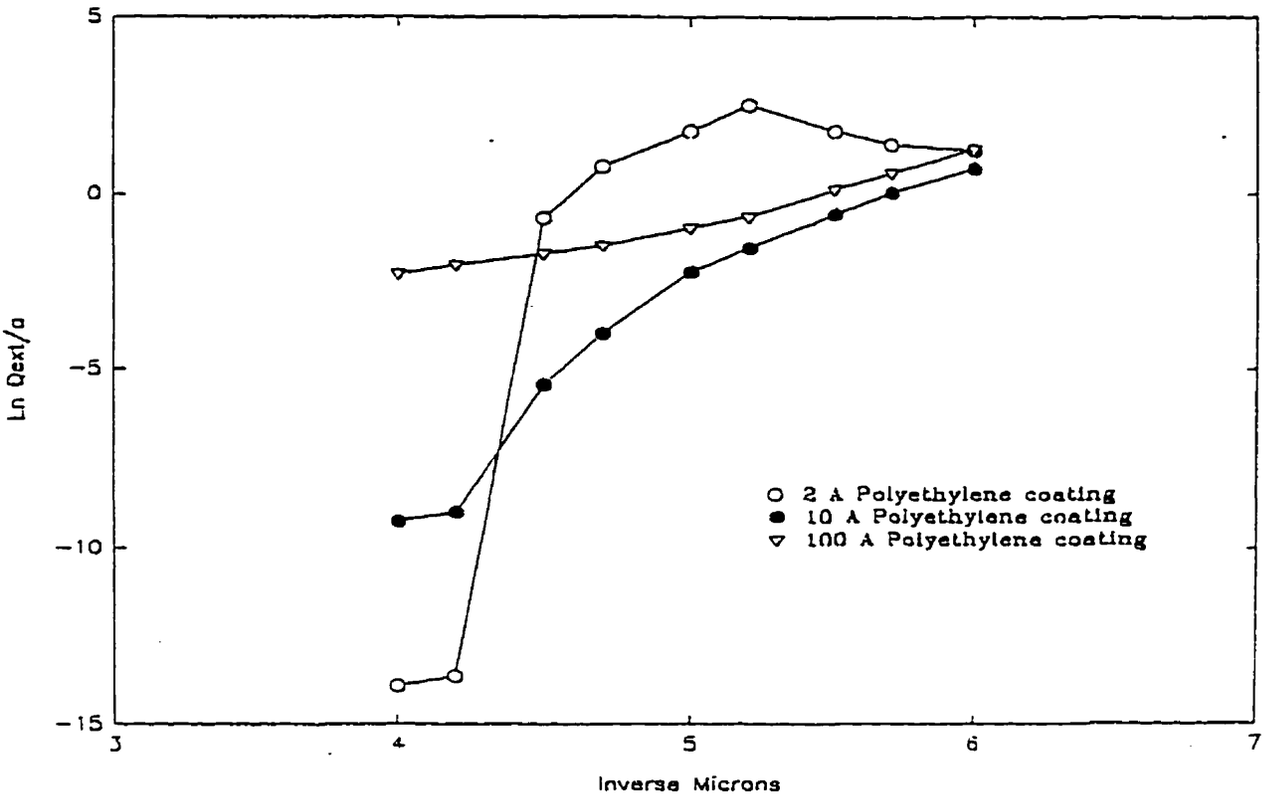


Figure 9 Mie scattering calculation illustrating the extinction from benzene spheres embedded in polyethylene.

broad extinction peak in this spectral region. The presence of hydrogen within the material is seen to diminish the peak (Blanco et al. 1991). Contrary to the results of Blanco et al. (1991), an absorption increase has been seen in this region in thermally annealed HAC films (McKenzie et al. 1983). Recently, Mennella et al. (1996) have shown partial spectra of UV irradiated HAC grains which seem to indicate the emergence of a broad peak in the 215nm spectral region. Similar partial spectra from Mennella et al. (1997) indicate that ion irradiation of HAC grains seems to shift a weak absorption peak from 203nm to 215nm. An opposite trend is observed for a-C grains as the peak shifts from 240nm to 218nm. Guillois et al. (1996) and Papoular et al. (1993) have observed this same spectral feature in reflection measurements on compressed pellets of coal. Experimentally, the absorption peak usually occurs at a wavelength near 240nm, but can be altered by annealing (Mennella et al. 1995) and varying the particle size distribution (Colangeli et al. 1986).

2.5 Carbon in Interstellar Infrared Spectra

Studies in the infra-red spectral region confirm the presence of carbonaceous material in the interstellar medium. The 3.4μm absorption feature is observed to occur on the line of sight to the galactic center in GC IRS6E & GC IRS7 (figure 10). This band seems to be ubiquitous in the diffuse intercloud medium and has been observed along various sightlines (Pendleton et al. 1994; Sandford et al. 1995). It is thought to be caused by the stretching of CH bonds in alkanes of various type. Alkanes are non-aromatic aliphatic hydrocarbon molecules where bonding consists entirely of C-C σ bonds, also known as saturated carbon bonds. Members of this group include methane, ethane, propane, etc., as well as all saturated cyclic or branched hydrocarbons. An alkane functional group is denoted by $R_3C\text{-}CR_3$ and can occur as a structural unit in a molecule containing other functional groups. The other aliphatic carbonaceous functional groups are both unsaturated and are denoted as alkene groups ($R_2C{=}CR_2$) and alkyne groups ($RC{\equiv}CR$). The unsaturated CH stretching features fall at different frequencies and can be easily distinguished from the interstellar absorption feature. Spectra of several materials have been studied in the lab and have been compared to the diffuse interstellar absorption feature with varied degrees of success (Pendleton 1994; Greenberg et al. 1995; Sandford et al. 1995), although general agreement on a particular example has not been reached.

A group of emission features collectively termed the unidentified infra-red (UIR) bands (3.3, 6.2, 7.7, 8.7, and 11.3μm) was first noticed by Duley & Williams (1981) to exhibit peaks in the same spectral region as those of common PAH molecules. A typical spectrum is illustrated in figure 11. These bands are characteristic of aromatic C=C and CH vibrations.

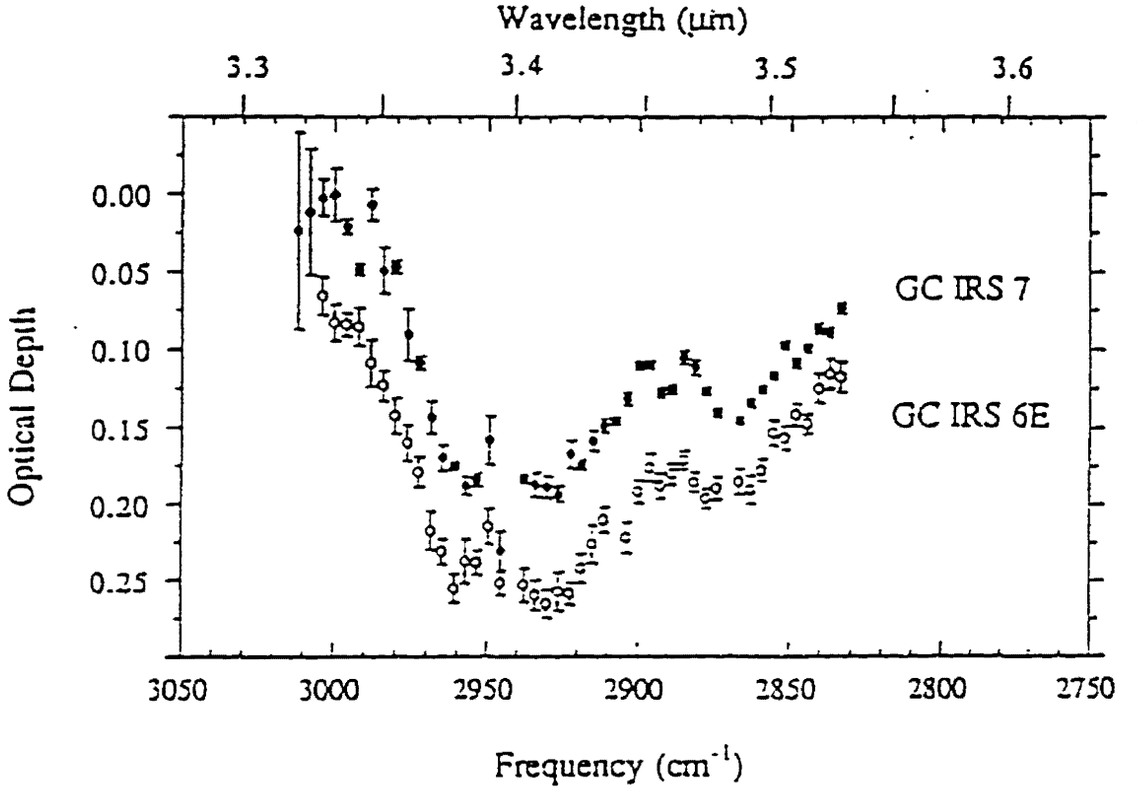


Figure 10 Infrared absorption towards the galactic center sources GC IRS6E and GC IRS7 (Pendleton et al. 1994).

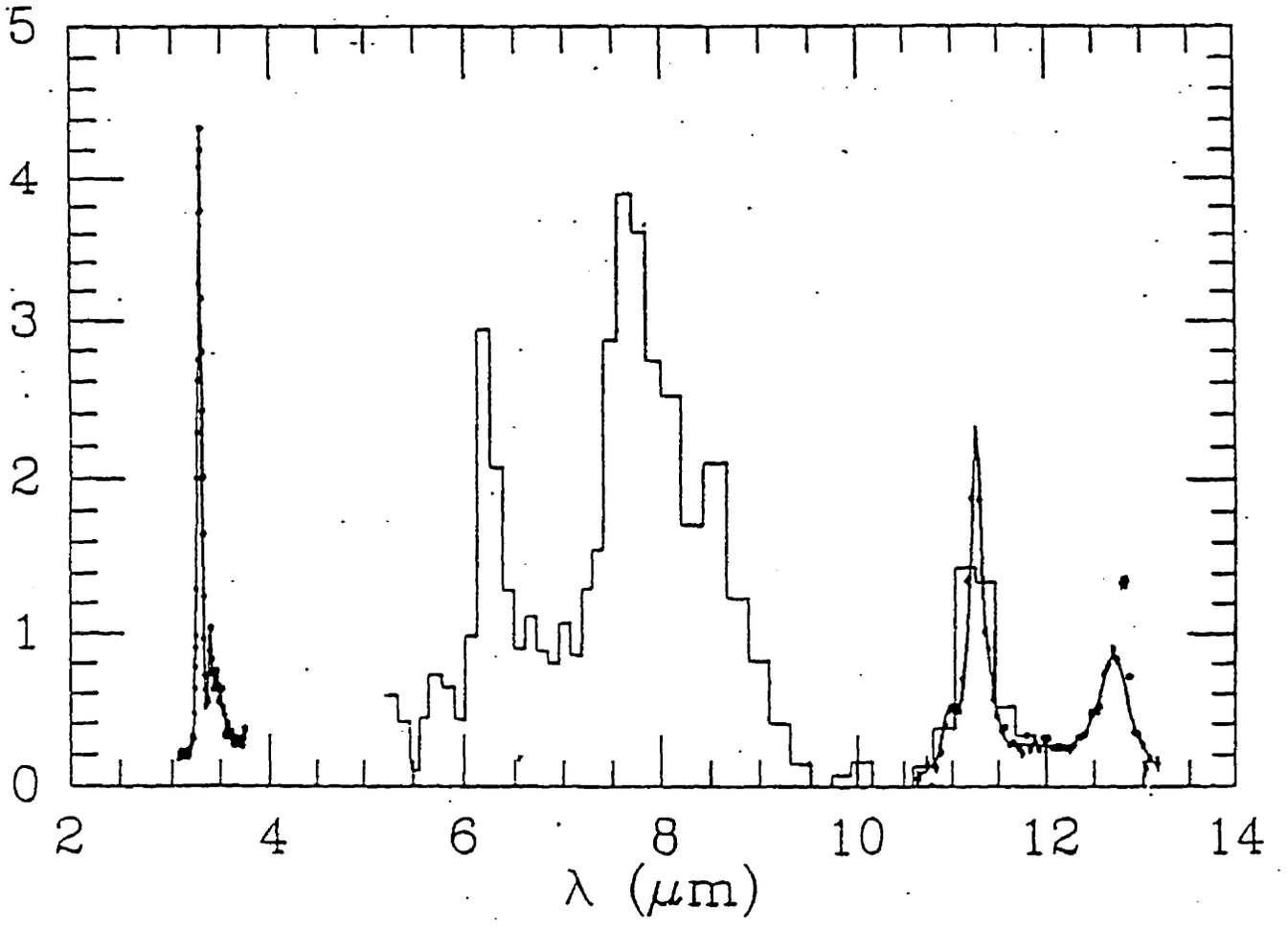


Figure 11 Infrared emission towards the Orion Bar, illustrating the aromatic C=C and CH vibrations typical of UIR emitting regions (Roche 1988).

Much debate has ensued over the major source of the UIR spectral features. Several studies have attempted to link these bands to a distribution of PAH molecules (Léger & Puget 1984; Allamandola et al. 1985; Allamandola et al. 1989; Duley & Jones 1990). Those who favour a solid state origin object to this possibility citing the fact that all of these PAH molecules have strong resonances in the UV which are not observed in the interstellar spectra (Donn et al. 1989; Leach 1987; 1995). Joblin et al. (1992) have shown that a large mixture of neutral PAHs might overcome this difficulty by washing out some of the expected sharp structure into a smooth peak near 220nm. Such a scenario is equally supportive of the solid state origin, since a condensed, partially graphitized HAC solid resembles a mixture of loosely connected PAH molecules. Allamandola et al. (1985) show that PAHs are expected to be ionized in the ISM. Recent experiments on matrix isolated ionized PAHs show that the UV absorption of PAHs is somewhat diminished compared to the neutral species (Lee & Wdowiak 1993; Robinson et al. 1997).

Another objection is that excited PAHs are expected to emit lines in the visible region of the spectrum (Salisbury et al. 1988). Such an interstellar emission has not been observed. Proponents argue that perhaps radical or dehydrogenated PAHs, which have not been studied quite as extensively in the lab due to practical difficulties, might not show spectral features in this region. Another possibility is that internal conversion of the energy from an absorbed photon will occur in the larger, more stable PAHs effectively preventing significant emission of the more energetic visible photons (see Allamandola et al. 1989 for a more complete description). Internal conversion is the name for a process in which an excited molecular bond relaxes to a lower energy state by transferring its energy to the surrounding bonds in the molecule. A radiationless internal conversion will result from the interaction of an excited

electronic state with the higher vibrational levels of a lower electronic state. If the internal conversion rate is much faster than the emission rate ($\sim 10^8 s^{-1}$ for allowed transitions) then there will be little chance of visible photon emission from the particular PAH. Because of this possibility the diffuse interstellar bands (DIBs), seen only in absorption throughout the visible region of the interstellar spectrum, have also been attributed to a mixture of PAHs (Léger & d'Hendecourt 1985; van der Zwet & Allamandola 1985; Crawford et al. 1985; Ehrenfreund et al. 1992; Parisel et al. 1992; Salama et al. 1996) although we must await experimental verification of these claims. If this identification is correct, then the broad width of these bands (0.4-100Å) might be attributable to the extremely short lifetime of the initial excited state produced by absorption of a visible photon (van der Zwet & Allamandola 1985). To cause an observable broadening of $1 cm^{-1}$, the lifetime of the unstable state follows from the Heisenberg uncertainty principle and is given by:

$$\Delta\tau \geq \frac{1}{4\pi c \Delta \upsilon} \qquad 20$$

In this case, the lifetime $\Delta\tau \leq 3 \times 10^{-12} s$ is four orders of magnitude smaller than the photon emission process. This result implies that any state which is observably broadened by internal conversion would not generally be seen in emission.

Proponents of the 'pure PAH' model argue that HAC solids, being larger than PAHs in general, are not expected to reach the observed IR colour temperatures by absorption of light alone. Due to the large number of vibrational modes available to a HAC grain, photo-absorption should result in purely thermal grain emission. It should be noted at this time that HAC is observed to fluoresce in the visible upon UV absorption. This broad band-gap emission centered near 640nm wavelength is identifiable as the extended red emission (ERE) seen in

energetic nebulae (Duley 1985; Witt & Boroson 1990; Furton & Witt 1993). The possibility that lower energy bands could be excited in a non-thermal manner leads into the raging debate over the efficacy of the 'hotspot model' for thermal spiking in HAC solids.

Several authors have noted that the near IR colour temperature of most objects is on the order of 1000K, regardless of the distance from or temperature of the central source (Sellgren 1984, Sellgren et al. 1985; Léger et al. 1988, Roche 1988). The colour temperature is calculated by fitting a gray body spectrum to the observed near IR continuum of the astronomical source (Sellgren et al. 1983). This is evidence for an origin in very small grains or large molecular entities (~40-100 C atoms, ~10Å radius) which could exhibit thermal spiking upon absorption of a single UV photon (~10eV). They argue that HAC grains, with many more vibrational degrees of freedom than a PAH molecule, would vibrationally redistribute the incoming energy on a timescale of 10^{-11}s, much faster than the timescale necessary for IR emission (~10^{-2} - 1 s). Thus HAC solids should not exhibit non-equilibrium IR emission. HAC proponents have countered with the controversial 'hotspot' model in which the aromatic islands in the HAC grain are poorly connected by the aliphatic bonds in such a way as to slow the transfer of vibrational energy and concentrate absorbed photonic energy in a single aromatic entity (Duley & Williams 1988, Papoular et al. 1988). This would make the HAC grain respond like a collection of smaller aromatic entities which could each undergo thermal spiking upon absorption of an energetic photon. Boutin et al. (1995) counter, noting that experiments quoted as evidence for thermal decoupling (Malinovsky 1987), although they do show localized annealing effects, fall short of the time-scale necessary for emission by several orders of magnitude. At this point it seems likely that the hotspot model is in need of stronger experimental evidence if it is to be salvaged as a viable method of producing all of the observed

emission. It may very well be that some mixture of HAC and PAHs is necessary to account for the UIR bands.

Work along these lines has been reported by Rosenberg (1988) who has investigated pulse excitation due to low thermal conductivity of amorphous materials. It might be possible that an extremely low density fractal grain will show the necessary thermal localization effects. The theoretical basis for this effect centers on high energy phonons whose wave-vectors are larger than the associated mean free path in a highly scattering medium. Such phonons cannot be transmitted and will remain localized in the area of excitation.

The observed near-IR continuum in reflection nebulae might also be contributed to by band-gap emission from graphitized HAC. The ERE which is observed in many reflection nebulae has been identified as bandgap emission from polymeric HAC (Duley 1985; Whittet 1992). If some of the dust in reflection nebulae is being processed toward a more graphitic state, then the bandgap will narrow and the ERE will shift to longer wavelength (Iida et al. 1984; Furton & Witt 1993). Such low band-gap HAC emission might resemble a hot thermal continuum.

Mixtures of PAHs also exhibit very little continuum extinction, requiring a solid state admixture of dust to contribute this component. Some authors suggest that coal can be used as a model for a large distribution of PAH molecules (de Muizon et al. 1990). Papoular et al. (1988) and Guillois et al. (1996) have shown that observed IR emission features correspond roughly in position to absorption features seen in vitrinites and semi-anthracite coals (figure 12). These coals seem to resemble solid state HAC more than they would a free mixture of PAH molecules. Their carbon bonding structure is of biological origin ranging in composition from highly polymeric to highly graphitic.

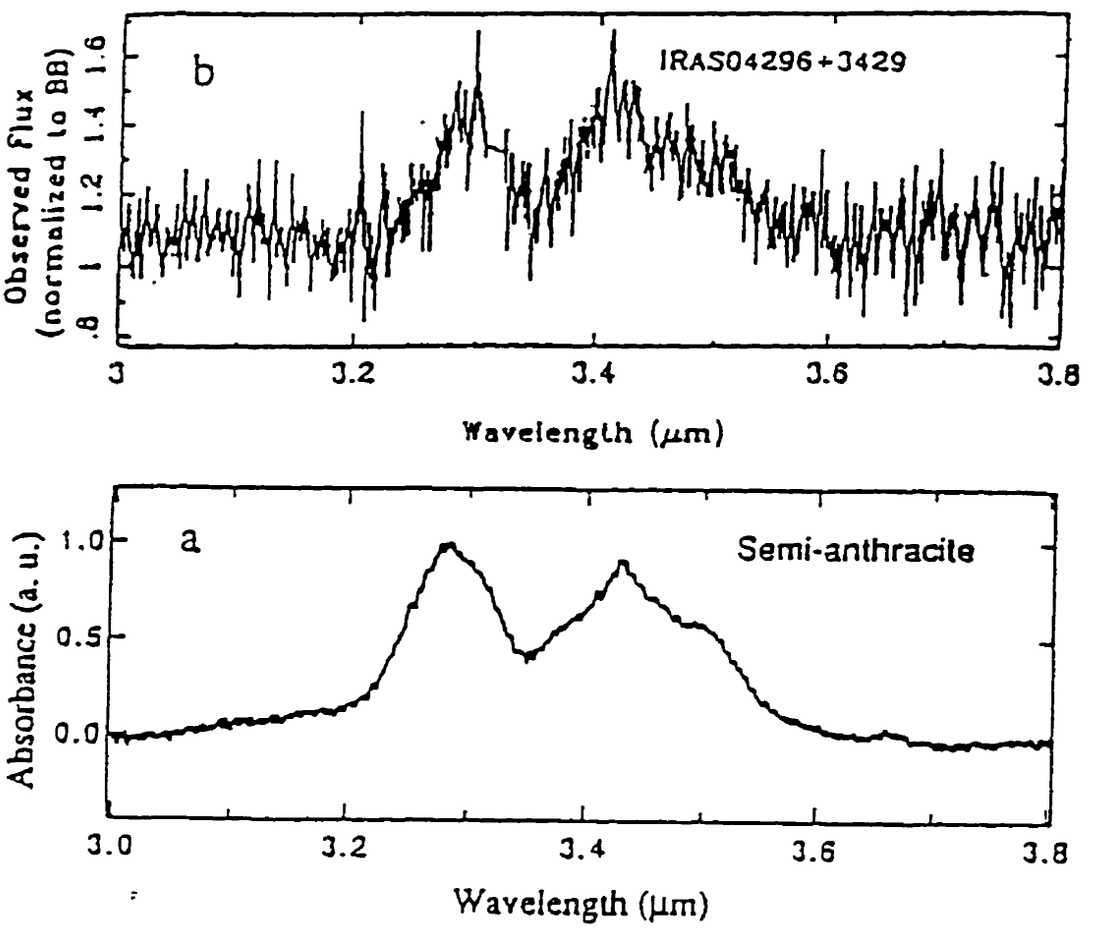


Figure 12 Comparison of infrared emission from IRAS 04296+3429 to absorption from semi-anthracite coal (Guillois et al. 1996).

Léger et al. (1988) suggest that the observed differences between IR emission and absorption can be explained by a two component system of large grains and PAH molecules. In such a system, the large dust grains would dominate the diffuse medium absorption due to their size, but would be ineffective as UIR emitters by the same criterion, maintaining a thermal equilibrium based on their distance from an exciting source. These high UV flux areas would exhibit non-thermal emission from the free PAH molecules. De Muizon et al. (1988) point out that the 3.4 and 3.5μm emission features remain unexplained in such a scenario, requiring a colour temperature greater than 2000K to excite the higher order vibrational overtones in this region. It is possible that IR active sidegroups on PAH molecules could provide the necessary emission (Talbi et al. 1993; Geballe et al. 1994; Bernstein et al. 1996).

An important diagnostic for the presence of interstellar hydrocarbons is the CH IR stretching band. This vibration occurs at 3.3μm in aromatic compounds and at 3.4μm for aliphatic hydrocarbons. The strongest UIR band occurs at 3.3μm, illustrating the aromatic character of the typical emitter. A small multi-peaked side band is often observed at 3.4μm possibly indicating the additional presence of aliphatic emitters. The variation of the 'R' = 3.3/3.4μm peak intensity ratio has been observed in several sources. Magazzù & Strazzulla (1990), observing planetary nebulae (PNe), noted that R decreases from ~1.6 to ~1.2 with increasing size (and age) of the source (figure 13). Roche et al. (1996) observe that R is negatively correlated with nitrogen abundance in 'normal' emitters, falling roughly into two separated groups of high and low R. One group has very weak or undetected 3.4μm band emission which is independent of the 3.3μm equivalent width, and the second group shows increasing 3.4μm band emission with increasing 3.3μm emission: this second group consists of nitrogen-rich objects. This correlation may be due to one of two factors, one of which might be

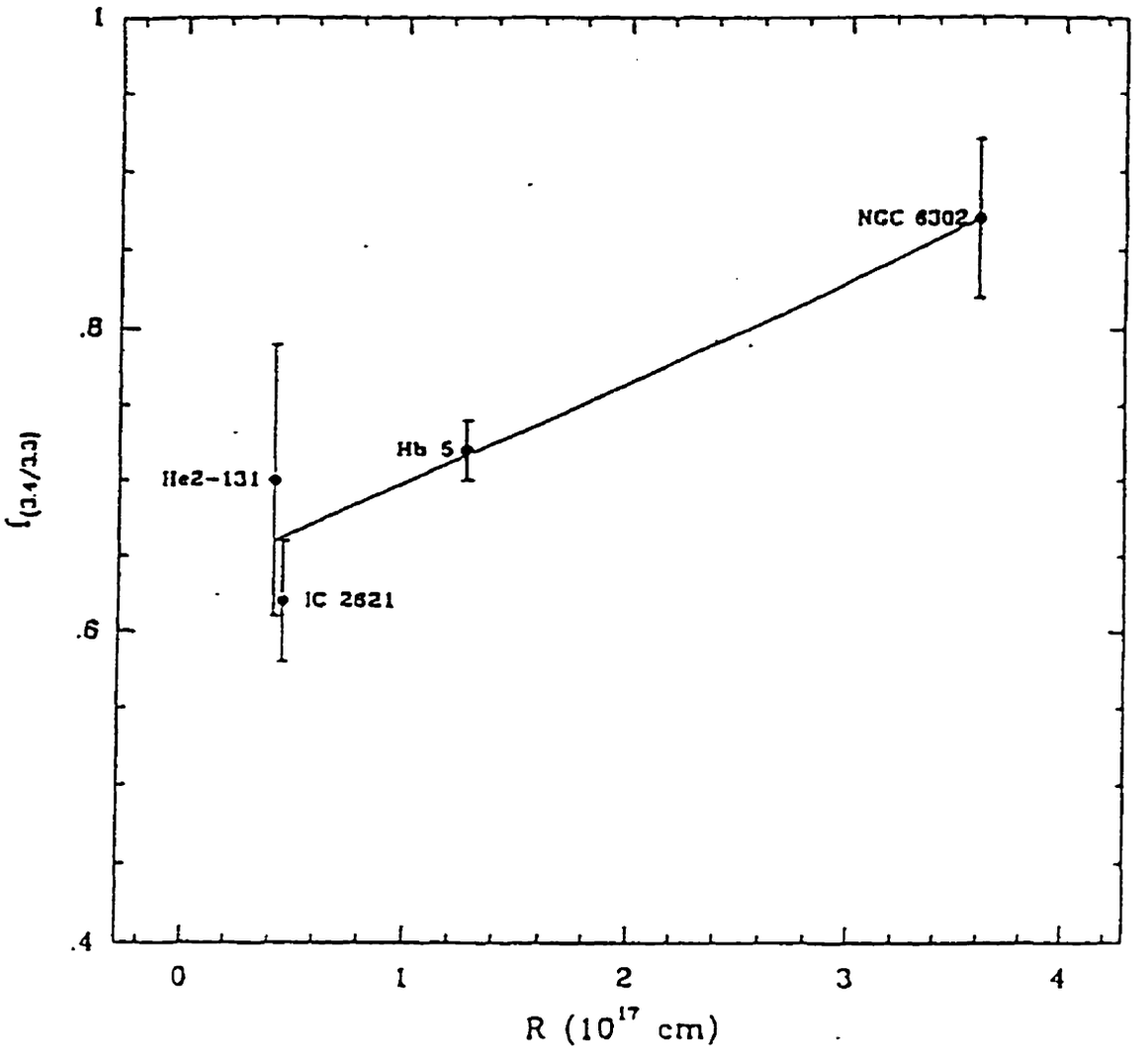


Figure 13 Graph illustrating the relationship between size and 3.4μm/3.3μm flux ratio for planetary nebulae (Magazzù & Strazzulla 1990).

that cold molecular clouds have a broad absorption from 3.3-3.6μm which remains unidentified. Whittet et al. (1996) conclude that this long wavelength wing of the strong 3.08μm water-ice band is likely due to a mixture of ammonium hydrate and other nitrogen-bearing molecules. Roche et al. speculate that N-rich polycyclic molecules are contributing to the emission complex between 3.4 and 3.6μm. The second possibility is that a different property of the N-rich nebulae is contributing to the strong 3.4μm band. High nitrogen abundance is often associated with more massive precursors in planetary nebulae. This gives rise to a larger nebula with a cool outer shell. This fact is consistent with the 3.4μm carrier surviving only in zones farther from the central star amongst neutral, cooler material, similarly to the results of Magazzù & Strazzulla (1990).

The width of the interstellar 3.3μm feature also varies from region to region. Observing the IR emission from HD44179 'the Red Rectangle', Geballe et al. (1987) recorded a fairly 'normal' off-source spectrum. The spectral width of the 3.3μm peak in Geballe's data is the same as that of NGC 7027, another 'normal' UIR emitter. Later, Tokunaga et al. (1988) observed an anomalously narrow 3.3μm feature in the spectrum of HD 44179 showing no evidence of the 3.4μm feature (figure 14). The only difference in method was that Tokunaga's spectrum was taken with a narrow beam aperture centered on the source. This indicates a change in the emitting material as one moves away from the central star. The increasing width of the 3.3μm peak as one moves away from the star likely reflects the increasing range of radiative environments which the aromatic emitters are experiencing. This observation can be explained in the PAH model as growth from initially small PAH molecules to larger entities as one moves out from the star (Allamandola et al. 1989). The narrow peak observation is also

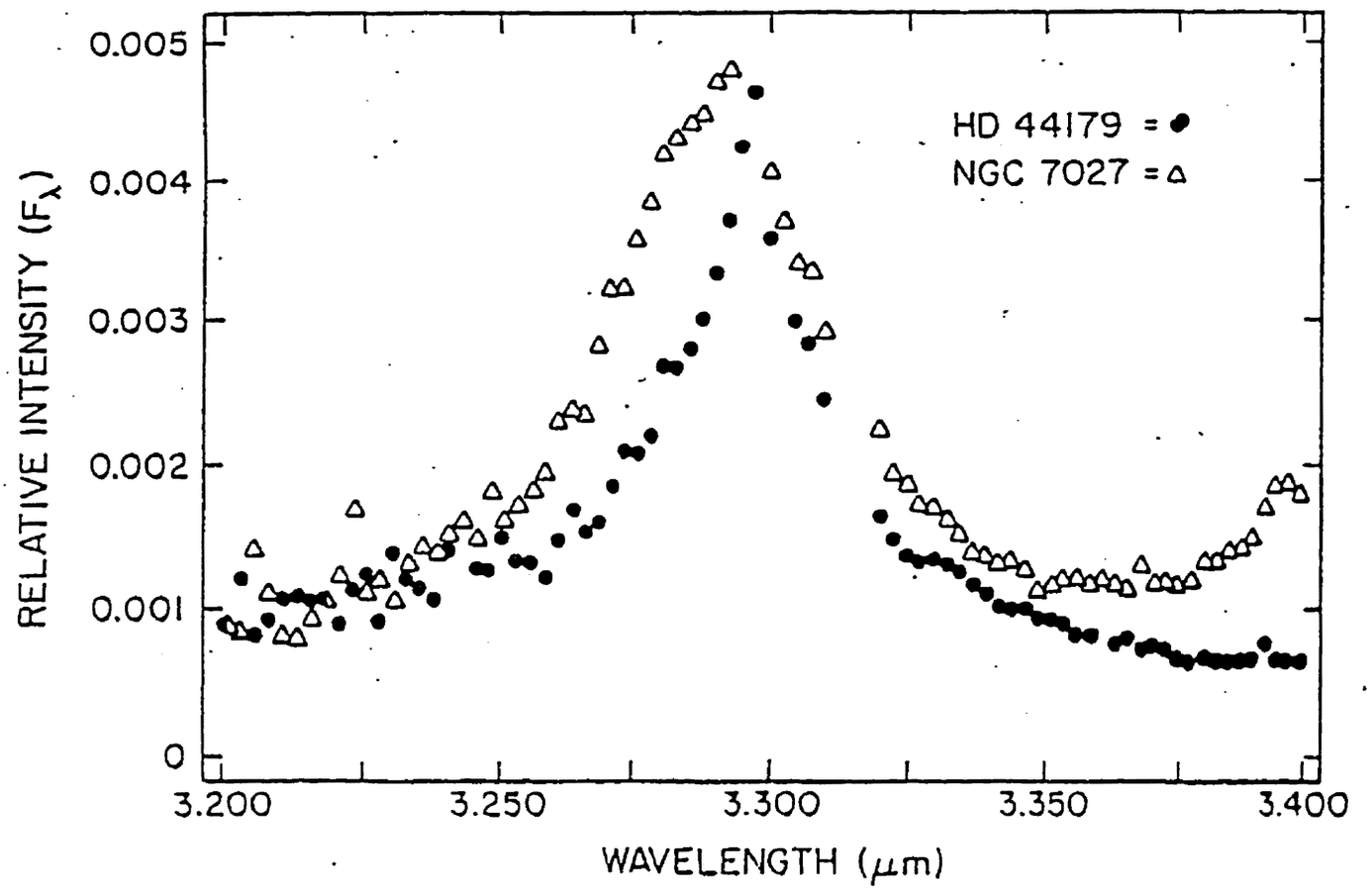


Figure 14 Observations of UIR emitters HD 44179 (The Red Rectangle) and NGC 7027 illustrating variations in 3.3μm peak width (Tokunaga et al. 1988).

consistent with a model in which a range of PAHs are being formed from dust as demonstrated by Scott & Duley (1996b) and Scott et al. (1997b), with the least stable ones being destroyed in the highly energetic region nearest the star.

3. EXPERIMENTAL SYSTEM

3.1 UV Spectrometer with In-Situ Sample Preparation

The experimental apparatus for UV spectroscopy is illustrated in figure 15 (Scott & Duley 1996a). It consists of a Hellma Cells V05 ruggedized high output deuterium lamp with a magnesium fluoride output window which is scanned through a Minuteman Labs Inc. 302VM monochromator with an aluminum-magnesium fluoride coated holographic grating over the wavelength range 300-140nm at a rate of 4nm·min^{-1}. The preliminary detector is an EMI 9558Q photomultiplier while the main detector is a Hammamatsu 9189 photomultiplier with signal output to a photon counting apparatus operating in ratio mode to eliminate lamp fluctuations as a possible source of error. In front of each detector is a thin fused silica window coated on the vacuum side with sodium salicylate. This substance fluoresces in the visible upon the absorption of an ultraviolet photon with quantum efficiency approaching one and allows the detection of photons outside the normal wavelength range of the detectors. For maximum efficiency, the thickness of the sodium salicylate coating should result in a white film which is translucent to opaque optically. If the coating is too thick it results in a loss of photons through multiple scattering. Conversely, if it is too thin, many of the high frequency photons will not interact with the substance and will end up being absorbed in the quartz window. The photon counter sends a digital signal to a custom built microprocessor system. The 8052 based controller, described in Appendix 1, synchronizes the photon counter to the wavelength of the monochromator through an encoder-decoder circuit and a counter control line. The wavelength is calibrated for each spectrum using the deuterium line at 486nm and the observed ratio of 4 encoder pulses/Å. The slits are set at 30μm for a good signal to noise ratio giving a measured spectral resolution $\Delta\lambda/\lambda$ of approximately 5×10^{-3} at the 486nm deuterium peak. For increased resolution during the calibration process, the slits are narrowed to ~15μm. Both

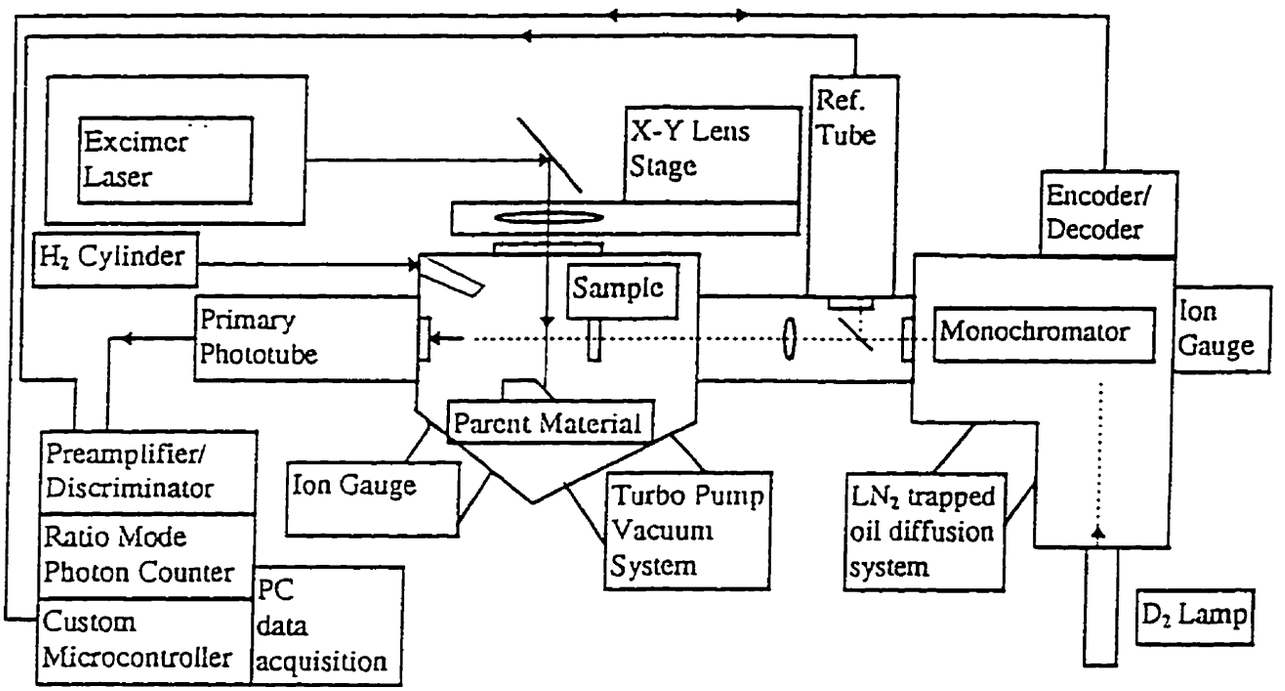


Figure 15 Block diagram of UV spectrometer with in-situ sample deposition.

monochromator and sample chambers are evacuated to base pressures from 6-10x10^{-6} torr using a well-trapped oil diffusion pump for the monochromator and a Varian V-60 turbo pump on the main chamber. This choice eliminates hydrocarbon contamination of the sample. This can be an especially troublesome source of error if the sample is being studied at cryogenic temperatures. Originally the apparatus consisted of nitrogen trapped mercury diffusion pumps. Operating at cryogenic temperatures, the spectrum was constantly being contaminated by a growing absorption feature of mercury, matrix isolated in water ice, at approximately 180nm. If it is necessary to take spectra at low temperatures, the effects of various ices must be carefully eliminated. The use of a cold radiation shield helps in this regard, as its larger surface area will tend to adsorb most of the available impurities.

The sample substrates consist of 1mm thick magnesium fluoride windows which are mostly transparent down to about 120nm. Due to absorption in the optics and scattering by the sodium salicylate, signal levels become very low at wavelengths shorter than 140nm. If the sample is highly absorbing in this region the transmitted signal will be negligible and the resultant spectrum will resemble an inversion of the deuterium lamp emission spectrum. In effect, what is happening is that the main detector is counting photons from dark counts and scattered light only. The count rate will be effectively constant, while the bin time is regulated by the preliminary detector. Thus, when the lamp signal is highest, the counter output will be small due to the smaller integration time. The effect of dark counts can mostly be eliminated by taking a spectrum with the main phototube shutter closed. This process assumes that the lamp output is relatively constant between runs, but it is necessary for improving the signal to noise ratio at the short wavelength end of the spectrum. Scattered light can also produce an artificial peak at the limit of detectability. This common artifact was seen in all of our spectra below 140nm. This stray light originates from surface reflections, imperfections in the optics, diffraction effects and optical aberration. When making measurements at an absorbance maximum, the shorter and longer wavelength parts of the stray light are attenuated less so that the measured absorbance is too low. This has the effect of creating an apparent absorption

peak where none exists. Another observable effect is that of overlapping orders in the spectra. The deuterium lamp has an intensity peak near 160nm which can be aliased up to 320nm. This is the reason that our spectra were recorded below 300nm only. The effect of this problem is to create another apparent absorption peak in the spectrum. This is because the absorption at 160nm is much greater than that at 320nm in most cases. Therefore, the apparent absorption at 320nm will be increased relative to the transparent substrate.

The samples are deposited by laser induced vaporization from a solid rod of graphite or mineral silicate, depending on the experiment, in vacuum or hydrogen atmosphere. The laser was a XeCl Lumonics Hyper-Ex 400 excimer laser operating at 10Hz with a pulse energy of approximately 70mJ at a wavelength of 308nm focused onto a spot of approximately 1mm diameter. This results in a fluence of approximately $9J \cdot cm^{-2}$ on the target during the 30-50 nsec laser pulse. Molecular hydrogen, when present in the deposition chamber at a pressure of 0.1-1torr is dissociated by the energetic plasma and becomes incorporated into a HAC film. At pressures >1torr, the extent of the visible plasma is greatly diminished, and most of the carbon is probably incorporated into methane before it can deposit. At pressures <.1torr, the hydrogen content of the HAC film is negligible. The plasma created by the laser surface interaction was collected by a spectroscopic substrate placed a distance of 2-3cm from the target resulting in an amorphous thin film. These substrates were mounted on a cold finger which can be cooled to 77K with liquid nitrogen. No more than 5 minutes were necessary to produce near opacity in the far UV portion of the spectrum with a thickness on the order of 100nm. For ir absorbing and emitting films, larger thicknesses were required. 40-60 minutes of ablation produced films on the order of 1μm thickness.

For UV photo-processing of the films, the unfiltered spectrum of the deuterium lamp was incident at 45° upon the sample surface. Spectral studies indicate that the photon flux below ~140nm was being absorbed in a thin coating on the output window of the lamp, contributing a negligible amount to the total flux. The photon flux at 160nm is typically $\sim 1.4 \times 10^{12}$ photons$\cdot cm^{-2} \cdot sec^{-1} \cdot nm^{-1}$ (Key & Preston 1980). The integrated photon flux over the

140-300nm range at the surface of our samples is estimated by integrating the measured output intensity spectrum, normalized to the absolute radiance given in Key and Preston (1980), and then correcting for losses due to absorption in the optics. The resulting value is approximately 2.7×10^{14} photons·cm^{-2}·sec^{-1}. One can then estimate the total UV exposure of these films and relate this value to a time base for carbonaceous dust particles in the interstellar medium. Quantitatively this exposure is estimated to be 9.8×10^{17} photons·cm^{-2}·hr^{-1}. Since the integrated interstellar flux between 100-300nm is $\cong 5 \times 10^{6}$ photons·cm^{-2}·sec^{-1} inside a diffuse cloud with A_V=0.5 (Habing 1968, Duley & Williams 1984), one hour of this exposure would be equivalent to 6.2×10^{3} years under interstellar conditions. For long processing times (~48hrs), the effects of the photoprocessing should be comparable to the effects experienced over the lifetime of a young interstellar grain of $\sim 3 \times 10^{5}$ yr. age. This analysis assumes that the photons above 140nm wavelength are sufficiently energetic to produce similar effects to the full interstellar radiance spectrum. If important effects are taking place at higher energies they will not be observed here.

3.2 FTIR Spectroscopy

The infrared emission spectra were taken using a Bomem MB-100 Michelson interferometer. This apparatus has a selectable resolution up to 1 cm^{-1} but is typically used at 4 cm^{-1} for our purposes. The optics consist of a KBr external emission port and gold coated mirrors, while the detector is a liquid nitrogen cooled MCT model D11B. The quoted spectral range is from 500 to 6000 cm^{-1}. For absorptivity measurements there is an internal blackbody reference source.

Samples were deposited in the same way as before, using 0.25" KCl substrates for IR transmittance instead of the magnesium fluoride which was necessary for the UV spectroscopy. For emission work, samples were deposited on thin stainless steel rectangles. Background spectra were taken using identical substrates observed under identical conditions.

The emission chamber, illustrated in figure 16, was evacuated to a base pressure of approximately 10^{-2} torr with a liquid nitrogen trapped rotary pump. The outer walls were *usually* water cooled to minimize the thermal background. The sample was placed on the side of a central stainless steel cylinder which directly faced the emission port. Contained within the cylinder was a heater coil controlled by a variac. An ice reference iron constantan type J thermocouple in contact with the sample surface was used to measure the sample temperature. Maximum achievable sample temperatures depended on the amount of surface contact with the substrate, and were typically 800-850K. Temperatures could be increased by adding a few torr of helium to increase the amount of heat conducted to the sample. Aluminum substrates could

reach a temperature ≈900K at which point they began to melt, making them less than satisfactory for our purposes.

Contamination problems in the 3μm spectral region were encountered during some very low signal emission measurements. Figure 17 shows the absorption from the apparent contaminant spectrum compared to an astrophysical emission source encountered in this study. The existence of this contamination was noticed by fitting a smooth cubic function to the background emission spectra. The effects of this contamination on the measured spectra should be eliminated when the background is ratioed out of the data. Any changes in the contaminant level, or small non-linearities in the detection system could, however, cause an incomplete cancellation of this feature resulting in an apparent emission feature where none existed. Large portions of the data were ignored as a result of this unfortunate coincidence. To check the consistency of our results several emission annealing sequences were run on another FTIR instrument. Unfortunately, the identical contaminant was visible in that machine, leading us to believe that this feature is rather widespread. Communications with BOMEM, the FTIR manufacturer, indicated that this feature was present, to a certain extent, in all of their machines. The absorption spectra of several oils and greases were measured in an attempt to identify the compound. Most of these were deficient in the 3.38μm region, suggesting a relative lack of CH_3 side groups in the long hydrocarbon chains. A serendipitous discovery was made when a large amount of lead solder happened to melt in the emission chamber, leading to the conclusion that the contaminant spectrum was very similar to solder flux. This material usually consists of an acidic hydrocarbon resin, although the exact chemical formula is a trade secret amongst its manufacturers.

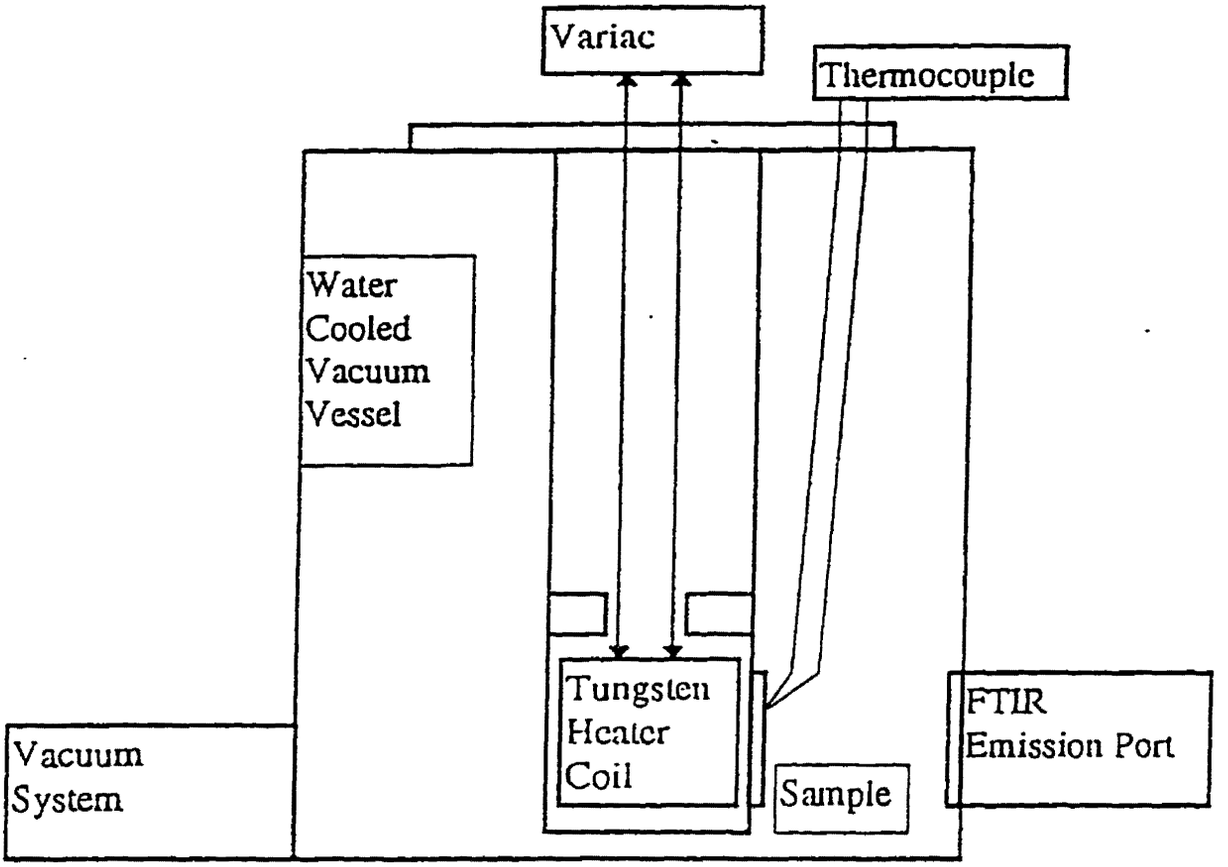


Figure 16 Block diagram of IR emission chamber.

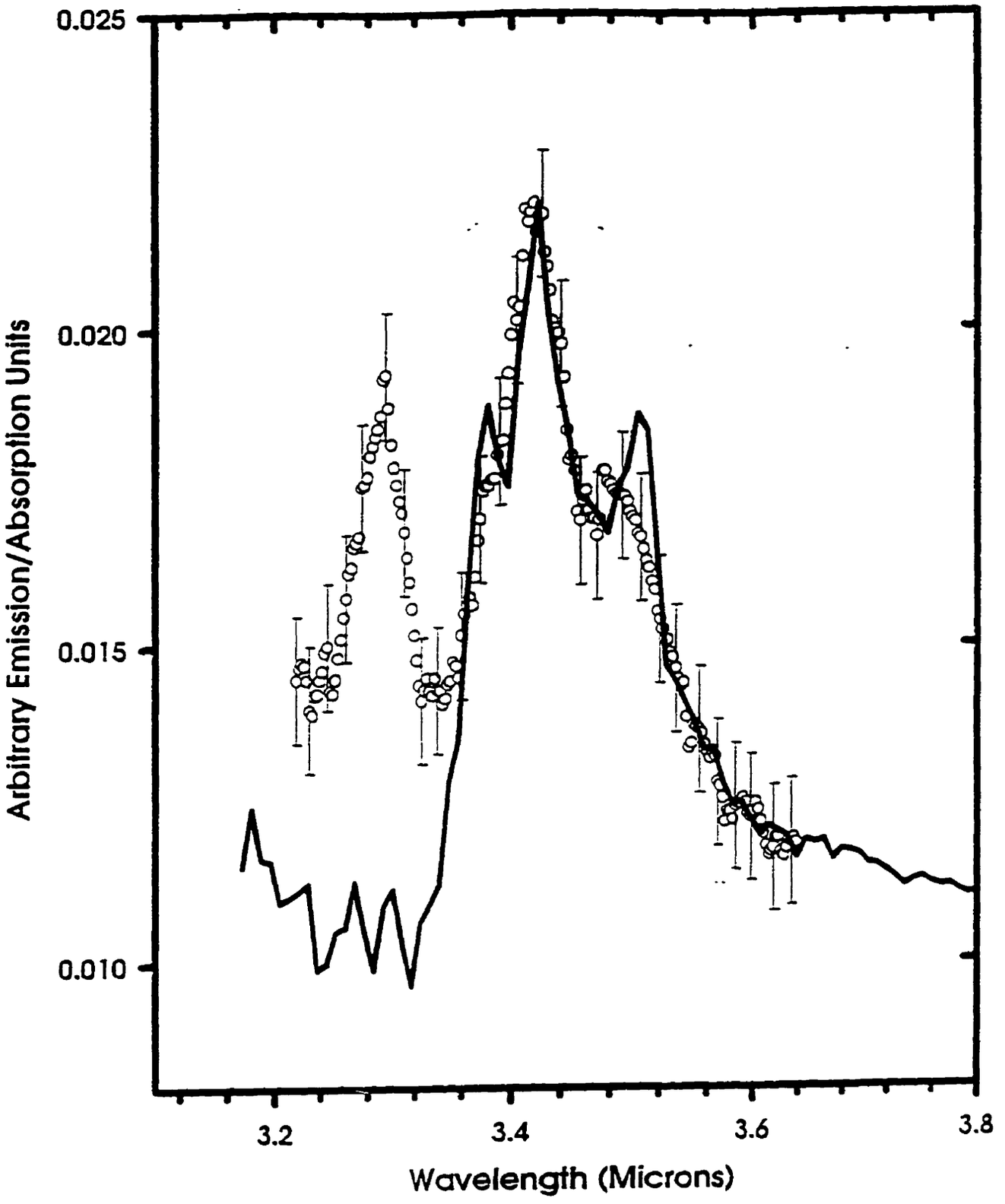


Figure 17 FTIR contaminant spectrum (solid line) compared to IRAS 05341+0852 emission (circles) (Joblin et al. 1996).

A scanning IR spectrometer was built using a rotating filter wheel and an MCT detector (Pinho & Duley 1995). The signal to noise levels were low, and the resolution was poor, but the polymeric HAC spectra (largest signal to background ratios) were qualitatively identical to those observed with the FTIR instrument.

To further improve the quality of the reported data, emission spectra of a-C and graphite were measured with the FTIR instrument. These non-hydrogenated materials have no 3μm CH stretching features, and were used to ensure that total cancellation of the contaminant feature was occurring upon analysis.

3.3 Data Reduction for Emission Spectra

Spectra were processed by ratioing the emission from HAC to that of an uncoated stainless steel substrate at the same temperature, followed by a cubic polynomial baseline correction. This process was necessary to eliminate unwanted spectral contamination due to the substrate and the surroundings. The ratioing process is the best way to eliminate artifacts due to contaminant absorptions in the system, as well as any non-linear spectral response of the detector, since these are all multiplicative. As annealing progresses in a HAC film, it darkens and begins to absorb more of the emission from the underlying steel substrate. Eventually the steel is mostly obscured, and at this point the baseline subtraction is very important to eliminate the spectral deviation from a black body which is introduced by dividing by the steel background. The choice of baseline polynomial introduces some uncertainty, but a careful choice can diminish offsets caused by absorption in the sample and background divergence from a true blackbody. For comparison to interstellar emissions, the resulting spectra were multiplied by a blackbody spectrum of the corresponding temperature when necessary.

This process is analogous to the process used by observational astronomers in many cases (Geballe et al. 1992; Justtanont et al. 1996) in which a 'flux calibration' method is used to ratio out telluric absorptions.

3.4 Thickness Measurement

Various methods were employed to gauge the thickness of the samples for use in determining their optical constants. The dynamics of laser deposition resulted in films with a slight thickness gradient across their surface, with the thickest region closest to the center of the plasma plume. For UV spectroscopy, the beam is centered on the thickest region of the sample and is small enough so that the region of the film sampled does not have a detectable gradient. In the IR, the beam has a diameter on the order of 1" so that the thickness gradient must be considered when modelling the film transmittance. The use of a rotating sample substrate during deposition is suggested for further studies to simplify the measurement of optical constants in both regions.

The thickness of films deposited on KCl substrates for IR spectroscopy was measured using scanning electron microscopy (SEM). The substrate was sanded down to a thin disc which was then cleaved near the center to expose a full cross section. One half was mounted in a groove on an aluminum SEM stub and set in a conducting graphite glue with the cross section facing upwards. A sputtered coating of gold (~40-50nm) was necessary for conductivity to prevent charging of the sample. This was well within the error for thickness determination and did not affect the final measurement. Several pictures of the cross section were then taken along the length of the sample to ensure that a proper measurement of the thickness gradient could be established. By averaging a large number of thickness measurements from a single film, a representative thickness could be arrived at with an associated standard deviation. Typical thicknesses were in the range of 1-1.5μm,

corresponding to 0.5-1 hour of laser deposition. These larger thicknesses were necessary to achieve an easily measurable absorption level in the IR while minimizing interference effects.

For the very thin films used for UV spectroscopy another method was necessary due to the relatively poor resolution of the available SEM. Transmittance electron microscopy (TEM) was impractical due to the large amount of time necessary for sample preparation as well as the need for sample conductivity. Ellipsometry was finally decided upon as being ideal for these films.

Ellipsometric measurements were carried out on a prototype system developed by Dr. Jack Ord at the University of Waterloo. A polarized HeNe laser beam is incident on the film at a certain angle, and the reflected beam is observed through another polarizer. The rotation of the angle of polarization due to the beam interacting with the sample is measured by rotating the polarizers until a 'null' is produced. The amount of rotation depends on the angle of incidence, the index of refraction of the sample and its thickness. Sources of error include large thickness gradients, rough surfaces, and non-homogeneous films. The ellipsometer incorporates a closed-loop electronic feedback system to rotate the polarizer and analyzer, locating a null in real-time. Multiple measurements were made on each film in a variety of areas, sampling multiple thicknesses in an attempt to provide more constraints on the solution. By plotting the nulls from various points of different film thickness on a graph of polarizer angle versus analyzer angle, it is possible to create a trajectory which can be fit using a small combination of physical parameters. In this way, a range of possible values was obtained for thickness and refractive index.

3.5 Laser Ionization Mass Spectroscopy (LIMS)

LIMS was used to study the microstructure of HAC films, as well as the molecular products of HAC decomposition in vacuum. The apparatus used is shown in figure 18. HAC films were deposited on copper and aluminum substrates using the method described in section 3.1 and were then mounted on the sample wheel in a chamber evacuated to a base pressure of 10^{-6} torr by a turbo-molecular pump. The sample wheel was at a potential of +4 kV DC, while the 4 accelerator grids were at +3, +2, +1 kV and 0 kV DC respectively. The ions were accelerated over a distance of 6.5cm and passed into a flight tube with a length of 88.8cm. The detector was a dual chevron micro channel plate with the front surface held at -2 kV DC, and the back surface at 0 kV DC, giving a detection gain of 10^7. Single atoms could be detected. The output was capacitively decoupled and was measured and averaged by a 150 MHz Lecroy oscilloscope. The data was downloaded to a PC through an RS232 interface. The beam from the XeCl excimer laser described in section 3.1 passed through an adjustable iris set at a diameter of 0.8cm which was positioned on a bright, uniform portion of the beam. The resulting pulse energy was diminished to the desired value (0-10 mJ/pulse) by placing partially absorbing quartz and glass plates in the beam path. The iris was imaged upon the sample plane by a quartz lens of 10cm focal length at an incident angle of 45°. The resultant spot, measured by ablating a hole in a solid piece of polyvinylchloride, was an ellipse with major axis of 320μm and minor axis of 200μm. This resulted in a total photo-affected area of ~$2x10^{-7}m^2$. The laser was operated in single shot mode and the sync output pulse from the laser was used to trigger the oscilloscope. The LIMS data for ~0.5-1μm thick HAC films deposited on copper and

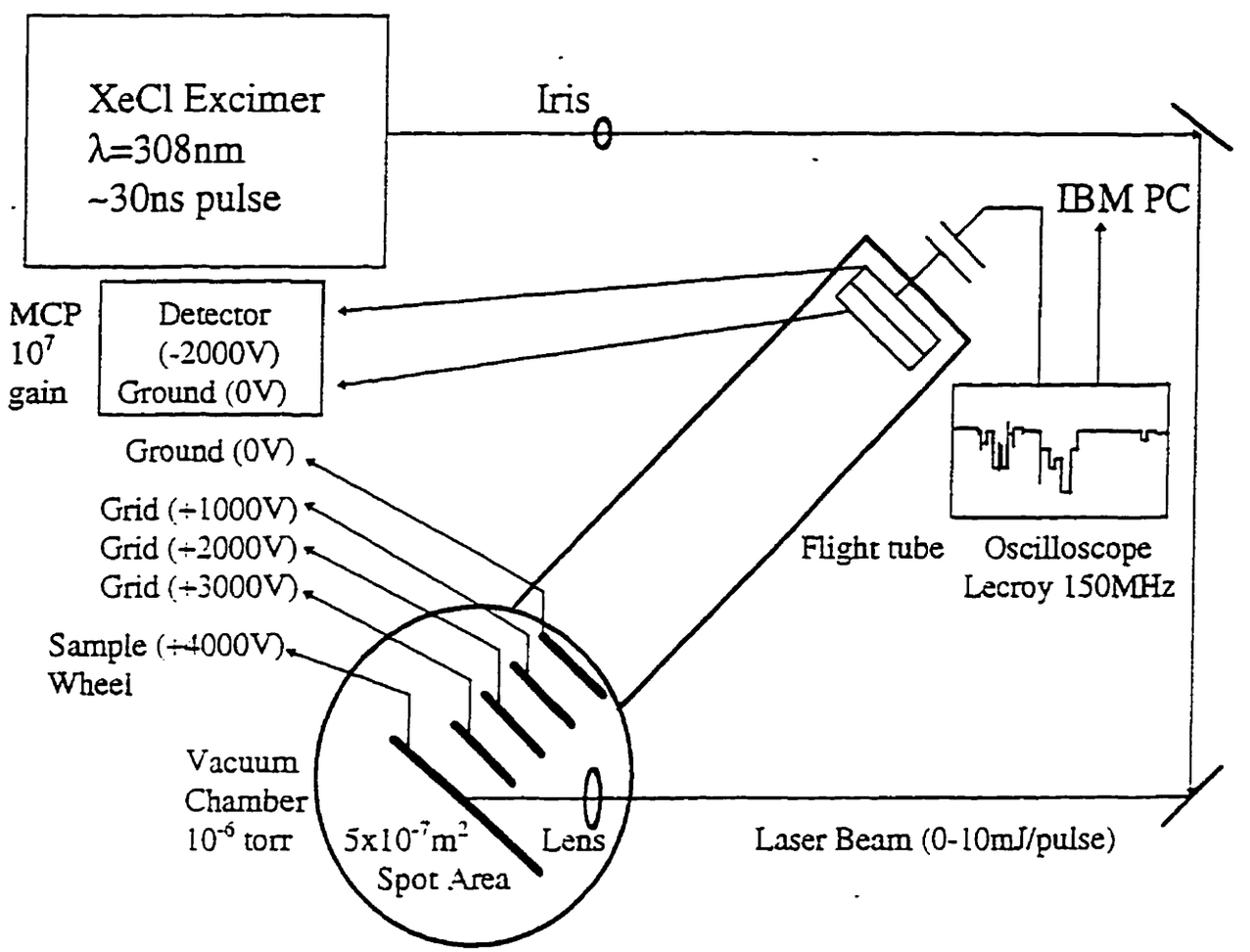


Figure 18 Block diagram of time of flight spectrometer for LIMS experiment

aluminum substrates spanned laser energies from 0.18-9.5 mJ/pulse. This corresponded to fluences in the range of $9.0x10^2$-$4.8x10^3$ $J \cdot m^{-2}$, and intensities of approximately $3x10^{10}$-$1.6x10^{11}$ $W \cdot m^{-2}$.

The detector, which was sensitive to photons as well as to particles, registered a distinct peak within less than a microsecond of the trigger pulse. This light peak was used to calibrate the starting point for all of the resulting spectra. The majority of the recognizable signal occurred in the first 50μs after the pulse. To correctly calibrate the time of flight to mass relationship it is necessary to have a minimum of two known peaks in the mass spectrum. Theoretically one can calculate the expected relationship between time of flight (*TOF*) and mass to charge ratio, but there are practical concerns which limit the accuracy of such a simple approach. The theoretical relationship was used as an aid in deciding which peaks represent which ionic species for a more accurate calibration. Assuming that: i) the ions are created at the surface of the sample, ii) the kinetic energy imparted by the laser interaction is negligible compared to that resulting from the accelerating voltage, iii) all of the ions are created simultaneously, iv) the electric field in the accelerating region is homogeneous and v) relativistic effects are negligible, one derives the following relationship for the mass to charge ratio *m/e* using simple Newtonian concepts:

$$\frac{m}{e} = \frac{TOF^2 \cdot V}{2(\frac{D}{2} + d)^2} \qquad 21$$

where V is the accelerating voltage, D is the length of the field free flight tube and d is the length of the accelerating region. To analyze the assumptions we find that assumption i) will hold for most particles in cases of low laser fluence where there are few collisions in the plasma (see Duley 1996b chpt. 5.2 for a more complete discussion). Assumption ii) will also depend on the laser fluence to a large extent. If we assume a smooth energy distribution amongst the ionized particles, then this may result in peak broadening as well as a shift to shorter *TOF* for all particles since kinetic energy is directly proportional to TOF^2. Gilgenbach & Ventzek (1991) observe a maximum plume expansion velocity of 3.4×10^4 $m \cdot s^{-1}$ for 248nm excimer laser ablation of an aluminum surface at a fluence of 7.2×10^4 $J \cdot m^{-2}$. To compare this to velocities acquired by electrostatic ion acceleration, we find that a similar velocity should be reached by particles of mass 670u. If the particles ablated from HAC surfaces were to acquire similar velocities from the laser interaction, the *TOF* results for larger particles would be strongly shifted. The Gilgenbach & Ventzek study uses at least an order of magnitude larger fluence than that used in this study. We must analyze the laser-material interaction to see if this should result in velocities which are more compatible with assumption ii). Aluminum, being a metal, has a similar UV absorption coefficient to polymeric HAC, a semiconductor. Therefore, the volume of material affected by the laser beam should be comparable between the two studies. The density of aluminum is only about a factor of ~2 higher at $2.7 g \cdot cm^{-3}$, so if similar fractions of the incident energy are transferred to the desorbed particles, one would expect that comparable fluences should result in similar velocities within a factor of ~2. This analysis suggests that reliable results can be acquired at low laser fluences, but care should be taken when calibrating the higher mass peaks. A mass spectroscopic study of 193nm laser ablation of

polystyrene using VUV laser ionization of the resulting products (Feldman et al. 1987) showed that the kinetic energy of product molecules peaked at about 0.7eV which is much smaller than the 4 keV energy imparted to ions in this study. To a first approximation the axial velocity imparted by the laser should not be a problem. Assumption iii), that all ions are created simultaneously, depends on factors similar to those discussed for assumption i) and may be violated in the case of dense plumes and high fluences when ions can be created by secondary processes. Duley (1996b chpt. 5.2) compiles evidence from several sources which suggests the existence of a delay in the production of large fragments from laser ablation. Assumption iv) may introduce a possible source of error in the case of stray fields and build up of charge on the stainless steel chamber while assumption v) will hold since the velocity of a hydrogen ion at 4 keV is only $9x10^5 m \cdot s^{-1}$.

The data presented here were calibrated using low energy ablation of aluminum. Assuming that the H^+ and Al^+ ions are the two major peaks near 1 u and 27 u and using the scaling of equation 14, the mass to time of flight relationship can be recalculated. Resulting spectra have an estimated mass uncertainty of +/-4% up to ~360u. Above this mass, axial energy imparted by the laser was sometimes seen to shift the peaks to shorter *TOF*. The high mass ends of these spectra were corrected when necessary. The peak resolution, $\Delta M/M$, is measured to be ~0.02.

4. RESULTS

4.1 HAC Thin Films

HAC films were deposited with a thickness of ~0.1μm on MgF_2 and ~1μm on KCl and steel substrates at room and liquid nitrogen temperatures (297 & 77K respectively). The laser energy was approximately 70mJ/pulse in a 45-50 nsec pulse. This energy, along with the small beam size at the focal point (~1mm diameter), resulted in a fluence on the target of approximately $9J \cdot cm^{-2}$. This was enough to create a hot plasma which was visible in the deposition chamber as a white or purple plume depending on the ambient H_2 gas pressure as well as the laser fluence. By examining the appearance and spectral properties of the resulting films it became apparent that a threshold fluence near this value was necessary to induce CH bonding in the HAC. At fluences below this value, films appeared very dark and showed no characteristic CH absorption peaks in the 3.4μm spectral region. This threshold behaviour is likely due to the fact that individual excimer photons at 308nm are not energetic enough to dissociate H_2 molecules (4.5eV dissociation energy) and thus will not create the hydrogen atoms and ions necessary for hydrogenation. Therefore, the temperature of the plasma plume must reach a point at which the molecular hydrogen can dissociate and combine chemically with the atomic and ionic carbon from the ablated graphite surface (Bourdon et al. 1991). When the laser fluence was above this threshold, the resulting films were polymeric in character with a band-gap of ~2-3eV estimated using the method of Tauc (1973). Films deposited at 77K appeared grainy and yellowish, with band-gaps in the upper part of the range, while those deposited at 297K had a smooth brown appearance with a lower band-gap. Polymeric HAC has a density of about 1.2-1.5 $g \cdot cm^{-3}$ (Smith 1984; Angus et al.

1986). The hydrogen content of HAC films can be estimated by measuring the intensity ratios amongst the infrared 3.4μm CH stretching features. HAC absorption spectra were fit by the theoretical model of Dadswell & Duley (1997a; 1997b), which uses empirical values for the various band widths, central wavelengths and oscillator strengths to reproduce experimental absorption spectra. The only free parameters are the hydrogen atom fraction and the percentage of sp^2 hybridized carbon contained in six membered aromatic rings. Figure 19 shows fits to various HAC films deposited at both 77 and 297K. The 297K films show hydrogen contents of between 30 and 40% which are roughly 10% lower than those at 77K. The aromatic ratios of the as-deposited films are consistently low, with 3-5% for the 297K films and 0-3% for those at 77K. Some films were deposited at lower energy (~40mJ/pulse) on fused silica substrates for qualitative comparisons. These had virtually no bonded hydrogen and appeared smooth and black. Data on these and other films are summarized in Table 2.

Film to substrate adhesion strength was estimated by observing the macroscopic properties of the deposited HAC films. Certain parameters of the deposition process were seen to consistently produce smooth, well-adhered films. Thin, polymeric HAC films which were deposited on magnesium fluoride or fused silica substrates tended to remain tightly bonded to their respective substrates. HAC deposited on the steel substrates used for IR emission studies was also well adhered. Thick HAC films on KCl substrates often lost adhesion and became wrinkled. This usually occurred on exposure to the atmosphere and was exacerbated by humidity. These films often cracked and curled at the edges of the wrinkled area after undergoing thermal processing. In some films flaking was observed to have occurred during

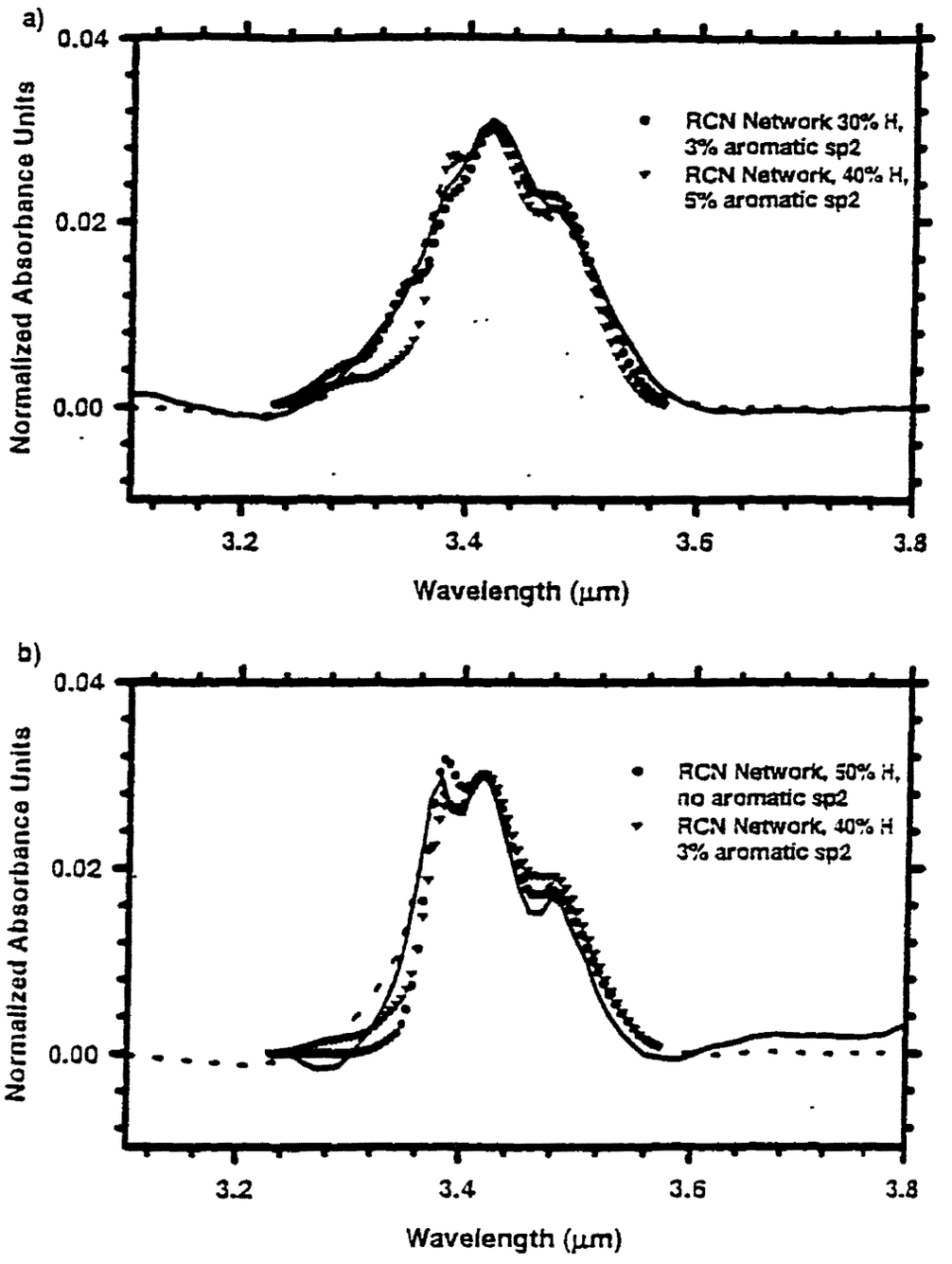


Figure 19 Model fits (Dadswell & Duley 1997b) to HAC absorption spectra. Solid and dashed lines show spectra of 2 different HAC films for each deposition temperature a) 297K; b) 77K, showing spectral differences under similar deposition conditions. Circles and triangles show a range of similar hydrogen and aromatic fractions.

the deposition process. This process was confined to the thickest regions of films and was less evident in the highly polymeric films.

Similar phenomena are frequently observed in the deposition of semiconductor thin films. Thin films on alkali halides are known to be poorly adhered due to residual adsorbed water (Angus et al. 1986). Atmospheric water vapour can enhance this effect if it enters between the film and the substrate and explains the substrate adhesion dependence which was observed in thick HAC films.

The wrinkling and delamination of the films are due to the buildup of internal stresses in the amorphous structure. In a general review of thin carbon films, Angus et al. (1986) provide an estimate of the typical values of stress reached (up to 10^{10} $N \cdot m^{-2}$) and discuss the speculation linking this stress to the presence of hydrogen in the films (Enke 1981). Non-hydrogenated a-C films do not exhibit the wrinkling and cracking seen in HAC films. Figure 20 taken from Enke (1981) shows a plot of the intrinsic film stress versus deposition parameters for a DC discharge deposition method. A locus of high stress is observed running diagonally from low voltage, low gas pressure to high voltage, high gas pressure conditions. To the upper left of this locus HAC has a more graphitic form with a lower hydrogen content, while below and to the right of this locus HAC is in a softer polymeric form.

Nir (1984) observed and quantified the buckling process in HAC. Figure 21 compares the stress relief patterns of Nir's diamond-like carbon with those produced in this study. The presence of humidity was seen to accelerate the observed buckling in all cases. The cracking which was observed in our thermally annealed films was also observed by Nir (1984), and supports our observation that this process is able to delaminate large chunks of the film. Nir's

Table 2 Physical properties of HAC films

	Deposition Conditions		
	77K, ~9J·cm^{-2}	297K, ~9J·cm^{-2}	297K, ~5J·cm^{-2}
Fused Silica Substrate, ~0.1μm thickness film.	N/A	N/A	smooth, black, no bonded hydrogen, 0-0.5eV bandgap, cracking and flaking in thickest areas.
MgF_2 Substrate, ~0.1μm thickness film.	smooth, clear-yellowish, highly hydrogenated, 2.5-3eV bandgap.	smooth, yellowish-brownish, hydrogenated, 1.9-2.7eV bandgap.	N/A
KCl Substrate, ~1μm thickness film.	grainy, yellowish-brownish, highly hydrogenated polymeric, fair adhesion to substrate--wrinkled rarely.	semi-smooth, brown-black, hydrogenated, poor adhesion to substrate--wrinkled often, cracking and flaking in thickest areas.	N/A
Stainless Steel Substrate, ~1μm thickness film.	grainy, yellowish-brownish, highly hydrogenated polymeric, strong adhesion.	semi-smooth, brown-black, hydrogenated, strong adhesion, cracking and flaking in thickest areas.	N/A
Copper Substrate ~0.5μm film.	N/A	smooth, clear to dark, strong adhesion.	N/A
Aluminum Substrate ~0.5μm film.	N/A	semi-smooth, yellowish with poor adhesion and flaking.	N/A

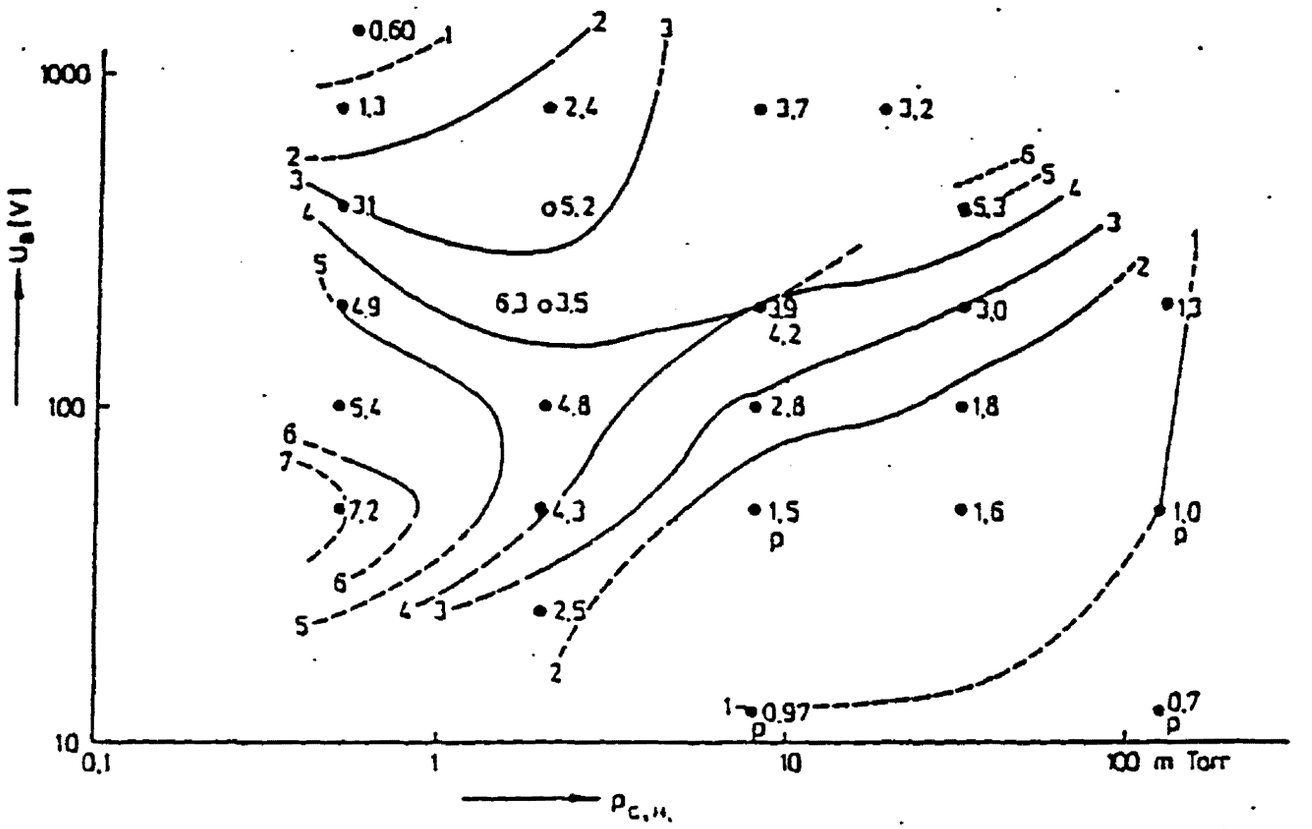


Figure 20 Curves of equal compressive stress of i-carbon layers deposited on glass substrates in units of 10^9 Pa as functions of the bias voltage U_B and the ethylene pressure p_{C2H4} (Enke 1981).



Figure 21 Stress relief patterns in thin HAC films. Upper: Nir (1984); Lower: Present study.

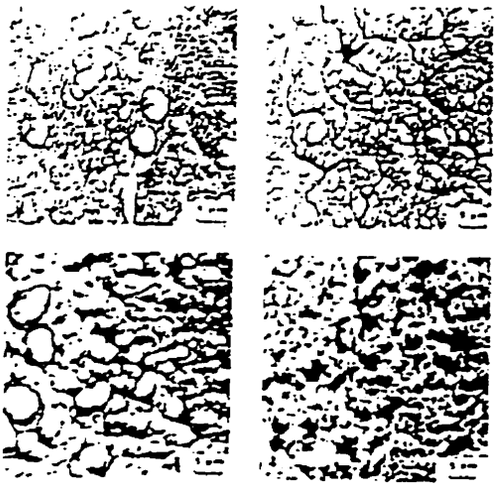


Figure 22 Cracking patterns in thin HAC films. Upper: Nir (1984); Lower: Present study.

example is shown in figure 22 alongside a thermally annealed thick HAC film which has wrinkled and cracked as a result of processing. Nir speculates that this process occurs only in the hardest films which cannot undergo bending. Whether or not this process occurs on dust in interstellar space is unknown. This may be only a macroscopic effect which is unimportant for particle sizes and thicknesses found in space. To further explain these results it is necessary to understand the microstructure of thin HAC films.

In general, the microstructure of optical thin films is strongly columnar with a large internal surface area and void volume (Macleod, 1982). The principal features are common to a wide variety of films regardless of chemical composition. This purely physical phenomenon arising from all forms of vapour deposition has been modelled with very few basic assumptions. By considering the stacking of spheres incident on a substrate, Dirks & Leamy (1977) were able to reproduce a dendritic structure with voids. If the incident particles have zero mobility, the resulting film has a loosely packed structure of chains that branch and combine in a random fashion. With limited mobility, long dendritic chains several molecules in diameter were found to grow away from the substrate. By permitting relaxation of the particles, the dendritic deposit was replaced by a very loose deposit containing irregularly shaped voids. Ross & Messier (1980) have used chemical etching to show that void networks exist in a-Ge:H and a-Si sputtered films. These films should be physically similar to HAC. Swab et al. (1980) have shown that the size of the voids depends on the thickness of the film, with thicker films having larger structural components. This is because the atomic scale columnar structures tend to cluster together on ever larger scales as the film thickness increases. This process is illustrated in figure 23 which shows a black germanium surface at

several different magnifications (Swab et al. 1980). Each of the scales shown in the figure has its own characteristic void structure. This columnar growth pattern can be observed in laser deposited HAC by examining SEM images of the HAC surfaces as in figure 24. Figure 24a shows the surface of HAC which has been deposited at 77K. This can be compared to the film illustrated in figure 24b which was subsequently photoprocessed by an ultraviolet lamp. Photoprocessing was used to enhance the columnar nature of the deposit. UV exposure was found to enhance pre-existing void structure in an analogous way to the chemical etching of Swab et al. (1980). Upon absorption of an energetic photon in a skeletal bond, surface groups are released from HAC into the gas phase. As noted previously, UV exposure will tend to graphitize the HAC film and will ultimately result in destruction of the film due to the outgassing of volatile hydrocarbons. Notice the cauliflower like appearance in the high resolution images which indicates the existence of structure at smaller scales (figure 24a & b). This structure was not as pronounced in the room temperature deposits. Figures 25 and 26 illustrate the large scale structure of HAC surfaces. Figure 25a is a SEM micrograph of a HAC film deposited at 300K, while figure 25b was deposited at 77K. The difference in bulk density becomes apparent here when the grainier, void-filled 77K film is compared to the apparent smoothness of HAC deposited at 300K. Figure 26 shows two photoprocessed films, one deposited at 77K (top), and the other deposited at 300K (bottom). These films are not very different from their unprocessed counterparts, but the grainy structure is somewhat enhanced. Since this columnar growth pattern is due solely to the physics of kinetic vapour deposition, the same growth habit with scale-dependent density can also be expected to occur in interstellar HAC.



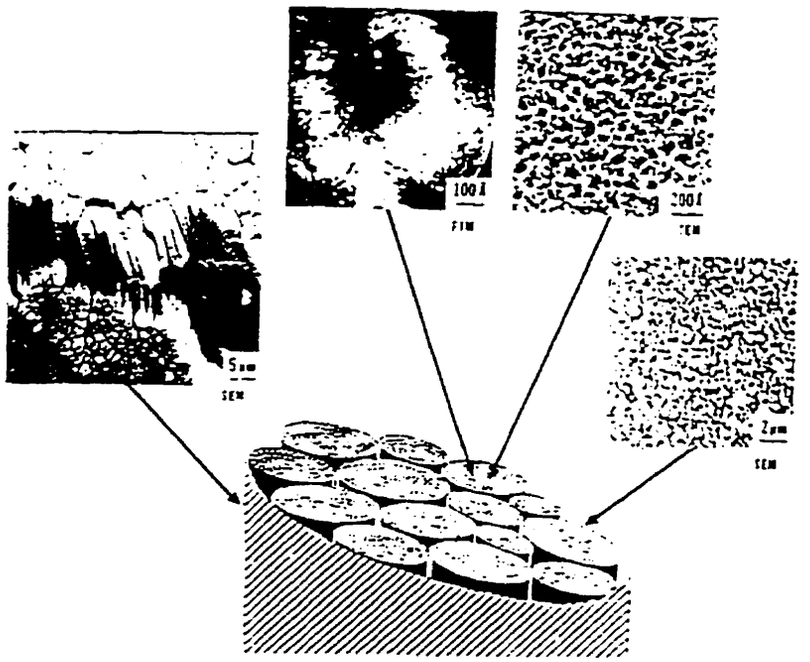
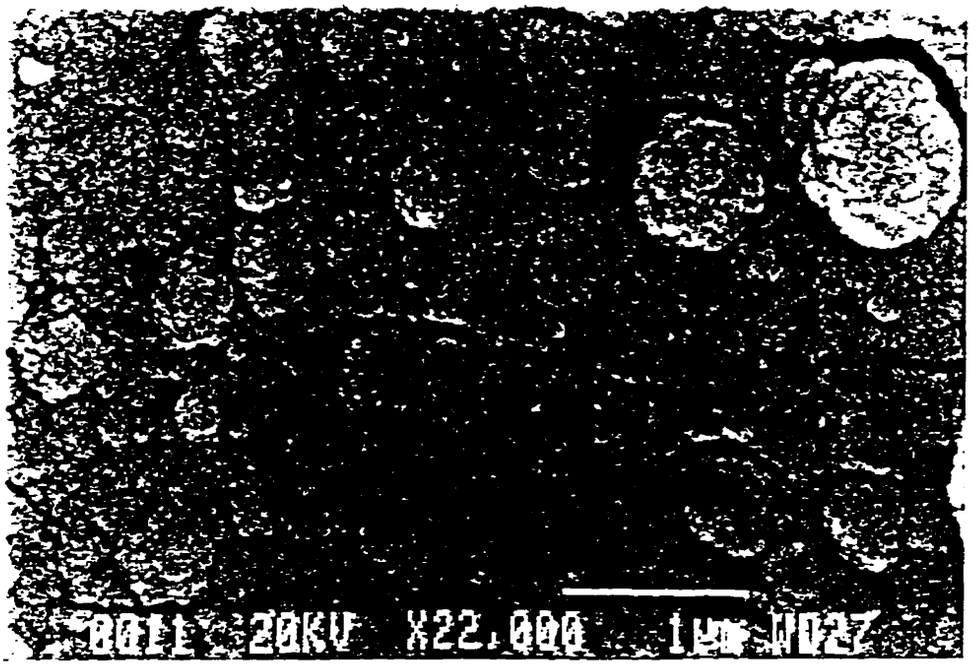


Figure 23 Energy and thickness dependent structures illustrated on chemically etched Germanium films (Swab et al. 1980). Upper: Film surfaces RF deposited at increasing gas pressure: Lower: Analysis of dendritic and void structures in a single film at different magnifications, showing similar clustering features at each scale (Macleod 1982).

a)



b)

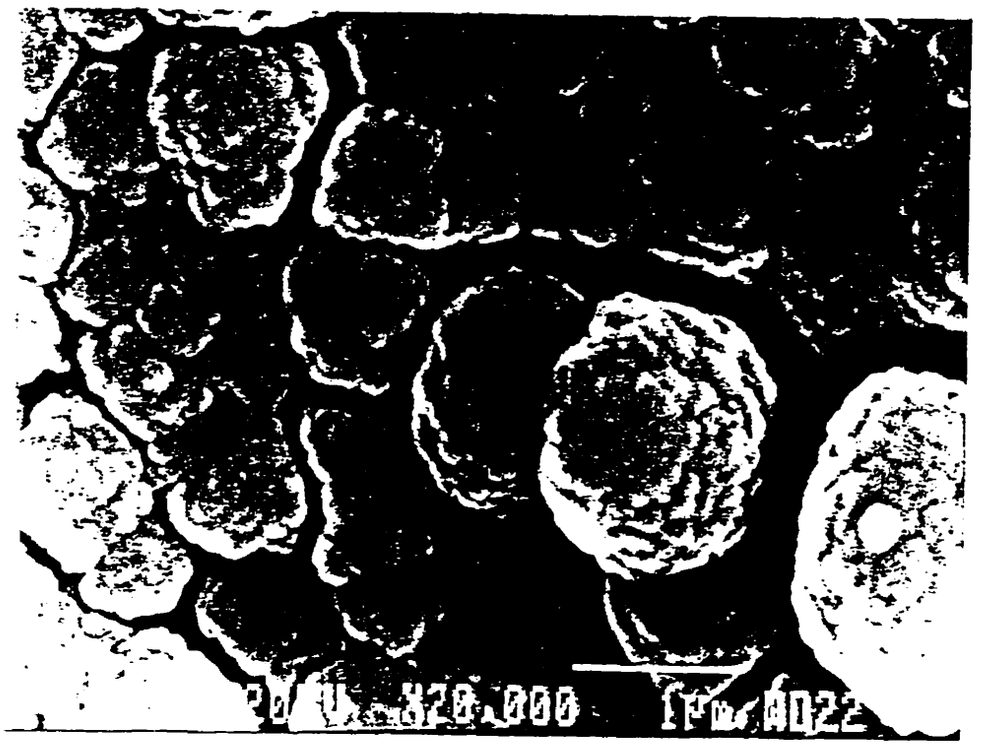


Figure 24 SEM of HAC surfaces deposited at 77K (a) before and (b) after exposure of film to UV radiation.

a)

b)

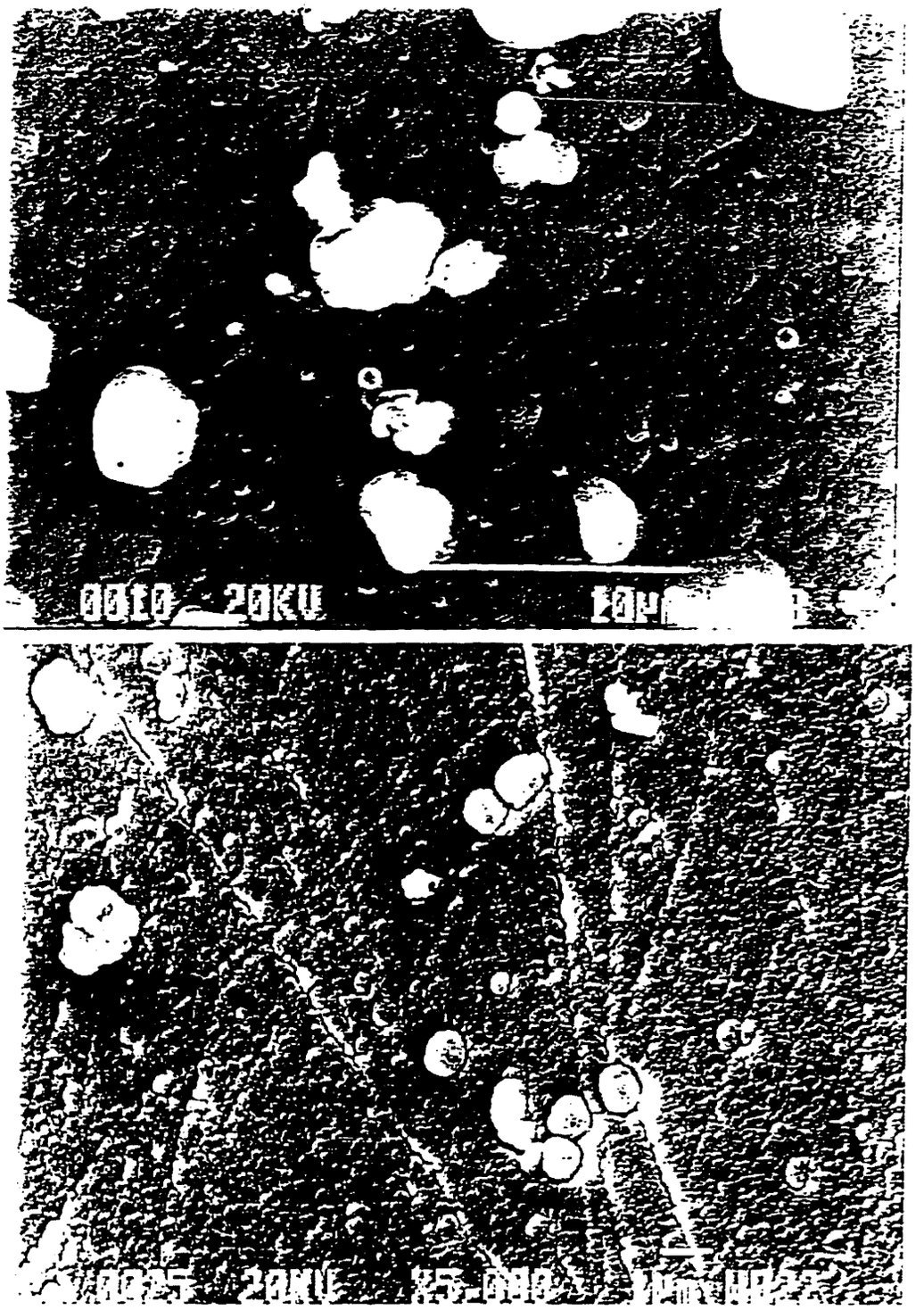


Figure 25 SEM of HAC surfaces deposited: (a) at 300K: (b) at 77K.

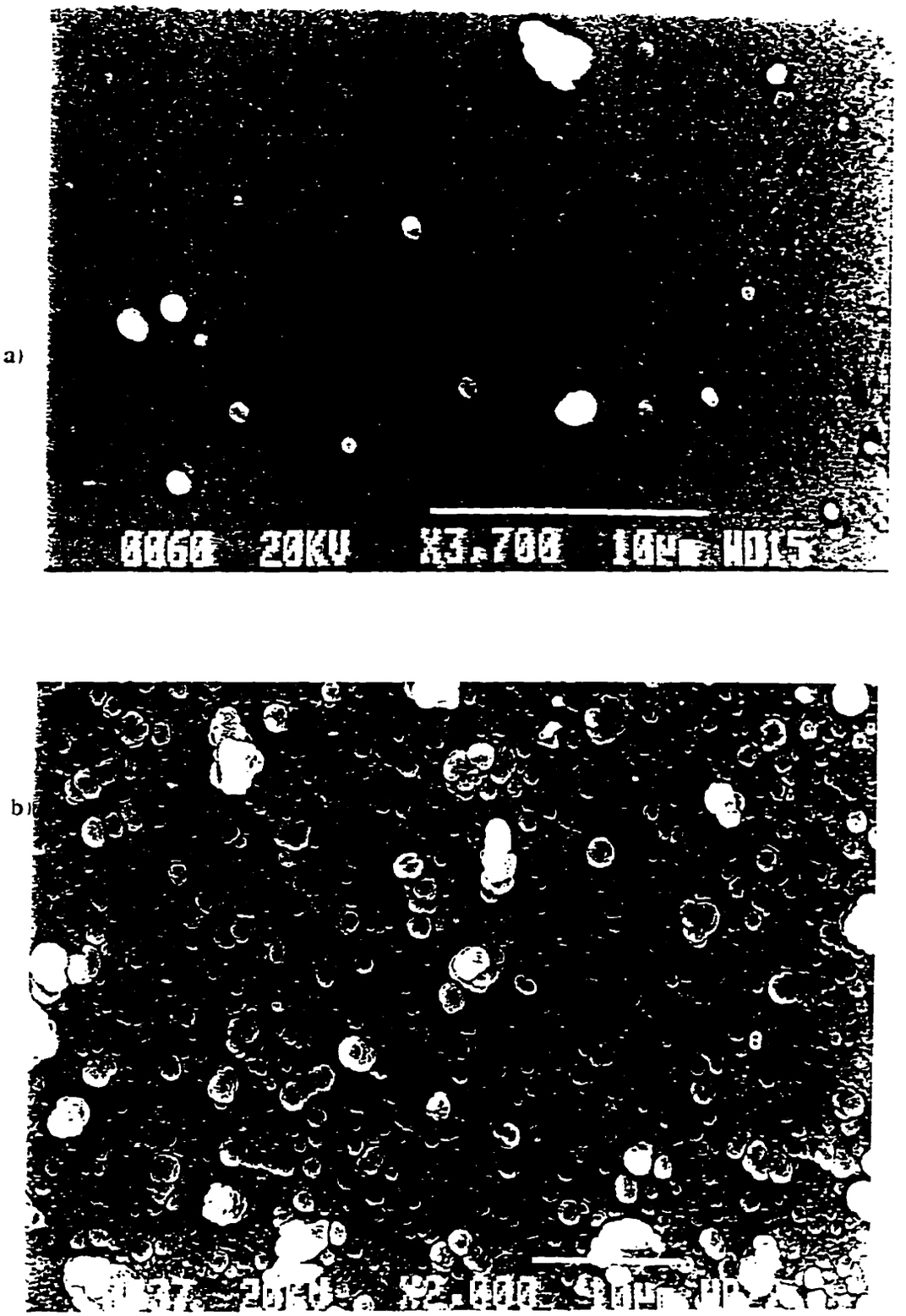


Figure 26 SEM of HAC surfaces after UV photo-processing: (a) deposited at 300K; (b) deposited at 77K.

Hoffman et al. (1961; 1970; 1971; 1972) describe how intrinsic stress arises through the mutual attraction of the thin film columns. The exact value of this stress depends on the surface energy of the columns and their various interactions. Anything which affects the surface energy of these columns would result in a change of the intercolumn forces. Pulker (1982) shows that the presence of water, by virtue of its relatively low surface energy, tends to relieve film stress through adsorption onto intergrain boundaries. The fact that increased humidity accelerates delamination of HAC is likely a result of water ingress between the film and the substrate. This possibility is mentioned by Hansen et al. (1979) who note that in certain films water is evenly distributed with depth, while in others it is concentrated at the substrate/film interface.

The effects of thickness on adherence are also explained by Pulker (1982) who indicates that in amorphous MgF_2 films, the internal stress ($N \cdot m^{-2}$) is constant, but the total stress ($N \cdot m^{-1}$) in a growing film increases with increasing film thickness. This may explain the observation of flaking in HAC films with large thickness gradients. These films must also have a large gradient in their total stress which would tend to cause ripping and flaking.

In this work, the optical absorption of HAC films of varying thickness was measured in an attempt to derive a consistent set of optical constants for use in the modelling of interstellar HAC dust. The possibility of a thickness dependent void structure raises difficulties in the comparison of optical constants between the thin films used for UV indices and the thicker ones used for the IR. Macleod (1982) quantifies the problem in terms of a packing density, p:

$$p = \frac{\text{Volume of the solid part of the film}}{\text{Total volume of the film}} \qquad 22$$

This density variation would then affect the measured refractive index, n. Harris et al. (1977) show that:

$$n = pn_s + (1-p)n_v \qquad 23$$

where the subscript s denotes the refractive index of the pure solid, and the subscript v denotes the void component. In vacuum, $n_v = 1$. This is simply a linear interpolation between the two extreme values and is not valid for all cases, but it serves to illustrate the differences that one should expect when comparing the refractive indices of a thin film to a thick film with a smaller packing density. In this work, thicker films were observed to follow this trend, having a lower apparent n value (due to lower p) than thin films. To consider the astrophysical implications of these results we must have an estimate of the thickness of HAC solids in the interstellar medium. Due to the abundance constraints of carbon, one expects that the thickness of HAC mantles on refractory cores should be very small, on the order of 1-3 monolayers (Duley et al. 1989a). Models incorporating independent carbonaceous grains would allow for larger thicknesses of HAC. Then, when modelling the extinction of interstellar dust it would be wise to consider the effects of packing density and film thickness. The n and k values reported here should be treated as lower limits when considering polymeric HAC films of thickness < ~0.5μm. As previously shown, the increased density of a very thin layer of HAC would result in a corresponding increase of both n and k. Further work could be done in quantifying the various relationships amongst the thickness, density and refractive indices of these films.

In addition to thickness variation, changing the substrate temperature will also alter the packing density of HAC (Macleod 1982; Shen et al. 1996; 1997; Cho et al. 1992). Following the previous general discussion, the atomic components of a film are able to locate a more

stable energetic configuration when there is more thermal energy available, thus increasing p. This mobility may enhance the effect of increased temperature on the chemistry of a HAC film. As noted, the hydrogen content of HAC films is the main factor in determining physical characteristics such as band gap, density, etcetera. The CH bond energy is ~3.5eV while C-C bond strengths in graphite and diamond are 7.43eV and 7.41eV respectively. Therefore, increasing the energy available to the film upon deposition should preferentially dehydrogenate the film and, at the same time, reduce the void component thus increasing p and the refractive index accordingly.

Higher concentrations of chemically bonded hydrogen will tend to decrease the connectivity of the carbonaceous skeleton of the HAC film. This is because hydrogen atoms have only a single valence electron and will therefore act as chain terminators in the polymeric solid. Overall, a decrease in connectivity would tend to increase the void size, promoting columnar growth over the homogeneity of pure a-C. This in turn would allow for attraction between adjacent micro-columns providing a link between hydrogen incorporation and film stress. Enke (1981) noticed that a-C films were relatively stress free in comparison to HAC and speculated on possible mechanisms for hydrogen-induced stress. The dependence of film stress on void size cannot be a simple linear function, and at some critical p the intrinsic film stress must begin to decline as the attracting columns grow further apart. The effect of hydrogen concentration on HAC film stress can be seen in figure 20. One would expect that lines of constant hydrogenation would run roughly parallel to the central locus of maximum stress. Thus, as one varies the hydrogen content, the intrinsic film stress will increase to a maximum and then decrease into the highly polymeric, low p regime.

In summary, a thick film is expected to have a lower packing density than a thin film produced under identical conditions. A HAC film deposited at low temperature will have a higher hydrogen density and thus exhibit a higher void content and a smaller overall density than a similar thickness film deposited at room temperature. These structural changes were all observed to affect the optical constants measured in these experiments.

Earlier in the research program some of the dark, poorly hydrogenated thin HAC films were studied using transmittance electron microscopy (TEM). The bulk of these films appears completely amorphous and smooth under high magnification. In electron diffraction, the amorphous areas exhibit diffuse ring structures (figure 27). These films exhibit cracking around areas of increased density, which seem to have pulled away from the surrounding film. The film discontinuity may be due to the high internal stress gradient which would build up around areas of enhanced thickness. Figures 28 and 29 are TEM images of microscopic high density areas in these low hydrogen HAC films. Electron diffraction spectra of these areas of increased density show distinct bright dots superimposed at varying positions on the amorphous ring structures and imply the existence of multiple tiny crystallites oriented semi-randomly inside the film. After careful analysis, it has been determined that the radii of the rings containing these dots are consistent with those of crystalline graphite, rather than diamond.

To find the interplanar d-spacing in deposited films, the radius of the visible diffraction rings or ring fragments was measured and used to solve the following equation:

$$d = \frac{L\lambda}{r} \qquad 24$$

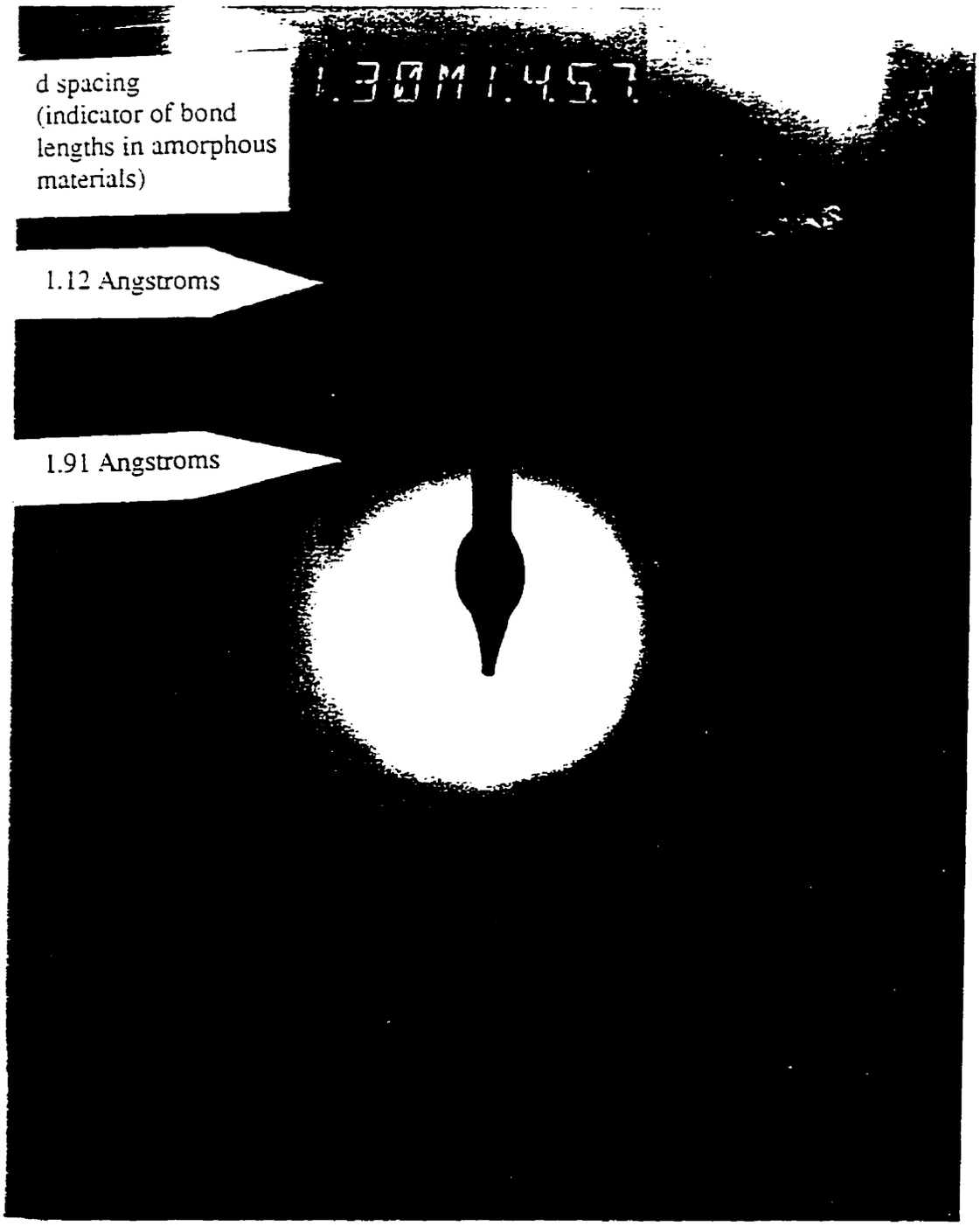


Figure 27 Electron diffraction image of amorphous low hydrogen content HAC film.



Figure 28 TEM image of enhanced density area on low hydrogen content HAC film magnified 30,000x.

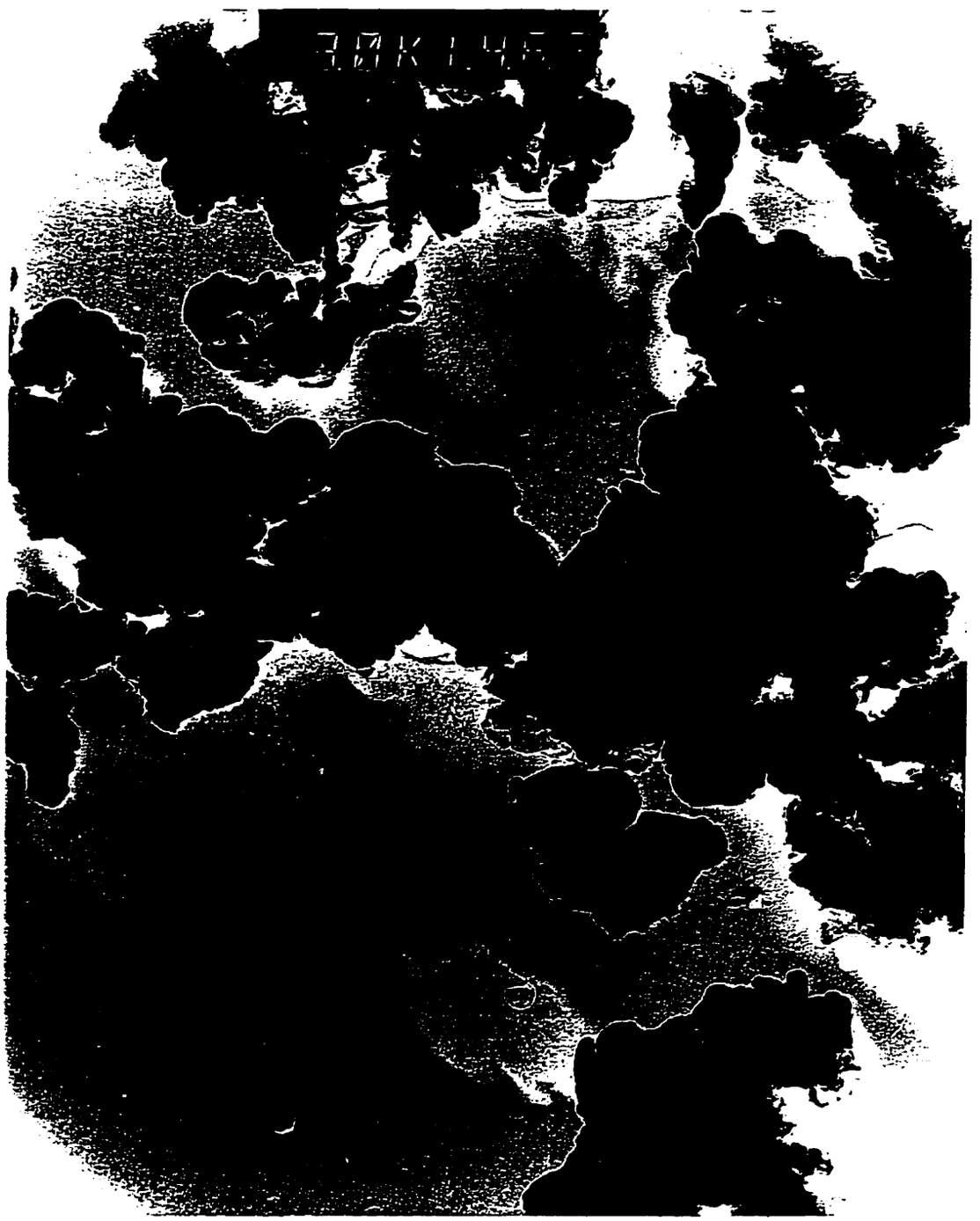


Figure 29 TEM image of enhanced density area on low hydrogen content HAC film magnified 13,000x.

where d is the apparent layer spacing, L is the electron path length, r is the ring radius on the photographic negatives, and λ is the electron wavelength. Equation 24 is the Bragg condition for coherent scattering in the limit $L/r \gg 1$. For the TEM measurements, L=1.3 meters, and λ =0.025Å.

The typical diffuse diffraction pattern from these low hydrogen HAC films consists of two broad rings produced by scattering from irregular atomic networks with characteristic spacings of approximately 1.9Å and 1.1Å. The calculated d-spacings do not coincide with those of the crystalline allotropes, graphite and diamond (Table 3). These results indicate that the HAC is amorphous, lacking any significant mid to long range order.

An analysis of the electron diffraction from an area of enhanced density can determine what degree of crystallization, if any, is present. The scattered bright spots seen on the rings indicate the existence of randomly oriented crystallites. Table 4 and Table 5 show the results of the Bragg analysis of the rings in figures 30 and 31, respectively. Some of the rings are very faint, but those showing crystallization all fall near a graphitic diffraction maximum, indicating the existence of small graphitic crystallites.

It is possible that, during the ablation process, these grains were dislodged from the graphite rod as molten blobs retaining much of their original graphitic character during the transition to the film surface. Such undissociated inclusions are common when ablating with the lower energy excimer wavelengths (Herman et al. 1992). Often, orange streaks can be seen in the laser induced plasma as small incandescent particles are ablated off the graphite surface. The relative sharpness of the diffraction rings exhibited by the graphitic areas as compared to the purely amorphous regions indicates a lack of bond stress. The presence of

Table 3 Allowed diffraction maxima for diamond and graphite.

The following values were calculated with a=3.567Å as the lattice constant of diamond and a=2.463Å and c=6.714Å as the lattice constants for graphite.

Diamond		Graphite	
Planar Spacing (Å)	Allowed Maxima h,k,l	Planar Spacing (Å)	Allowed Maxima h,k,l
2.52	110	3.36	002
1.26	220	2.13	100
1.07	113	2.03	101
0.89	004	1.800	102
0.82	331	1.678	004
		1.544	103
		1.232	110
		1.158	112
		1.138	105
		1.120	006

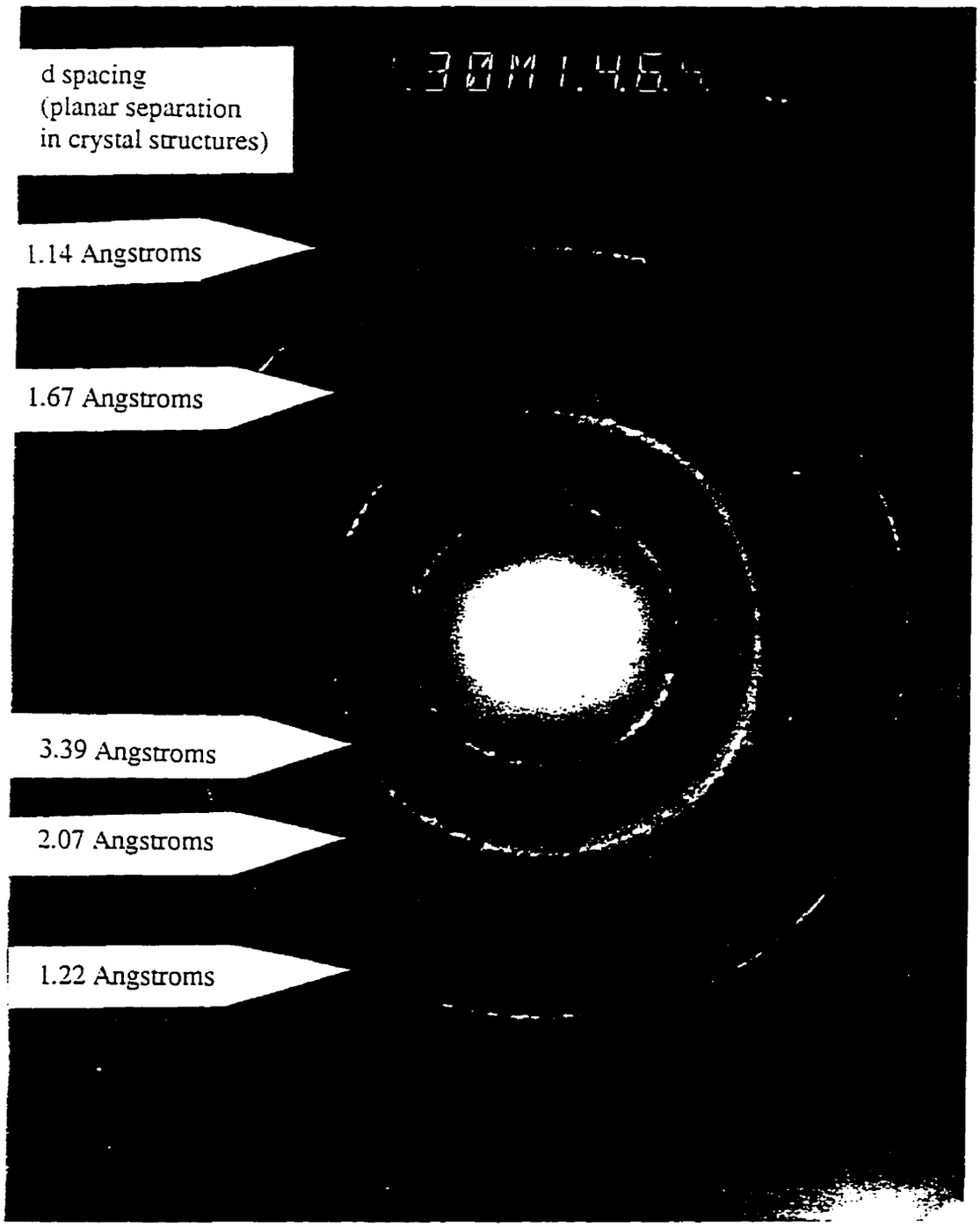


Figure 30 Electron diffraction image of enhanced density area from figure 28.

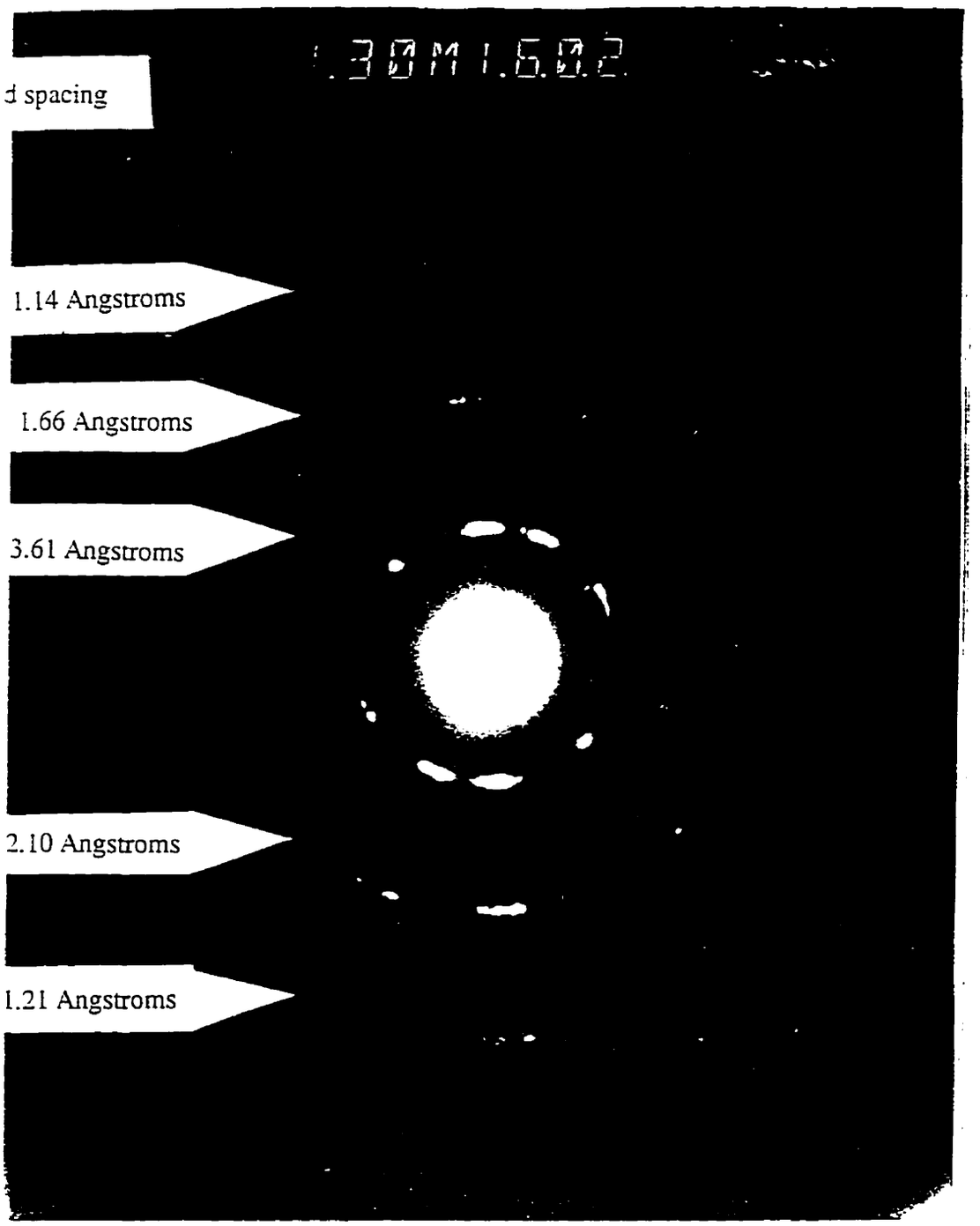


Figure 31 Electron diffraction image of enhanced density area from figure 29.

Table 4 Diffraction maxima for dense region in figure 28.

Observed d spacing (Å)	Nearest Crystalline Carbon Peak
3.39	3.36 graphite
2.07	2.03 graphite
1.67	1.678 graphite
1.22	1.232 graphite 1.26 diamond
1.14	1.138 graphite

Table 5 Diffraction maxima for dense region in figure 29.

Observed d spacing (Å)	Nearest Crystalline Carbon Peak
3.61	3.36 graphite
2.10	2.13 graphite
1.66	1.678 graphite
1.21	1.232 graphite 1.26 diamond
1.14	1.138 graphite

stress would tend to alter the interplanar spacing causing a broader diffraction maximum than in samples with low stress. If these graphitic areas are deposited during laser vaporization of the graphite rod then they are of little consequence to this study.

A similar type of diffraction feature indicating the existence of micro-crystallites is expected from partially annealed HAC films in which aromatic ring growth has occurred. Such a material would have a proto-graphitic structure lacking long range order (see section 2.2). It is possible that some of these dense regions originated from within the HAC layer as a result of stress-induced bond reorganization. There is evidence that highly stressed saturated bonding structures like cyclo-butane will transform into unsaturated bonding structures more quickly than their unstressed counterparts (Akkerman et al. 1996). A region experiencing extreme stress may undergo a partially graphitizing transformation and could result in more unsaturated bonds having fewer interconnections with the surrounding film, enabling a microscopic crack to form. In the vicinity of a crack, intrinsic bond stress is relieved (Nir 1984).

In order to become heavily graphitized, the local density must increase and carbon atoms must be able to alter their position. This rearrangement is necessary because the graphitic C=C bond length is shorter than the diamond-like or polymeric C-C bond length and the graphitic bonding angles are more constrained. Further graphitization could therefore be facilitated near cracks in the film where bond stress is relieved.

Whatever the cause of these graphitic regions, they have been found to a certain extent in all of our low energy (low hydrogen content) laser deposited films in both UV photo-processed and as prepared samples. It is possible that some of these graphitic areas were created by photo-processing and thermal annealing of the film by scattered laser radiation and interactions with the carbon plasma during deposition. It is interesting to note that these

microscopic high density regions are similar to those observed by Koike et al. (1994) who reported that the wavelength and strength of enhanced UV absorption in amorphous carbon samples seem to depend on the size of the microcrystalline particles. If this enhancement arises only in dense micro-fragments of amorphous carbon, then it is easy to see why such a feature has not been observed to a large extent in smooth films such as ours.

The formation of large graphitic islands necessary for strong UV absorption may occur more readily in small particles. The relatively high surface to volume ratios of these micro-particles ensures that a large fraction of the carbon atoms will be free to rearrange themselves into a planar six-membered aromatic bonding configuration. Thermodynamic calculations indicate that carbon atoms above absolute zero temperature, constrained in an amorphous solid will not form appreciable concentrations of aromatic rings (Efsthadias et al. 1996) but this calculation assumes that the stabilizing energy of an aromatic resonance is small compared to the total bond energy. Blanco et al. (1991) report a weak broad absorption enhancement in small carbonaceous particles centered near 220nm. They do not, however, consider the possible effects of stress and bond mobility on the formation of graphitic islands in HAC.

4.2 HAC Refractive Indices

To derive the refractive indices *n* and *k* of a thin film at least two independent measurements are necessary. In this study, the spectral transmittance and the thickness were measured. The thickness of the films was measured according to the procedure described previously (section 3.4). The thin films studied in the UV region were further analyzed using the ellipsometric method. A series of measurements was taken across the sample surfaces at the HeNe wavelength of 632.8nm and 45° incidence, thus sampling a small thickness gradient. These points were then plotted and fit using a custom-made program (Ord, 1996) assuming constant *n* and *k* values and varying the thickness, t. The calculated solutions comprised a set of self consistent *n*, *k* and t values. The transmittance at 632.8nm was measured using a simple photodiode/laser/chopper configuration for each thin film. Knowing *n*, t and the observed transmittance at a certain wavelength, it is possible to derive *k* numerically (an analytical solution could not be derived) by referring to the exact solution given by Heavens (1955). For normally incident radiation on an absorbing film-transparent substrate the transmittance is given as:

$$T = \frac{n_2}{n_0} \frac{\left[(1+g_1)^2 + h_1^2\right]\left[(1+g_2)^2 + h_2^2\right]}{e^{2\alpha_1} + (g_1^2 + h_1^2)(g_2^2 + h_2^2)e^{-2\alpha_1} + C\cos 2\gamma_1 + D\sin 2\gamma_1} \qquad 25$$

$$g_1 = \frac{n_0^2 - n_1^2 - k_1^2}{(n_0 + n_1)^2 + k_1^2} \qquad h_1 = \frac{2n_0k_1}{(n_0 + n_1)^2 + k_1^2}$$

$$g_2 = \frac{n_1^2 - n_2^2 + k_1^2}{(n_1 + n_2)^2 + k_1^2} \qquad h_2 = \frac{-2n_2 k_1}{(n_1 + n_2)^2 + k_1^2}$$

$$\alpha_1 = \frac{2\pi k_1 d_1}{\lambda} \qquad \gamma_1 = \frac{2\pi n_1 d_1}{\lambda}$$

Figure 32 is a schematic diagram of this process. A self consistent set of n, k and t values was then approached iteratively by applying the Kramers-Kronig relations:

$$n(\omega) = 1 + \frac{2}{\pi} P \int_0^\infty \frac{\omega' k(\omega')}{\omega'^2 - \omega^2} d\omega' \qquad 26$$

$$k(\omega) = -\frac{2\omega}{\pi} P \int_0^\infty \frac{n(\omega')}{\omega'^2 - \omega^2} d\omega' \qquad 27$$

where P is the Cauchy principal value of these integrals.

By extrapolating k values outside the measured spectral range, the corresponding n values may be calculated. At high photon energy (hv > 10eV), values of k were taken from Rouleau & Martin (1992) after modification by a constant factor to account for difference in density. The adjustments were made to force the value of n in a direction which would make it consistent with the ellipsometric and transmittance observations.

In summary, the following procedure was followed to calculate the HAC refractive indices in the UV:

- ellipsometry gives several possible n, k and t combinations
- input n, t and T into thin film equation to get k for measured spectral region
- adjust extrapolated k values and run Kramers-Kronig integration to get new n values
- return to thin film equation with new n and t values and repeat until solution converges.

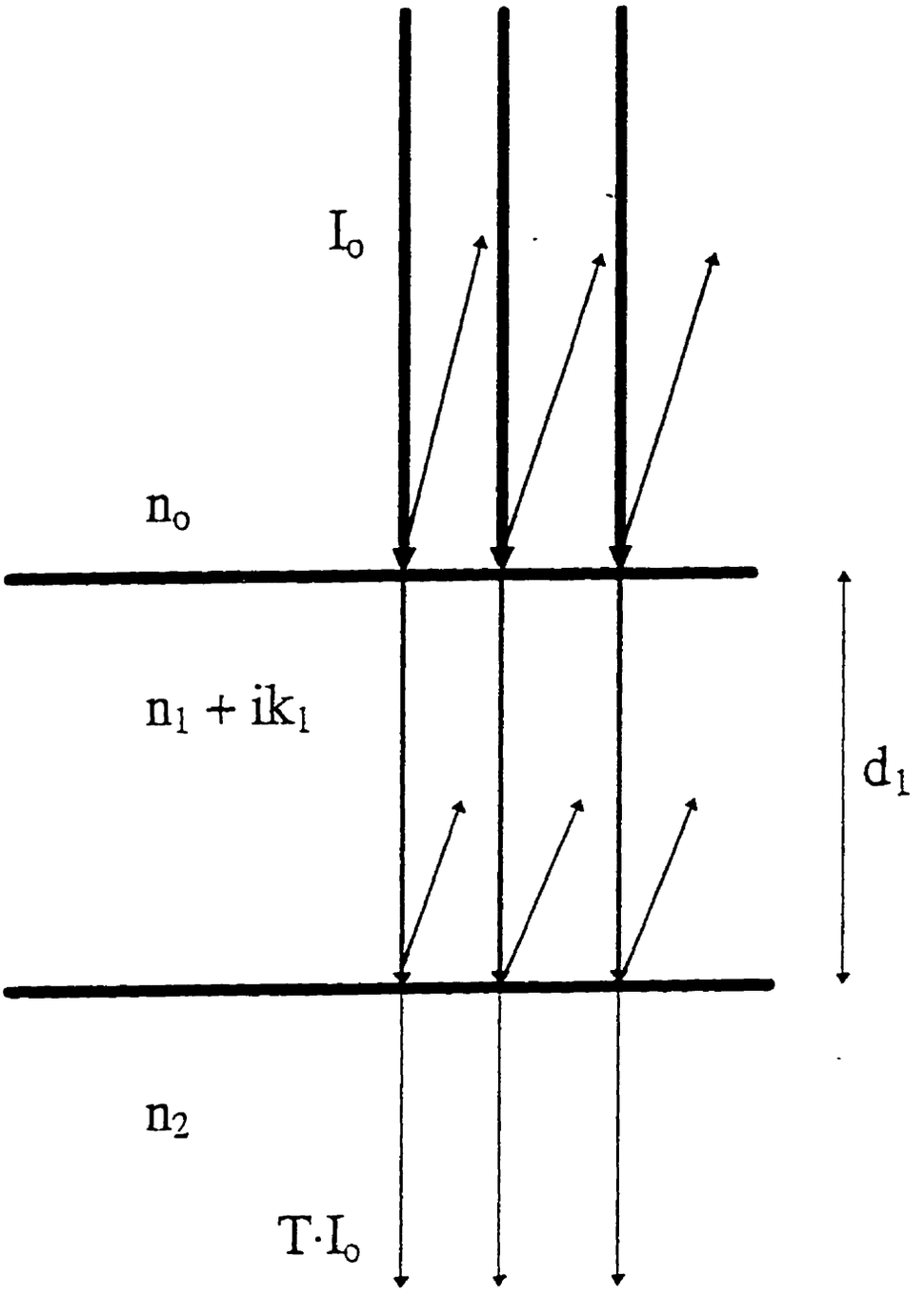
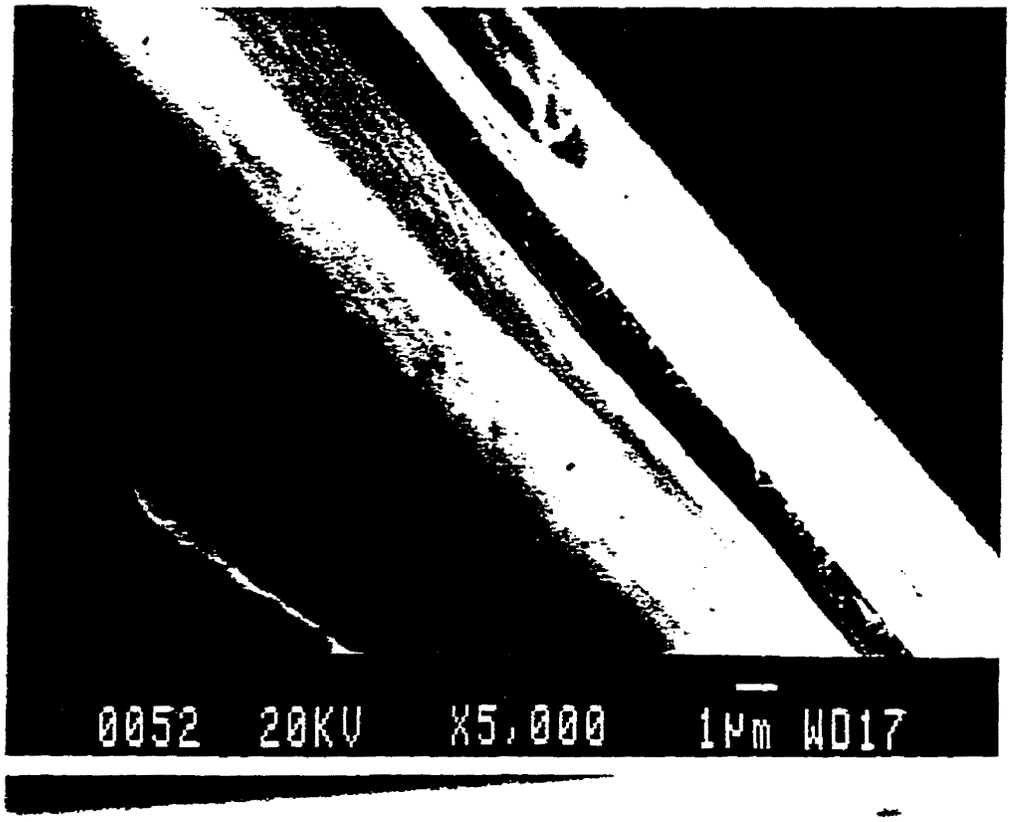


Figure 32 Schematic diagram of light impinging normally on an absorbing film deposited upon a transparent substrate.

a)



b)

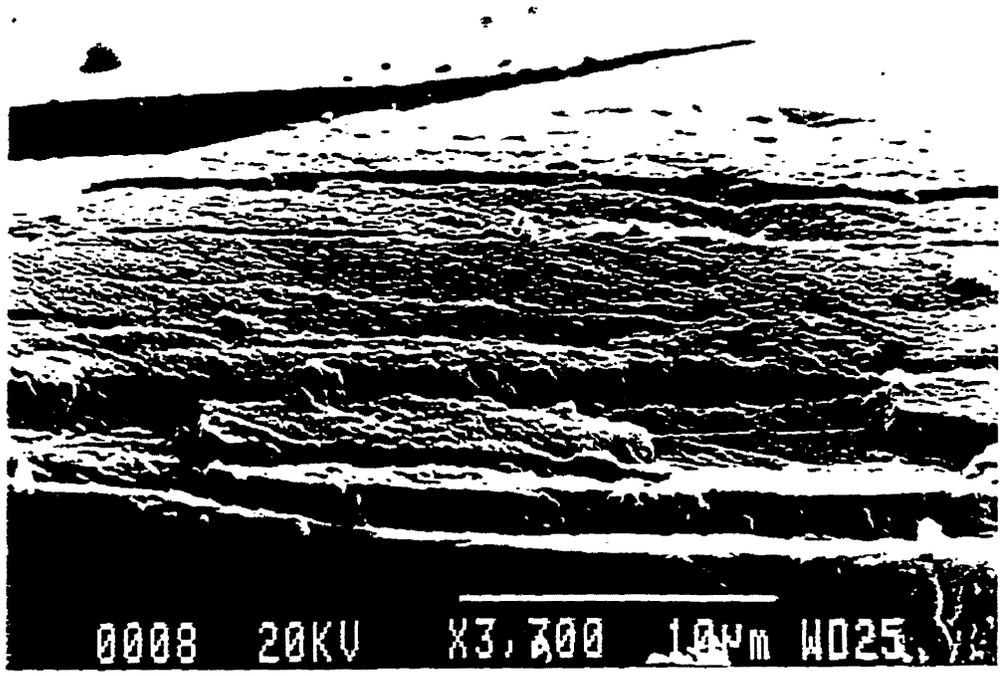


Figure 33 SEM of HAC film cross sections deposited at 300K: (a) as deposited; (b) photo-processed with UV radiation.

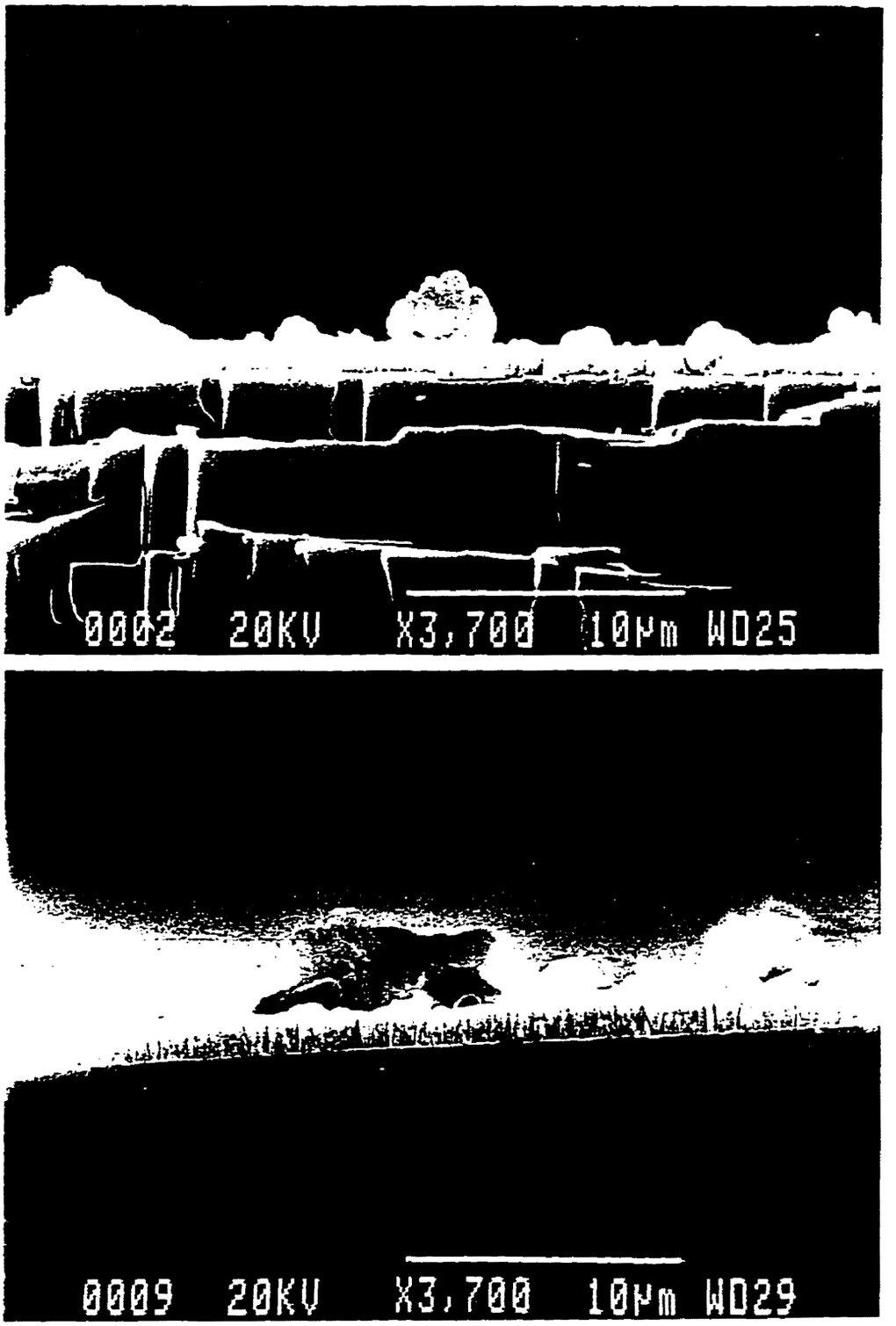


Figure 34 Cross sections of HAC films deposited at 77K.

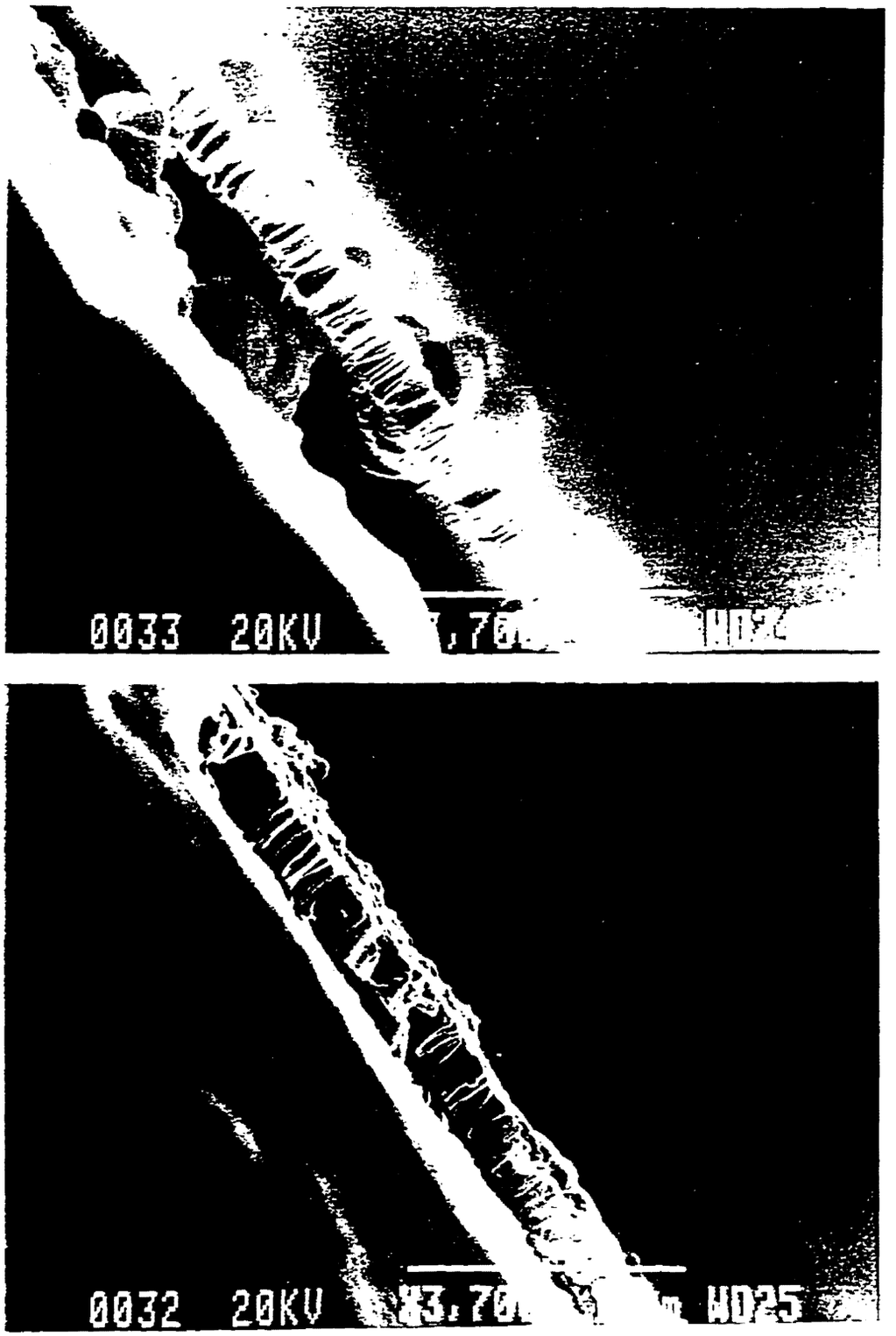


Figure 35 Cross sections of HAC films deposited at 77K after UV photo-processing.

The difference for the IR films is that the thickness is directly measured from SEM images of cross sections and is not derived from the values of n and k. Figures 33-35 show typical HAC cross sections used in thickness measurements. To obtain non-zero k values from the IR transmittance data and the thin film equation it was necessary to arbitrarily reduce k values in the UV extrapolation by up to 25% below the values previously derived from the denser thin films. This would result, due to Kramers-Kronig relations, in a lowering of the index of refraction by 10-20% in the IR spectral region and thus increase the calculated transmittance, making it comparable to observations. As explained previously and observed on the SEM micrographs, this lowering of the refractive index in the thicker films is indicative of a smaller packing density. The magnitude of the correction was limited in this study to the minimum shift necessary to produce non-zero k values in the thin film calculation.

Once consistent n and k values were obtained for each of four films at each temperature and spectral range, the resulting k values were averaged to produce two independent data sets at each temperature. The extrapolation of both IR data sets into the UV yielded k values which were 10-15% lower than those calculated for the UV data sets in the same region. It was this observation which originally suggested that the thicker films used to make the IR data sets were physically different from the thin UV films. As well, k values of films deposited at 77K were systematically 15-20% smaller than for those deposited at room temperature. To make up a single full spectrum HAC data set for each deposition temperature, the UV and IR spectra were combined by direct averaging of the k values followed by a Kramers-Kronig integration to find the index of refraction. The results of this process are shown in figures 36 and 37 with error bars reflecting the standard deviation of the observed indices. This large variation is

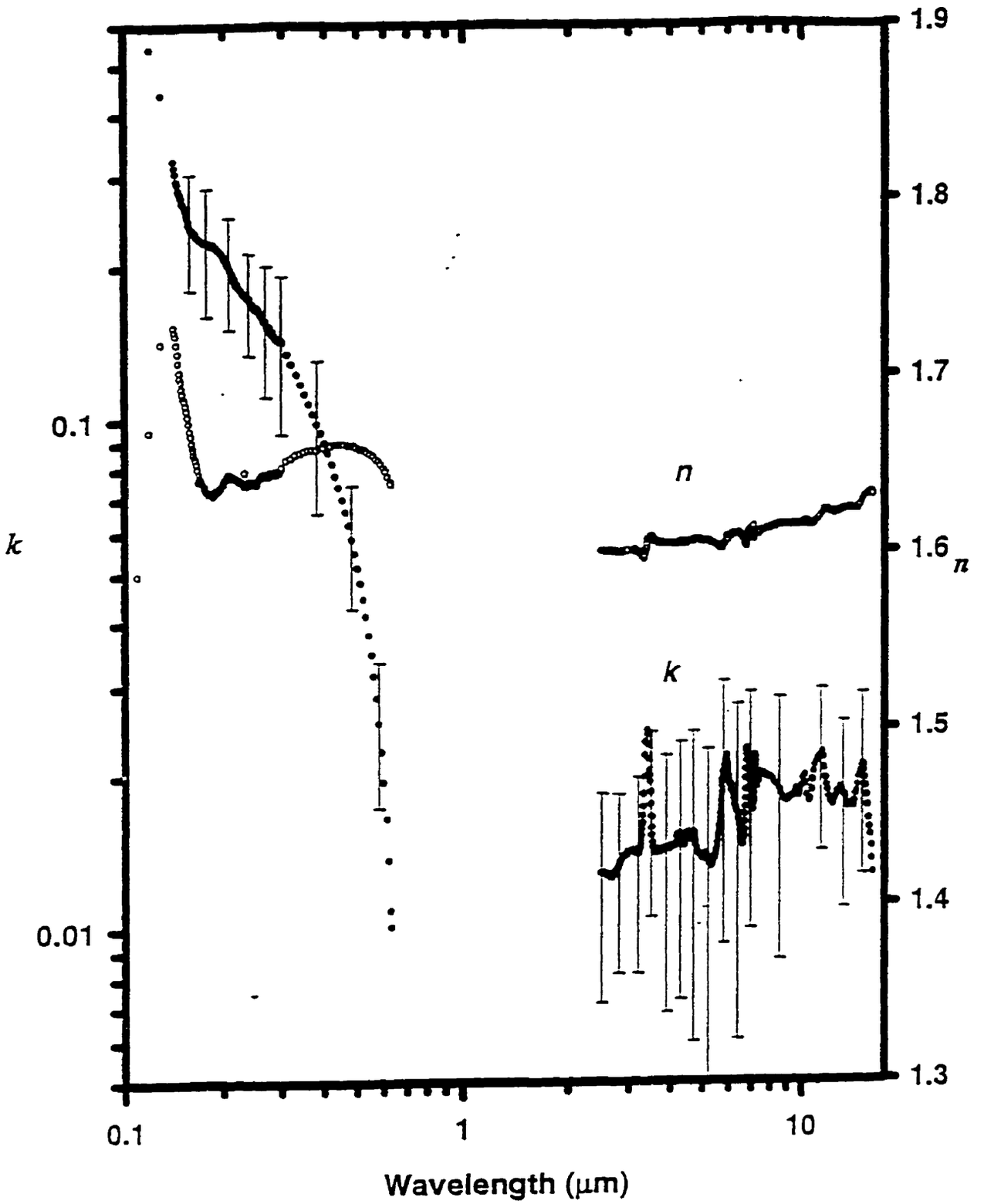


Figure 36 Measured indices of refraction n and k for HAC films deposited at 77K.

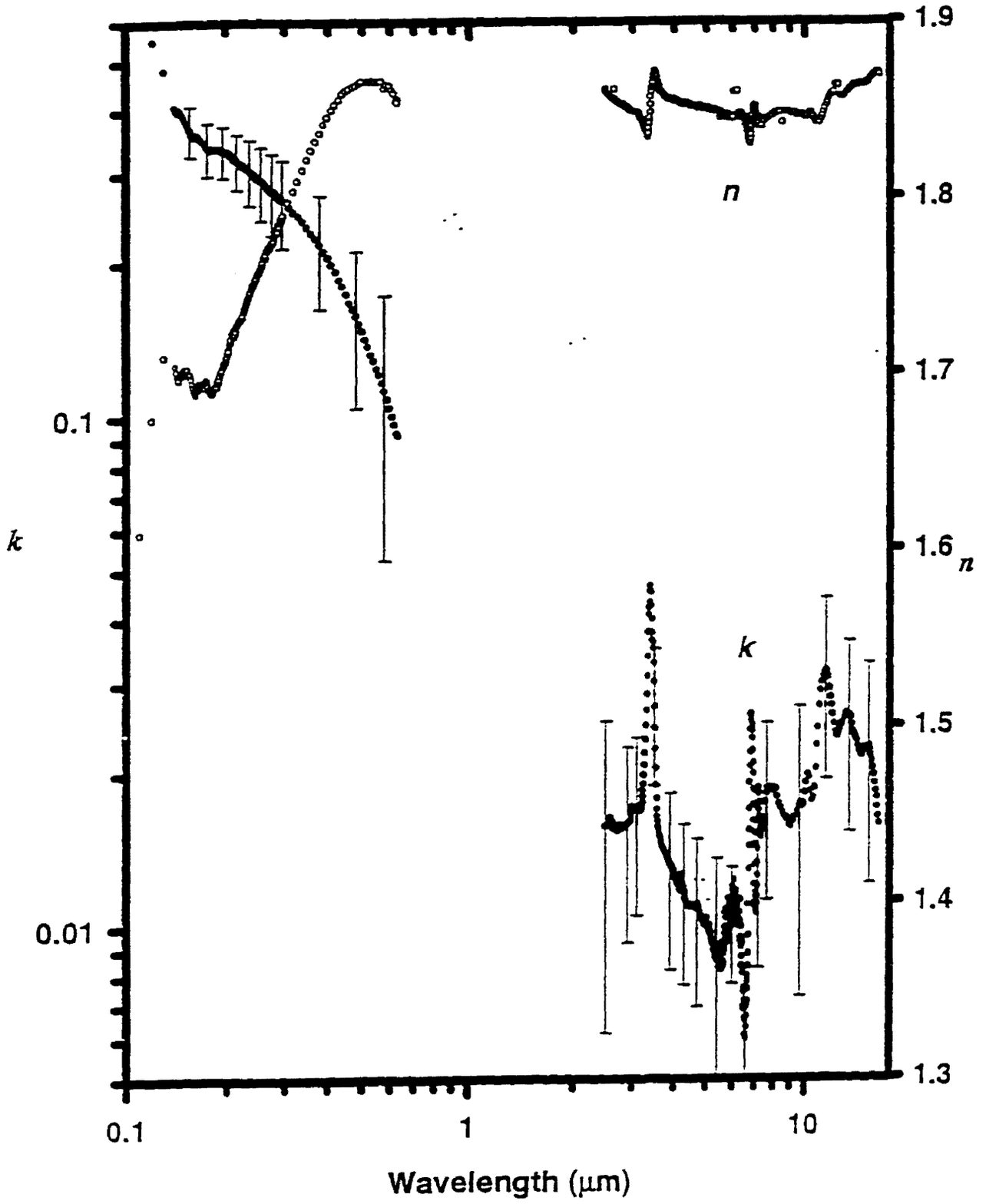


Figure 37 Measured indices of refraction n and k for HAC films deposited at 300K.

due primarily to fluctuations in hydrogen pressure, laser power and focal size during the film deposition process. Small changes in these variables can result in large differences in the observed HAC optical constants. Assuming the differences between the thick and thin films are due to packing density, as was suggested earlier, then the overall *n* and *k* values would change depending on the thickness of the film by up to +/-10%. Thin films would have higher optical constants while the thick films would have lower *n* and *k* as was observed.

The main observed difference between the optical constants of HAC deposited at 77K and at 300K is an increase in *n* and *k* for films deposited under warmer conditions. This can be understood if, as other studies indicate, hydrogen content decreases with increasing deposition temperature (Anderson 1977; Lin & Feldman 1983; Efstathiadis et al. 1996). Decreased hydrogen content would result in a lower band gap due to an increase in sp^2 bonded carbon, thus making the film darker. It will also result in an increase in density due to the mass ratio of hydrogen to carbon. The effects of the difference due to deposition temperature can be noted in the structure of the 3.4μm absorption feature (figures 38 and 39). The 77K films have sharper, more separated peaks than those deposited at 297K. As well, the intensities of individual peak components are slightly different for films deposited at 77K. The chemical origins of the peaks in the 3.4μm region are identified in Dischler et al. (1983a) and Allamandola et al. (1992). The main peaks which can be identified in these HACs are at 3.38, 3.42, and 3.47μm and correspond respectively to primary ($-CH_3$), secondary ($-CH_2-$), and tertiary (>CH-) CH stretches. If equal numbers of each type of carbon were present in the film then the expected ratio of intensities would be about 3:2:1 (Allamandola et al. 1992). For the 77K film, the 3.38μm feature is roughly equal in intensity to the 3.42μm feature which

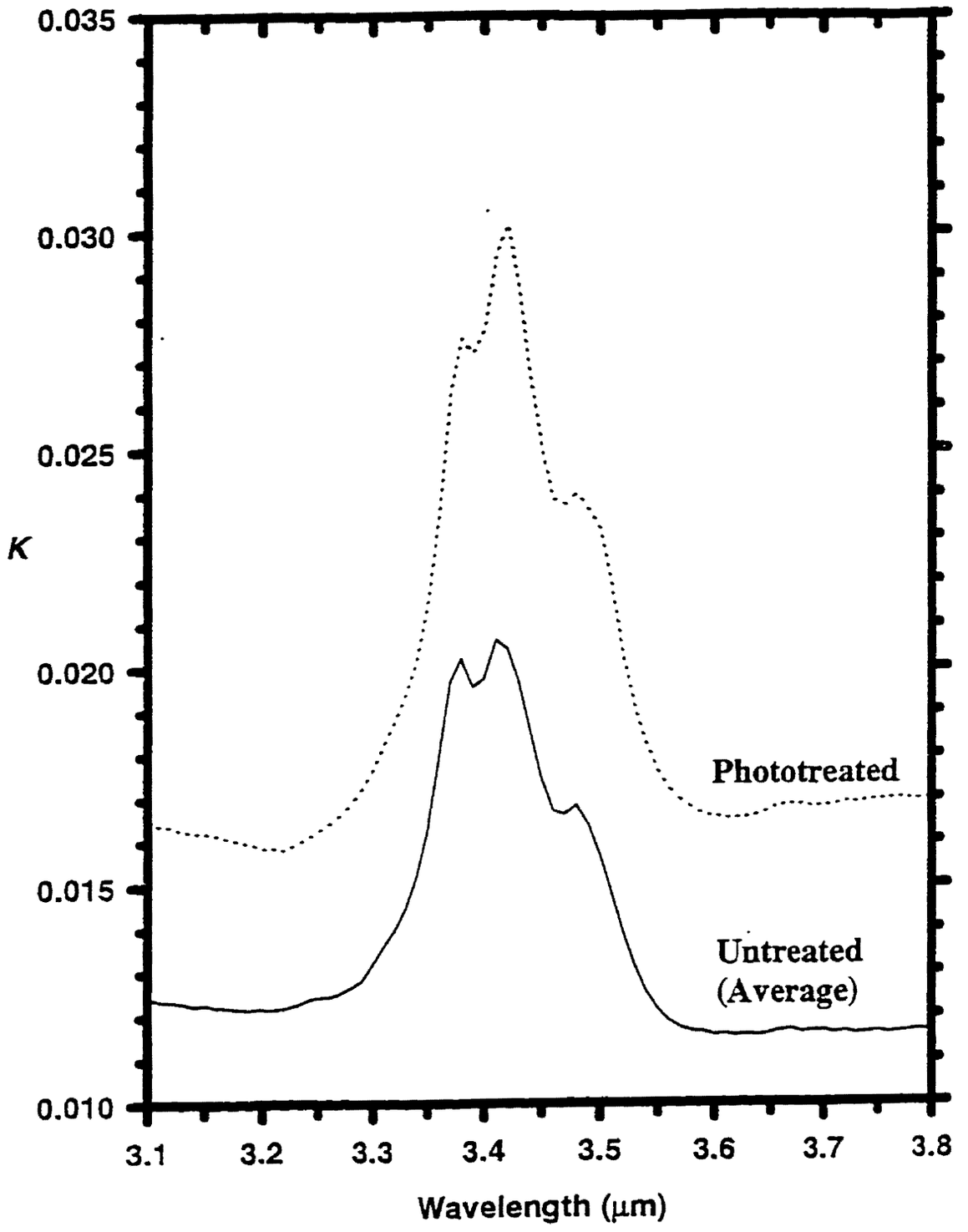


Figure 38 Effects of UV photo-processing on aliphatic CH stretching feature in HAC films deposited at 77K.

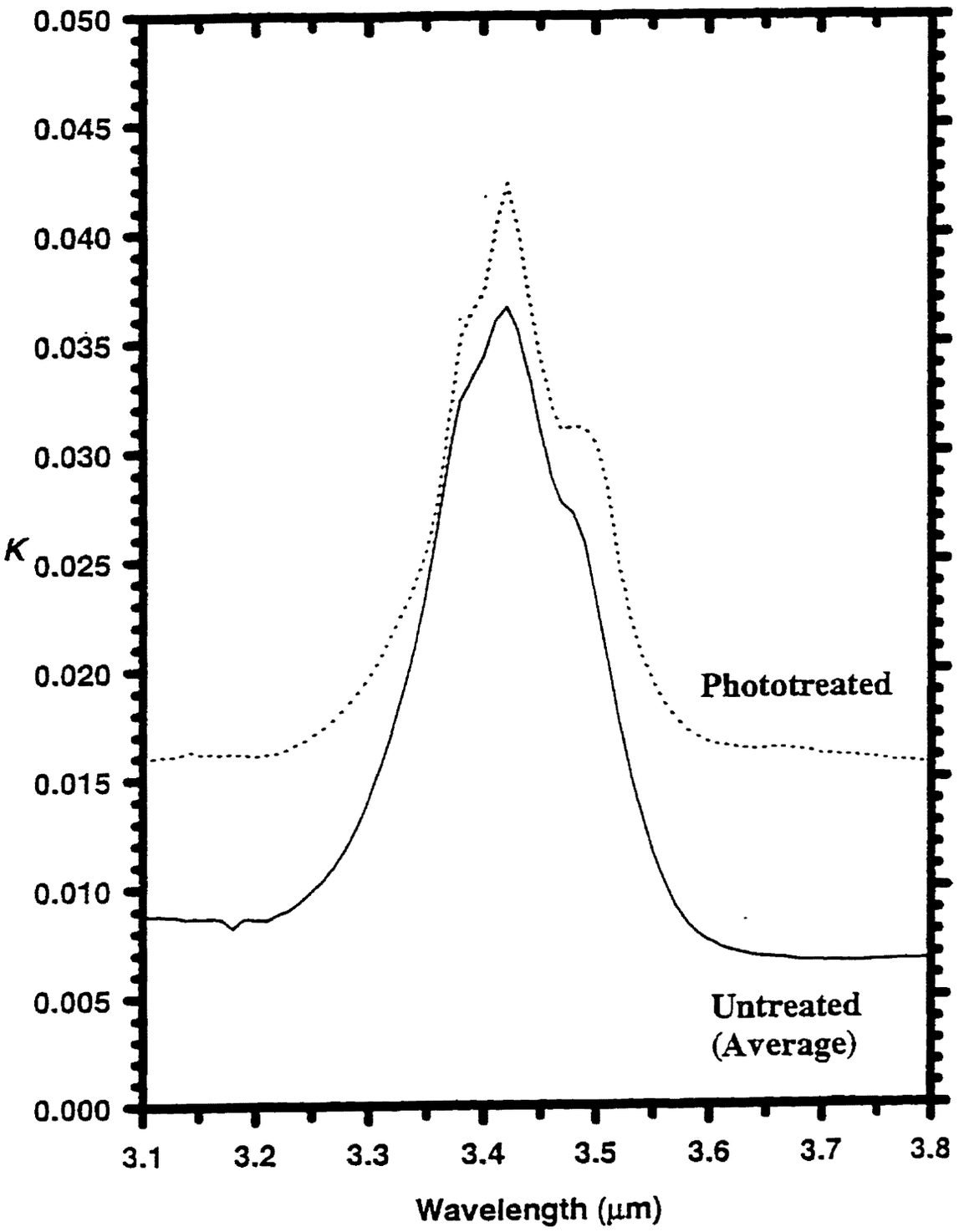


Figure 39 Effects of UV photo-processing on aliphatic CH stretching feature in HAC films deposited at 300K.

corresponds to a 10:8:5 ratio of tertiary to secondary to primary carbons. The peak ratios are about 11.5:9:5 in the 297K films indicating their lower degree of hydrogenation.

The effects of long duration (48-72hrs.) ultraviolet processing on these films are illustrated in figures 38 and 39 for HAC deposited at 77 and 300K respectively. We can see that the peak ratios change in the expected fashion and reflect a small decrease in bonded hydrogen content over time. There is no evidence of an increased intensity of the aromatic CH vibrations at 3.3μm in these UV treated films. This indicates that individual photons of energy < ~7.7eV are incapable of promoting ring growth, or that rings are being formed without any peripheral hydrogen bonds. Referring back to Eq. 3 we see that a typical as-deposited HAC with a bandgap of ~2.5eV should have a maximum aromatic cluster size of 3-4 aromatic rings. Assuming that a temperature excursion of ~400K above room temperature is necessary to promote aromatization (Smith 1984), one can calculate the threshold photon energy necessary for additional growth in a pre-existing 4 ring aromatic island. Referring back to equation 18, we find that a photon of 1.5eV should be sufficient. This classical approximation, however, tends to be a poor one at such small cluster sizes (Allamandola et al. 1989). For a more accurate estimate one can determine the maximum cluster size reached by the aromatic subunits of a HAC film irradiated by 7.7eV photons. In this case equation 18 suggests that cluster growth will cease at a size of ~30 aromatic rings. This leads to the conclusion that ring growth promoted by the UV photons from the lamp should occur to some extent. Perhaps this reaction occurs accompanied by loss of bonded hydrogen, keeping the 3.3μm aromatic CH peak at an undetectable level. The sp^3 to sp^2 transformation is known to occur along with a partial loss of bonded hydrogen during thermal annealing of polymeric HAC (Bounouh et al. 1995).

The density of HAC films depends mainly on the hydrogen content and the fraction of voids. By thermally annealing the films, hydrogen can be driven off (Smith 1984) and the remaining carbon will assume a more graphitic bonding character. Laser deposited HAC is similar to the 'plasma polymers' mentioned in Angus et al. (1986) with a density of ~1.2 g/cm^3. The HAC in the experiments of Smith (1984) initially had a density of 1.35g·cm^{-3} at 250°C. After annealing to 750°C the density increased to 1.64g·cm^{-3} which is in the range of density for 'dense hydrocarbons' (1.5-2.0g·cm^{-3}). During thermal annealing these films also underwent significant mass loss, likely in the form of volatile breakdown products such as methane and the more complex PAH molecules which are formed in this process. Dischler et al.(1983a) and Fink et al. (1984) have also studied the thermal annealing of HAC and find that between 400 and 600°C hydrogen is evolved and the carbon skeleton is transformed to a completely sp^2 bonded structure. Long range graphitic order is not achieved until heating to temperatures between 600 and 1000°C (Fink et al. 1984).

4.3 Optical Constants of Amorphous Silicates

Amorphous silicate films were studied to find their refractive indices in both the UV and IR spectral regions. The films were deposited in vacuum upon suitable spectroscopic substrates as described in the experimental section. The laser beam was focused upon chips of geological samples of the parent mineral. This appeared to be polycrystalline for both enstatite ($MgSiO_3$) and forsterite (Mg_2SiO_4) and contained trace amounts of iron as indicated by electron dispersive x-ray analysis (EDX). ~0.1μm thick films of amorphous forsterite and amorphous enstatite were deposited on MgF_2 substrates for VUV spectroscopy. As well, thicker films (~1μm) were deposited on KCl substrates for FTIR studies. These were deposited

at room temperature at a pressure of approximately $1x10^{-5}$ torr. Excimer laser deposition of refractory solids under these conditions with UV radiation is known to yield thin films with a composition close to that of the parent material (Duley 1996b). Comparative studies using electron dispersive x-ray analysis on a scanning electron microscope are consistent with this expectation. This is demonstrated in figure 40 which compares the average peak strengths associated with various elements in the parent material with those in the deposited films.

Figures 41 and 42 show the refractive indices n and k derived using a method similar to that described in section 4.2. Error bars are shown to reflect the standard deviation of thickness measurements in the IR, and the range of k observed in the UV films. The experimental data cover the range from 0.07 to 0.43 eV (0.057-0.347 μm^{-1}) in the infrared and from 4.7 to 10 eV (3.80-8.08 μm^{-1}) in the UV. The extrapolated k values were estimated using data for astronomical silicate (Draine & Lee 1984) (0-0.07 eV, >20 eV) and from reflection measurements on crystalline forsterite (Nitsan & Shankland 1976) (10-20 eV) normalized to our experimental values of k at 0.07 eV and 10 eV.

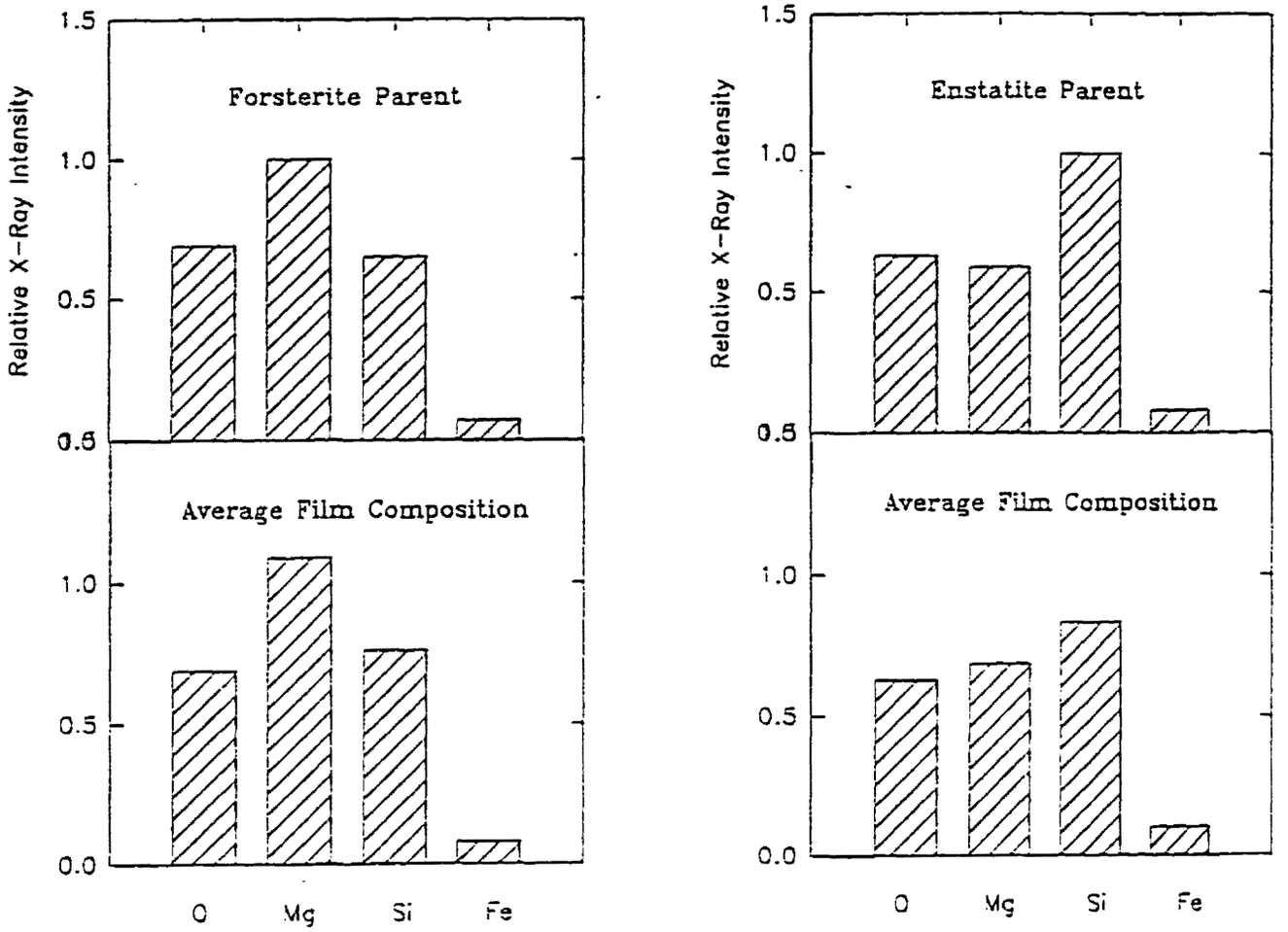


Figure 40 Electron dispersive x-ray analysis study illustrating the retention of parent crystal stoichiometry during excimer laser ablative thin film deposition of amorphous silicates.

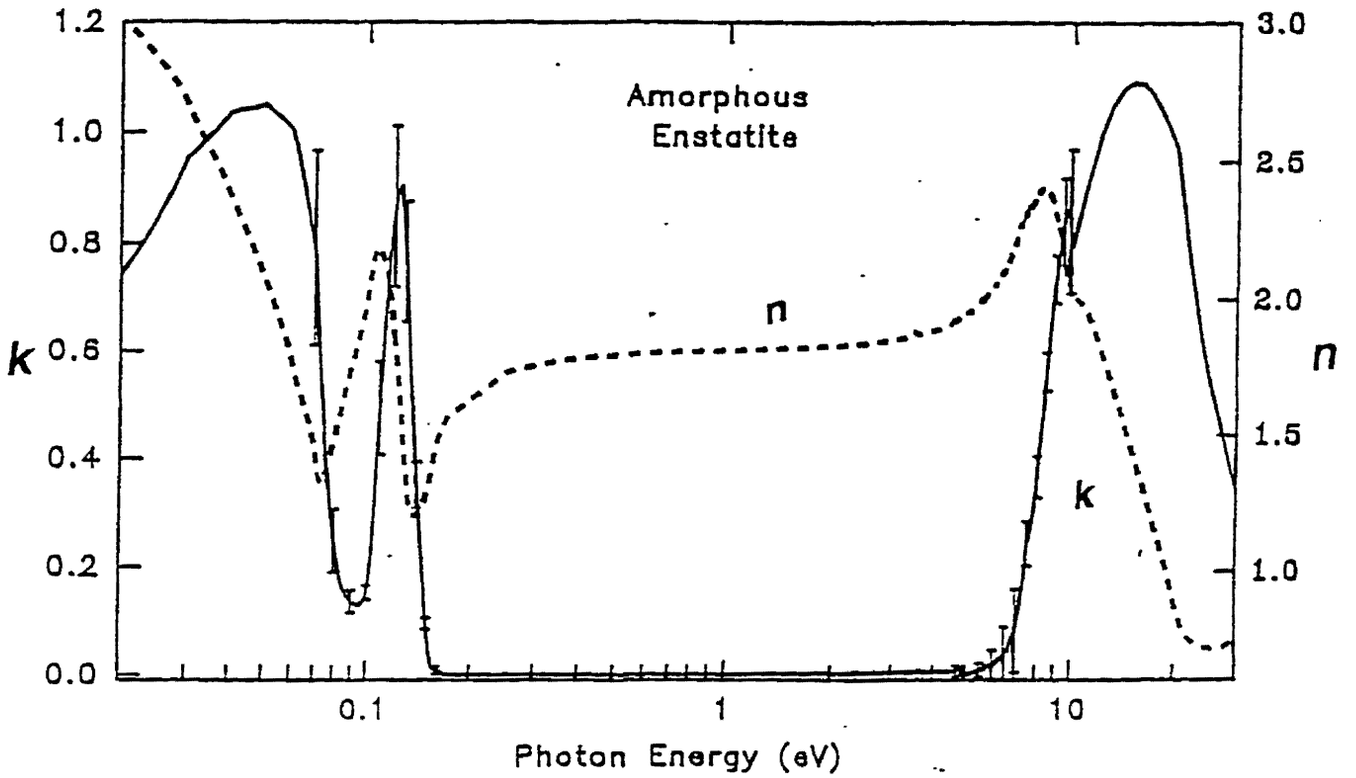


Figure 41 Measured indices of refraction n and k for amorphous enstatite.

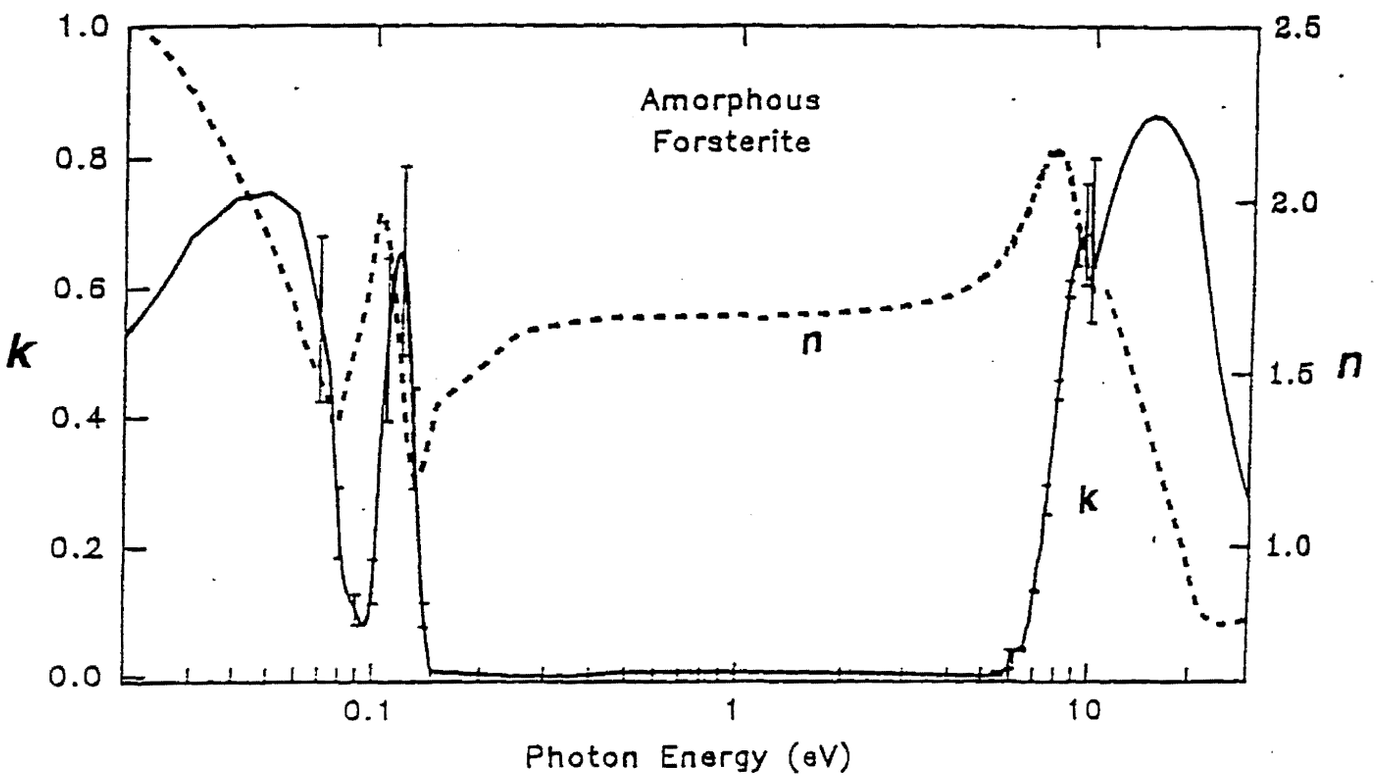


Figure 42 Measured indices of refraction n and k for amorphous forsterite.

4.4 IR Spectra and Annealing of HAC

Examining the infrared spectrum of HAC can lead to further insights into its bonding structure and its response to various environments. The IR absorption spectrum of laser deposited HAC is similar to that of the 'a-C:H' films shown in Dischler et al. (1983b). Figure 43 is a series of FTIR absorption spectra which illustrates the effects of annealing on a laser deposited HAC film. The 3.3 μm aromatic feature appears at about 673K, in agreement with Fink et al. (1984). As the annealing temperature increases, the ratio of 3.3/3.4μm absorption strength also increases due to a rapidly decreasing 3.4μm band. This is consistent with the continued outgassing of hydrogen and altered bonding characteristics of the carbon skeleton.

As predicted, the IR absorption spectrum of HAC prepared at 300K shows the 3.4 and 6.9 μm features attributable to CH_n vibrations in aliphatic and olefinic hydrocarbons. That at 7.28 μm can be attributed to CH_3C groups, while that at 10.3 μm likely arises from cyclo-compounds such as cyclohexane (Rappoport 1967). The presence of aromatic CH is indicated by the broad absorption band at ~ 11.4 μm and the weak peak near 6.14 μm. These structures are all known to be components of HAC (Robertson & O'Reilly 1986).

On heating, HAC evolves toward a protographitic material through loss of hydrogen, desorption of hydrocarbon molecules and the growth of sp^2 hybridized bonded aromatic rings (Hauser 1977; Dischler et al. 1983a; Smith 1984; Fink et al. 1984; Schenk et al. 1992). This

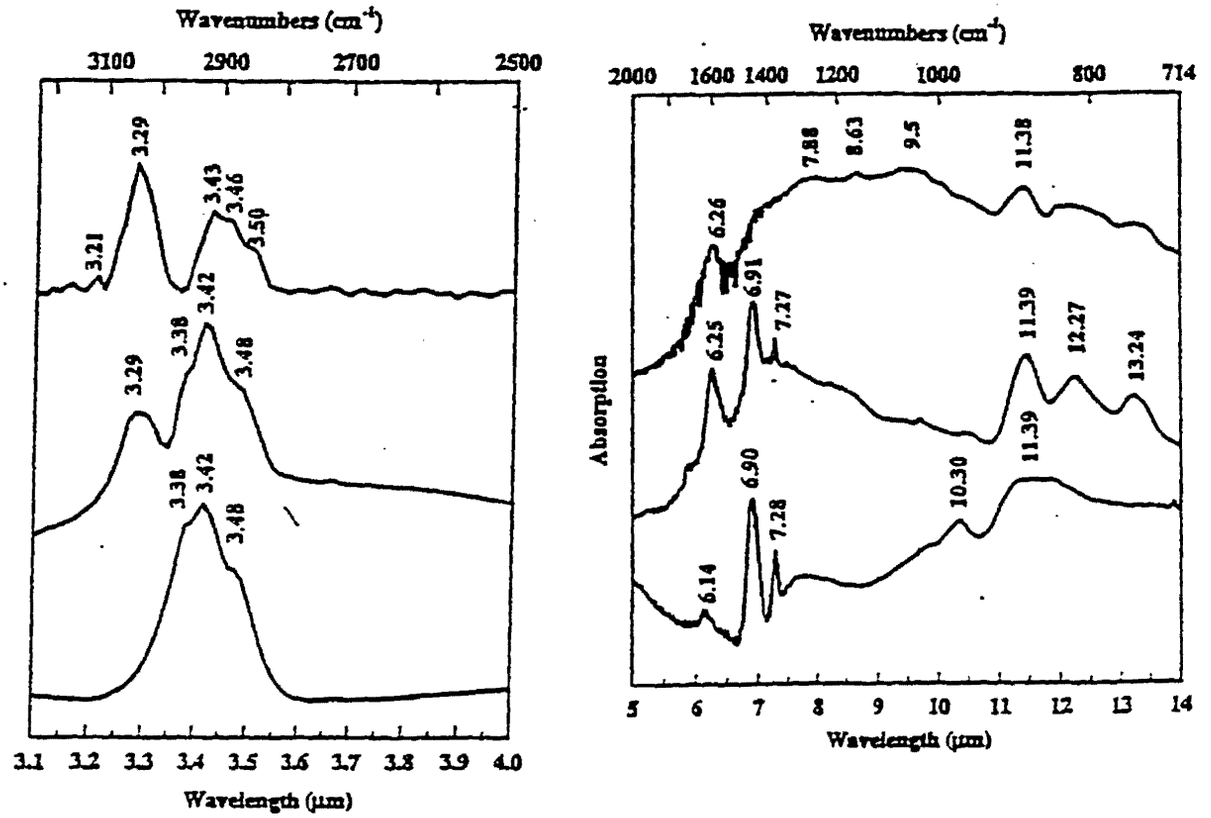


Figure 43 (a) IR absorption spectrum of HAC, as deposited (bottom); heated to 700K (middle); and heated to 800K (top). Spectral range 3.1-4.0μm., zero shifted for clarity; (b) Same as (a), but for spectral range of 5.0-14μm

can be followed in the absorption spectrum through the weakening of the 3.4 and 6.9 μm bands and the enhancement of spectral features such as those at 3.29, 6.26 and 11.4-13.24 μm attributable to aromatic rings. When this is occurring, HAC often loses its mechanical integrity as voids grow in the film.

Scanning tunnelling microscope (STM) images of the surface of HAC, recorded before and after heat treatment in vacuum are shown in figure 44. An image of the surface of crystalline graphite is also included for comparison. These images are similar to those reported by Cho et al. (1992) for amorphous carbon (aC) films deposited at high temperature. Figure 44b. shows the growth of graphitic islands (seen edge on) as the volatile hydrocarbon component is removed from HAC. A higher magnification STM image reveals the hexagonal structures associated with graphitic material in the upper right quadrant of figure 44d. Such graphitic islands are separating from the HAC framework as decomposition proceeds. The resulting solid is a loosely connected highly friable structure analogous to an aerogel of aromatic clusters similar to those discussed by Duley (1993). This process is observed macroscopically on HAC films which have delaminated from their substrates. Without this support to hold them together, the protographitic film wrinkles, cracks and curls, releasing small particles of soot-like material into the air.

Prior to the decomposition of HAC in vacuum, absorption bands attributable to 2 and 3 adjacent H atoms on aromatic rings (12.27, 13.24 μm respectively) decline, leaving the 11.39 μm feature of solo CH. This suggests that dehydrogenation is almost complete by the time HAC decomposes.

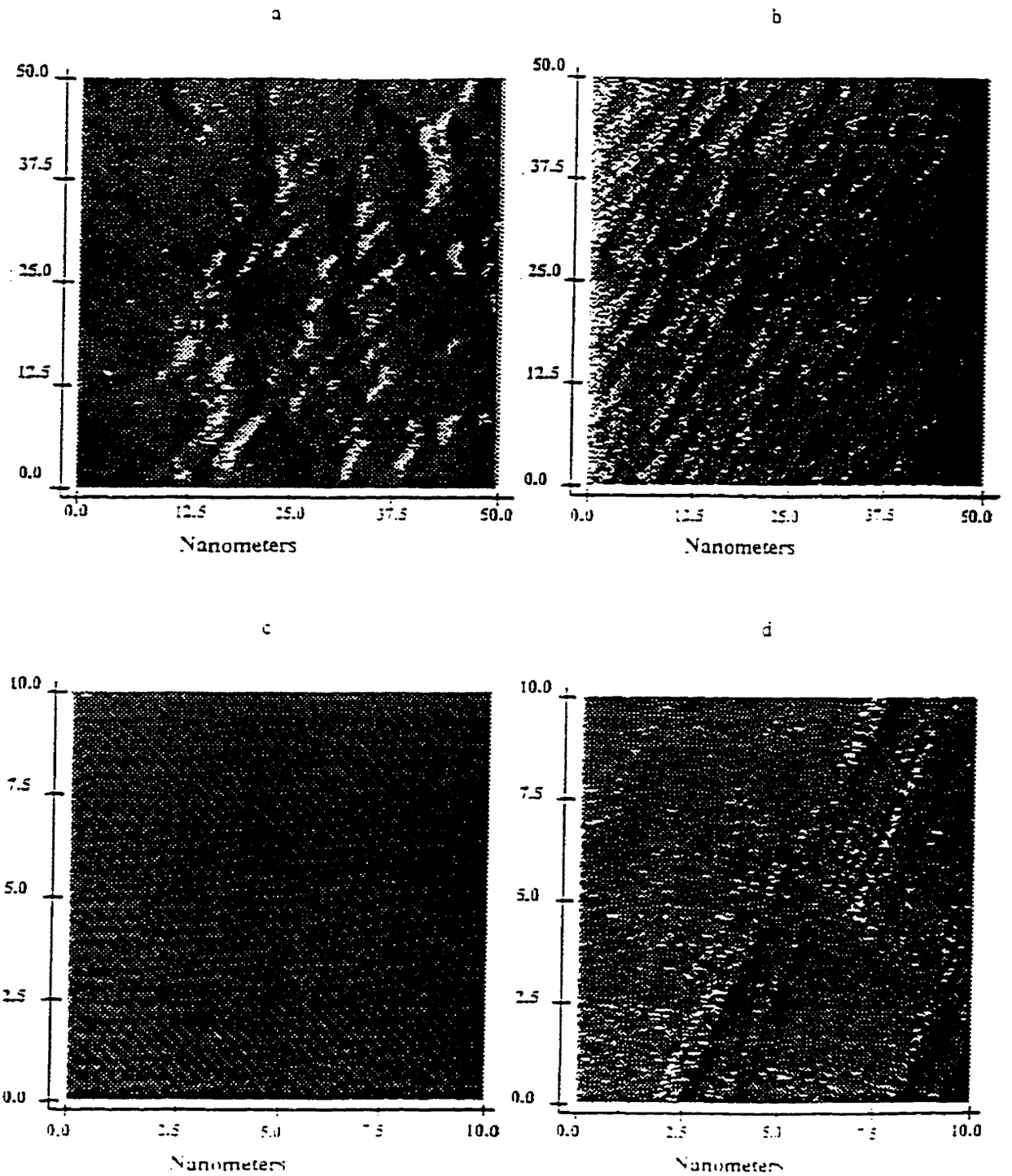


Figure 4.1 STM images of carbonaceous surfaces. (a) HAC as deposited; (b) HAC after annealing in vacuum to 800K; (c) graphite; (d) annealed HAC at higher magnification. Note ordered graphitic structures in upper right quadrant of (d).

Infrared emission from thermally excited HAC has been observed in the lab for the first time. Thin (~1μm) HAC films deposited onto stainless steel substrates were heated in vacuum and their emission spectra were recorded on a Michelson FTIR spectrometer. The observed IR emission falls into broad vibrational bands, superimposed upon a thermal continuum of emission. This emission was also observed using an alternate FTIR and emission chamber, and subsequently using a custom built scanning filter wheel IR spectrometer for further confirmation (Pinho & Duley 1995).

Figure 45 shows a characteristic sequence of HAC emission spectra spanning the temperature range from 573-773K. These spectra have been presented following the method outlined in section 3.3, except that they have not been multiplied by a blackbody function. The 3.2-3.6μm region shows a structured emission band near 3.4μm which is characteristic of aliphatic hydrocarbons. As the temperature of the sample is increased, the structure and intensity of this feature decrease and a new emission band appears near 3.29μm. This new emission can be attributed to the CH stretching vibration in aromatic hydrocarbons (Duley & Williams 1981). Its appearance at high temperature accompanies the transformation of HAC from a polymeric to a proto-graphitic solid (Scott & Duley 1996b).

Emission from the longer wavelength region (5-15μm, figure 45) shows an enhancement in the relative amplitude of the aromatic C-C ring vibration at 6.2μm and the 11.3μm aromatic CH bending vibration at high temperature. Emission peaks due to CH bending modes in molecular groups with 2 and 3 adjacent H atoms on aromatic rings are also apparent at ~12.3 and 13.2μm at 773K. Emission spectra at lower temperature are characterized by sharper spectral features at ~5.8, 6.9, 7.3 and 10.4μm and weaker emission at

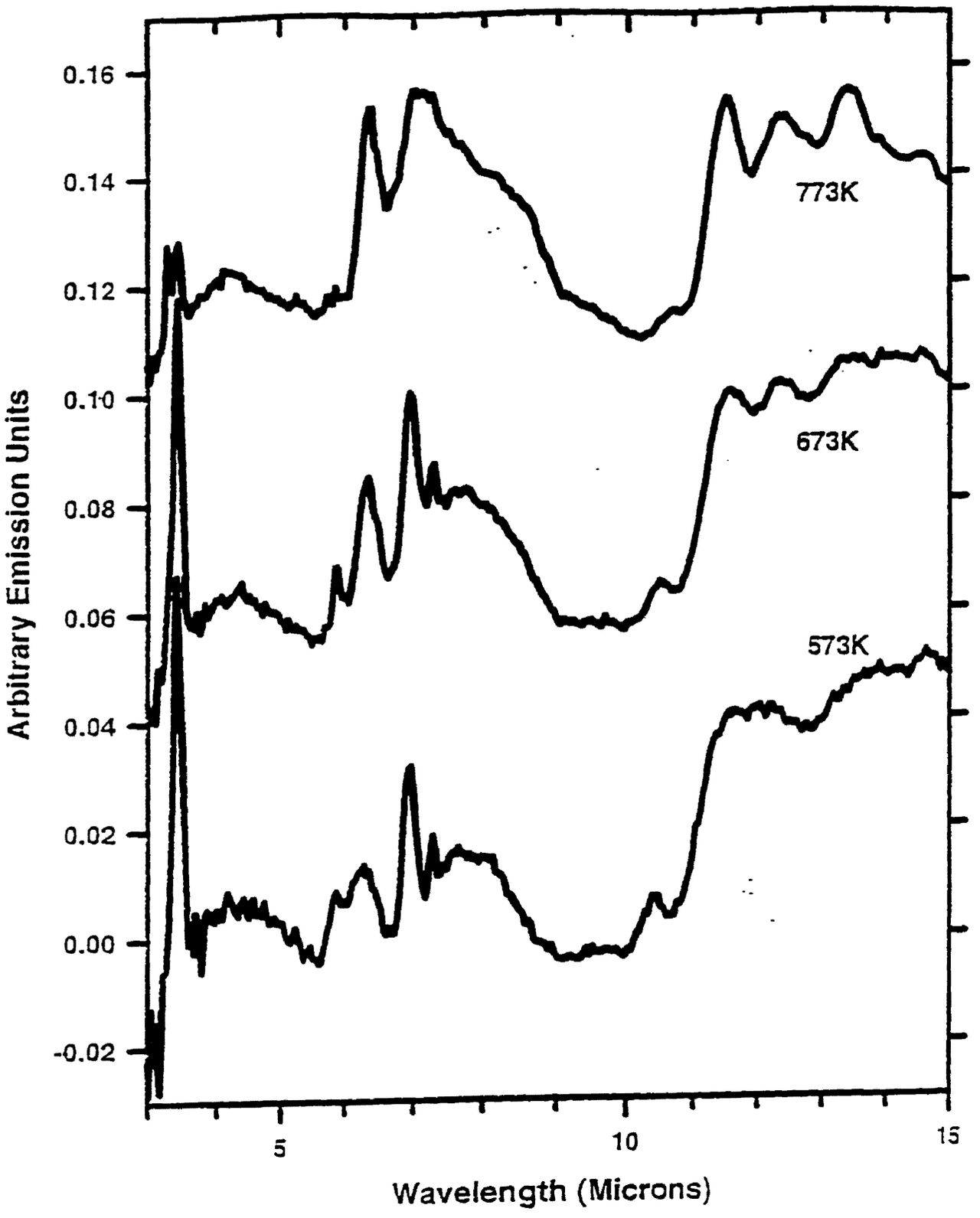


Figure 45 IR emission from HAC at various annealing temperatures (in vacuum) from 573-773K in the spectral range of 3-15μm, zero shifted for clarity.

6.2 and 11.3μm. The feature at 5.8μm is likely due to an aldehyde group (Rappoport 1967). The group of emission bands at 6.9, 7.3 and 10.4μm are observed only at low temperature and are attributable to vibrational modes in non-aromatic hydrocarbons. The appearance of these bands is then indicative of HAC material which has not been heated to temperatures above ~700K.

In general, emission spectra of HAC at a given temperature are similar to those observed in absorption. Some differences are found however, particularly with respect to the relative amplitude of individual components. This may be attributed, in part, to difficulty in assigning the baseline in emission spectra together with the broadness of some of the spectral features. Table 6 summarizes the differences between absorption and emission spectra of HAC. The major difference is the appearance of a broad feature in thermal emission spectra between 5.7 and 9.0μm. The peak of this emission is near 8.0μm, but a secondary maximum occurs near 8.6μm in emission spectra at 773K. A variety of aromatic C-C, CH and aliphatic CH modes appear in this spectral range (Rappoport 1967).

Figure 46 shows a characteristic sequence of HAC emission spectra spanning the temperature range from 573-723K in the vicinity of the 3μm CH stretching feature. As can be seen, the peak ratio, 'R', of 3.3/3.4μm band emission depends on the degree of annealing and, with careful control of conditions could be made to take on any value. In polymeric HAC, the 3.3μm aromatic CH stretch emission peak is not observed. For strongly annealed HAC, the 3.4μm emission is indistinguishable from the continuum to our level of accuracy. With continued annealing, the 3.3μm feature begins to diminish as well and will eventually disappear as the HAC becomes completely dehydrogenated. The 3.3μm feature to continuum ratio for

Table 6 Comparison between spectral features seen in emission from HAC and those in absorption spectra.

Absorption*	Emission[+]
3.21μm	Not seen
3.29	No change
3.38	No change
3.42	No change
3.46	Broadens
3.50	Shift to 3.51μm
	5.9 (likely aldehyde contamination)
6.25	No change
6.91	No change
7.27	No change
7.88	Broad peak 5.7-9.0
8.63	
9.5	Not seen
	10.3-10.5†
11.4	No change
12.3	No change
13.2	No change

* At 300K, after heating to 700-800K in vacuum (Scott & Duley 1996b)

[+] At 700-800K

† shifts to longer wavelength with increasing annealing temperature

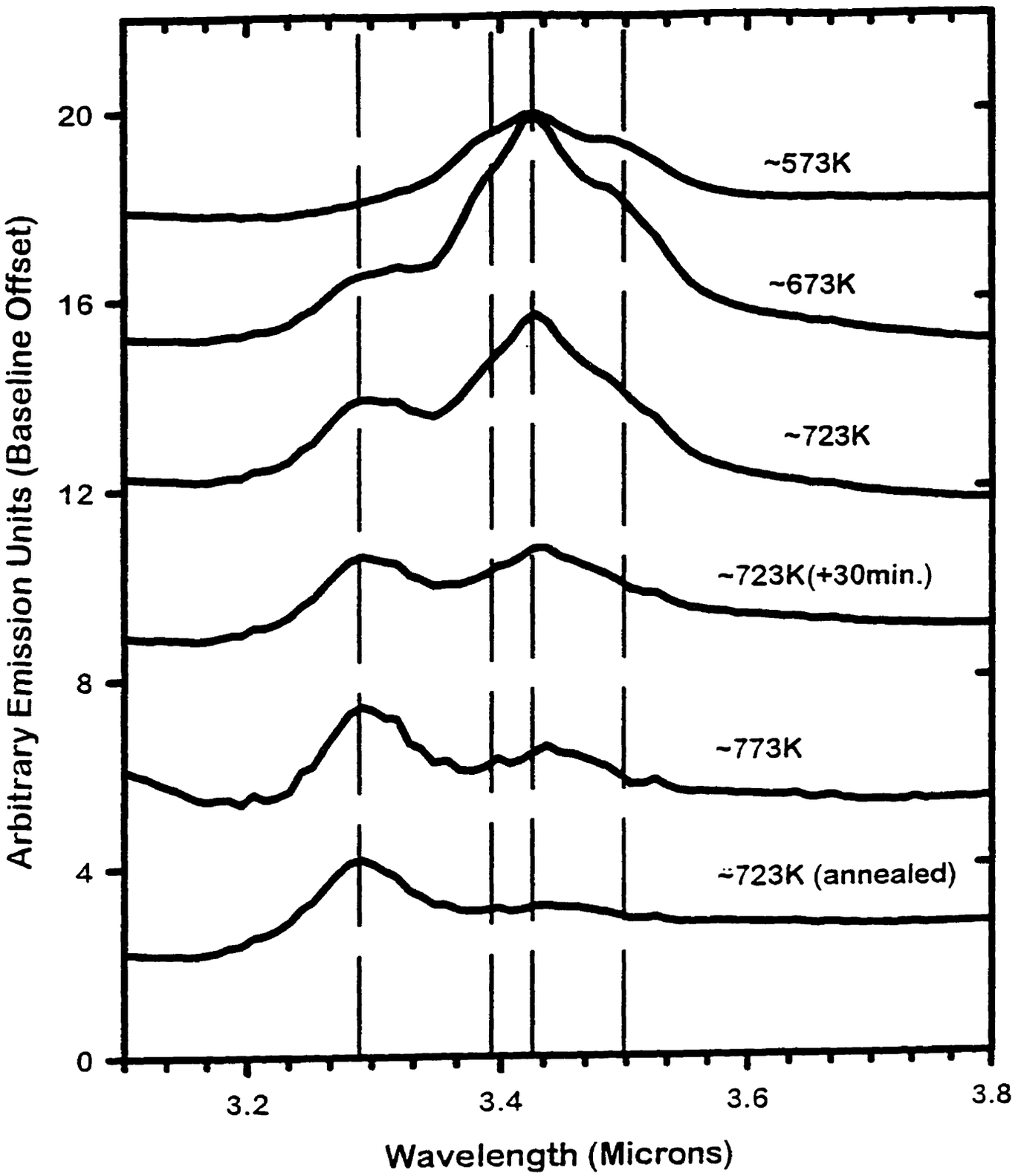


Figure 46 IR emission from HAC at various annealing temperatures (in vacuum) from 573-723K in the spectral range of 3.1-3.8μm.

thermal HAC emission depends on the estimated baseline, the amount of annealing and the extent of dehydrogenation. This is because of the fact that annealing darkens the film, resulting in an ever increasing continuum while the aromatic content is also increasing. It is estimated that this ratio reaches a maximum ≡ 2 for our films. Polymeric HAC has a 3.4μm feature to continuum ratio which can approach 7. These estimates depend on the assumed baseline position and have large associated uncertainties as a result. As the annealing process continues, the feature to continuum ratio in HAC solids will fall off rapidly from this value. During this process, the band-gap narrows causing the broad thermal continuum emission throughout the infrared to increase. One would expect the feature to continuum ratio to be much larger in the case of non-thermal UV-pumped emission. Such a phenomenon, if it exists, would require that the localization of the absorbed photon's energy in a PAH-like surface group would prevent its redistribution amongst all available modes.

In an attempt to identify spectral features caused by the incorporation of other common elements, HAC was annealed directly under atmospheric conditions. Figure 47 shows a representative absorption sequence annealed from 400-600K in air. After the initial annealing, the film appeared black and grainy. Approximately 80% of the film had delaminated from the substrate. As can be seen, the components of air react quickly with HAC to produce new absorption features. Further annealing at 600K completely destroyed the bulk of the film, leaving a barely visible yellowish glaze adhered to the KCl substrate. By comparing various library spectra to these absorption features and noting the commonalties between the successful matches, the source of these peaks can be determined. Table 7 lists the tentative identification of the observed features.

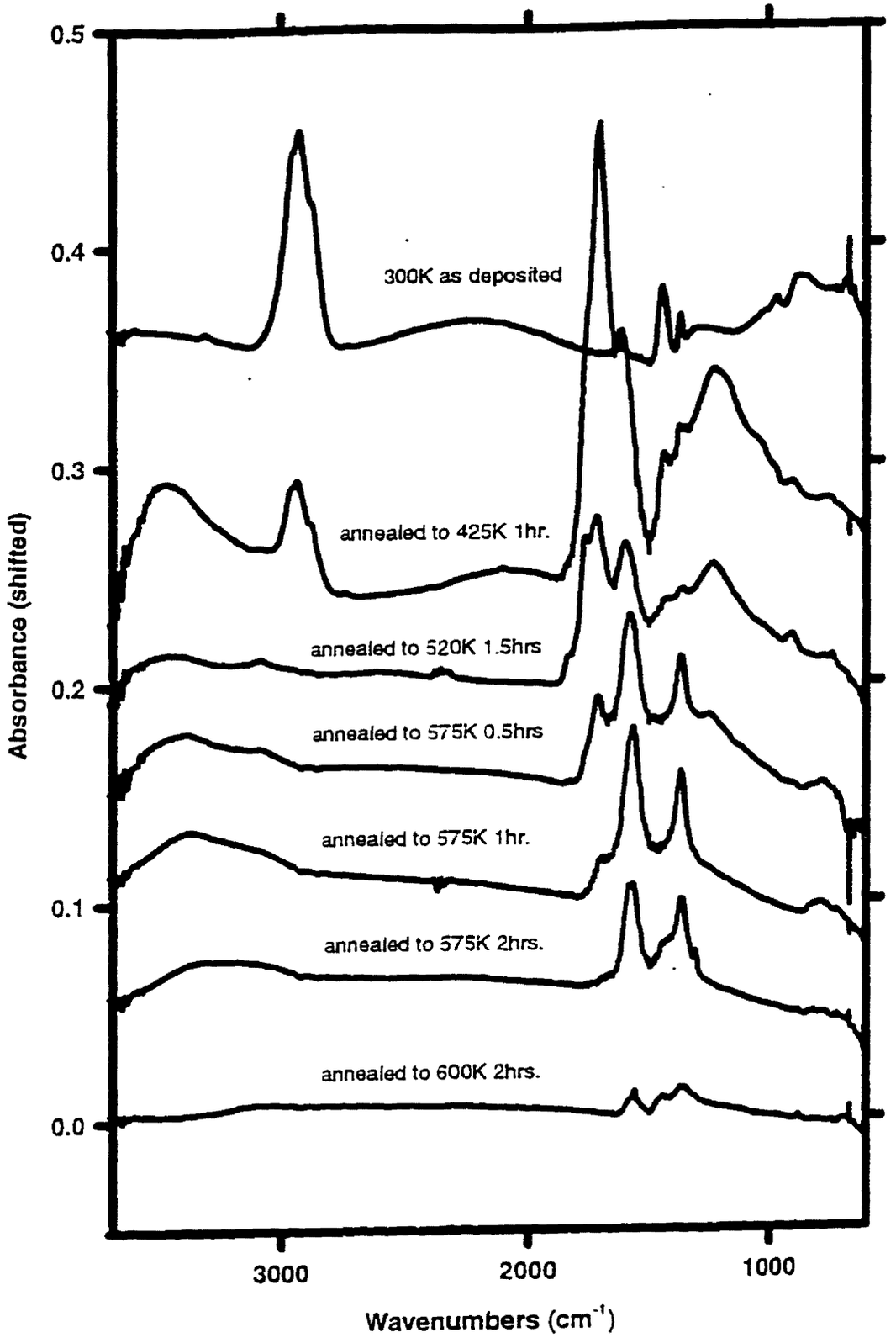


Figure 47 IR absorption spectra of HAC after annealing to various temperatures (in air) from 300K (top) to 600K (bottom) in the spectral range of 3700-600cm^{-1}.

Table 7 Identification of observed IR modes in carbonaceous films with contributions from nitrogen and oxygen

Observed peak absorption (μm)	***Identification***
†~2.9 (broad)	N-H stretch
†3.37, 3.40,3.46	CH stretch aliphatic
4.6	C≡N stretch
4.7	C=O stretch
†5.65	O=C-NH-C=O skeletal stretch, / \ anhydrides
†5.77-5.83 (strong)	>C=O aliphatic skeletal stretch, esters, aldehydes, ketones
†6.15-6.38 (strong)	aromatic skeletal stretch
6.4 (strong)	nitrogenated aromatic stretch
6.5 (strong)	oxygenated aromatic stretch
†7.3 (strong)	Phenyl-C=O and similar stretch, \ O-R
†8.07 (broad)	R-O-C=O; >N- aliphatic vibrations, \ ethers, esters. R

† seen in HAC films annealed in air.

As seen in figure 47, the spectrum is originally dominated by the expected aliphatic modes, and as the annealing temperature is increased, aromatic and phenyl dominated vibrations take over. This sort of behaviour is expected as the HAC film is slowly destroyed by oxidation.

To extend this study, the emission characteristics of HAC annealed in an oxygen atmosphere of ~5 torr were obtained. Figure 48 illustrates the major features of the resultant spectra. Of particular note is the strong onset of emission at ~5.5μm extending to longer wavelengths, consistent with the onset of aliphatic C=O vibrations seen in the absorption experiment. The broad peak at 8μm is enhanced, strengthening the association with oxygen noted in table 7. An extra peak at ~4.7μm is also seen in emission, probably corresponding to C=O stretching vibrations. The strong 6.38μm aromatic vibration observed in the thermal annealing of HAC in air is shifted slightly to ~6.5μm in the oxygen-annealed spectra.

For the incorporation of nitrogen into a HAC film, it was necessary to deposit the film in an ammonia atmosphere. Molecular nitrogen did not seem to incorporate well, likely due to its higher dissociation energy. The resultant N-HAC film emission spectrum and its vacuum annealed counterpart are illustrated in figure 49. The 2.9μm N-H stretch is visible before annealing as expected. Also visible is the 6.9μm aliphatic stretch seen in polymeric HAC. In this film, the strong emission onset observed at 5.5μm in oxygenated HAC is shifted to ~6.0μm which is a lower frequency than in the oxygen-annealed HAC. An extra peak at ~4.6μm is also seen in emission corresponding to C≡N stretching vibrations. A strong, persistent aromatic vibration is observed at ~6.4μm as in the other spectra. Here also, the

broad 8μm vibration is seen upon continued annealing. This is likely due to the weakening of surrounding bands, leaving only the skeletal nitrogen vibrations behind.

Figure 50 shows the response of an N-HAC film upon annealing in ~5 torr of oxygen. Here, the 6.9μm peak is quickly destroyed, and the >C=O aliphatic stretch appears at 5.9μm. As usual, the aromatic vibration is visible in the 6.5μm region, along with the broad 8μm feature.

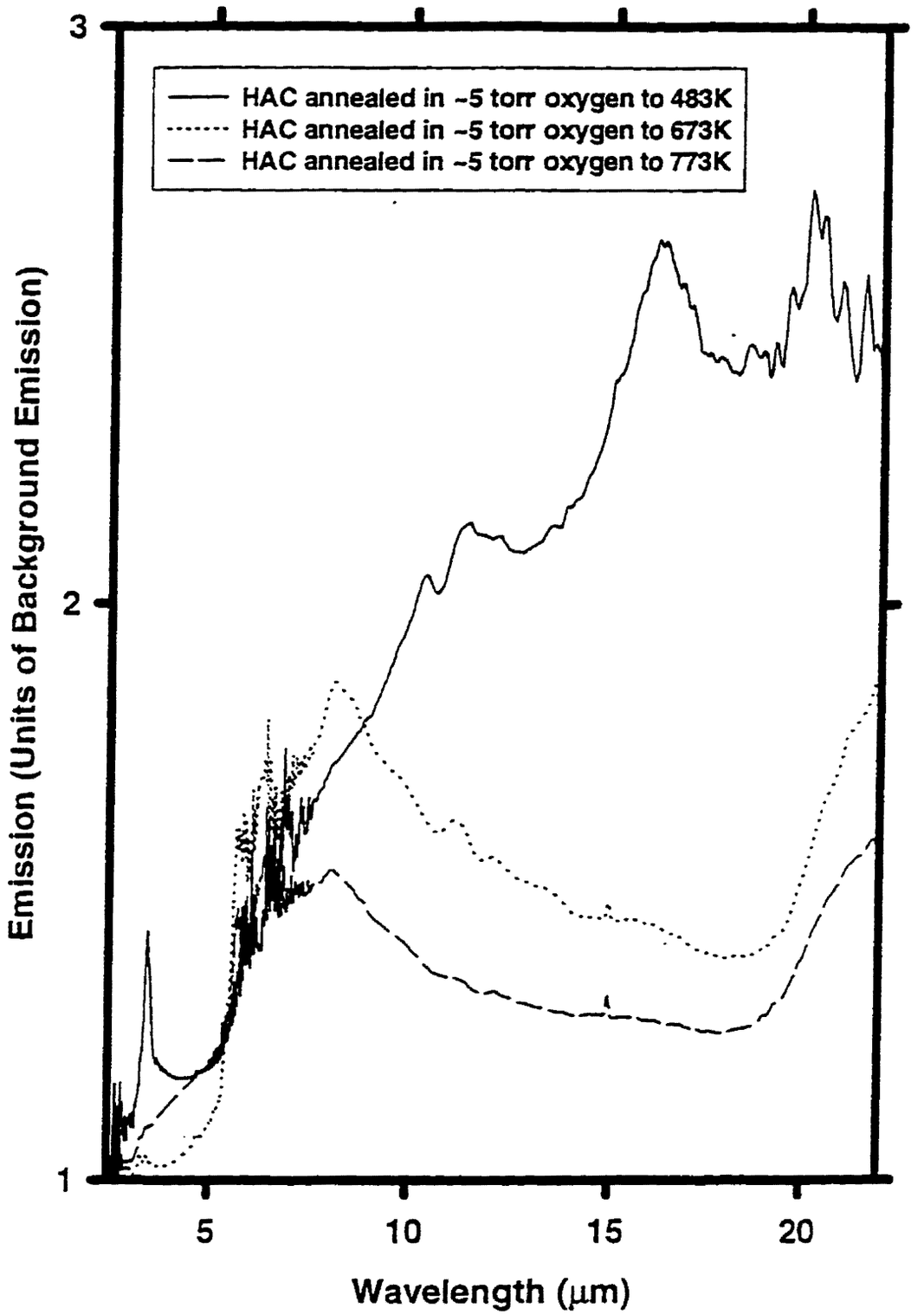


Figure 48 IR emission from HAC annealed in an oxygen atmosphere to 483, 673 and 773K.

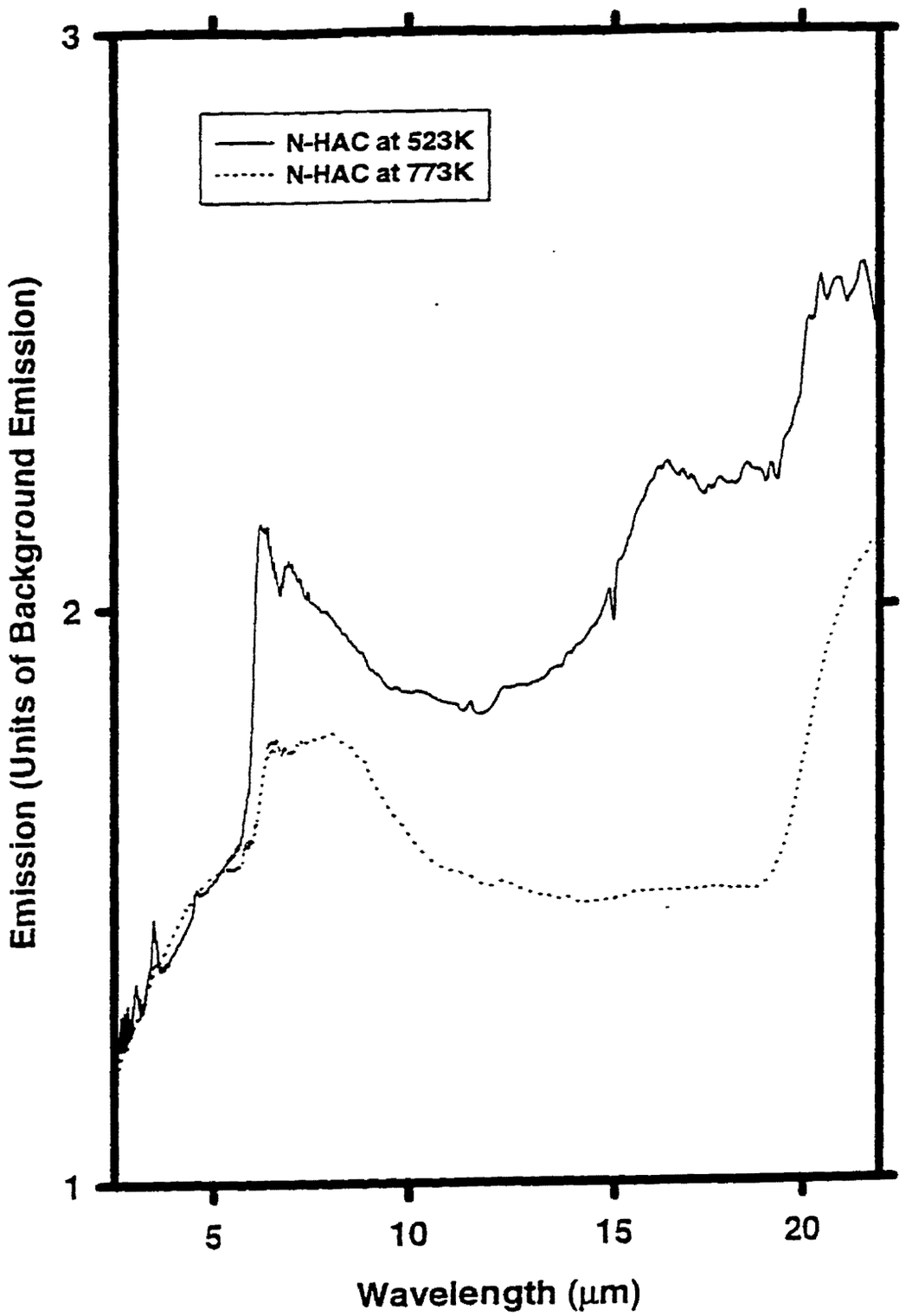


Figure 49 IR emission from nitrogenated HAC annealed in vacuum to 523 and 773K.

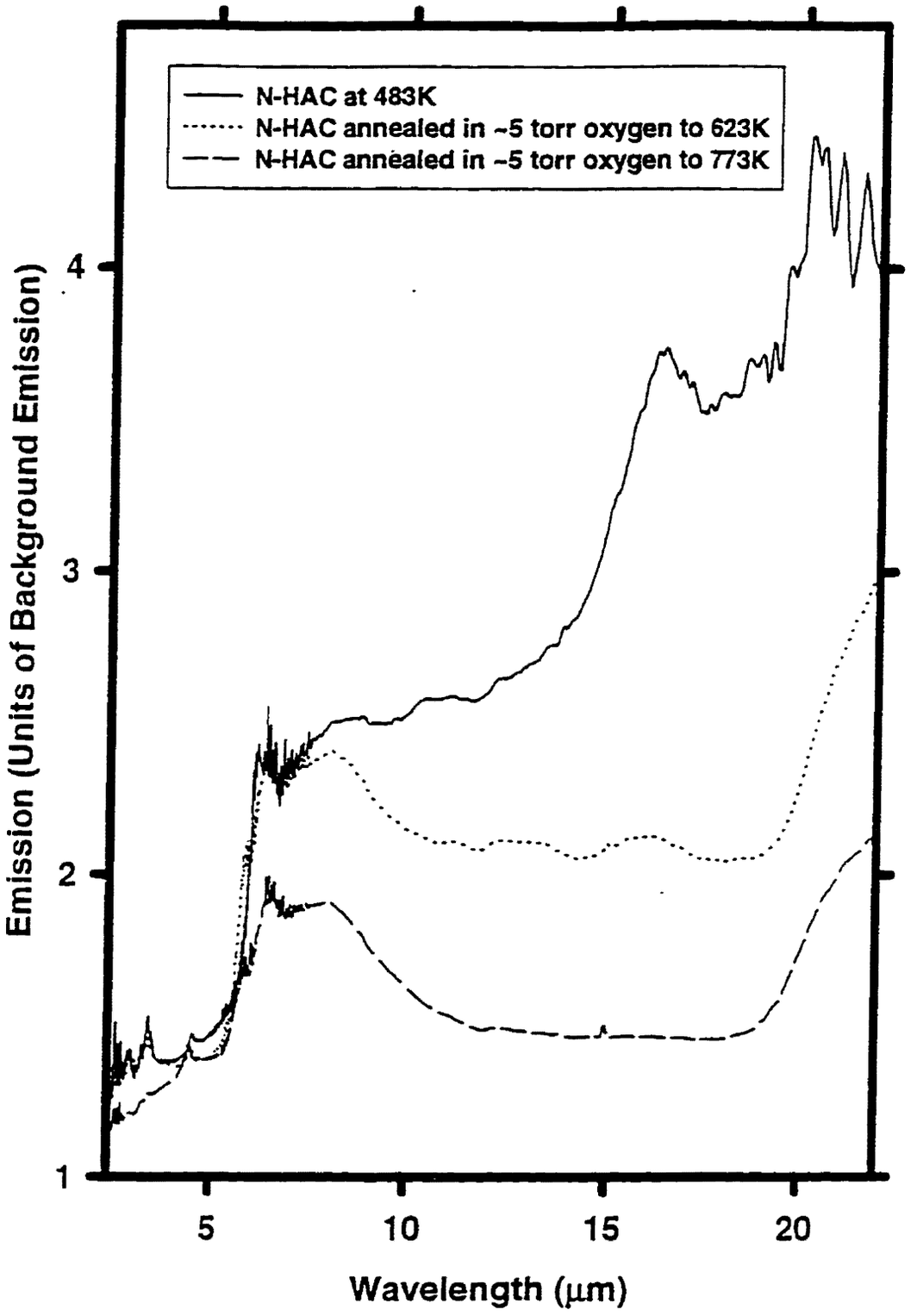


Figure 50 IR emission from N-HAC at 483K and annealed in oxygen to 623 and 773K.

4.5 LIMS of HAC

The experimental apparatus for this procedure is described in section 3.5. 308nm excimer laser radiation was focused onto thin HAC films in vacuum, and the mass spectrum of the resulting ionized debris was measured with a time of flight mass spectrometer. The effect of single shots at pulse energies of 0.09 $J \cdot cm^{-2}$ on the target were difficult to evaluate visually, while those with pulse energies of 4.8 $J \cdot cm^{-2}$ caused darkening and flaking of the film in an area much larger than the actual beam size. Multiple shots at low laser pulse energy caused a darkening of the interaction region, while multiple shots at high pulse energy resulted in the destruction of HAC within the interaction region. Films deposited on aluminum substrates tended to flake away after only a few laser shots due to poor adhesion to the substrate.

Knowledge of the composition of ablated material near the ablation threshold fluence is extremely important. Fragments produced at low laser fluence are more likely to convey information about the chemical structure of the parent films than those created at higher fluences where plasma interactions may become significant. High incident fluence tends to produce dissociation, creating a much larger proportion of single atom species than would otherwise be the case (see section 3.5; Leddingham & Singhal 1992). A range of fluences from 0.09 to 4.8 $J \cdot cm^{-2}$ were applied to HAC films in ablation experiments. In all cases except for pulses at the highest energy, photo-chemical effects were seen to alter the distribution of molecular fragments produced over successive laser shots. In the 4.8 $J \cdot cm^{-2}$ case, physical effects (film disruption and flaking) made multiple shots impractical. When the spectra produced appeared qualitatively similar on the oscilloscope, shots were averaged to produce a single trace. Using these averages as a guideline, typical single shot spectra were selected for

presentation to eliminate the peak-broadening effects of averaging. Due to the uncertainty in mass calibration and the observed peak jitter from shot to shot of ~4 u in the 0-240u mass region, it would be inappropriate to give the precise peak positions undue credence. The accuracy of the data allows confident statements to be made about the number of carbon atoms contained in the major ionized fragments, with due consideration given to multiplicity caused by hydrogenation of the larger species. It was found that the time delay of large mass fragments (>300u) was altered depending on the flux of smaller particles for each shot. Small offsets in the positions of known peaks indicate that the largest fragments were accelerated, possibly by collisional effects, whenever a large population of smaller fragments existed over the target. The mass axis calibration above 300u was corrected when necessary to account for this shift. Obviously enhanced peaks due to the closed shell fullerenes C_{50}, C_{60} and C_{70} were selected and then shifted slightly to 600, 720 or 840u respectively. The corrected mass scale was then merged discontinuously with the pre-existing scale at 300u due to a lack of any peaks near that mass. Such corrections were unnecessary in cases where the small fragments were absent.

The general features of a typical HAC LIMS spectrum are as follows: i) the strongest peaks are located at 24-30u, and 38-42u, representing C_2 and C_3 hydrocarbons; ii) sharp, clear peaks separated by approximately 12 u are seen from ions corresponding to C_8-C_{20} hydrocarbon species; iii) A broad structureless continuum (at our resolution) of large ionized molecules or very small grains (VSGs) is seen beginning around C_{40}, peaking in the vicinity of C_{100}-C_{150}, and extending out to ~C_{300}. The fact that sharp structure is not resolved for this continuum makes it conceivable that this peak is associated with the presence of energetic

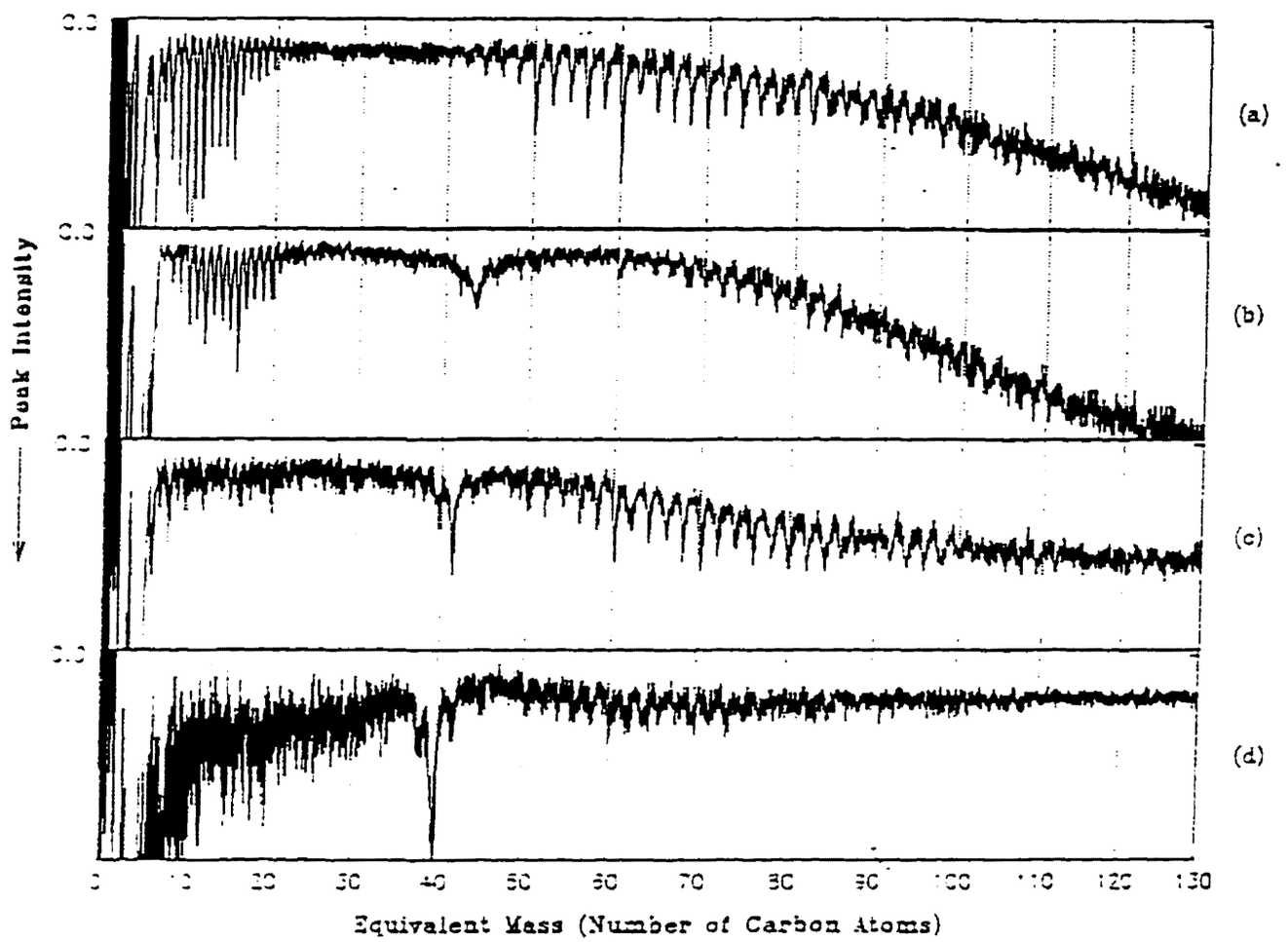


Figure 51 LIMS of HAC on copper at 0.13 J/cm^2. Successive shots on one location showing effects of photoprocessing and ablation (a) 5th shot; (b) 10th shot; (c) 18th shot; (d) 24th shot

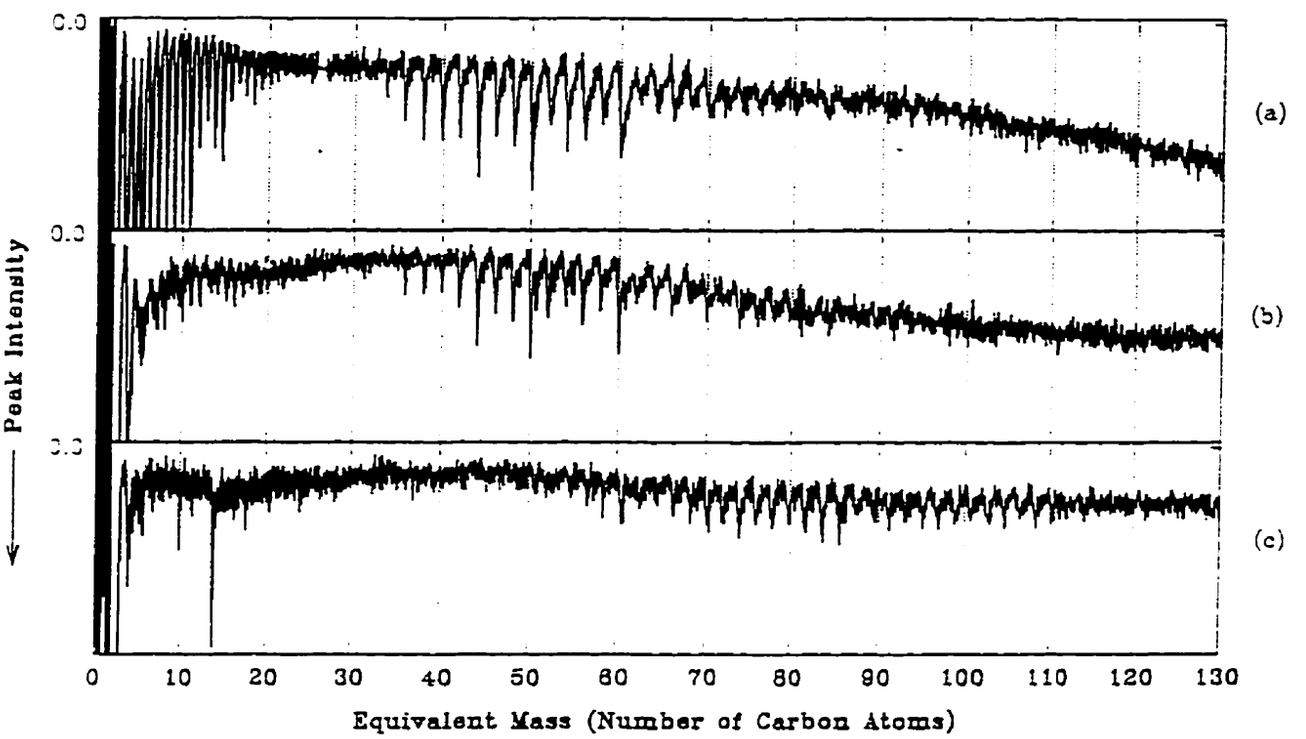


Figure 52 LIMS of HAC on aluminum at 0.20 J/cm^2 (a) 1st shot; (b) 2nd shot; (c) 3rd shot

neutral fragments created in the plasma. The fact that the continuum appears in nearly the same position for laser fluences ranging from 0.09-0.25 $J \cdot cm^{-2}$ would seem to argue against an interpretation based on neutral fragments. Evidence which suggests that this peak is ionic in nature is that it moves to longer *TOF* and increases in width when the accelerating voltage is decreased.

Figure 51 illustrates a sequence of LIMS spectra taken from the same spot on a HAC surface with the beam just above the threshold fluence for a detectable signal at 0.13 $J \cdot cm^{-2}$, showing the effects of photoprocessing and ablation. In figure 51a, before significant photo-processing has occurred, a mass fragment spectrum is obtained which is superficially similar to those seen from the ablation of graphite (Heath et al. 1987; Leddingham & Singhal 1992). A distribution of distinct small mass peaks spaced ~12 u apart up to ~ C_{20} is visibly separated from a population of larger fragments consisting of sharp peaks separated by ~24 u from ~C_{42} to ~C_{100}. Such a pattern is characteristic of condensed aromatic hydrocarbon molecules (Heath et al. 1987). Individual peaks at C_{50}, C_{60} and C_{70} are seen to be slightly enhanced. These enhancements indicate that the condensed aromatic structures are curling up into a further stabilized fullerene geometry. Typically, these distinct peaks, attributed to PAH and fullerene ions, are superimposed upon the rising edge of the broad high mass VSG distribution which is observed to extend out to ~C_{300}. In this sample the underlying continuum feature peaks at approximately C_{150}.

Upon continued photo-processing a narrow distribution of PAH molecules spanning the range from ~C_{38} - C_{44} emerges, coincident with the decline of the small mass fragment distribution (figure 51b & c), and eventually the decline of the larger mass PAHs as well (figure 51d).

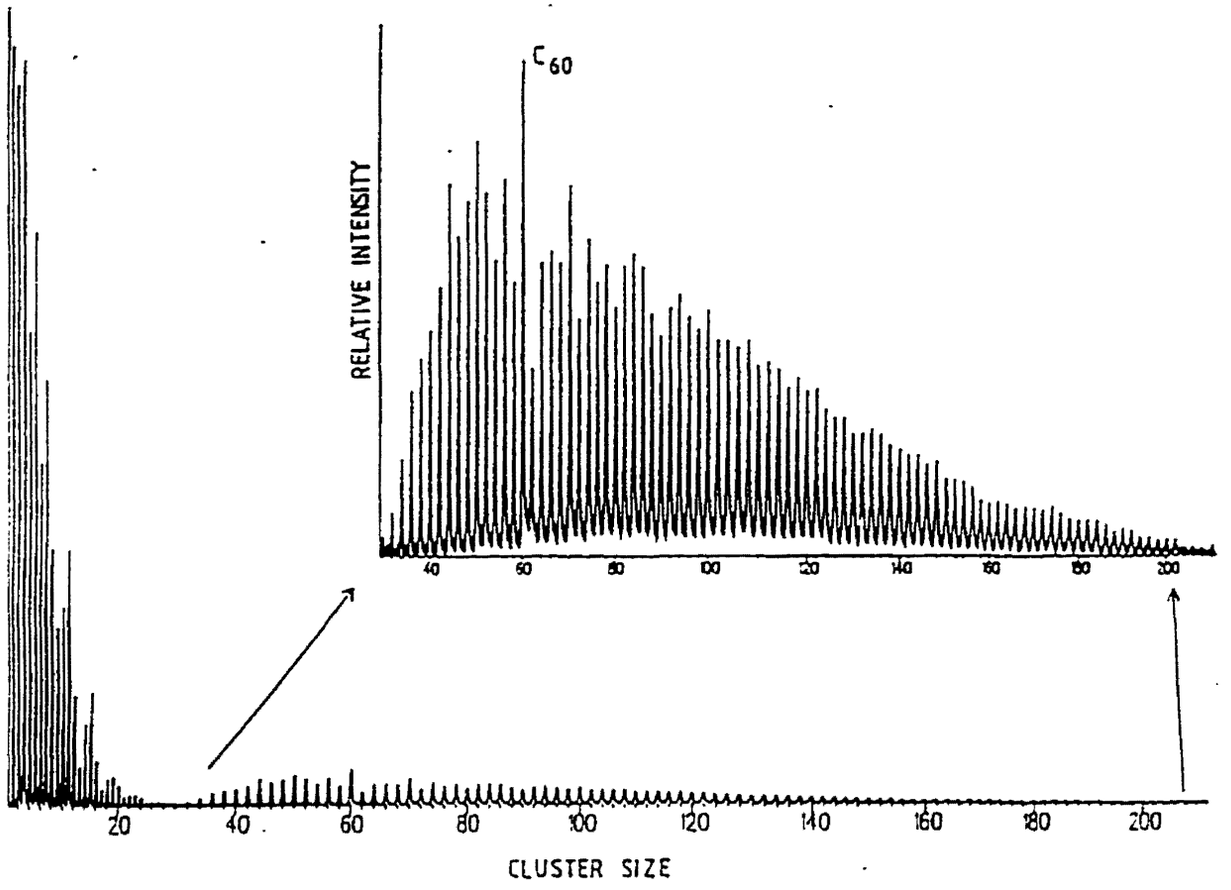


Figure 53 LIMS of graphite at 10^{12} W·m^{-2} and 532nm wavelength showing characteristic fullerene peaks (Leddingham & Singhal 1992).

The assumption that the broad featureless peaks seen in these spectra are due to high mass fragments could be incorrect if there is significant ion fragment production due to thermal processes in the HAC film. In this case there could be a delayed emission of ionic fragments. Such a time delay would be mistaken as associated with a large ionic fragment. Such delays would need to be on the order of 20μs to account for the observed timing and it is hard to imagine a thermal process which would have its peak ion production occurring at such long delay times.

Figure 53 shows the LIMS spectrum of graphite taken at a power density of $10^{12}\,W{\cdot}m^{-2}$ and 532nm laser wavelength, which shows similar signatures to those seen in figures 51 and 52 which were obtained with a laser intensity of $\sim 10^{10}\,W{\cdot}m^{-2}$ and 308nm wavelength.

Figures 54 and 55 illustrate the low mass end of some typical HAC LIMS spectra. The mass uncertainty in the calibration of these plots must be stressed (see section 3.5 for discussion). The first few pulses always lead to an enhanced C_2H_x/C_3H_x species production ratio but this ratio decreases to < 1 as the number of pulses increases. In figure 54(a) we see a relatively smooth distribution amongst the various C_nH_x peaks visible up to n = 15, except for those near n = 10 and 14 which would likely correspond to the aromatically stabilized, dehydrogenated naphthalene and anthracene radical cations respectively. The fact that there exist peaks for each n value suggest that there is a strong production of linear, or branched carbon chains of varying length. There is also evidence for the production of $(C{=}C)_nH_m$ molecular fragments with $m \leq 4$, but this cannot be definitely confirmed due to uncertainties in the mass calibration.

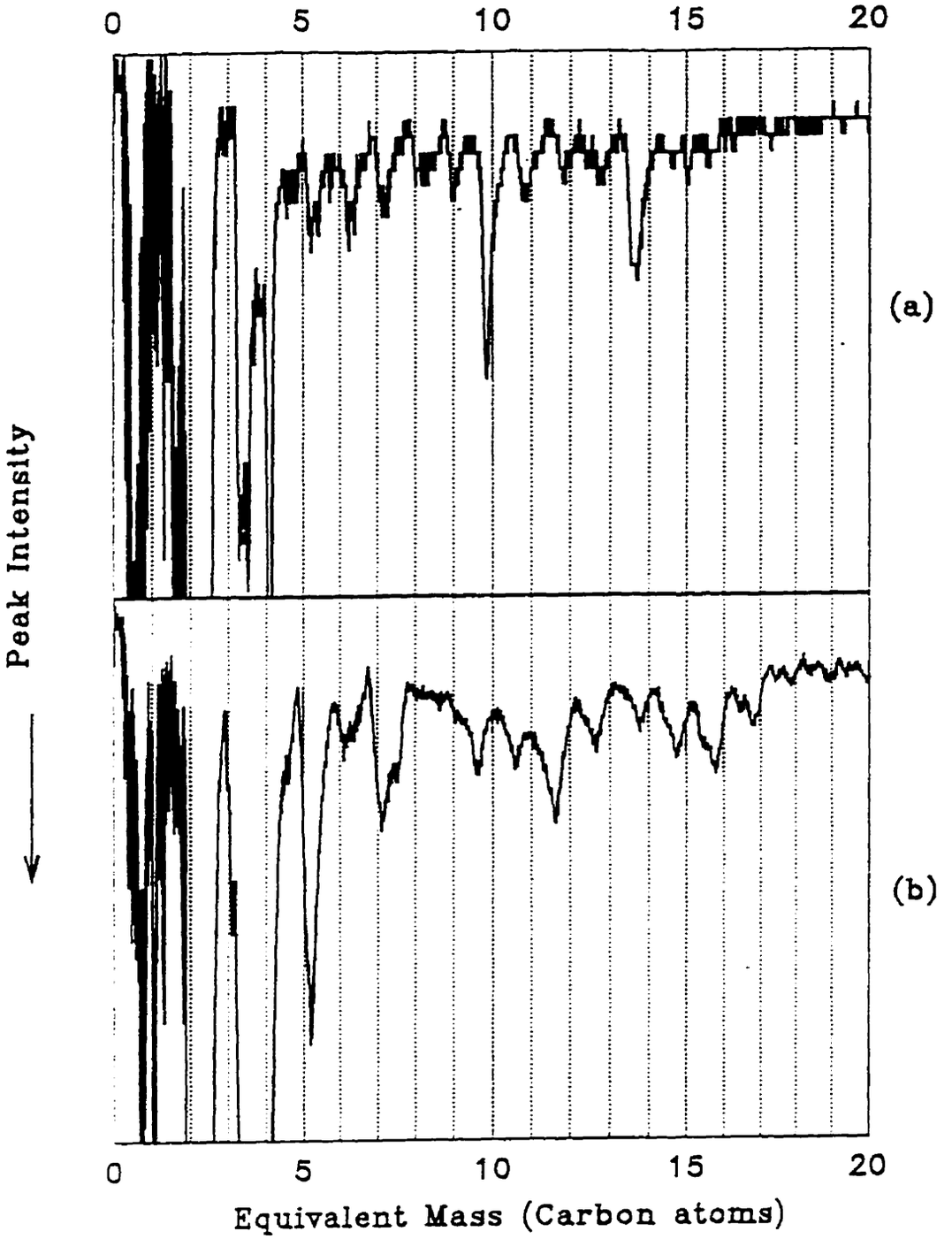


Figure 54 LIMS of HAC on copper (a) 1st shot at 0.09 J/cm^2; (b) shots 3-8 at 0.09 J/cm^2

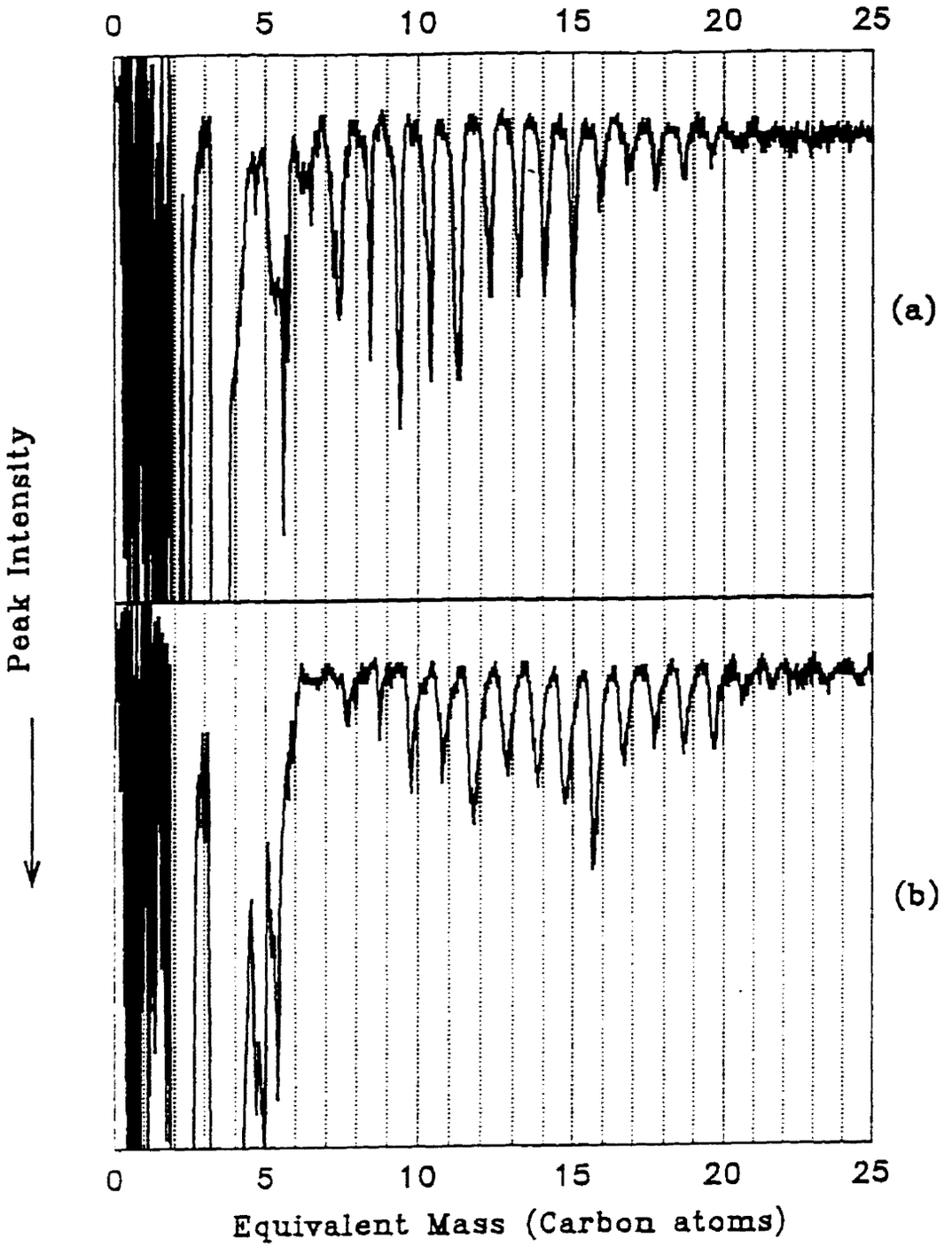


Figure 55 LIMS of HAC on aluminum (a) 1st shot at 0.20 J/cm^2; (b) 2nd shot at 0.20 J/cm^2

In figure 54(b), C_nH_x peaks are seen corresponding to n = 9 to 16. These are likely due to a smooth distribution of aliphatic hydrocarbon chains of varying length. The strongest among these are the $C_{11}H_x$ and $C_{15}H_x$ peaks where $x < 12$. It is interesting to note that these peaks may be methylated derivatives of naphthalene and anthracene radical cations. Indeed, the strong peak at ~84-92 u may correspond to the methylated benzene cation.

Data in figure 55(a) and (b) were obtained at a laser fluence of 0.20 J/cm^2 and both show clear mass peak definition out to C_{20}. It is unclear whether the offset in peak positions between the two shots arises from actual mass differences in the species produced, or whether these are due to electric field inhomogeneities in the LIMS apparatus. The obvious similarities to data in figure 54 are reassuring, increasing confidence in the reproducibility of the results.

The results of the near threshold LIMS of polymeric HAC films can be summarized as follows: i) initial pulses release a distribution of carbonaceous fragments from the film surface including small aromatic species such as naphthalene and anthracene. Linear carbon chains are also present. These species are detectable up to a mass of ~C_{25} in some cases. Most of the ionic flux is present in the form of C_2 hydrocarbons, with molecules having C_3 and C_5 groups present at a lower intensity. A smooth distribution of VSGs is observed from ~C_{40} to C_{300}, with a peak near ~C_{150}; ii) continued photo-processing causes noticeable changes in the product distribution and it appears that large condensed PAHs and fullerenes (~C_{42}-C_{100}) are produced on the surface of the film and released. The flux of C_2 diminishes and comparable quantities of C_3 and C_5 fragments are also produced. The flux of C_7 - C_{35} ions disappears, coincident with the emergence of a new peak at ~C_{40}.

All of these results can be explained in terms of existing theories of HAC structure (Robertson & O'Reilly 1986; Duley & Williams 1988; Duley 1996a). In this interpretation, the

linear chains which come off the surface earliest make up the polymeric backbone of the HAC solid (refer to figure 4a). The VSGs (C_{50} - C_{300}) consist of various numbers of graphitic islands connected together by the remaining polymeric chains which may be removed from the film surface as a unit. The lack of peak definition in this broad component is due to the varying hydrogenation of these multi-island subunits. The largest condensed PAH molecules and closed shell fullerenes, represented by the sharp peaks from ~C_{40}-C_{100}, are probably formed on the surface of the HAC during UV photo-processing as the relative ease with which these peaks are observed indicates an efficient production mechanism. Similar molecules have been observed during intense electron bombardment of a-C (Ugarte 1994), and in the laser ablation of graphite (Leddingham & Singhal 1992). It is possible that these molecules are formed in HAC when multiple graphitic islands merge into a single aromatic unit. The peak centered near C_{40} represents the typical size of an individual graphitic island (see next paragraph). This peak does not emerge from the background until the polymeric connecting structure has been removed by previous shots. The removal of the polymeric backbone is likely also the reason why the broad VSG peak eventually disappears. With fewer interconnections available it becomes less likely that multiple interconnected islands will be removed from the film.

The precise size of individual graphitic islands is of particular interest as it is known that the bandgap in HAC scales with the size of its internal aromatic clusters (see section 2.2). From equation 3, it is apparent that a compact aromatic group with 40 carbon atoms, corresponding to $M \approx 12$ would have a band gap E_g of ~1.6eV. This is quite consistent with a partially graphitized HAC solid (Iida et al. 1984; Jenniskens et al. 1992), indicating that laser energy may be promoting ring growth during the LIMS process. Using equation 12 one derives a rough estimate of the temperature excursion of a 38 carbon aromatic group in

response to the absorption of a 308nm photon corresponding to ~430K. Assuming an ambient temperature of 290K, this results in a maximum cluster temperature of ~720K. For a C_{42} aromatic cluster, the same photon would produce a maximum temperature of only ~680K. For clusters <300 atoms, equation 12 tends to overestimate the actual temperature excursion experienced (Allamandola et al. 1989). In section 4.4 it was seen that thermal annealing of HAC films began to produce characteristic aromatic features in the IR spectra at a minimum temperature of ~673K. Therefore, one would not expect photo-thermal ring growth to take place for graphitic islands larger than this size.

5. DISCUSSION OF ASTROPHYSICAL IMPLICATIONS

5.1 The Role of HAC

HAC is currently thought by many to play an important role in the structure of interstellar dust (Jones et al. 1990; Whittet 1992; Dorschner & Henning 1995). This widespread agreement is due to a number of factors. These include the following: (i) carbon is substantially depleted in the ISM gas phase; (ii) non-equilibrium deposition conditions hinder the formation of crystalline solids; (iii) optical HAC luminescence is the most likely source of the extended red emission; (iv) IR absorption bands in the diffuse ISM are similar to aliphatic CH stretching in solids.

An in-depth analysis of the results presented in the previous section will help to determine whether the laboratory HAC films produced through laser ablation are similar to the material existing in interstellar dust grains.

The 3.4μm absorption of a HAC film deposited at 77K compares quite well with that observed along the line of sight to the galactic center, as well as from the Murchison meteorite (figure 56; Duley 1994b). Other methods of deposition can result in very different HAC compositions and spectral band ratios, giving the impression that HAC is a poor candidate for a major interstellar dust component. One such material is shown in figure 57 (Pendleton 1994) along with other materials which have been proposed as sources of interstellar extinction. Deposition of amorphous films through the method of laser ablation seems to produce materials with properties similar to those found in the ISM (Scott & Duley1996a).

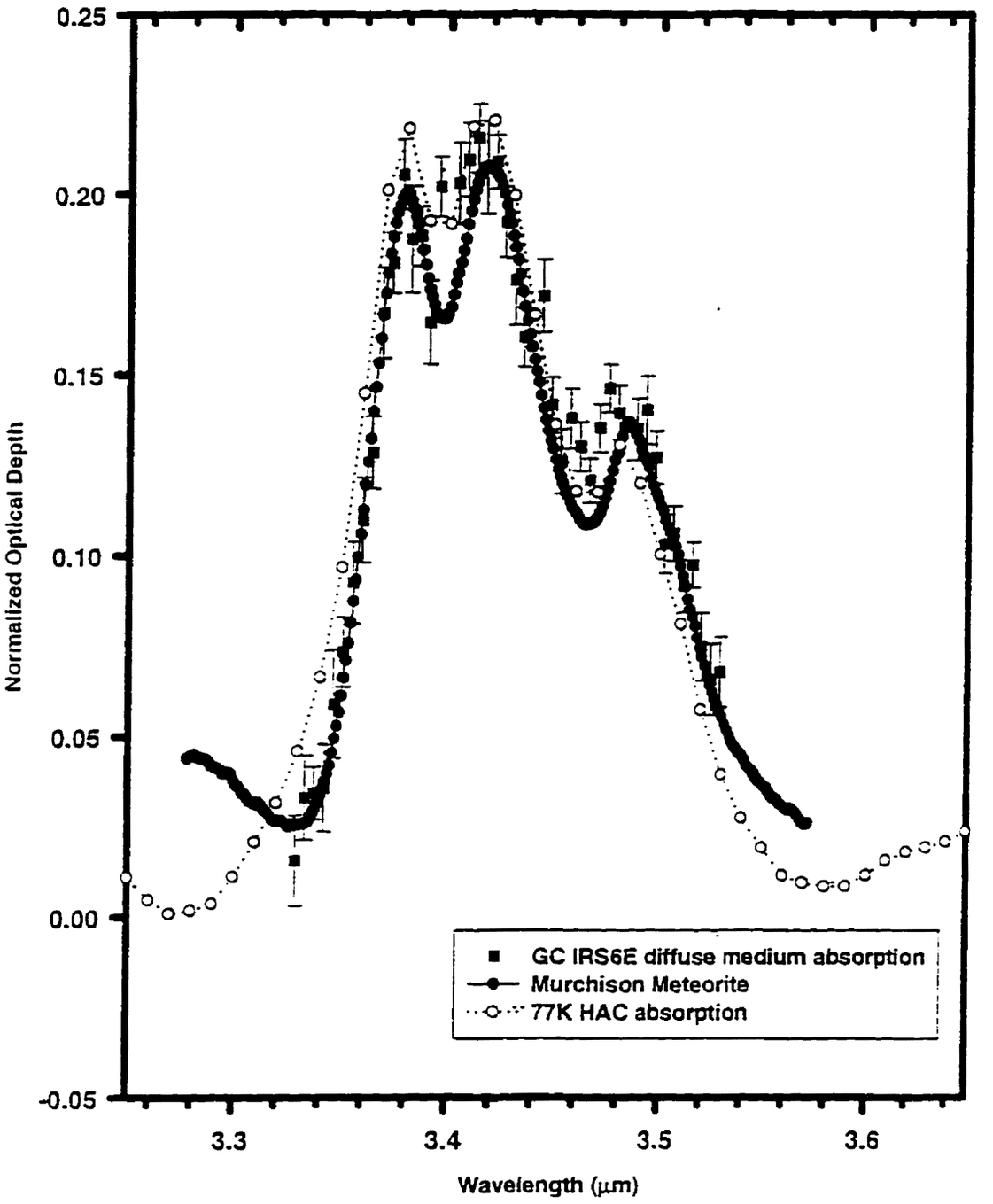


Figure 56 IR absorption spectrum of HAC deposited at 77K compared to astronomical observations of GC IRS6E and the Murchison Meteorite (Pendleton et al. 1994)

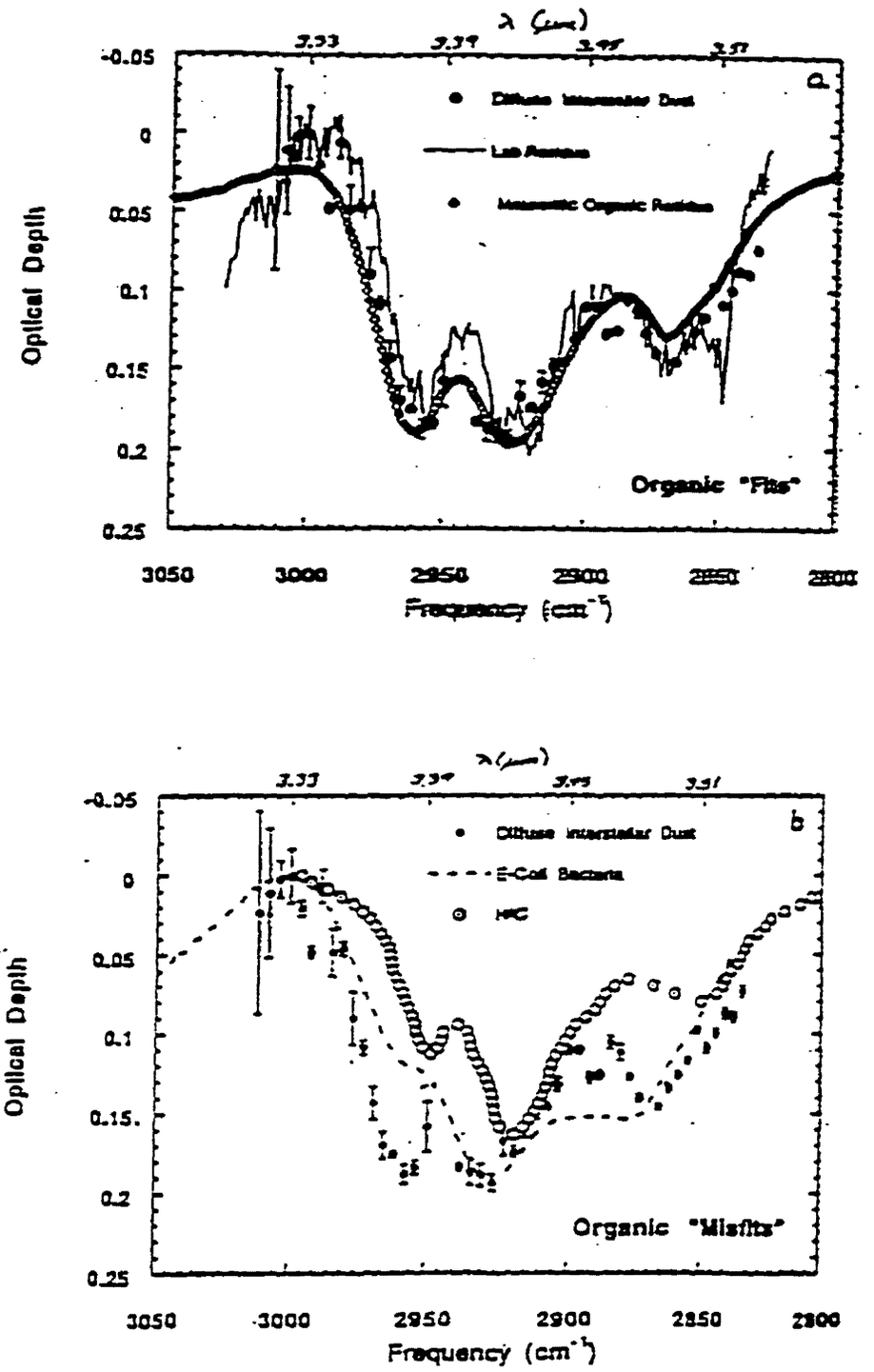


Figure 57 Various fits to the 3.4μm interstellar absorption feature (Pendleton 1994)

The physical and chemical processes observed in a carbonaceous laser-induced plasma can, therefore, serve as a model for the processes occurring in dust forming regions of space.

Recent observations of UIR sources have led to a three tiered classification scheme for the observed spectra. The most common sources, labelled 'type A' by Geballe (1996) and Tokunaga (1996), exhibit sharp infrared emission features at characteristic wavelengths. Such sources include planetary nebulae, HII regions, young stars, reflection nebulae and galaxies. The archetypal type A source is the bright reflection nebula NGC 7027. The sharp, highly aromatic, non-thermal bands of the type A sources make them the best candidates for an identification with free, gas-phase PAHs. Contrary to many astronomers' beliefs, a 'pure PAH' model cannot easily account for all UIR observations (see section 2.5). As yet there is no clear indication of PAHs in IR, visible or UV spectra (Tokunaga 1996). The observed continuum emission of most UIR sources requires extremely high PAH excitation temperatures (Allamandola et al. 1989). Mixtures of PAHs do not reproduce many anomalous emission features such as those observed in the extremely rare protostars HD 97048, HR 4049 and Elias 1 (Schutte et al. 1990) which are dominated by 3.43 and 3.53μm spectral features. These three UIR sources are labelled 'type C'. The third class of source is somewhat more numerous, including such infrared objects as IRAS 07134 (Buss et al. 1990), IRAS 04296+3429, IRAS 22272+5435 (Geballe et al. 1992), and IRAS 05341+0852 (Geballe & van der Veen 1990). These objects, labelled 'type B', are all carbon-rich post-AGB stars characterized by broad emission bands at 21, 12.2, 11.5, 10.5, 6.9, 6.2, 3.4 and 3.3μm and with R values which are much smaller than for type A sources. Figures 58 and 59 from Tokunaga (1996) illustrate typical spectra from all three types of UIR source.

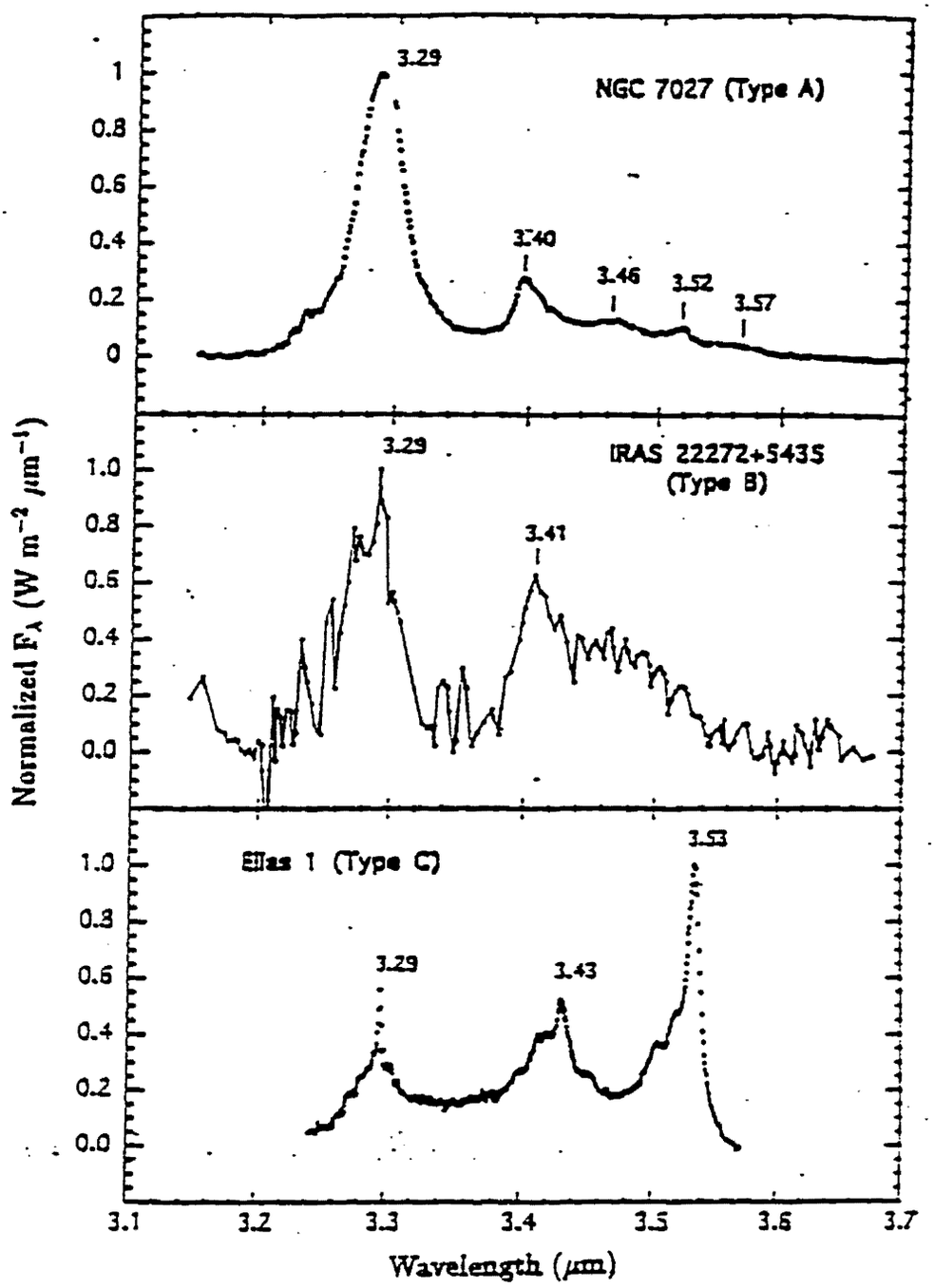


Figure 58 3μm emission region for the three basic types of UIR source (Tokunaga 1996).

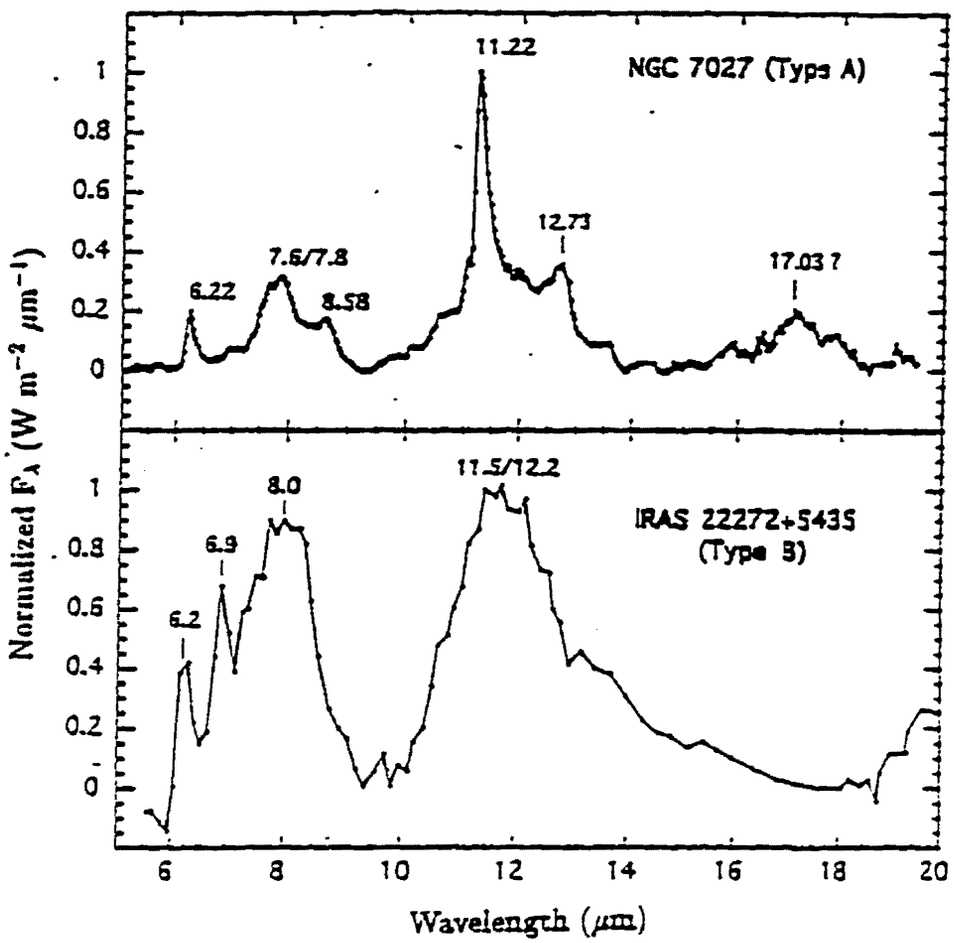


Figure 59 Mid-IR emission region for type A and type B UIR source (Tokunaga 1996).

The presence of large quantities of hot polymeric HAC dust is the most likely explanation for the unique spectral features appearing in type B sources. These carbon-rich AGB stars undergo significant mass loss (Frenklach & Feigelson 1989; Egan & Leung 1995). As the expanding debris shell cools, solid grains of silicon carbide can form which, along with any silicate grains from the ambient interstellar medium, may serve as substrates for the deposition of polymeric HAC mantles in a process similar to laboratory plasma deposition.

Dust in the newly forming proto-planetary nebula can be heated by stellar radiation to the temperatures necessary for thermal emission. As the envelope expands, more and more dust is thermally annealed into an aromatic structure, releasing PAH radicals to the gas phase. As this process continues, a type B post-AGB transition object evolves into a type A planetary nebula. Physically such objects would have dense circumstellar clouds of newly outgassed material. These would be much younger and more compact than commonly observed planetary nebulae (PNe). Geballe et al. (1992) show three such sources with R values ranging from ~1 to 1.5, suggesting that they lie along an evolutionary pathway from the post-AGB star to the PNe.

Other astronomical objects with aliphatic and aromatic CH stretching features of comparable intensity have been identified. The infrared emission of comets Halley, Wilson, Bradfield and Hale-Bopp have similar spectra in that they all exhibit R values less than 1 (Allen & Wickramasinghe 1987; Baas et al. 1986; Brooke et al 1989). Colangeli et al. (1990) conclude that the 3μm emission spectrum of comet Halley is produced by solid carbonaceous grains similar to HAC or vitrinite coals. Novae also exhibit type B emission features in the 3μm region (Hyland & McGregor 1989). Geballe (1996) concludes, however, that the 5-14μm

spectra of these objects are type A, making them an interesting hybrid classified by Tokunaga (1996) as type A/B.

It has been shown in section 2.5 that the principal astronomical IR emission peaks at 3.3, 6.2 and 11.3 μm can be assigned to PAHs. Absorption features at 3.4 and 6.9 μm in low temperature HAC deposits are dominated by bands arising from aliphatic hydrocarbons. Theorists suggest that energetic processing in the interstellar medium will cause interstellar HAC dust to evolve away from its original polymeric structure to a proto-graphitic configuration (Jones et al. 1990; Sorrell 1990; 1991; Duley 1996a). In this section, some experimental data are discussed which lead to the conclusion that PAHs can easily be formed in HAC solids.

5.1.1 HAC Absorption

From figure 43 we see that, before annealing of the HAC solid is complete, the absorption spectrum contains all the major infrared components seen in emission in energetic nebulae. This observation provides an important link between HAC solids and PAHs in the gas phase. Many authors have noticed the similarities between the frequencies of the major UIR bands, and their counterparts in carbonaceous solids (Duley & Williams 1981; Blanco et al. 1988). Jones et al. (1990) and Duley (1993) have suggested that such a link between the PAHs and HAC solids should exist, based on HAC's natural propensity to form aromatic rings under energetic conditions. If PAH compounds are being formed in HAC solids and released to the gas phase in energetic areas of the interstellar medium, one would expect that IR absorption of the processed HAC would begin to match the emission spectrum of a PAH mixture.

The appearance of absorption bands in annealed HAC at the characteristic UIR wavelengths of 3.3, 6.2, and 11.3 μm shows that a connection exists between molecular groups seen in IR emission in photodissociation fronts and other sources, and those present in HAC as it decomposes. Figure 60 illustrates the similarities between the absorption spectra of HAC in various stages of annealing and the emission from three IRAS sources which show carbonaceous features. Our experimental data then support a model in which PAH molecules are produced from HAC through sputtering and shock heating (Duley 1986; Rössler 1986; Duley 1989; Duley 1995. Allain et al. 1996; Duley & Smith 1997). Such a violent process is likely to result in the liberation of PAH radicals, rather than fully hydrogenated molecules such as naphthalene, anthracene, phenanthrene and coronene. This may account for many of the difficulties encountered in obtaining a spectroscopic simulation of the 'aromatic' PAH IR emission features in laboratory experiments. From UIR observations, Giard et al. (1994) infer a tenfold increase in PAH abundance at the interface of a molecular cloud with an HII region indicating the possible release of PAH fragments from grains due to energetic processing.

5.1.2 HAC Physical Structure

The appearance of cyclical graphite-like bonding structures in annealed HAC films (figure 44) demonstrates a physical connection between HAC and PAH clusters. The observation of physical decomposition and flaking of these partially graphitized HAC films can be extrapolated to dust particles in an astrophysical environment. Similar processes may occur on the surface of HAC grains as the internal structure of the polymeric material is transformed to its more graphitic bonding structure along with a release of internal stresses. This cracking process would compete with other mechanisms such as cosmic ray desorption and shock

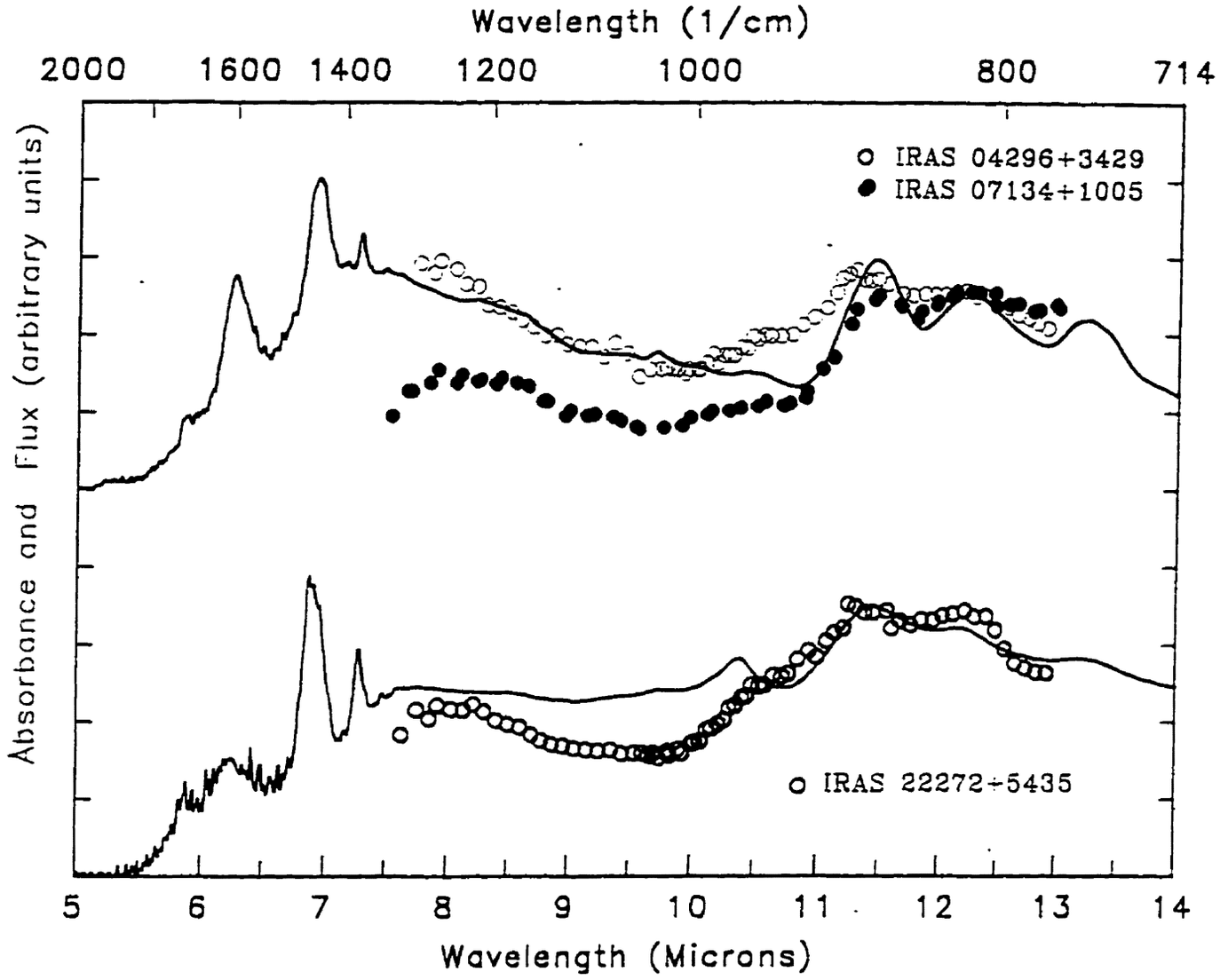


Figure 60 Comparison of IRAS emission spectra to IR absorption spectrum of polymeric HAC (lower solid curve) and partially annealed HAC (upper solid curve)

sputtering of carbonaceous solids (Willacy & Williams 1993; Taylor & Williams 1993) to populate the gas phase of energetic nebulae with large aromatic molecules.

5.1.3 HAC Emission

The IR emission spectrum of warm HAC films exhibits PAH-like emission features at the same wavelengths as the UIR bands, just as expected from the absorption experiments. Figure 61 contrasts the IR emission of annealed HAC with a type A UIR spectrum as seen in NGC 7023 (Cesarsky et. al 1996a). The UIR peaks are seen to be sharper than the broad HAC emission bands. Notice that the 12.7μm type A feature in HAC is a weak shoulder on the stronger type B 12.2μm feature.

Figure 62 compares an annealed HAC laboratory emission spectrum with the characteristic 3.3μm feature of the bright type A planetary nebula, IRAS 21282+5050. Also shown for comparison is the absorption spectrum of coal tar. Although these materials do not provide an acceptable match, the 3.3μm HAC feature has the same peak wavelength and FWHM as the astronomical source. Pure HAC emission cannot fully account for the type A 3.4μm feature, but may contribute a portion of the observed flux in regions where carbonaceous dust is being heated. In addition to this discrepancy, the observed intensity ratio of the 3.3μm feature to the continuum in type A reflection nebulae is larger than that observed in thermally excited HAC films. As noted in section 2.5, it is generally thought that a non-thermal emission component is necessary to explain the observed peak ratios in UIR regions and PAH molecules released from HAC surfaces may then account for this observation.

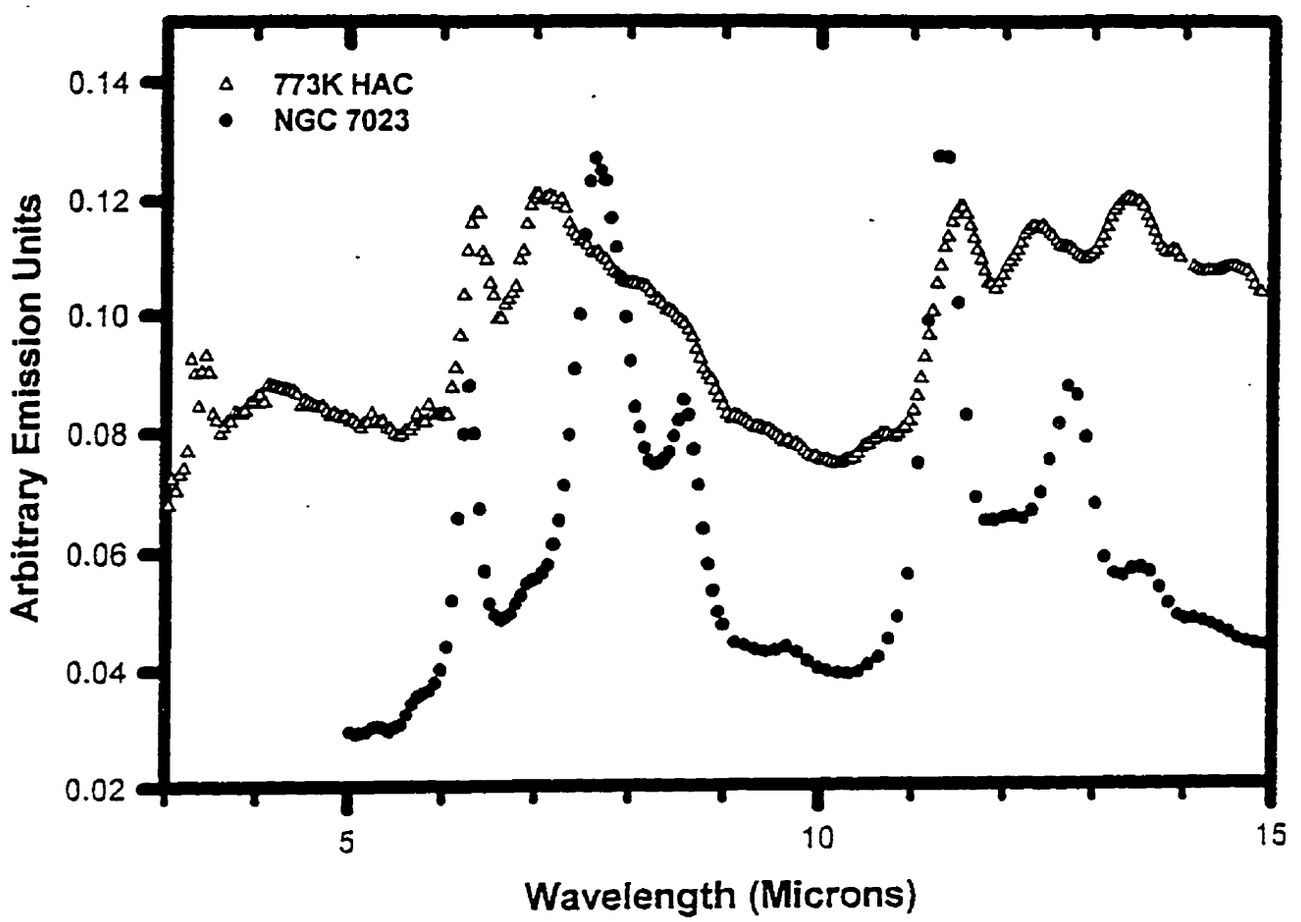


Figure 61 Comparison of type A UIR emission spectrum (NGC 7023) to emission from HAC annealed to 773K

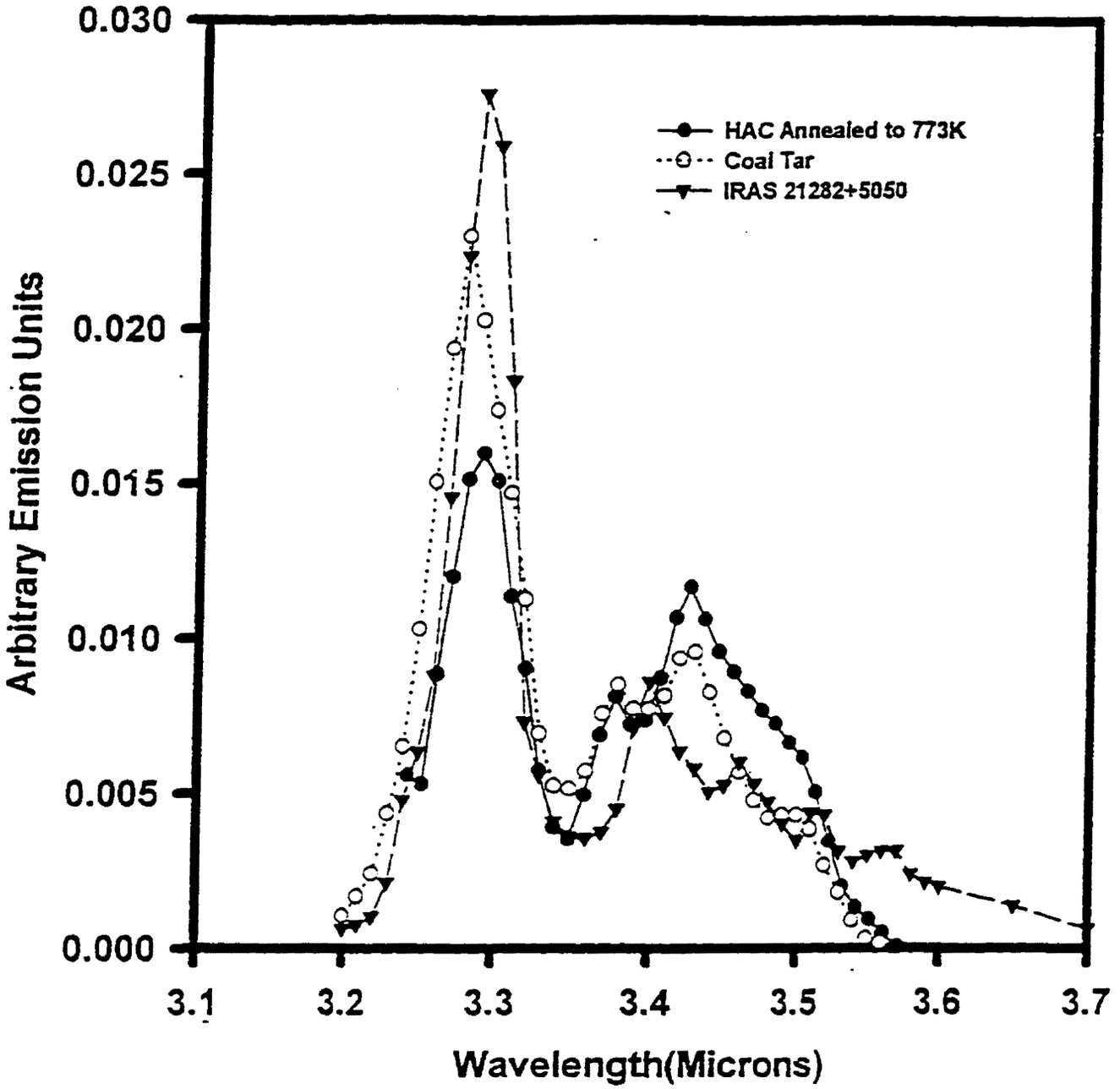


Figure 62 3.1 - 3.8μm emission from HAC annealed to 773K, coal tar (de Muizon et al. 1990), and IRAS 21282+5050 (type A UIR emitter)(de Muizon et al. 1990)

Figure 63 shows comparisons between emission from HAC (baseline removed) in various stages of the annealing process to the 3μm emission features seen in IRAS 04296+3429, and CRL 2688 (Geballe & van der Veen 1990, Geballe et al. 1992). These are type B IRAS sources and the 3.4μm emission is comparable in strength to the peak at 3.3μm. For these sources, the 3.3μm peak to continuum ratio appears to range from about 1.1 to 1.7 which is comparable to the ratio seen in thermally excited HAC films.

Type B sources often exhibit a strong emission at 6.9μm typical of alkane hydrocarbons. Figure 45 shows how the 6.9μm alkane feature in as-deposited HAC is destroyed by annealing and thus the 6.9μm emission peak can be a useful indicator of the presence of hot polymeric HAC dust in interstellar sources. In a particular environment such as an evolved planetary nebula, where all of the available HAC has been annealed to its more aromatic form, this emission will be absent.

Visual observation of HAC emission spectra indicates that an admixture of polymeric and annealed HAC may reproduce the observed type B CH stretching feature. An example of such a fit to the 3-4μm spectrum of IRAS 05341+0852 (Joblin et al. 1996) is shown in figure 64. In this fit, emission in the 3.4-3.6μm range is produced primarily by HAC which has not been heated to temperatures in excess of 650K. The 3.29μm emission is from the warmer HAC dust that has been heated to temperatures between 773 and 873K.

Figure 65a-d compares HAC emission in the 7-13μm region to that of various IRAS sources identified by Justtanont et al. (1996) as having the characteristic type B 21μm emission features in their mid-IR spectrum. This 21μm feature itself remains unidentified, but there is some speculation that it could be due to either vibrations of SiS_2 (Goebel 1993) or

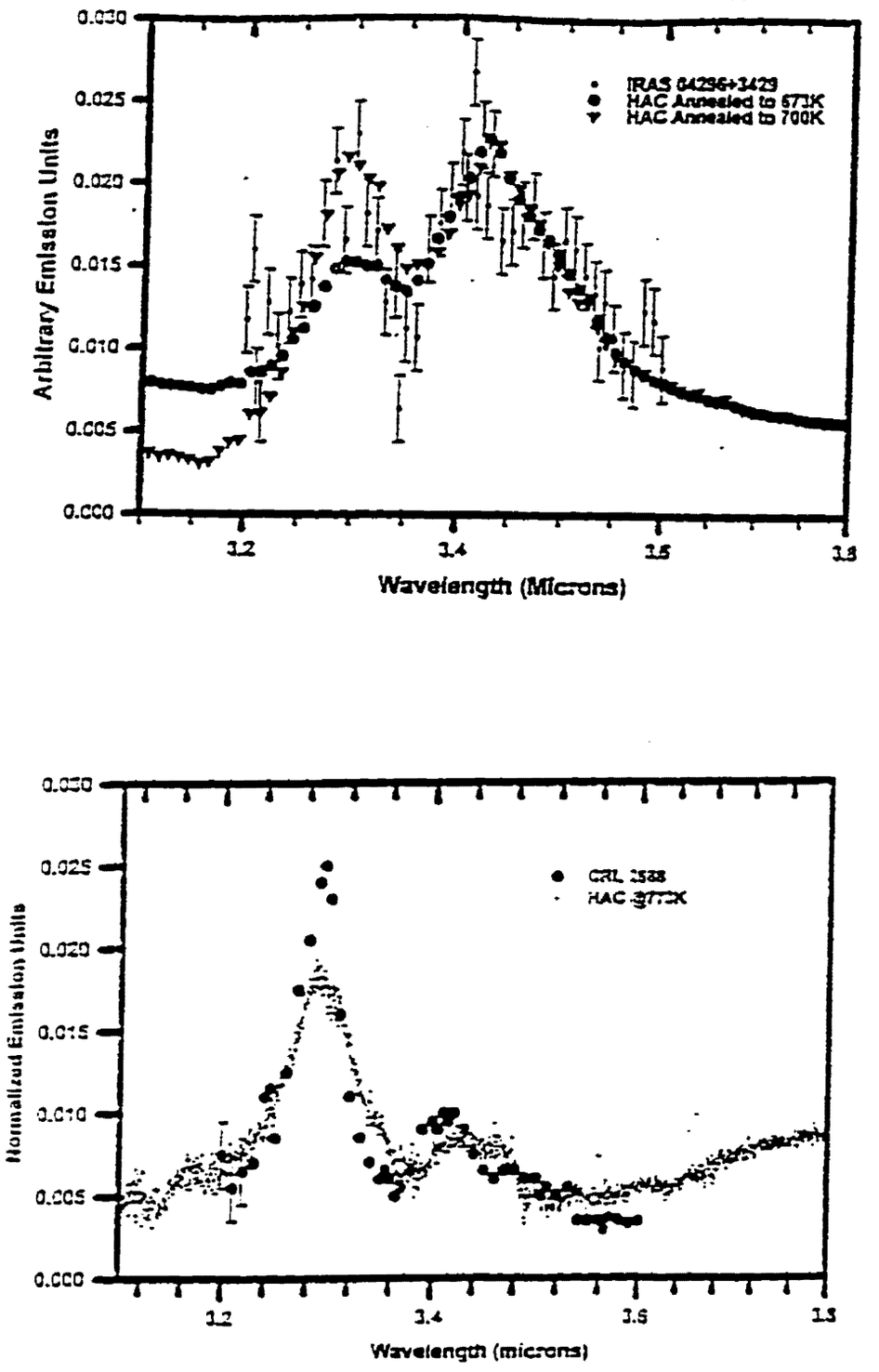


Figure 63 Comparison of normalized 3.1 - 3.8μm HAC emission to various astronomical sources. HAC emission at 673 & 773K vs. IRAS 04296+3429 (Upper); HAC emission at 773K vs. CRL 2688 (Lower) (Geballe & van der Veen 1990; Geballe et al. 1992)

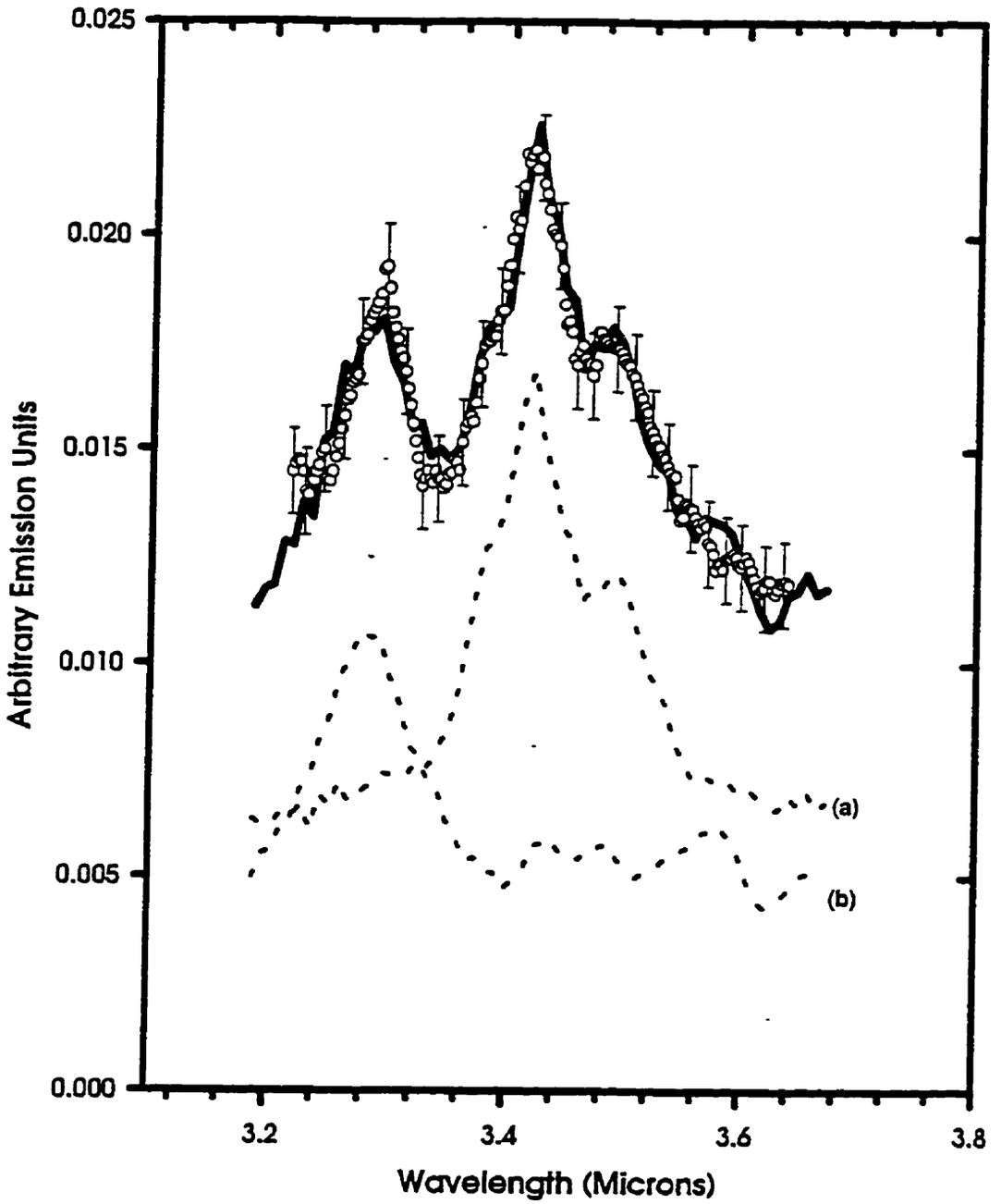


Figure 64 Comparison between thermal emission of IRAS 05341+0852 (circles) (Joblin et al. 1996) and that from a two component HAC dust mixture (solid line). Component (a) is the 650K emission from HAC which was deposited at 77K. Component (b) is the 800K emission from HAC which was deposited at 300K and subsequently annealed to ~850K.

hydrocarbons (Justtanont et al. 1996). There is evidence in the laboratory spectra for a HAC emission feature starting at ~20μm and extending longwards, but the spectral sensitivity is too low in this area to make any definite identifications. Sources with strong 21μm emission exhibit other emission features at 7.9, 8.2, 10.6, 11.5, and 12.2μm typical of type B sources. It is of interest that the HAC emission spectrum in this region is dominated by 10.5, 11.5 and 12.2μm features, and appears to provide an excellent match to the observations. Highly polymeric HAC also shows a broad emission feature centered on 16μm which is quickly destroyed upon minimal annealing. This feature has not been observed in astronomical spectra.

These comparisons suggest that hot dust grains are the source of enhanced 3.4μm emission in transitional objects. Furthermore, several objects with a warm dust population show spectral features which are characteristic of HAC. One could consider a scenario where polymeric HAC is deposited during outflow from a post-AGB star onto a refractory core (newly formed SiC or silicate from the ISM). Energetic atoms of hydrogen and carbon would impinge on a solid substrate and combine randomly, forming saturated HAC compounds. This deposition would be similar to that occurring in laboratory laser ablation. In a dense proto-planetary nebula, most of the newly deposited HAC will be shielded from the hot stellar surface by the dense cloud of material behind it. This will give rise to a mixture of spectral features, with hot dust on the inside of the envelope and somewhat cooler dust on the outside. As the expanding cloud moves outward from the star, stellar radiation anneals the polymeric dust, completing the transformation from aliphatic to aromatic HAC and causing the release of PAH molecules from the grain mantle.

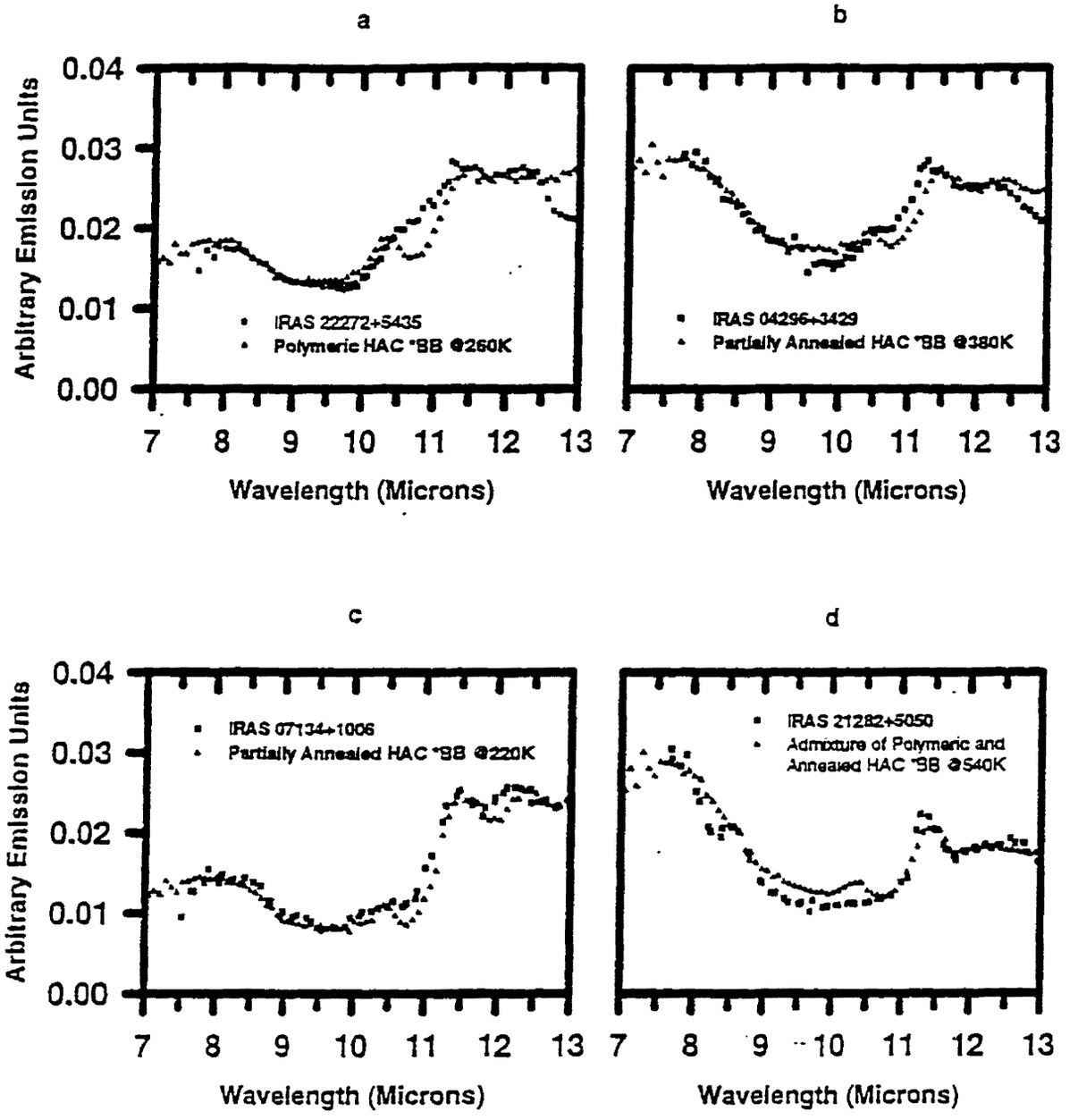


Figure 65 7 - 13μm emission comparisons: a) IRAS 22272+5435 vs. polymeric HAC (calculated at 260K); b) IRAS 04296+3429 vs. partially annealed HAC (calc. at 380K): c) IRAS 07134+1006 vs. partially annealed HAC (calc. at 220K): d) IRAS 21282+5050 vs. admixture of polymeric and annealed HAC (calc. at 540K). Temperatures used for calculations are generally higher than those estimated from observed 10/18μm flux ratios. (Justtanont et al. 1996)

Various evidence provides support for the presence of large PAH molecules in emitting nebulae. Sellgren (1984) has shown that the ultraviolet and visible photon fluxes in reflection nebulae are unable to sufficiently excite larger dust particles to emit in the 3μm region. This observation does not preclude emission from hot dust in circumstellar shells around post AGB stars, or in planetary nebulae which are being heated by a central source. Geballe et al. (1994) have detected the v=2-0 overtone of the 3.3μm CH stretching emission in IRAS 21282+5050 at a wavelength of 1.68μm. By comparing the intensity ratio of the 1.68 and 3.3μm bands they were able to determine a size of approximately 60 carbon atoms for the emitting PAH. It is likely safe to assume that the 1.68μm band will not be significantly excited in hot HAC. Williams & Leone (1995) have shown that the 3.3μm emission from UV pumped naphthalene molecules is quite similar to the interstellar 3.3μm feature. So far however, attempts to fit the type A 3.4μm emission feature to laboratory data have been unsuccessful. Proponents of the 'pure PAH' model suggest that either aliphatic sidegroups (de Muizon et al. 1986; Nagata et al. 1988; Joblin et al. 1996), higher vibrational transitions of the CH stretch (Barker et al. 1987; Allamandola et al. 1989; Talbi et al. 1993; Duley 1994a), overtone and combination bands involving C-C stretching fundamentals in the 5.52-9.52μm region (Allamandola et al. 1989), super-hydrogenated PAHs (H_n-PAHs) (Schutte et al. 1993; Bernstein et al. 1996), or some combination of these mechanisms could be responsible for the observed 3.4μm feature. De Muizon et al. (1990) and Joblin et al. (1996) show that overtone emission from PAHs cannot produce the necessary intensity to fully account for observations. Experimental difficulties have delayed the investigation of the other possibilities. PAH-like molecules containing aliphatic bonds may be able to provide enough intensity in the 3.4μm region to

overcome the deficits faced by the aromatic C-H overtones alone. Recently, Bernstein et al. (1996) have shown a suggestive match to the 3.4μm type A emission feature using a super-hydrogenated polycyclic (H-PAH) non-aromatic hydrocarbon molecule, hexahydropyrene.

Other evidence which is consistent with hot polymeric HAC as a source of broad band UIR emission comes from the observations of Tokunaga et al. (1988), who observed that the width of the 3.3μm feature can vary, becoming quite narrow in the absence of a 3.4μm emission. This observation supports the existence of two separate populations of emitting material. Annealed HAC solids could be associated with the broad 3.3μm feature and the weak 3.4μm structure, while a small distribution of compact PAH molecules could supply the narrow 3.3μm peak.

Observations by Boulanger et al. (1996) show that strong infrared continuum emission can be correlated with type A UIR band intensity in the dense cloud in Ophiucus. This may indicate that gas-phase PAH concentrations are enhanced in regions of warm dust. In highly energetic regions, PAH molecules released from HAC may be destroyed by photodissociation and coulombic explosion resulting from photoionization (Millar 1992). This would result in variations of the IR emission spectrum as one moves farther out from the central star. Cesarsky et al. (1996a; 1996b) observe variations in the UIR spectra of type A sources NGC 7023 and M17 which could be explained by the existence of an ubiquitous population of HAC dust. In both objects, type A UIR features are observed which peak in intensity near the boundary between an energetic interior region and an exterior molecular cloud. Figure 66 shows the IR spectra from two of the most energetic regions of M17 compared to the emission from polymeric and partially annealed HAC. These astronomical spectra exhibit strong continuum emission along with broad bands which are similar to those of HAC. The authors note that

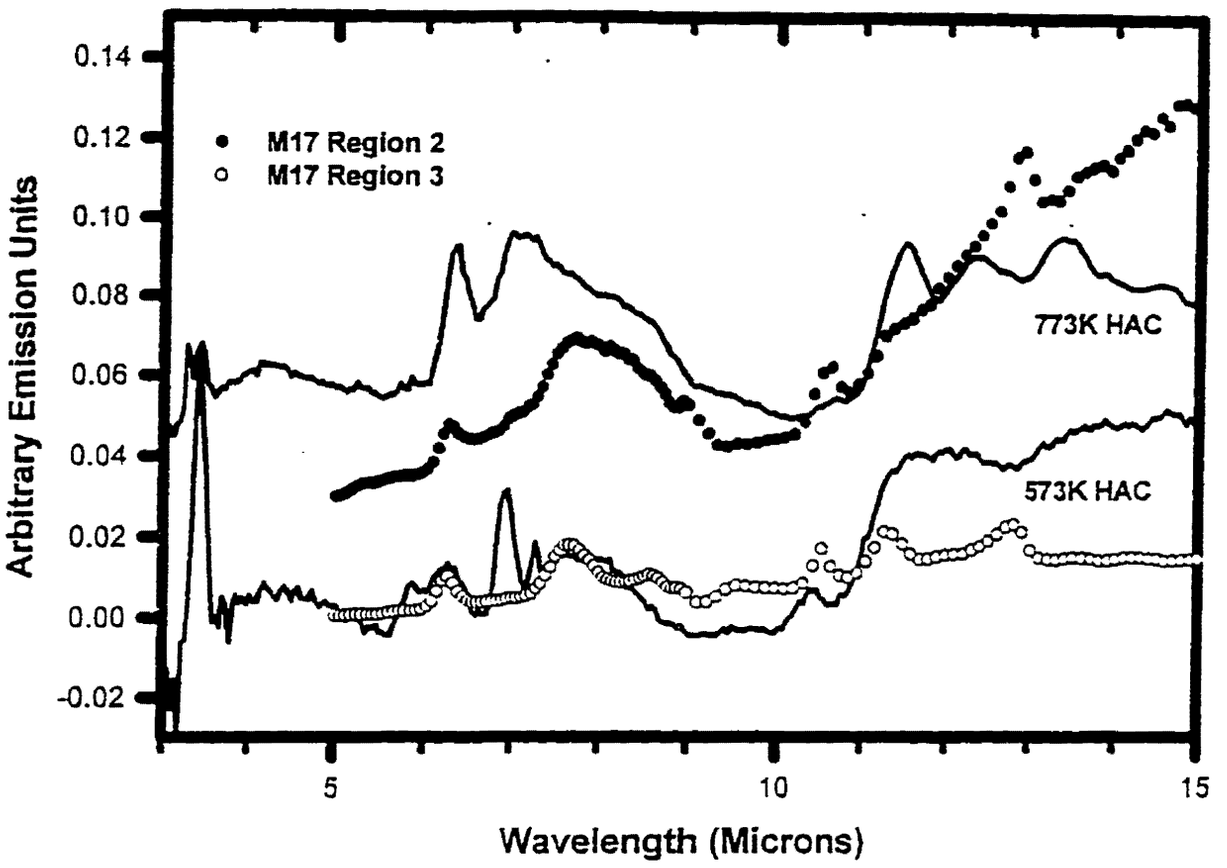


Figure 66 IR emission from energetic regions in M17 compared to emission from HAC at 573 and 773K (Cesarsky et al. 1996a; 1996b).

there are also broad components superimposed on the type A bands which extend from the boundary region out into the surrounding molecular cloud.

Recent observations of M17 by Verstraete et al. (1996) have uncovered new UIR features at 4.65, 6.35, 8.7 and 11μm. The former two are sharp, and the authors suggest that they originate in free PAH molecules. Wavelength similarities with the N-HAC emission shown in figure 49 suggest that the bands at 4.65 and 6.35μm arise due to the incorporation of nitrogen into a carbonaceous material. The 4.65μm vibration occurs at the frequency of the C≡N stretch and the strong peak at 6.38μm was assigned to the shifted 6.2μm aromatic skeletal stretch in the presence of nitrogen.

5.1.4 Breakdown products of HAC

It was shown in section 4.5 that near-threshold laser ionization of polymeric HAC surfaces results in the release into the gas of many C_2 and C_3 species along with a distribution of very small carbonaceous grains (VSGs), and long chains. Coincident with the smaller fragments was the production and release of large compact aromatic ions showing definite enhancements at the mass of the closed shell fullerenes C_{50}, C_{60} and C_{70}. Individual graphitic islands with mass ~C_{40} related to the laser photon energy were also released, coincident with the disappearance of the interconnecting hydrocarbon chains. Further photo-processing resulted in a sharper peak at this size and the disappearance of larger fragments.

Wild & Koidl (1987) studied the thermal effusion spectrum of HAC up to a mass corresponding to C_3H_3. Their results indicated, in accord with this study, that C_2 and C_3 species comprise a significant fraction of the products of polymeric HAC degradation.

The new data presented here support the prediction by Duley (1989) that the C_3H_2 molecule will be a major product of the degradation of HAC dust through photon-induced thermal spiking.

Grain-grain collisions induced by shocks in dusty clouds will provide another important route for HAC destruction. In laser ablation, the laser pulse deposits most of its energy within ~20 nsec. This interaction combines photochemical, thermal and mechanical effects (Duley 1996b) and will simulate, in part, processes occurring during collision of grains under interstellar shock conditions. For a central collision between two spherical grains, each of radius a(m) and density, ρ (kg/m^3), moving with a relative velocity, v (m/sec), the maximum energy deposition, ε, in J/cm^2 is:

$$\varepsilon \approx \frac{2}{3} a v^2 \rho \qquad 28$$

Then with a = 10 nm, v = 10 km/sec, $\rho = 2\text{x}10^3$ kg/m^3, $\varepsilon \sim 1.3\text{x}10^3$ J/m^2 or 0.13 J/cm^2, which are comparable to fluence deposited during laser sputtering. If gas phase concentrations of large molecular species are maintained by grain-grain collisions in interstellar shocks, then astronomical observations should be consistent with the existence of all the species seen in the simulated collisional process.

The existence of long chain polyynes in interstellar space has been confirmed through observations (Duley & Williams 1984 Table 1.6). The mass spectra presented in section 4.5 clearly illustrate what appear to be similar molecules effusing from the surface of HAC. Also present in these ablation spectra are peaks which can be associated with small methylated PAHs. A recent study by Sloan et al. (1997) produces spectral evidence for the existence of

methylated PAHs in close association with an ionization front in the Orion Bar. These smaller molecules (~C_6-C_{20}) are among the first produced from polymeric HAC in the simulations at a variety of laser intensities suggesting that they should be observed in association with most interstellar shocks.

The existence of long chain polyynes, large PAH particles, small graphite particles and fullerenes has been proposed as an explanation for many unexplained interstellar phenomena including the UIR bands (Duley & Williams 1981; Sellgren 1984; Allamandola et al. 1985; 1989), the DIBs (fullerenes: Léger et al. 1988; Webster 1992; 1993a,b,c; Foing & Ehrenfreund 1997; PAHs: Crawford et al. 1985; Ehrenfreund et al. 1992; Salama et al. 1996; polyynes: Douglas 1977), and the 217.5nm extinction feature (Gilra 1972; Hecht 1986; Sorrell 1990). The formation of these large molecules under interstellar conditions has been a subject of much speculation. Laser ablation of graphite is known to produce large aromatic clusters and long chain polyynes (Heath et al. 1987) and Kroto et al. (1985) first discovered Buckminster fullerene in a graphite ablation study similar to this one. The growth of aromatic islands due to photon induced thermal spiking in HAC solids has been postulated to occur in interstellar dust (Jones et al. 1990; Duley & Smith 1997). This mechanism, experimentally demonstrated here for the first time, is a possible formation route for such materials in interstellar dust.

The size of the graphitic platelets produced in the HAC films in this study can be estimated from the density of carbon in an infinite graphitic plane (3.73×10^{15} atoms·cm^{-2}). A compact aromatic molecule like hexabenzocoronene, containing 42 carbon atoms would have a radius of ~5Å. A HAC solid which is being processed by Lyman α photons should show ring growth reaching up to a maximum of ~100-110 carbon atoms. This corresponds to a compact

aromatic disk with a radius of ~9Å. This is a particularly important size regime in astrophysics as Sellgren (1984) first calculated that grains of ~10Å radius were required to model the continuum emission of visual reflection nebulae, underlying the UIR features. From comparison of the 3.3μm UIR feature intensity to those at 3.4 and 11.3μm Allamandola et al. (1985; 1989) calculate that the PAHs which dominate the infrared spectra contain between about 20 and 40 carbon atoms. Further evidence of interstellar molecular moieties in this size range has been collected through numerous observational studies (Ghosh & Drapatz 1986; Barker et al. 1987; Laureijs et al. 1996).

If these individual graphitic islands are so important in interstellar regions, the larger VSGs produced in this experiment may also be of astrophysical significance. Indirect evidence of large aromatic fragments in the ISM abounds. To model the 217.5nm extinction feature it is common to use a small population of graphite grains with sizes of 5-50Å (Hecht 1986; Sorrell 1990). Until now, it has been unclear how crystalline aromatic particles with such size could form under interstellar conditions.

5.2 The Role of Silicates

Values of the absorption coefficient k measured for amorphous forsterite and enstatite films are compared to those for astronomical silicate from Draine & Lee (1984) in figure 67. In the ultraviolet, the onset of absorption is caused by electronic transitions across the band gap to energy levels near the edge of the conduction band. An absorption tail extending from the band gap to lower energies is typically present in amorphous materials and reflects the variation in bond energy that may occur in such materials (Madan & Shaw 1988). This tail is observed to a limited extent as an increase in k at photon energies less than 8 eV in our spectra of both forsterite and enstatite. This feature is enhanced in the astronomical silicate. Impurities, such as the transition metal ions Fe^{2+}, Fe^{3+}, Mn^{2+}, Ni^{2+}, etc., may contribute to interstellar absorption in this region (Nitsan & Shankland 1976). The presence of Fe, in particular, will shift the onset of UV absorption to lower photon energies. Dorschner et al. (1995) have shown that increasing Fe content in pyroxene and olivine glasses also tends to increase the relative absorption in the trough between the 10 and 20 μm IR peaks, while increasing absorption in the near IR and shorter wavelengths.

In the infrared, the distinctive 10 μm SiO absorption peak in enstatite and forsterite films has approximately the same width as derived by Draine & Lee (1984), but the peak value of k occurs at shorter wavelength. Mie scattering calculations using our measured values of n and k give peak absorptivities at 9.59 and 10.06 μm for small particles of enstatite and forsterite particles. The results of these calculations for spherical particles of various sizes are shown in figures 68 and 69, respectively. Both resonances move to longer wavelength with an increase in particle size.

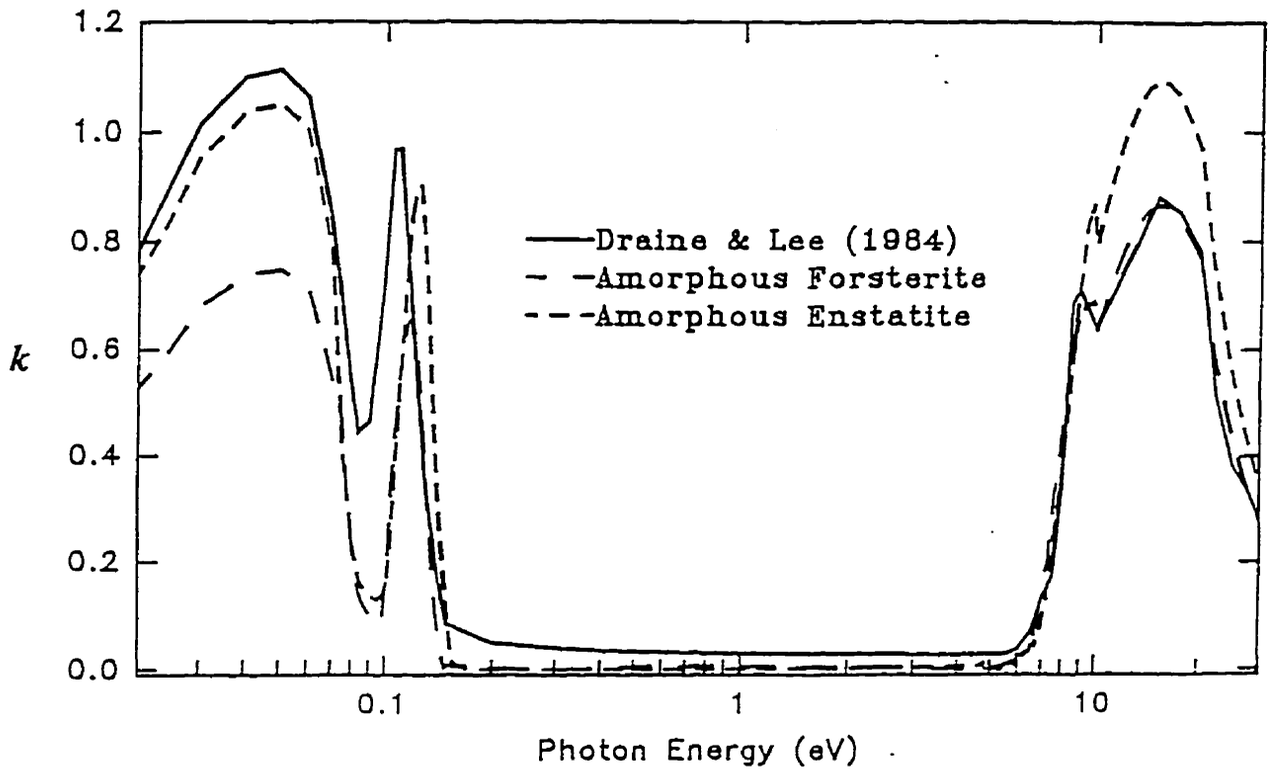


Figure 67 Values of the absorption coefficient k measured for amorphous forsterite and enstatite films compared to that from astronomical silicate (Draine & Lee 1984)

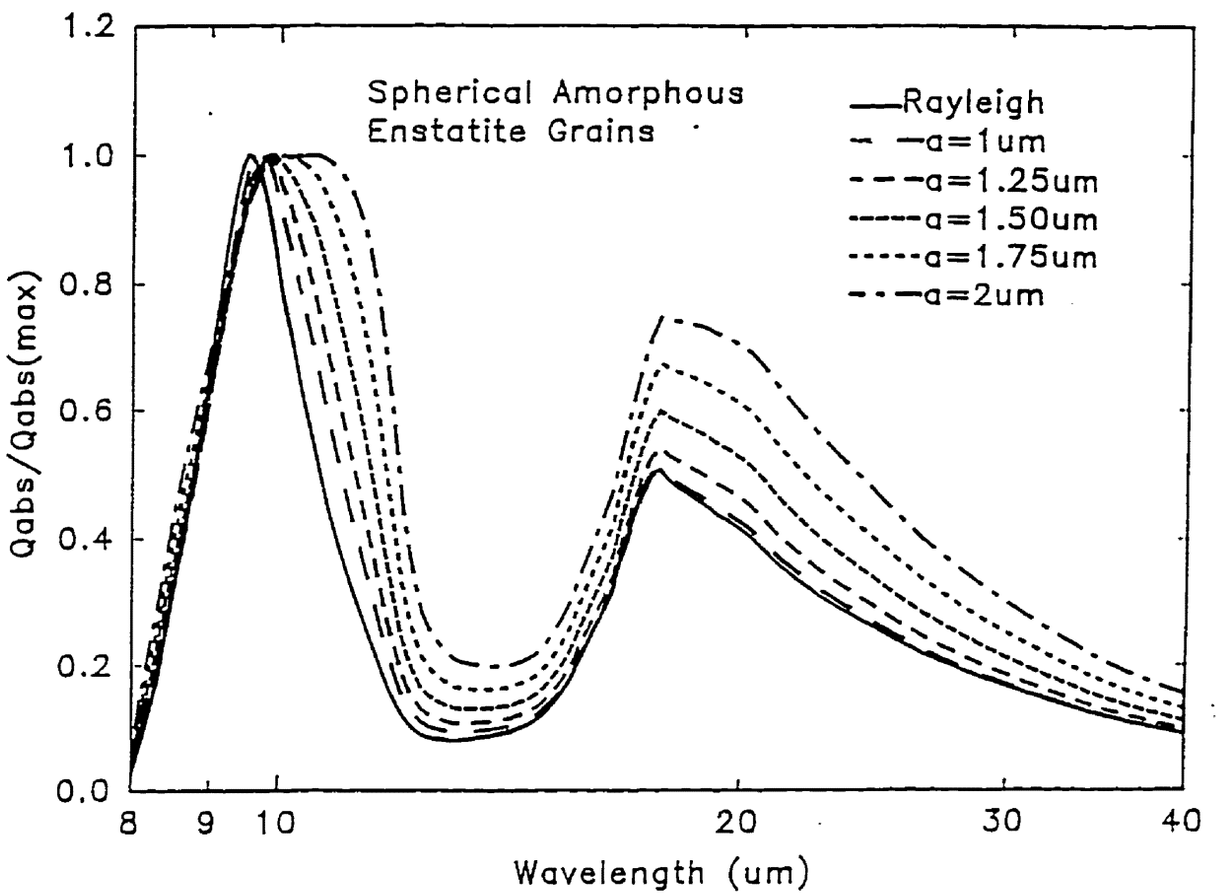


Figure 68 Mie calculations showing normalized absorption from spherical grains of amorphous enstatite.

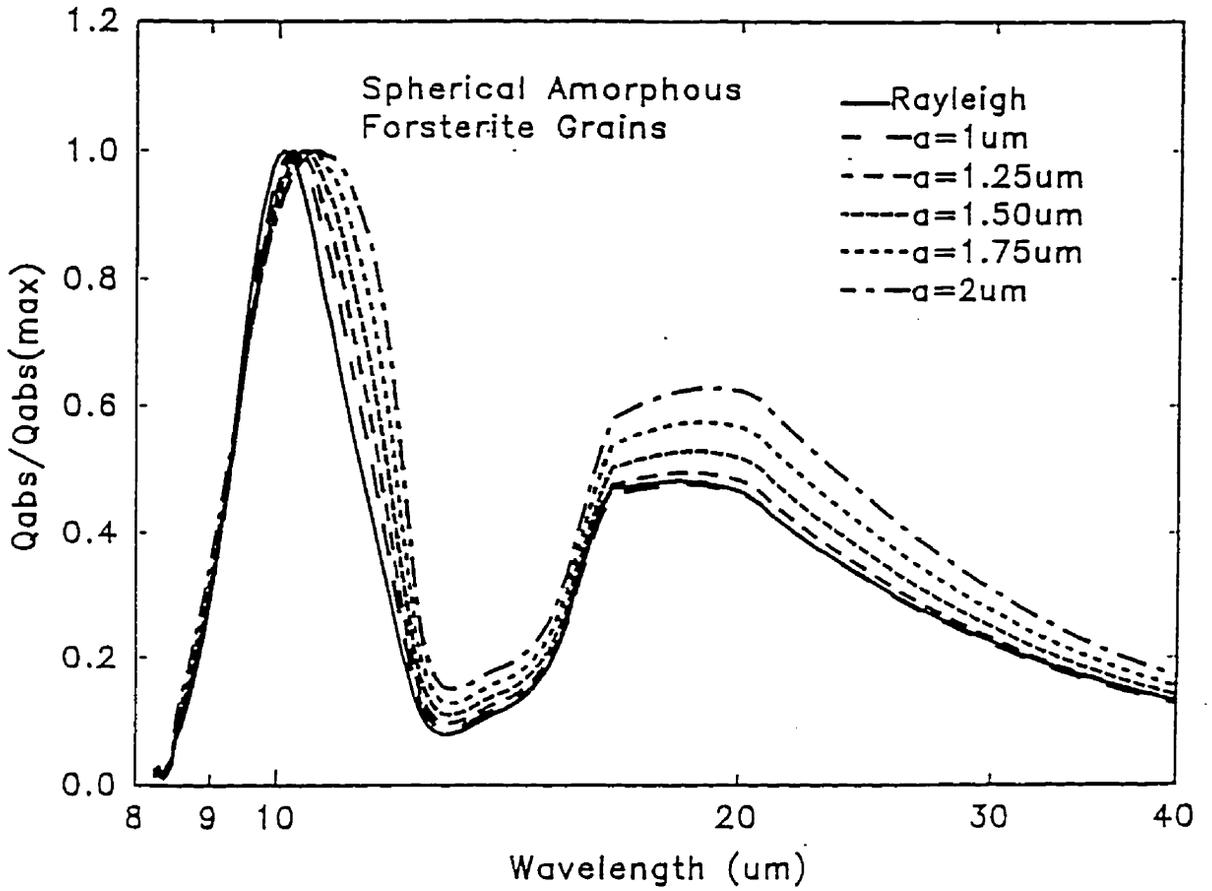


Figure 69 Mie calculations showing normalized absorption from spherical grains of amorphous forsterite.

Absorption coefficients for small spherical particles of both types of silicates are compared in figure 70 to those for silicate particles in the two distinct interstellar environments described by Pégourié & Papoular (1985). The normalized absorption coefficient of dust in the optically thin circumstellar envelope of the Mira star U Tel as determined from IRAS low-resolution spectrometer (LRS) spectra (Dorschner et al. 1995) is reasonably well simulated by small particles of amorphous forsterite. This is in agreement with the thermodynamic arguments presented previously in section 2.1 which show that forsterite forms first in a cooling stellar atmosphere. This figure also shows a good fit between the wavelength dependence of the absorption coefficient of enstatite and the opacity of silicate dust in protostars (Pégourié & Papoular 1985). On average, the dust surrounding protostellar objects could be older than dust surrounding Mira stars and would be expected to contain a higher proportion of pyroxenes such as enstatite.

The absorbance at 10 μm in our silicate samples is somewhat smaller than that derived by Draine & Lee (1984). However, the absolute strength of the SiO stretch band in silicates is somewhat uncertain, since it depends not only on composition but on crystal structure and on temperature (Day 1976). Furthermore, if one considers the possible effects of packing density as in the case of the HAC films (discussed in section 4.2), it is likely that the IR absorptivity could be affected by the film thickness. In this case, the calculated absorptivity could be increased in the IR region when considering very thin films (<0.1 μm). The amorphous nature of our enstatite and forsterite films is confirmed by the observed width and lack of structure within the 10μm peak as well as by scanning electron microscope studies.

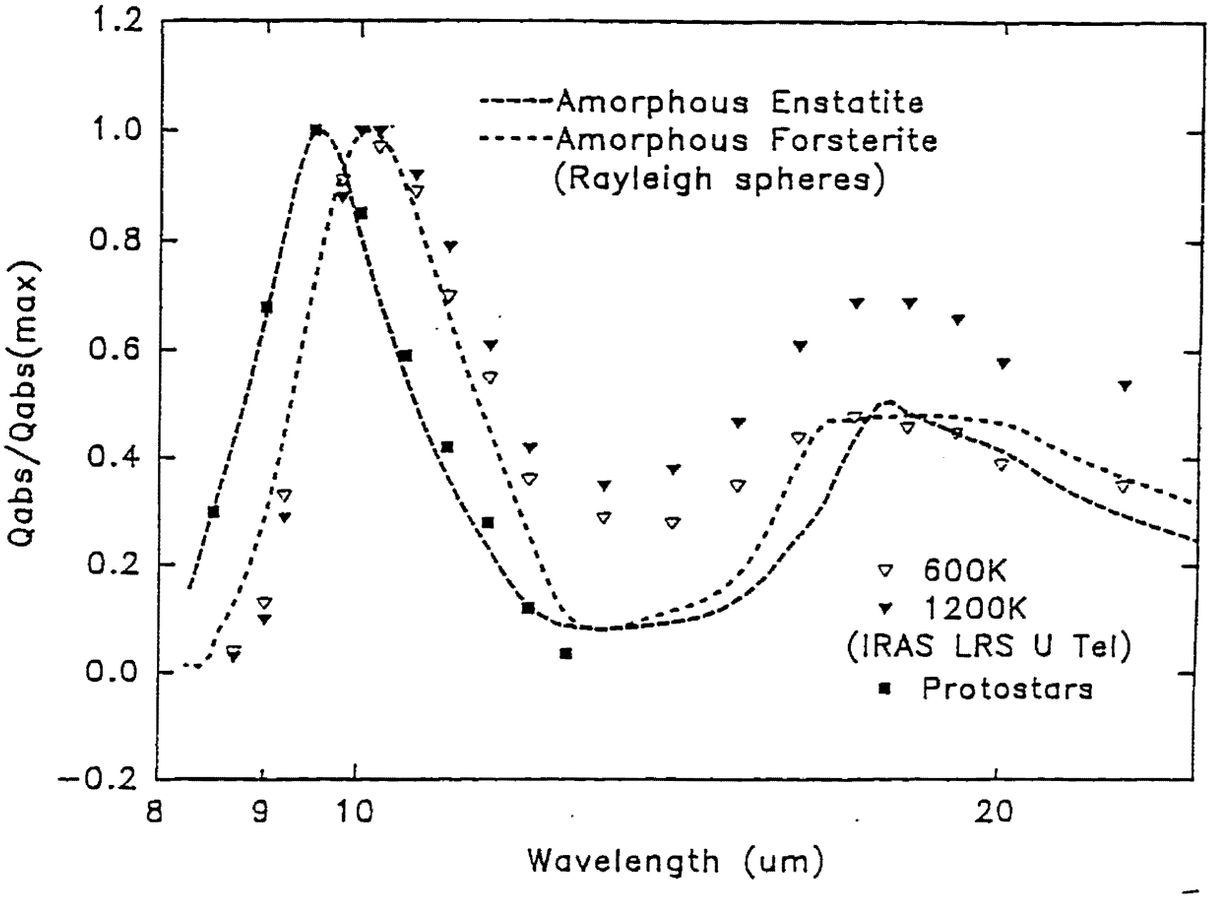


Figure 70 Absorption efficiency of Rayleigh sized amorphous forsterite and enstatite spheres compared to the silicate absorption feature towards Mira star U Tel (Dorschner et al 1995) and an average feature from several protostars (Pégourié & Papoular 1985).

5.3 Extinction Modelling

Various models of interstellar dust have been put forward in an attempt to account for the observed interstellar extinction and polarization (Mathis et al. 1977; Draine & Lee 1984; Duley 1987; Duley et al. 1989; Mathis & Whiffen 1989; Sorrell 1990). A typical model consists of multiple size distributions of dust particles, often having varying compositions. A population of large (~0.1μm) slightly oblong grains is necessary to account for the observed visual extinction and polarization. A separate population of very small grains (≤50nm) is often introduced to explain the observed far-UV extinction rise. In some models, the far-UV rise is due, instead, to particles of amorphous carbon which were shown by Duley (1984) to have a strong absorption increase in that region. A third population, usually of small graphitic spheres (~5-50Å), is necessary to fit the 217.5nm extinction feature. Figure 71 shows the calculated fit of Mathis & Whiffen (1989) as compared to the average interstellar extinction curve. Many different models can give an acceptable fit to the interstellar extinction. Constraints on the cosmic abundance of various model components can help to narrow the field. Often, the amount of carbon necessary can exceed the observed abundance (Snow & Witt 1995).

Extinction calculations using the silicate and HAC optical constants presented in this work have been completed by Sanjeev Seahra, a student in our group, in an attempt to reproduce the diffuse interstellar extinction curve. The model that was used consists of three separate distributions of particles to represent the components of interstellar dust responsible for the observed extinction. First, a population of graphitic onions of radius ~50Å similar to those seen by Koike et al. (1994) is proposed as the source of the 217.5nm extinction feature. These particles lock up 46% of the available cosmic carbon abundance given by Snow and Witt

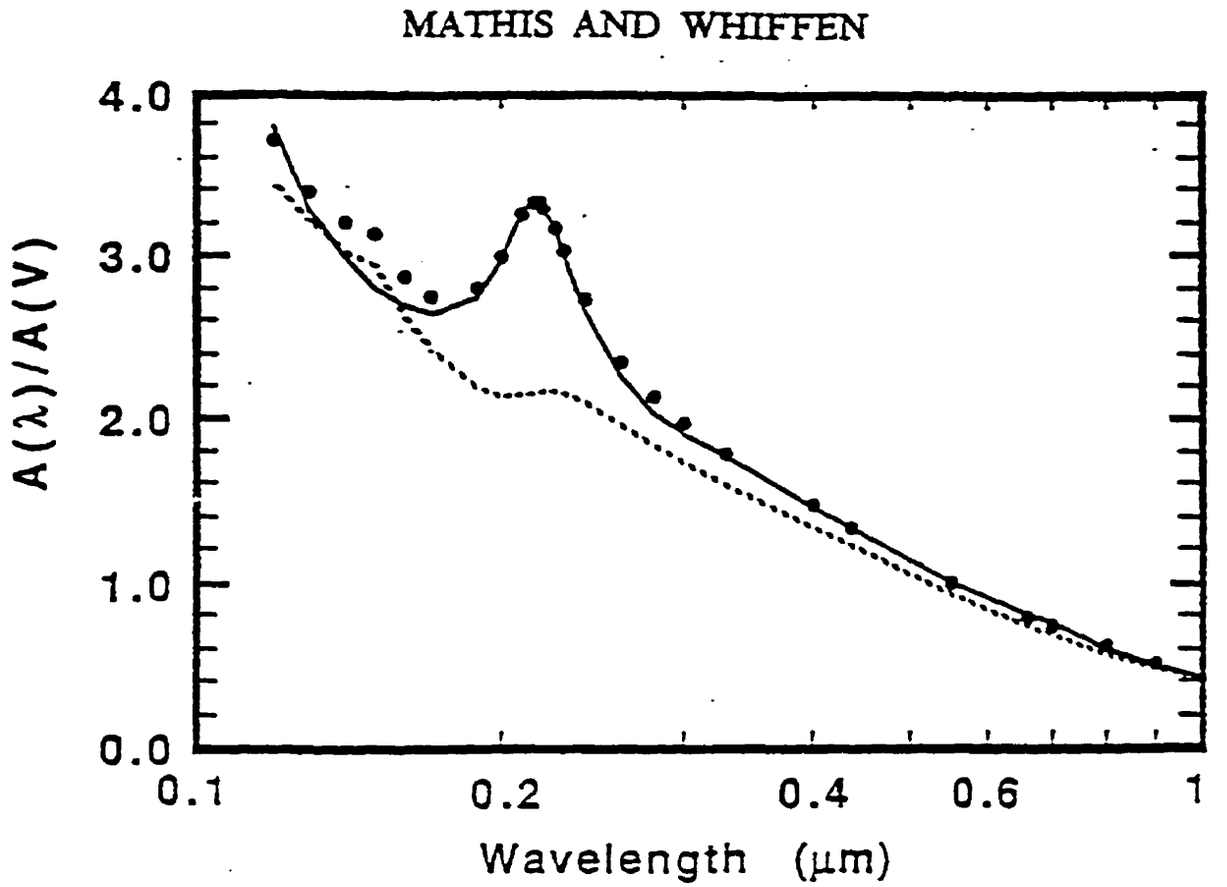


Figure 71 Interstellar extinction model of Mathis & Whiffen (1989). The calculated (*filled circles*) and observed (*solid line*) values of A(λ)/A(*V*) for the grain model. The extinction for the composite grains alone (without the small graphite particles) is shown in the dotted line.

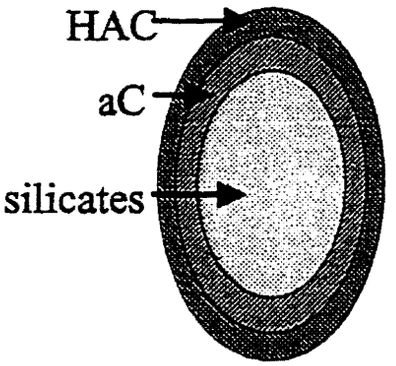
(1996). There are several possible routes for the formation of such particles. Koike et al. (1994) show how strong radiation can catalyze a transformation from a disordered carbonaceous solid to a graphitic onion configuration. The detection of fullerene clusters in the LIMS data presented in section 4.5 is evidence for the possible creation of interstellar crystalline carbonaceous structures through the interaction of radiation and HAC.

The rest of the dust in the model consists of two separate populations of amorphous silicate grains. The first silicate group is a population of small spherical particles with an MRN (Mathis et al. 1977) size distribution, coated by two monolayers of amorphous carbon and a further twelve monolayers of polymeric HAC with a typical density of $1.4 g \cdot cm^{-3}$. This model, similar to that presented by Jones et al. (1990) and Duley and Smith (1997), uses a realistic value of 24% of the cosmic carbon abundance reported in Snow and Witt (1996) for these small grain mantles. These grains carry the 3μm CH features, contribute to the 9.7μm silicate feature, and are primarily responsible for the far-UV rise in extinction.

The second silicate population consists of large, porous particles created through the collision and agglomeration of the smaller particles (Ossenkopf 1993). Each grain is 50% void by volume. This group has an exponential size distribution as given in Sorrell (1990), and the grains can become quite large and elongated. These irregular objects may be the source of the observed polarization of starlight in interstellar space. These largest particles are also responsible for the bulk of the visual extinction. The characteristics of the various grain populations are summarized in figure 72.

The other parameters of the model are presented along with the results in Table 8. We treat the boundaries of the size distribution of the small silicate particles, the fraction of cosmic silicon tied up in small grains, the density of the amorphous silicates, the minimum and

Population #1 - Small Layered Silicate Particles:

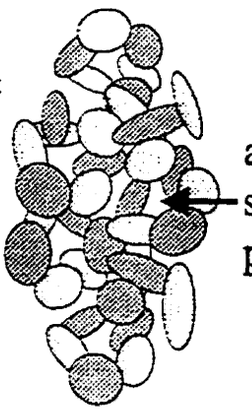


A population of small, double-layered silicate particles with inner mantles consisting of aC and outer mantles consisting of HAC. This population is the carrier of the 3.4μm HAC feature, contributes to the silicate feature and is primarily responsible for the far-UV rise. This population has an MRN size distribution given by:

$$dn = \begin{cases} A_1 n_H a^{-3.5} da, & 0.001\mu m \le a \le 0.050\mu m \\ 0, & \text{otherwise} \end{cases}$$

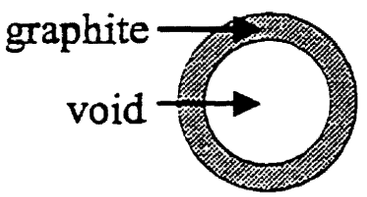
Population #2 - Large Porous Silicate Particles:

A population of large, porous silicate particles. Each grain is 50% void by volume. This population is almost exclusively responsible for the visible and near-UV extinction and is also the primary carrier of the 9.7 μm silicate feature. The population's size distribution is exponential in nature and is given by (with $a_0 = 0.100$ μm):



$$dn = \begin{cases} A_2 n_H a \exp(-a/a_o) da, & 0.005\mu m \le a \le 0.450\mu m \\ 0, & \text{otherwise} \end{cases}$$

Population # 3 - Graphitic Onions:



A population of graphitic onions. This population is exclusively responsible for the λ2175-Å feature and has the discrete size distribution (note: i is the thickness of the graphite shell in monolayers):

$$n_i = A_3 n_H i^{-3.5}, \quad 2 \le i \le 14, \quad a_{inner} = 0.002\mu m$$

Figure 72 Characteristics of various grain populations used in the extinction model.

maximum number of layers for the graphitic onions and the fraction of the cosmic abundance of carbon tied up in graphite as free parameters. In this model, 30% of available carbon is incorporated into the graphitic structures, while 16% is depleted into the HAC mantles.

The extinction curve which results is shown in figure 73 and observational data are compared with the model results in Table 8. Most of the calculated parameters show excellent agreement with observation. The strength of the model 3.4μm CH stretching feature is too low by a factor of ~4. One possible reason for this discrepancy is that the model uses only polymeric HAC as the grain mantle material. Evolutionary grain models often incorporate a layer of UV annealed HAC below the polymeric layer in dust mantles to reflect the energetic processing effects of the interstellar radiation field (Jones et al. 1990; Duley & Smith 1997). Such a material would have stronger visible and IR absorption due to its narrow bandgap. The incorporation of this material would also allow a significant reduction in the carbon abundance used in the graphitic onions, as they are partially responsible for the visible extinction. A further increase in the 3.4μm feature strength may occur if UV annealing is able to increase the bonded hydrogen content of the HAC mantles. It is well known that as-deposited HAC films contain a large proportion of unbonded interstitial hydrogen which can be chemically incorporated into the material upon UV irradiation (Furton & Witt 1993). The 3.4μm band strength would increase as a direct result of such an increase in bonded hydrogen. These corrections could theoretically reduce the present discrepancy.

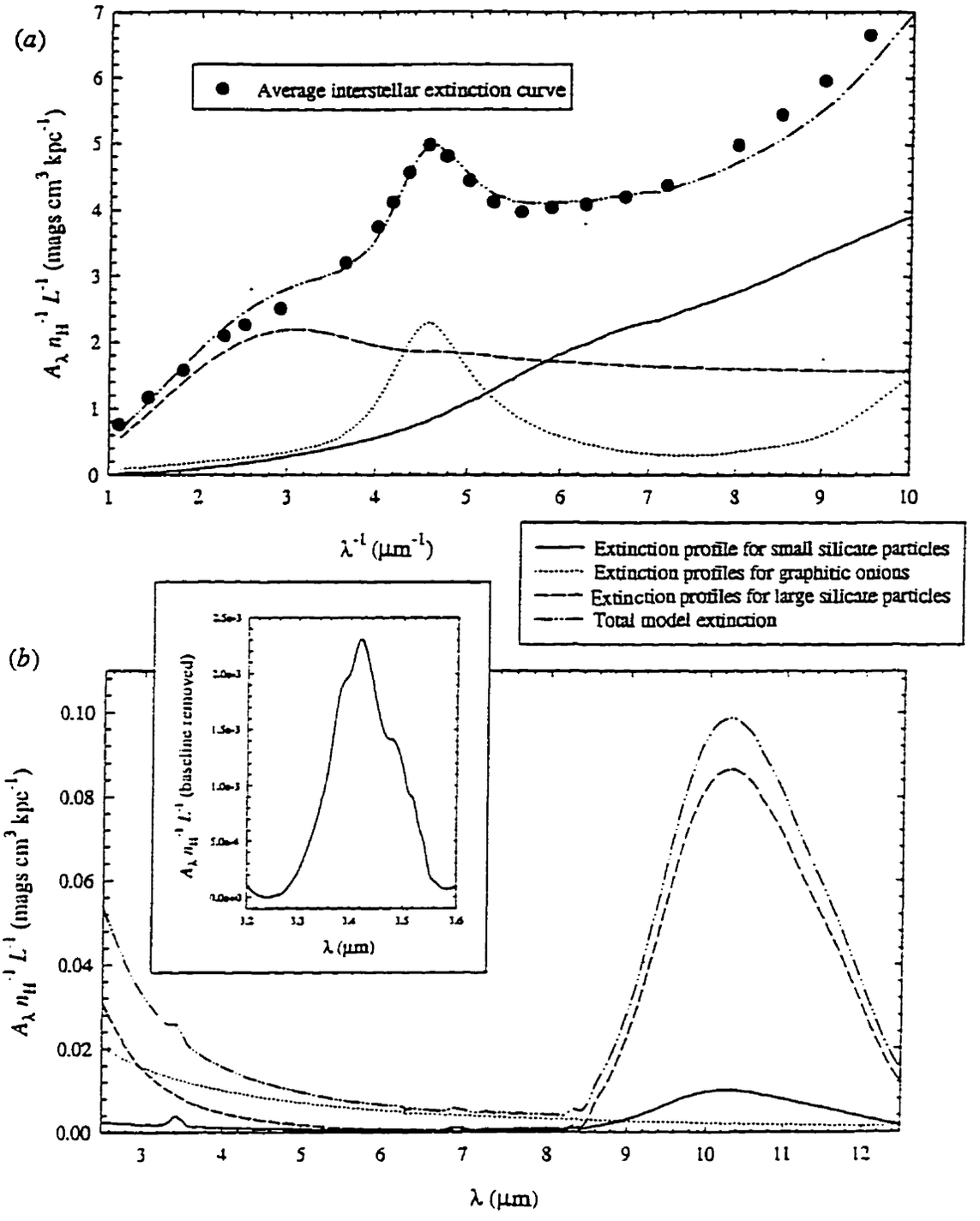


Figure 73 Model extinction curves (a) for the UV spectral region compared to the average interstellar extinction: (b) for the IR spectral region with inset of 3.4μm CH feature from HAC mantles.

Table 8 Parameters for interstellar dust extinction model.

Quantity	Model Value	Observed Average Value(s)
% depletion of Si, Mg and Fe	~100%	~100% for Si, Fe [*]
% depletion of cosmic Si present in small grains	30%	....
assumed silicate ($Mg_{1.1}Fe_{0.9}SiO_4$) density	1.77 gms cm^{-3}	....
% depletion of C	46%	~30% - 70% [*]
% depletion of cosmic carbon present as HAC	16%	....
% depletion of cosmic carbon present as graphite	30%	....
Total visual extinction, $A_V\ n_H^{-1}\ L^{-1}$	1.64 mags cm^3 kpc^{-1}	1.64 mags cm^3 kpc^{-1} [*]
Ratio of total to selective extinction, R_V	2.95	3.05±0.15 [*]
Central wavelength of the λ2175-Å peak, λ_o	2165 Å	2175 Å±17 Å [**]
FWHM of the λ2175-Å peak	1.01 μm^{-1}	0.77 μm^{-1} - 1.25 μm^{-1} [**]
Silicate feature strength, $\tau_{9.7\mu m}/A_V$	0.056 mag^{-1}	0.052 mag^{-1} [***]
HAC feature strength, $\tau_{3.4\mu m}/A_V$	0.0013 mag^{-1}	0.0040 mag^{-1} [****]

References: [*] Whittet (1992), [**] Draine & Malhotra (1993), [***] Draine & Lee (1984), [****] Pendleton *et al.* (1994)

6. CONCLUSIONS

The refractive indices of some important constituents of interstellar dust have been measured experimentally. In the case of the amorphous silicates, forsterite and enstatite, n and k have been derived from observations covering the energy range between 0.07-0.43eV and 4.7-10eV. Rayleigh-sized particles of forsterite are shown to reproduce the 10μm silicate absorption feature of evolved interstellar silicate dust, as observed in absorption towards protostellar objects. Small enstatite particles match the analogous 10μm absorption seen in oxygen-rich outflows as observed towards Mira-type stars. The observed differences in these distinct grain populations are expected from thermodynamic calculations, and are brought about by interaction with interstellar gas over the lifetime of the silicate grain. Both types of silicate have an onset of strong UV absorption near that of "astronomical silicate" (Draine & Lee 1984).

The refractive indices of polymeric HAC films have been measured at two deposition temperatures over the same spectral range. The apparent refractive indices are strongly dependent on the film thickness, deposition temperature and hydrogen content. All three variables are found to affect the void component of the resulting material which results in a variation in the effective n and k. The hydrogen content and deposition temperature is also found to influence the chemical bonding structure of HAC which can be dominated by polymeric, diamond-like, or graphitic regions. The 3.4μm absorption feature of HAC deposited at 77K is shown to be similar to that of dust in diffuse interstellar clouds with very little aromatic bonding. HAC deposited at 300K has a broader 3.4μm feature due the existence of aromatic islands which create a CH absorption at 3.3μm.

Thermal annealing of polymeric HAC solids deposited at 300K was seen to result in the emergence of infrared spectral features similar to those attributed to free PAH molecules. This is indicative of the growth of thermodynamically stable aromatic rings within HAC. Additional evidence of these PAH-like aromatic regions was provided by direct observation of annealed HAC with an STM. This evidence provides a plausible mechanism for the formation of large hydrocarbon molecules like PAHs in the interstellar medium. Given that polymeric HAC will form on dust grains under ambient interstellar conditions (Jones et al. 1990), it is expected that thermal processing due to stellar radiation will cause this HAC mantle to evolve over time, eventually resulting in the formation of large PAH molecules.

Evidence which supports the existence of interstellar PAHs is based mainly upon their spectral similarities with IR emission bands which are commonly observed in PNe. If PAHs are formed from HAC dust in the ISM, then the emission from laboratory HAC films should be comparable to emission from nebular regions where the dust is being thermally excited. The thermal emission of polymeric HAC solids was observed for the first time and was seen to increase in aromatic character as the solid was annealed to higher temperatures. The major IR emission features of annealed HAC are very similar to the UIR bands from rare type B sources, having definite peaks at 3.3, 3.4, 6.2, 6.9, 10.5, 11.5 and 12.2 μm. These bands are representative of a mixture of both aromatic and aliphatic hydrocarbons. For a detailed comparison, an admixture of polymeric and annealed HAC dust was shown to reproduce the 3-4μm emission spectrum of type B UIR source IRAS 05431+0852. Care was taken to eliminate possible contamination of the spectra by the 3.4μm absorption feature of solder flux which was present in all FTIR instruments studied. The flux feature was shown to also be similar to the aliphatic 3.4μm emission feature seen in type B UIR sources. The majority of type B UIR

spectra are observed in post-AGB objects having dense circumstellar clouds. These objects are thought to be precursors of the PNe which exhibit highly aromatic type A UIR emission bands commonly associated with gas phase PAHs. Emission experiments studying the incorporation of nitrogen and oxygen in HAC solids have led to the identification of two newly discovered UIR bands at 4.65 and 6.35μm.

If, as the evidence suggests, PAH molecules are formed from HAC dust in the ISM, a plausible mechanism must exist to break up HAC solids, freeing the constituent molecules to the gas phase. The formation and subsequent release of a mixture of PAH molecules, fullerenes, hydrocarbon chains and VSGs from the surface of HAC solids have been observed under conditions which simulate intergrain collisions in interstellar shocks. These data were consistent with observations which suggest that PAH abundances are enhanced at ionization shock fronts.

Repeated excimer UV photo-processing of HAC films was shown to result in the formation of particles in an astrophysically important size regime. The emergence of a sharp distribution of PAHs containing ~40 carbon atoms was interpreted as being the result of aromatic ring growth due to photon-induced thermal spiking as described in the model of Duley & Williams (1988). The products of the Lyman α UV processing of interstellar HAC solids can be predicted with this model. PAH subunits with a radius of up to ~9Å may form as a result of this mechanism. Particles in this size range have been predicted to be the source of the UIR emission bands.

Taken together, these results are consistent with a model wherein polymeric HAC is deposited in solid form in the cool outer reaches of the extended envelope of a C-giant star. PAHs are formed from the annealing of HAC solids by stellar irradiation. This results in the

emission of a type B UIR spectrum by a mixture of hot polymeric and annealed HAC dust. The by-products of the annealing process which include PAH subunits are subsequently released to the ISM in grain-grain collisions at the ionization shock front surrounding the star, resulting in the sharp non-thermal bands characteristic of type A UIR sources.

7. CRITICAL PERSPECTIVE AND FUTURE WORK

Before suggesting further possibilities for the continuation of this work, a review of the uncertainties mentioned in association with some of the previously presented experimental results is necessary to ensure an unbiased account.

The indices of refraction for polymeric HAC solids were found to depend on the density of the substance which is itself dependent on the thickness of the film produced. With increasing thickness, the void content also increases, thus decreasing the apparent indices of refraction. Due to this problem, difficulties arise when comparing indices derived from UV spectra of thin films ~100nm with indices from IR spectra of thick films ~1μm. The indices of refraction presented here resulted from the averaging of the two extremes and may be representative of polymeric HAC with an appreciable void content. The error bars show the standard deviation amongst the different films measured, indicative of fluctuations in density and hydrogenation. Other sources of error include uncertainties in thickness determination and the possibility of a hydrogenation gradient in the HAC films, with the lower layers being selectively dehydrogenated due to possible annealing effects during the deposition process (see Voevodin et al. 1996).

Extrapolating to the silicate case, there is the possibility that thickness dependent void structure may have resulted in a diminished value for k, below the intrinsic value, in the IR spectral region. Extinction models should take these uncertainties into consideration when making comparisons to astronomical observations.

The HAC emission spectra may have small uncertainties associated with the presence of absorption from solder flux resin. To deal with this problem, featureless background spectra

were obtained at various temperatures to ratio out the absorption and minimize detector non-linearity effects. Possible false peaks would appear while analyzing heavily annealed samples with weak intrinsic CH stretching peaks. Partially dehydrogenated HAC films with spectra showing band structure matching that of the contaminant were discarded at the experimenter's discretion. This procedure may have introduced some biasing of the results. Uncertainties are also associated with the removal of a smooth polynomial baseline as discussed in section 3.3. When comparisons are made to astronomical spectra, it is important to remember that most observational spectra have similar broad baseline uncertainties. This 'floating baseline' allows some freedom in the normalization of observed peaks and should be taken into consideration when comparing astronomical to laboratory spectra.

Interesting areas for future study include the experimental investigation of the hotspot model mentioned in section 2.5. Low signal levels have hindered preliminary attempts to detect UV-excited IR emission using the deuterium lamp and the FTIR emission port. The use of a defocussed excimer beam as an exciting source may eliminate this problem, but the pulsed nature of the beam makes the FTIR impractical as a detector. Unfortunately, annealing effects such as dehydrogenation occur quickly at laser fluences, further diminishing any hydrocarbon emission.

Another experiment which could be conducted is to observe both the emission and the extinction properties of the fragments created during the near-threshold laser ablation of HAC. It may be necessary to trap the fragments in a matrix to achieve a measurable signal. It would also be worthwhile to repeat the LIMS experiment using a different wavelength of laser photon. This would test the theory that the C_{40} peak is actually a result of photo-thermal ring growth in the HAC solid.

8. APPENDIX I

8.1 8052 Based Monochromator Controller

Figure 74 shows a box diagram of the system and its components. The monochromator grating is connected to a rotating shaft where one complete rotation is equivalent to a wavelength scan of 100 Å. To this shaft is connected a Bourns Rotary Optical Encoder model ENA1J-B28-L00100 which is a quadrature encoder with 100 cycles per revolution. The quadrature output is important in that it gives directional information to the decoder circuit. As well, this gives a pre-calibrated 400 decoder counts per revolution so that the wavelength to pulse ratio is 1 Å to 4 pulses.

The decoder circuit is based on a 74LS374 chip used as 4 D-type clocked data latches. The clock pulse is supplied by the ALE pulse from the 8052 controller at a very high frequency (~1mhz). It is important that the clock frequency is greater than the frequency of the encoder pulses, but not so fast as to confuse the 374 or 288 chips. The outputs from each of the latches are used as address inputs to a high speed 74S288 PROM which is programmed to give Count Up, Count Down, and Error pulses based on the pattern of inputs. Figure 75 shows the decoder circuit.

To keep track of the position of the monochromator it is necessary to count the output pulses from the decoder circuit. Our wavelength range of interest is from approximately 1500-4900 Å. This corresponds to a pulse range of 3400 Å x 4 pulses·$Å^{-1}$ = 13600 pulses. Using the 74LS193 counter chips in a cascade formation we will need a minimum of 4 4bit counters. This gives plenty of leeway to allow us to have the count correspond directly to wavelength x 4. That way our region of interest in counts is from 6000 to 19600 pulses which will easily fit on a 16 bit counter. The output of the 4 counters is latched onto the data bus by two 74LS373 data latches whose output control pins are connected to {(!y3 of the 138) OR (!write)} for the low byte and {(!y5 of the 138) OR (!write)} (all active low) for the high byte as shown in figure 76. The enable pin is hooked to the !ALE and DIS latching output from the 8052. The set inputs of the 193s are connected to the address/data bus on the latched side of the onboard 74LS245 chip. The Load inputs of the four chips will be triggered by {(!y7 output of the 138) OR (!read AND !psen)} for the low byte and {(!y6 of the 138) OR (!read AND !psen)} (all active low) for the high byte.

Therefore to set the counters use the command "xby(57344)=<low byte>" and "xby(49152)=<high byte>" where low byte = (wavelength/4) modulus 256, and high byte = (wavelength/4) div 256.

To read the counters use "low=xby(24576)" and "high=xby(40960)".

Figure 77 shows the relay circuit used to drive the motor in two directions. It requires two TTL outputs from the controller circuit. On/off and up/down will determine the state of the motor. These outputs are taken from another 74LS373 chip whose output control pin will be held low. The inputs are A/D7 and A/D6 taken directly from the address/data bus. The output control will be connected to {NOT ((!y2 of the 138) OR

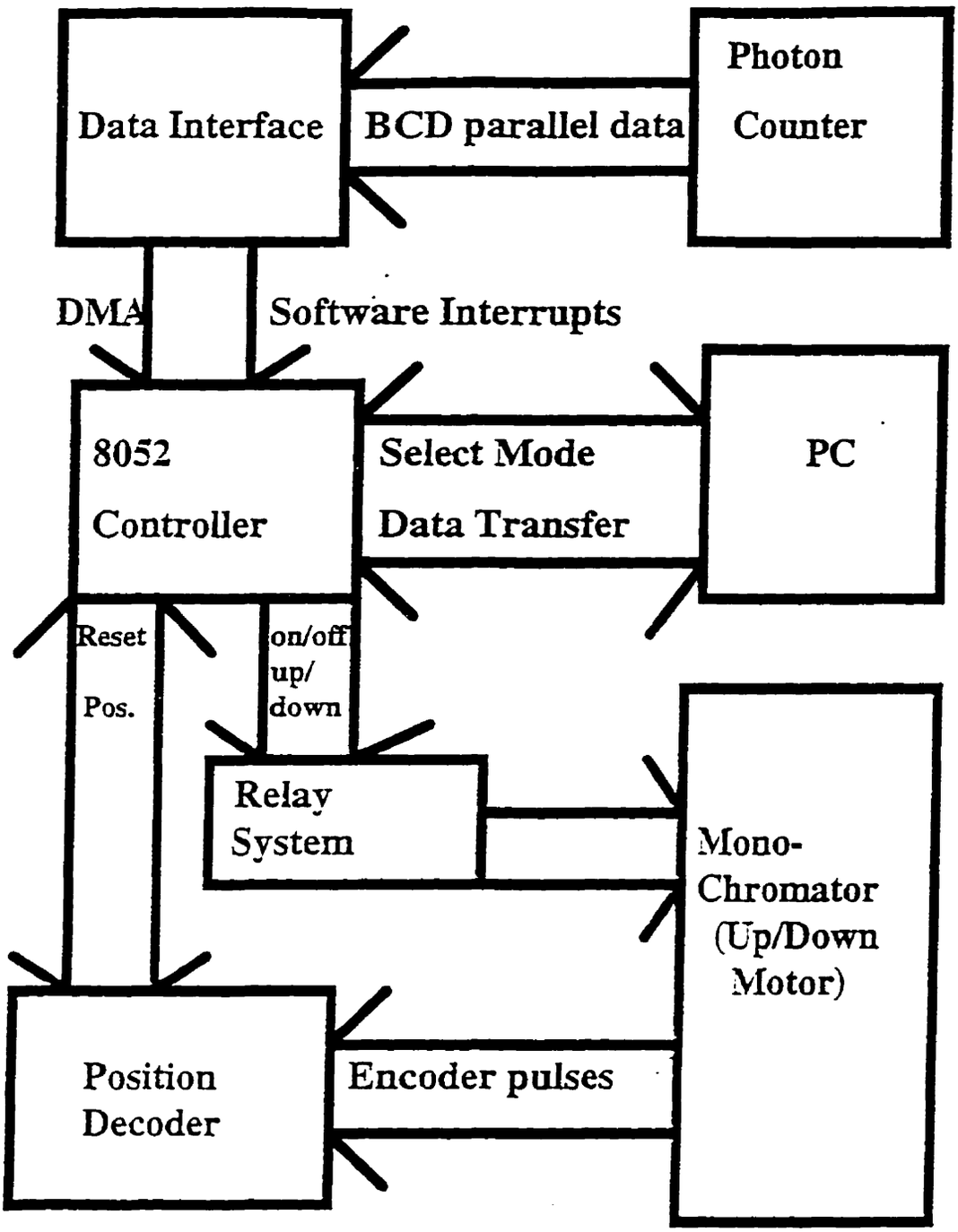


Figure 74 Box diagram of monochromator controller unit.

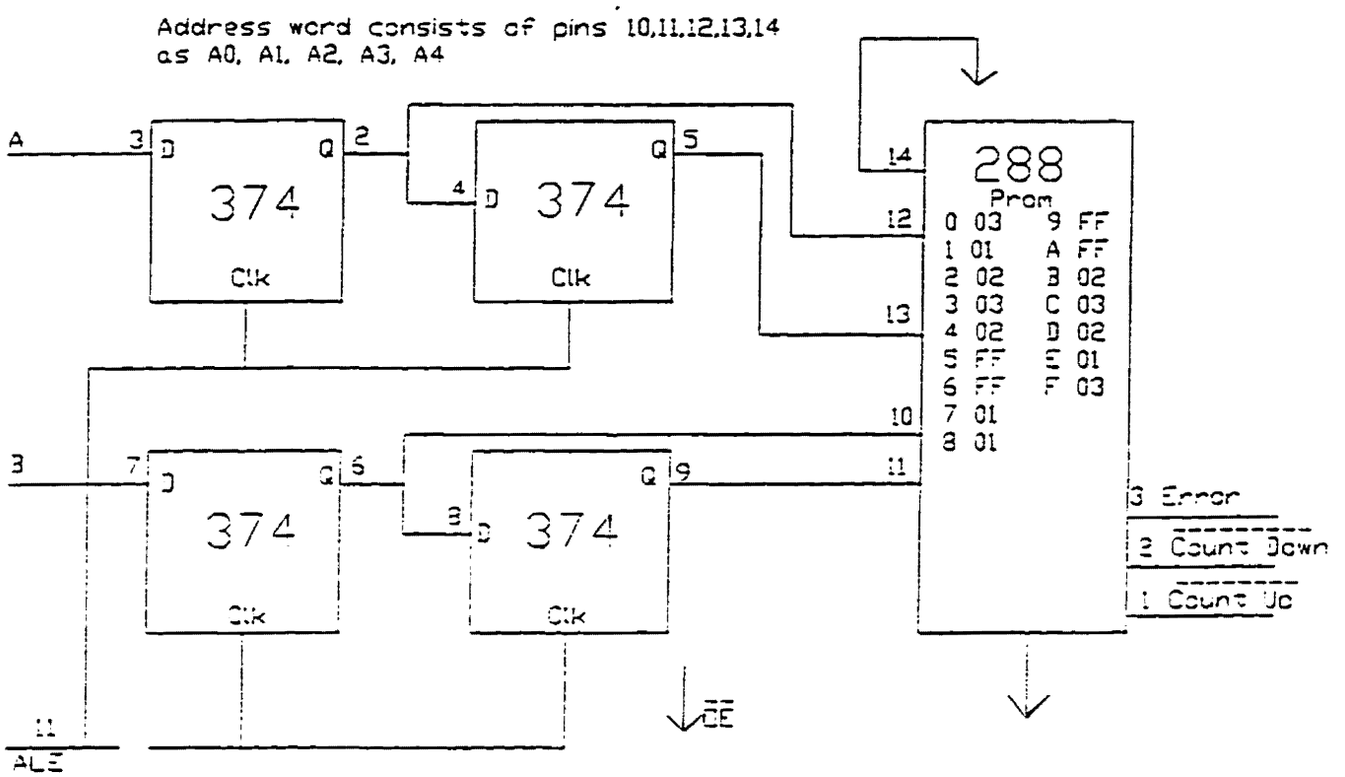


Figure 75 Decoder circuit for VUV monochromator encoder wheel.

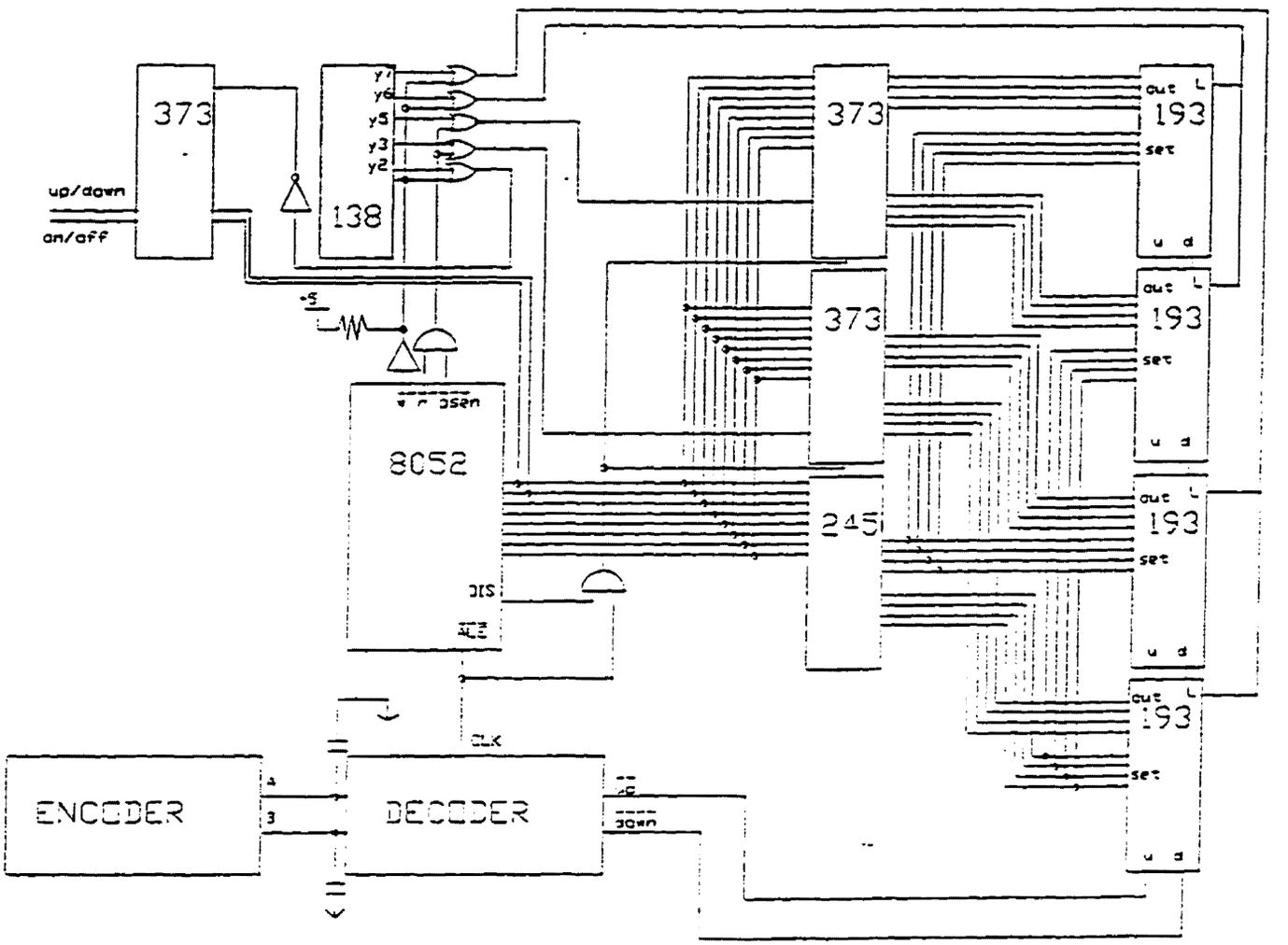


Figure 76 Circuit schematic showing wavelength counter and motor control.

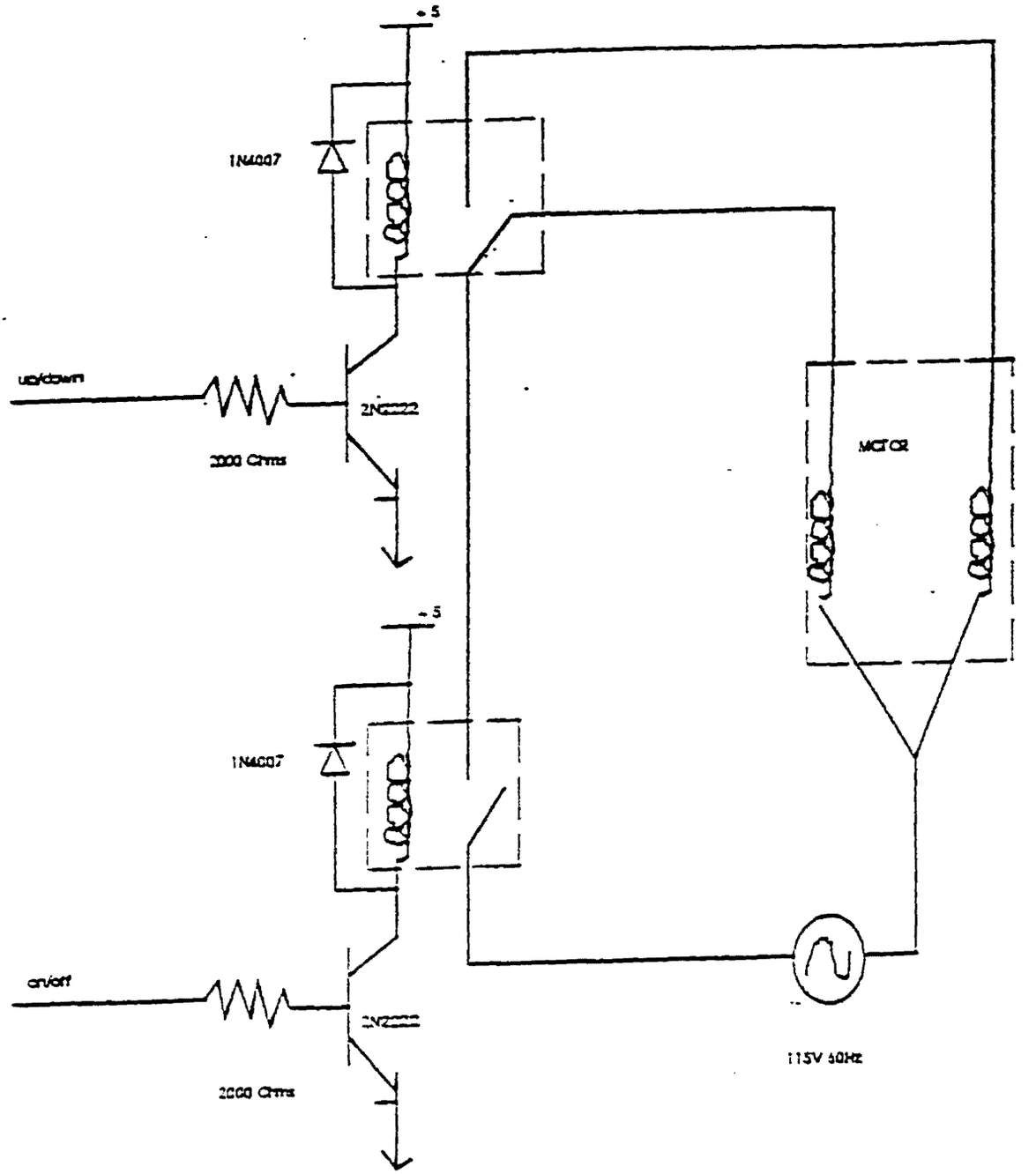


Figure 77 Schematic of relay circuit controlling monochromator motors.

(!write))} so that to change the state of the motor a value must be written to an external memory location from 16384 to 24575. A/D6 is the on/off control and A/D7 controls the direction.

Therefore to send the motor up use the command "xby(16384)=64". To stop upward motion use "xby(16384)=0". To send the motor down use "xby(16384)=128" and "xby(16384)=255" in two steps to allow the relays time to switch. To stop downward motion reverse these steps with "xby(16384)=128" and then "xby(16384)=0" to turn off all relays.

Data input is accomplished by reading the output of the PRA model 1770 photon counter. 24 pin parallel port is available with 4 bit parallel, 8 word serial !BCD output which dumps the digital counter output after every update. To accomplish this a direct memory access circuit was built which places the 8 !BCD words directly into upper memory on the external memory chip. Refer to figure 78 or the circuit and figure 79 or the timing diagram.

To utilize the DMA routine on the 8052 computer, two bits must be set on the IE register using "IE=IE.or.81H". Also DBY location 38 must be set using "DYB(38)=DBY(38).or.02H". This sets up the !INT0pin to act as a DMA request. The !Data Available output from the 1770 is connected to this pin. After receiving a low input on !INT0 the computer will complete its current command cycle and then interrupt its command processes, outputting a low on the !DMA ACK pin. This low can then be used to tri-state the onboard latches. The !DMA ACK is therefore connected through an inverter to the enable pins on the 2 245 chips and the output control pin of the 373 address latch. It is connected through a buffer to the output control pin of a 74LS374 data latch which is used for the actual DMA. It is also connected through the buffer to the G1 pin of the 74LS138 to set all of its outputs to high.

The four bits of !BCD data from the 1770 come in serial word form at a speed of 10khz. This frequency is also available on the Mux Clk output of the 1770. he circuit was designed to take advantage of the quoted 50% duty cycle of the Mux output. Unfortunately, the actual Mux output was only 5% high and 95% low, requiring a 74LS122 monostable vibrator with appropriate capacitors to adjust the duty cycle back to 50%.

To allow write access to the memory chip the !CS pin is changed from (!y0 of the 138) to {(!y0 of the 138) AND (!DMA ACK)}. Further, the !WR pin is changed from (!WR of the 8052) to {NOT[(!WR) NAND ((NOT(Mux Clk)) delayed by ~4 cycles of the ALE through 4 sequential latches))]} so that the DMA write pulse will lag the address and data latching by a short period.

To set the address of the DMA, the top nine address lines are tied high by a ten pin resistor pack on the memory side of the onboard latches. The lower four address lines are supplied by the 374 which is latched by the rising edge of {NOT(Mux Clk)}. To write the !BCD data into these addresses, the four !BCD lines are sent straight into the bottom four latches of the 374 and then on into the bottom four address/data lines on the memory side of the bus.

To update the address for each new !BCD word, the top four address latches in the 374 are supplied by the output of a 74LS193 counter chip which counts up on {(NOT(!Data Avail)) AND (Mux Clk)}. Due to the format of the 1770 output, !BCD data

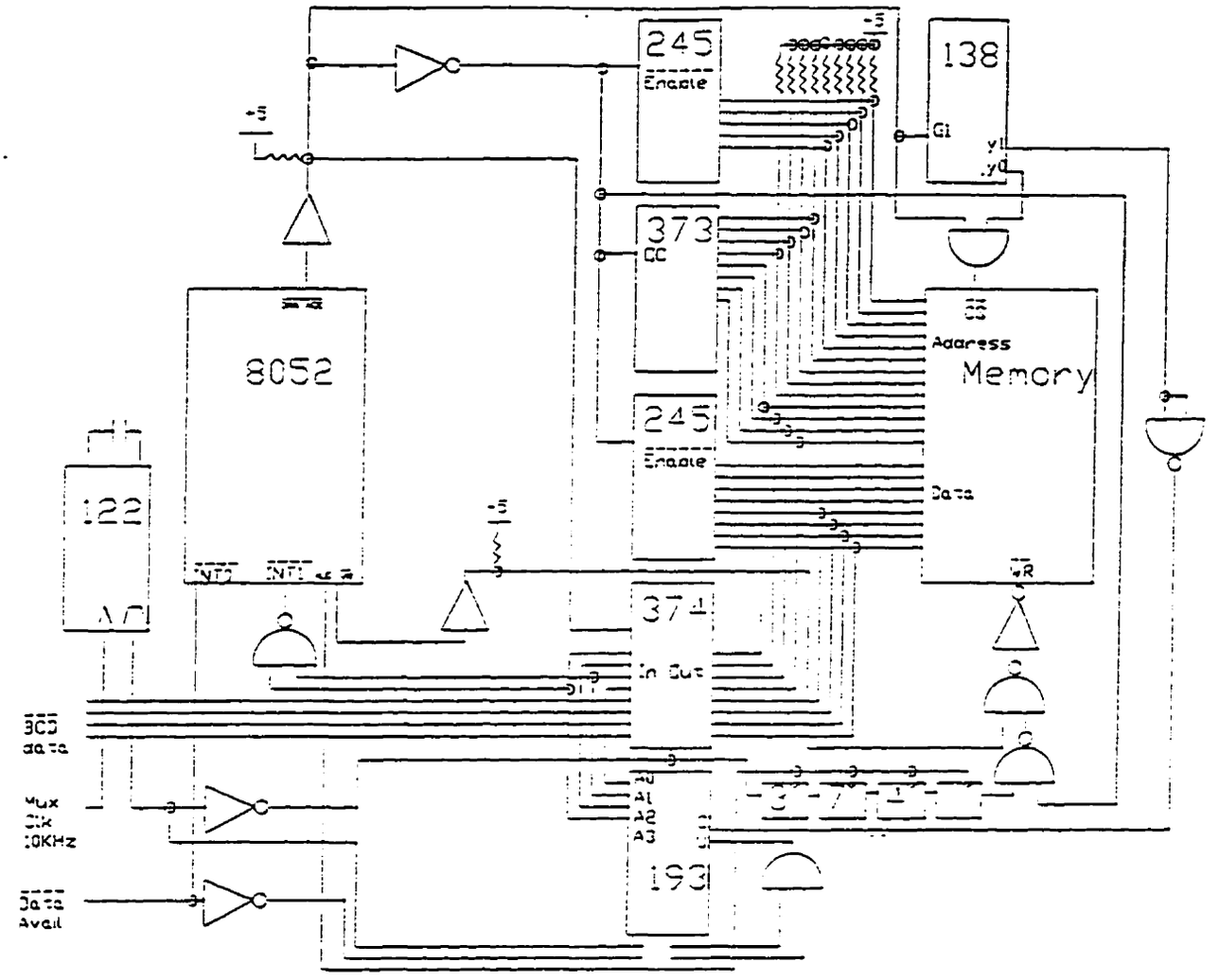


Figure 78 Circuit schematic showing photon counter interface and DMA addressing.

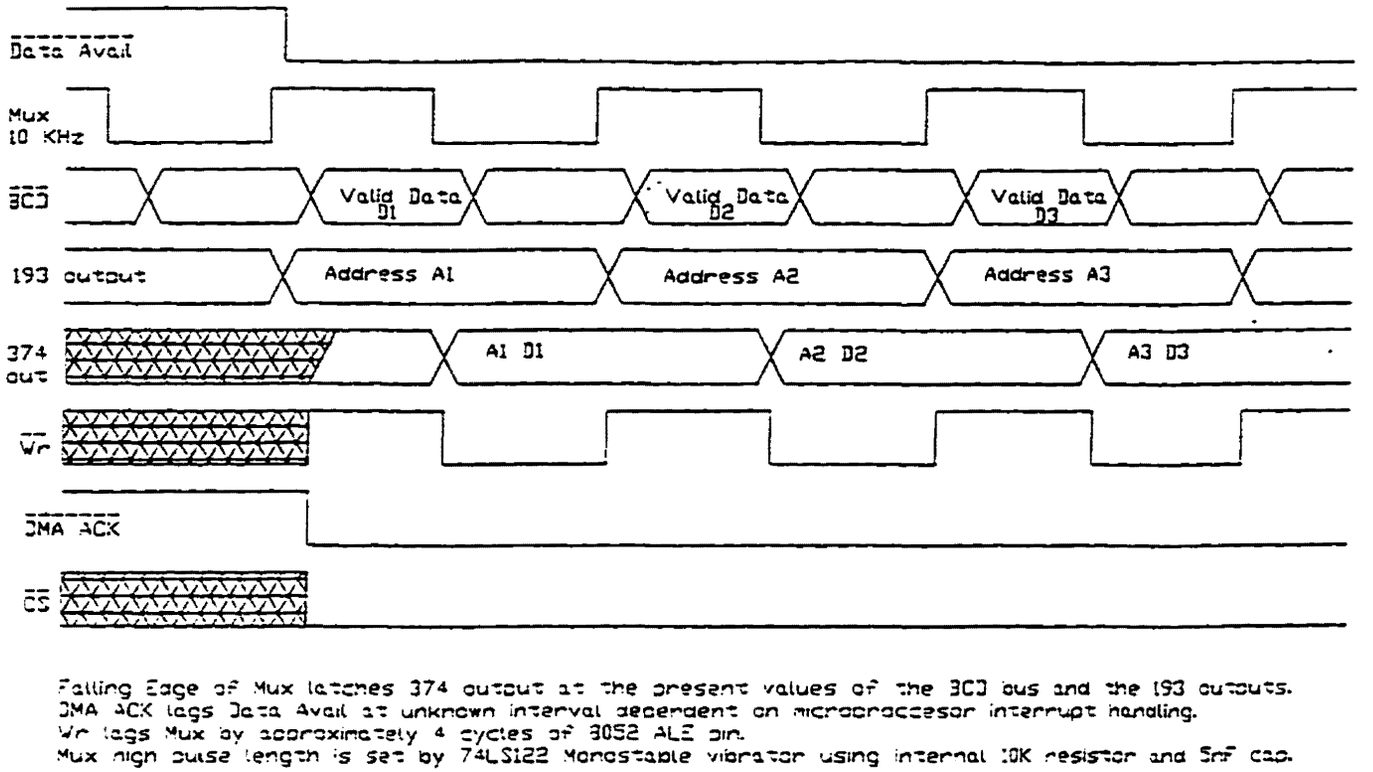


Figure 79 DMA timing diagram.

is not sent until the third Mux pulse after !Data Avail goes low. This gives some leeway for the 8052 to acknowledge the DMA request. Nothing will be written in DMA mode until the 8052 gives a low out on !DMA ACK, but no matter the delay, the addresses will be the same each time due to the hard wiring of the 193 directly to the output of the 1770.

To alert the 8052 that a DMA has occurred, !INT1 on the 8052 is triggered by (A3 AND A1) of the 193 counter which will happen after the tenth count up pulse in the DMA routine. This can then be processed as a software interrupt and the 8 digits can be read in order using the following routine:

```
for x=1 to 8:print 255-xby(8192-14+x):next x
```

Note that the line "ONEX1 <interrupt line number>" must be set before this interrupt will be processed. To return from the interrupt and reset the counter use:

```
xby(8192)=<dummy value>
ret1
```

The clear input on the 193 is connected to {(!y1) NAND (!y1)} because there were no more inverters left available on the board. This allows you to reset the counter after the DMA routine is complete, thus the first line of the above routine.

The BASIC software used is included below. The calibration routine will search for the Lyman Beta peak of the deuterium lamp which is located at 4860 Å.

```
5  xby(16384)=32:pl=4860*4/256:hb=int(pl):lb=256*(pl-int(pl))
10 xby(16384)=48:clock0:time=0:dby(71)=0
20 onex1 1000
30 dby(38)=dby(38).or.02H
40 ie=ie.or.81H
50 dis=0:ws=3500:we=1500:t=1:st=-5
60 ?:?:?"Data Collection Menu:"
70 ?"1. Calibrate Wavelength"
80 ?"2. Collect Data"
90 ?"3. Manual Collect"
100 choice=get
110 if choice=0 then 100
120 if choice>51.or.choice<49 then 60
130 on (choice-49) gosub 200,400,700
140 goto 60
200 rem Calibration Routine
210 close=0
215 gosub 4000:gosub 4100:rem clean out memory
220 ?:?"Now Calibrating."
230 t=.5
235 gosub 4000:gosub 4100:rem clean out memory
236 if close=0 then last=a
240 do
250 gosub 4000
```

```
260 gosub 2000:rem next bit chooses a direction to search
270 do :until time>t:gosub 4100
300 if dir=0 then gosub 800:fory=1to500:nexty
315 delta=a-last:last=a
320 until delta > .2*a:gosub 2000:p1=pos:close=dir:hi=0:rec=0
330 rem Large increase in counts kicks us out.
335 on dir gosub 2000,850,950
340 ?"Are we near 4860 Angstroms?"
341 c=get:if c=0 then 341
342 if c=78.or.c=110 then 235
343 ?"Set Monochromator to 200 and press a key."
344 c=get:if c=0 then 344
345 t=.1:gosub 900:rem back up until we're below the peak.
346 do
347 gosub 2000
348 until pos<p1-40:gosub 950
350 gosub 800:rem scan through the peak and find the highest counts.
355 gosub 4000:gosub 4100:rem clean out memory
360 do
361 gosub 4000
362 do:until time>t:gosub 4100
365 if a>hi.and.a-hi<5000 then hi=a:rem ignores noise spikes
370 gosub 2000
371 until pos>p1+40
372 gosub 850:gosub 900:rem scan back down through it again.
373 gosub 4000:gosub 4100:rem clean out memory
374 do
375 gosub 4000
376 do
377 until time>t
378 gosub 4100
379 if a>hi.and.a-hi<5000 then hi=a
380 gosub 2000:until pos<p1-40:gosub 950:gosub 800
381 do:rem scan back and forth till you nearly match the highest count.
382 if pos>p1+50 then gosub 850:gosub 900
383 if pos<p1-50 then gosub 950:gosub 800
385 gosub 4000
386 do
387 until time>t
388 gosub 4100
393 until abs(a-hi)<.05*hi:rem Very close to highest count is the peak.
394 xby(57344)=lb
395 xby(49152)=hb
396 rem on the peak
397 on dir gosub 2000,850,950
```

```
398 ?:?"Return Monochromater to scan speed 400."
399 dis=0:return
400 rem Collection Routine
405 if ws=we.or.ws<1000.or.we<1000.or.ws>5000.or.we>5000 then c=49:goto 440
410 ?"Scan from ",ws,"to ",we,"angstroms, step",st
420 ?"Change Defaults?(1=Yes,2=No)"
430 c=get:if c=0 then 430
440 if c=49 then input"Wavelength Start, End, Step (A)",ws,we,st:goto 400
445 ?"Ratio Mode(1) or Binned(2)"
446 c=get:if c=0 then 446
447 if c<49.or.c>50 then 446
450 if ws-we>0 then wl=ws+50 else wl=ws-50
460 do:gosub 2000
470 if pos-wl>0.and.dir=0 then gosub 900
480 if pos-wl<0.and.dir=0 then gosub 800
490 until abs(pos-wl)<10
495 if dir=1.and.ws-we>0 then gosub 850
496 if dir=2.and.ws-we<0 then gosub 950
500 ?"Beginning Scan"
515 if dir <> 0 then 530
520 if ws-we>0 then gosub 900 else gosub 800
5000 hwo=wv*4/256:lwo=int((hwo-int(hwo))*256):hwo=int(hwo)
5010 return
530 wv=ws:gosub 5000
540 do
542 until abs(xby(24576)-lwo)<=2
543 gosub 4000
551 dis=1
555 if c=49 then 600
560 rem Wavelength Bin Scan
570 do
571 wv=wv+st
572 gosub 5000
573 if time=0 then gosub 4000
574 do
575 until abs(xby(24576)-lwo)<=2
576 gosub 4100
577 gosub 2000
579 until abs(pos-we)<=abs(st)
580 dis=0:on dir gosub 2000,850,950:?"Finished Scan"
581 rem if wl-pos>0 then gosub 800 else gosub 900
582 rem do:gosub 2000:until abs(pos-wl)<=1
583 rem on dir gosub 2000,850,950
590 return
600 rem Ratio Scan
```

```
610 do
620 if time=0 then gosub 4000
630 do
640 gosub 2000
650 st=pos-wv
660 until time=0
670 wv=pos
675 if dir=1 then 685
680 until pos<we:goto 690
685 until pos>we
690 goto 580
700 rem Manual Collect
710 print"Press a key to begin scanning."
720 rem gosub 2000:print pos
730 c=get
740 if c=0 then 720
742 print"Press a key to stop."
745 gosub 4000:gosub 4100
750 dis=1
760 if time=0 gosub 4000
770 c=get
780 if c=0 then 760
785 dis=0
790 return
800 rem Start Relay Up
810 xby(16384)=112:dir=1
840 return
850 rem Stop Relay Up
860 xby(16384)=48:dir=0
890 return
900 rem Start Relay Down
910 xby(16384)=176:dir=2
920 for y=1 to 100:next y
930 xby(16384)=255
940 return
950 rem Stop Relay Down
960 xby(16384)=176:dir=0
970 for y=1 to 100:next y
980 xby(16384)=48
990 return
1000 a=0
1010 for x=0 to 7
1020 a=a+10**(7-x)*(255-xby(8192-13+x))
1030 next x
1040 gosub 2000
```

```
1050 if dis=1 then print a,pos-st/2
1060 xby(8192)=0
1070 clock0
1080 time=0
1090 dby(71)=0
1100 reti
2000 pos=(xby(24576)+256*xby(40960))/4
2010 return
4000 rem counter start
4010 if dir=2 then xby(16384)=208 else xby(16384)=16.or.(dir*64)
4020 if dir=2 then xby(16384)=240 else xby(16384)=48.or.(dir*64)
4030 clock1
4040 return
4100 rem counter stop
4110 if dir=2 then xby(16384)=224 else xby(16384)=32.or.(dir*64)
4120 if dir=2 then xby(16384)=240 else xby(16384)=48.or.(dir*64)
4130 return
```

9. REFERENCES

Aitken, D.K., Smith, C.H., and Roche, P.F. 1989, *Mon. Not. R. Astron. Soc.*, **236**, 919.

Akkerman, Z.L., Efstathiadis, H. and Smith, F.W. 1996, *J. Appl. Phys.*, **80**(5), 3068.

Allain, T., Leach, S. and Sedlmayer, E. 1996, *Astron. Astrophys.*, **305**, 616.

Allamandola, L.J., Sandford, S.A., Tielens, A.G.G.M. and Herbst, T.M. 1992, *Ap. J.*, **399**, 134.

Allamandola, L.J., Tielens, A.G.G.M. and Barker, J.R. 1985, *Ap. J.*, **290**, L25.

Allamandola, L.J., Tielens, A.G.G.M. and Barker, J.R. 1989, *Ap. J. (Suppl.)*, **71**, 733.

Allen, M. and Robinson, G. W. 1975, *Ap. J.*, **195**, 81.

Allen, D.A. and Wickramasinge, D.T. 1987, *Nature*, **329**, 615.

Anderson, D.A. 1977, *Philos. Mag.*, **35**, 17.

Angus, J.C., Koidl, P. and Domitz, S. In: "Plasma Deposited Thin Films." eds. J. Mort & F. Jansen, (CRC Press: Boca Raton Fla.), c1986.

Baas, F., Geballe, T.R. and Walther, D.M. 1986, *Ap. J.*, **311**, L97.

Barker, J.R., Allamandola, L.J. and Tielens, A.G.G.M. 1987, *Ap. J.*, **315**, L61.

Barlow, M.J. 1978, *Mon. Not. R. Astron. Sco.* **183**, 397.

Bell, M.B., Feldman, P.A. and Matthews, H.E. 1981, *Astron. Astrophys.*, **101**, L13.

Bernstein, M.P., Sandford, S.A. and Allamandola, L.J. 1996, *Ap. J.*, **472**, L127.

Birks, J.B. 1970, "Photophysics of Aromatic Molecules", (Wiley: London).

Blanco, A., Bussoletti, E. and Colangeli, L. 1988, *Ap. J.*, **334**, 875.

Blanco, A., Bussoletti, E., Colangeli, L., Fonti, S. and Stephens, J.R. 1991, *Ap. J.*, **382**, L97.

Boulade, O., Sauvage, M., Altieri, B., Blommaert, J., Gallais, P., Guest, S., Metcalfe, L., Okumura, K., Ott, S., Tran, D. and Vigroux, L. 1996, *Astron. Astrophys.* **315**, L85.

Boulanger, F., Reach, W.T., Abergel, A., Bernard, J.P., Cesarsky, C.J., Cesarsky, D., Désert, B.X., Falgarone, E., Lequeux, J., Metcalfe, L., Pérault, M., Puget, J.L., Rouan, D., Sauvage, M., Tran, D. and Vigroux, L. 1996, *Astron. Astrophys.*, **315**, L325.

Bounouh, Y., Thèye, M.L., Dehbi-Alaoui, A., Matthews, A. and Stoquert, J.P. 1995, *Phys. Rev. B.* **51(15)**, 9597.

Bourdon, E.B.D., Duley, W.W., Jones, A.P. and Prince, R.H. 1991, *Surface & Coatings Tech.*, **47**, 509.

Boutin, A., Léger, A., Désert, F.X., Boissel, P. and d'Hendecourt, L. 1995, *Mon. Not. R. Astron. Soc.*, **274**, 435.

Brooke, T.Y., Knacke, R.F., Owen, T.C. and Tokunaga, A.T. 1989, "The 3.4μm emission in comets.", eds. L.J. Allamandola & A.G.G.M. Tielens, NASA CP3036

Brooke, T.Y., Sellgren, K. and Smith, R. G. 1996, *Ap. J.*, **459**, 209.

Brown, P.D., Charnley, S.B. and Millar, T.J. 1988, *Mon. Not. R. Astron. Soc.*, **231**, 409.

Buch, V. 1989, *Ap. J.*, **343**, 208.

Buss, R.H. Jr., Cohen, M., Tielens, A.G.G.M., Werner, M.W., Bregman, J.D., Witteborn, F.C., Rank, D. and Sandford, S.A. 1990, *Ap. J.*, **365**, L23.

Carnochan, D.J. 1986, *Mon. Not. R. Astron. Soc.*, **219**, 903.

Carnochan, D.J. 1987, *Mon. Not. R. Astron. Soc.*, **231**, 455.

Cesarsky, D., Lequeux, J., Abergel, A., Perault, M., Palazzi, E., Madden, S. and Tran, D. 1996a, *Astron. Astrophys.*, **315**, L305.

Cesarsky, D., Lequeux, J., Abergel, A., Perault, M., Palazzi, E., Madden, S. and Tran, D. 1996b, *Astron. Astrophys.*, **315**, L309.

Cherchneff I., Barker, J.R. and Tielens, A.G.G.M. 1991, *Ap. J.*, **377**, 541.

Cho, N.H., Veirs, D.K., Ager, J.W., Rubin, M.D., Hopper, C.B. and Bogy, D.B. 1992, *J. Appl. Phys.*, **71**, 2243.

Clar, E. 1972, "The Aromatic Sextet", (Wiley: London).

Cohen, M., Tielens, A.G.G.M. and Bregman, J.D. 1989, *Ap. J.*, **344**, L13.

Colangeli, L., Capozzi, V., Bussoletti, E. and Minafra, A. 1986, *Astron. Astrophys.*, **168**, 349.

Colangeli, L., Schwehm, G., Bussoletti, E., Fonti, S., Blanco, A. and Orofino, V. 1988, In: "Infrared Spectroscopy in Astronomy: Proceedings of the 22nd Eslab Symposium held in Salamanca, Spain 7-9 Dec. 1988", ed. B.H. Kaldeich, (ESA Pub.: Paris), 49.

Colangeli, L., Bussoletti, E., Papoular, R. and Mennella, V. 1990, *Icarus*, **86**, 198.

Compagnini, G., Foti, G., Reitano, R. and Mondio, G. 1990, *Appl. Phys. Lett.*, **57**, 2546.

Cook, D.J., Schelmmer, S., Balucani, N., Wagner, D.R., Steiner, B. and Saykally, R.J. 1996, *Nature*, **380**, 277.

Crawford, M.K., Tielens, A.G.G.M. and Allamandola, L.J. 1985, *Ap. J.*, **293**, L45.

Czyzak, S.J., Hirth, J.P. and Tabak, R.G. 1982, *Vistas Astron.*, **25**, 337.

Czyzak, S.J. and Santiago J.J. 1973, *Astrophys. Sp. Sci.*, **23**, 443.

Dadswell, G. and Duley, W.W. 1997a, *Ap. J.*, **476**, 184.

Dadswell, G. and Duley, W.W. 1997b, in press.

Day, K.L. 1981, *Ap. J.*, **246**, 110.

Day, K.L. 1979, *Ap. J.*, **234**, 158.

Dirks, A.G. and Leamy, H.J. 1977, *Thin Solid Films*, **47**, 219.

Dischler, B., Bubenzer, A. and Koidl, P. 1983a, *Solid State Commun.*, **48** (2), 105.

Dischler, B., Bubenzer, A. and Koidl, P. 1983b, *Appl. Phys. Lett.*, **42** (8), 636.

Donn, B.D., Allen, J.E. and Khanna, R.K. 1989, In: "Interstellar Dust", eds. L.J. Allamandola & A.G.G.M. Tielens, (Kluwer: Dordrecht).

Dorschner, J. and Henning, T. 1986, *Astrophys. Sp. Sci.*, **128**, 47.

Dorschner, J. and Henning, T. 1995, *Astron. Astrophys. Rev.*, **6**, 271.

Dorschner, J., Begemann, B., Henning, Th., Jäger, C., and Mutschke, H. 1995, *Astron. Astrophys.*, **300**, 503.

Douglas, A.E. 1977, *Nature*, **269**, 130.

Draine, B.T. 1989, In: "Interstellar Dust", eds. L.J. Allamandola & A.G.G.M. Tielens, (Kluwer: Dordrecht), Proc. IAU Symp. **135**.

Draine, B.T. 1990, In: "The Evolution of the Interstellar Medium", ed. L. Blitz, (Astronomical Society of the Pacific: San Francisco), Conf. Series **12**, 193.

Draine, B.T. 1994, In: "The Infrared Cirrus and Diffuse Interstellar Clouds", eds. R. Cutri & W.B. Latter, (Astronomical Society of the Pacific: San Francisco), Conf. Series **58**, 227.

Draine, B.T. and Lee, H.M. 1984, *Ap. J.*, **285**, 89.

Draine, B.T. and Malhotra, S. 1993, *Ap. J.*, **414**, 632.

Duley, W.W. 1984, *Ap. J.*, **287**, 694.

Duley, W.W. 1985, *Mon. Not. R. Astron. Soc.*, **215**, 259.

Duley, W.W. 1986, In: "Polycyclic Aromatic Hydrocarbons and Astrophysics", eds. A. Léger, L. d'Hendecourt & N. Boccara, (Reidel Publishing Co.: Dordrecht), 373.

Duley, W.W. 1987, *Mon. Not. R. Astron. Soc.*, **229**, 203.

Duley, W.W. 1989, In: "The Physics and Chemistry of Interstellar Clouds", eds. G. Winnewisser & J.T. Armstrong, (Springer: New York), 353.

Duley, W.W. 1993, In: "Dust and Chemistry in Astronomy", eds. T. J. Millar & D.A. Williams, (Institute of Physics: Bristol), 71.

Duley, W.W. 1994a, *Ap. J.*, **429**, L91.

Duley, W.W. 1994, *Ap. J.*, **430**, L133.

Duley, W.W. 1995, *Astrophys. Sp. Sci.*, **224**, 217.

Duley, W.W. 1996a, *Mon. Not. R. Astron. Soc.*, **283**, 343.

Duley, W.W. 1996b, "UV lasers: effects and applications in materials science", (Cambridge University Press: Cambridge).

Duley, W.W., Jones, A.P., Whittet, D.C.B. and Williams, D.A. 1989a, *Mon. Not. R. Astron. Soc.*, **241**, 697.

Duley, W.W., Jones, A.P. and Williams, D.A. 1989b, *Mon. Not. R. Astron. Soc.*, **236**, 709.

Duley, W.W., Jones, A.P., Taylor, S.D. and Williams, D.A. 1993, *Mon. Not. R. Astron. Soc.*, **260**, 415.

Duley, W.W. and Jones, A.P. 1990, *Ap. J.*, **351**, L49.

Duley, W.W. and Smith, R.G. 1997, Unpublished.

Duley, W.W. and Williams, D.A. 1981, *Mon. Not. R. Astron. Soc.*, **196**, 269.

Duley, W.W. and Williams, D.A. 1984, *Mon. Not. R. Astron. Soc.*, **211**, 97.

Duley, W.W. and Williams, D.A. 1986, *Mon. Not. R. Astron. Soc.*, **219**, 859.

Duley, W.W. and Williams, D.A. 1988, *Mon. Not. R. Astron. Soc.*, **231**, 969.

Dwek, E., A'Hearn, M.F., Becklin, E.E., Brown, R.H., Capps, R.W., Dinerstein, H.L., Gatley, I., Morrison, D., Telesco, C.M., Tokunaga, A.T., Werner, M.W. and Wynn-Williams, C.G. 1983, *Ap. J.*, **274**, 168.

Dwek, E., and Scalo, J.M. 1980, *Ap. J.*, **239**, 193.

Edvardsson, B., Anderson, J., Gustafsson, B., Lambert, D.L., Nissen, P.E. and Tomkin, J. 1993, *Astron. Astrophys.*, **275**, 101.

Efstathiadis, H., Akkerman, Z. and Smith, F.W. 1996, *J. Appl. Phys.*, **79(6)**, 2954.

Egan, M.P. and Leung, C.M. 1995, *Ap. J.*, **444**, 251.

Ehrenfreund, P., d'Hendecourt, L., Joblin, C. and Léger, A. 1992, *Astron. Astrophys.*, **266**, 429.

Enke, K. 1981, *Thin Solid Films*, **80**, 227.

Feldman, D., Kutzner, J., Laukemper, J., MacRobert, S. and Welge, K.H. 1987, *Appl. Phys.*, **B44**, 81.

Fink, J., Muller-Heinzerling, T., Pfluger, J., Scheerer, B., Dischler, B., Koidl, P., Bubenzer, A. and Sah, R.E. 1984, *Phys. Rev. B* **30**, 4713.

FitzGerald, M.P.V., and Peterson, C.J. 1991, Ad Astra vII. To be published by Wuerz publishing, Winnipeg, MB, Canada.

FitzPatrick, E.L., and Massa, D. 1986, *Ap. J.*, **307**, 286.

Foing, B.H. and Ehrenfreund, P. 1997, *Astron. Astrophys.*, **319**, L59.

Forest, W.J., McCarthy, J.F., and Houck, J.R. 1979, *Ap. J.*, **233**, 611.

Frenklach, M. and Feigelson, E.D. 1989, *Ap. J.*, **341**, 372.

Furton, D.G. and Witt, A.N. 1993, *Ap. J.*, **415**, L51.

Geballe, T.R. 1996, In: "From Stardust to Planetesimals", eds. Y. Pendleton & A.G.G.M. Tielens, (ASP: San Francisco).

Geballe, T.R., Joblin, C., d'Hendecourt, L.B., De Muizon, M.J., Tielens, A.G.G.M. and Léger, A. 1994, *Ap. J.*, **434**, L15.

Geballe, T.R., Lacy, J.H, Persson, S.E., McGregor, P.J. and Soifer, B.T. 1985, *Ap. J.*, **292**, 500.

Geballe, T.R., Tielens, A.G.G.M., Kwok, S. and Hrivnak, B.J. 1992, *Ap. J.*, **387**, L89.

Geballe, T.R. and van der Veen, W.E.C.J. 1990, *Astron. Astrophys.*, **235**, L9.

Ghosh, S.K, and Drapatz, S. 1986, In: "Polycyclic Aromatic Hydrocarbons and Astrophysics", eds. A. Léger, L. d'Hendecourt & N. Boccara, (Reidel Publishing Co.: Dordrecht), 317.

Giard, M., Bernard, J.P., Lacombe, F., Normand, P. and Rouan, D. 1994, *Astron. Astrophys.*, **291**, 239.

Gilgenbach, R.M. and Ventzek, P.L.G. 1991, *Appl. Phys. Lett.*, **38**, 399.

Gillet, F.C., Forrest, W.J. and Merrill, K.M. 1973, *Ap. J.*, **183**, 87.

Gilman, R.C. 1969, *Ap. J.*, **155**, L185.

Gilra, D.P. 1972, In: *The Scientific results of the Orbiting Astronomical Observatory OAO-2*. ed. A.D. Cole, NASA Sp. 310.

Goebel, J.H. 1993, *Astron. Astrophys.*, **278**, 226.

Greenberg, J.M. 1989, *Proc. IAU Symp. 135*, eds L.J. Allamandola, & A.G.G.M. Tielens, (Kluwer: Dordrecht), 345.

Greenberg, J.M., Li, A., Mendoza-Gómez, C.X., Schutth, W.A., Gerakinhs, P.A. and de Groot, M. 1995, *Ap. J.*, **455**, L177.

Grigorivici, R., Dévényi, A., Gheorghiu, A. and Belu, A. 1972, *J. Non-Crystalline Solids*, **8-10**, 793.

Grossman, L. 1972, *Geochim. and Cosmochim. Acta*, **36**, 597.

Guillois, O., Nenner, I., Papoular, R. and Reynaud, C. 1996, *Ap. J.*, **464**, 810.

Habing, H.J. 1968, *Bull. Astron. Soc. Netherlands*, **19**, 421.

Hansen, W.N., Pearson, L., Hansen, G. and Anderson, W.J. 1979, In: "Laser Induced Damage in Optical Materials", eds. H.E. Bennett, A.J. Glass, A.H. Guenther & B.E. Newnam, (U.S. Dept. of Commerce, National Bureau of Standards: Gaithersburg Md.).

Harris, M., Macleod, H.A., Ogura, S., Pelletier, E. and Vidal, B. 1979, *Thin Solid Films*, **57**, 173.

Hauser, J.J. 1977, *J. Non-Crystalline Solids*, **23**, 21.

Heath, J.R., O'Brien, S.C., Curl, R.F., Kroto, H.W. and Smalley, R.E. 1987, *Comments Cond. Mat. Phys.*, **13**(3), 119.

Heavens, O.S. 1955; 1991, "Optical Properties of Thin Solid Films", (Dover: NewYork).

Hecht, J.H. 1986, *Ap. J.*, **305**, 817.

d'Hendecort, L.B., Allamandola, L.J., Baas, F. and Greenberg, J.M. 1982, *Astron. Astrophys.*, **109**, L12.

Herman, I.P., Tang, H. and Leong, P.P. 1992, *Mat. Res. Symp. Proc.*, **236**, 563.

Hoffman, R.W. et al. *AEC Techn. Rep.*, **18** (1961), **64** (1970), **76** (1971), **79** (1972).

Hsu, W.L. 1988, *J. Vac. Sci. Technol. A*, **6(3)**, 1803.

Huffman, D.R. 1970, *Ap. J.*, **161**, 1157.

Huffman, D.R. 1977, *Adv. Phys.*, **26**, 129.

Huffman, D.R. and Stapp, J.L. 1971, *Nature*, **229**, 45.

Hyland, A.R. and McGregor, P.J. 1989, In: "Interstellar Dust", Contributed Papers, NASA Conf. Pub. 3036, eds. A.G.G.M. Tielens & L.J. Allamandola, (NASA: Santa Clara), 101.

Iida, S., Ohtaki, T. and Seki, T. 1984, *Am. Inst. Conf. Proc.*, **120**, 258.

Jager, C., Mutschke, H., Begemann, B., Dorschner, J. and Henning, Th. 1994, *Astron. Astrophys.*, **292**, 641.

Jenniskens, P., Baratta, G.A., Kouchi, A., de Groot, M.S., Greenberg, J.M. and Strazzulla, G. 1992, *Astron. Astrophys.*, **273**, 583.

Jennikens, P. and Blake, D.F. 1996, *Ap. J.*, **473**, 1104.

Jenniskens, P. and Greenberg, J.M. 1993, *Astron. Astrophys.*, **274**, 439.

Joblin, C., Léger, A. and Martin, P. 1992, *Ap. J.*, **393**, L79.

Joblin, C., Tielens, A.G.G.M., Allamandola, L.J. and Geballe, T.R. 1996, *Ap. J.*, **458**, 610.

Jones, A.P., Duley, W.W. and Williams, D.A. 1990, *Q. J. R. Astron. Soc.*, **31**, 567.

Jones, A.P., Tielens, A.G.G.M., Hollenbach, D.J. and Mckee, C.F. 1994, *Ap. J.*, **433**, 797.

Justtanont, K., Barlow, M.J., Skinner, C.J., Roche, P.F., Aitken, D.K. and Smith, C.H. 1996, *Astron. Astrophys.*, **309**, 612.

Key, P.J. and Preston, R.C. 1980, *J. Phys. E. Sci. Instrm.*, **13**, 866.

Kim, S. and Martin, P.G. 1995a, *Ap. J.*, **442**, 172.

Kim, S. and Martin, P.G. 1995b, *Ap. J.*, **444**, 293.

Koike, C., Kaito, C. and Shibai, H. 1994, *Mon. Not. R. Astron. Soc.*, **268**, 321.

Krätschmer, W. and Huffman, D.R. 1979, *Astrophys. Sp. Sci.*, **61**, 195.

Kroto, H.W. and McKay, K. 1988, *Nature*, **331**, 328.

Larimer, J.W. 1979, *Astrophys. Sp. Sci.*, **65**, 351.

Laureijs, R.J., Acosta-Pulido, J., Ábráham, P., Kinkel, U., Klaas, U., Castaneda, H.O., Cornwall, L., Gabriel, C., Heinrichsen, I., Lemke, D., Pelz, G., Schulz, B. and Walker, H.J. 1996, *Astron. Astrophys.*, **315**, L313.

Leach, S. 1987, In: "Polycyclic Aromatic Hydrocarbons and Astrophysics", eds. A. Léger, L. d'Hendecourt & N. Boccara, (Reidel: Dordrecht).

Leach, S. 1995, *Planet. Space Sci.*, **43**, 1153.

Leddingham, K.W.D. and Singhal, R.P. 1992, In: "Applied Laser Spectroscopy", ed. D.L. Andrews, (VCH Publishers Inc.: New York).

Lee, W. and Wdowiak, T.J. 1993, *Ap. J.*, **410**, L127.

Léger, A. and d'Hendecourt, L.B. 1985, *Astron. Astrophys.*, **146**, 81.

Léger, A., d'Hendecourt, L.B., Verstraete, L. and Ehrenfreund, P. 1988, In: "Infrared Spectroscopy in Astronomy: Proceedings of the 22nd Eslab Symposium held in Salamanca, Spain 7-9 Dec. 1988", ed. B.H. Kaldeich, (ESA Pub.: Paris), 189.

Léger, A., d'Hendecourt, L., Verstraete, L. and Schmidt, W. 1988, *Astron. Astrophys.*, **203**, 145.

Léger, A. and Puget, J.L. 1984, *Astron. Astrophys.*, **137**, L5.

Lillie, C.F. and Witt, A.N. 1976, *Ap. J.*, **208**, 64.

Lin, S.H. and Feldman, B.J. 1983, *Phys. Rev. B.*, **28**, 413.

Macleod, H.A. 1982, *SPIE*, **325**, 21.

Madan, A. and Shaw, M.P. 1988, "The Physics and Applications of Amorphous Semiconductors", (Academic Press: New York.).

Magazzù, A. and Strazzulla, G. 1990, *Astrophys. Sp. Sci.*, **171**, 199.

Maldoni, M.M., Smith, R.G. and Robinson, G. 1997 In Press.

Malinovsky, V.K. 1987, *J. Non Crystalline Solids*, **90**, 37.

Mathis, J.S. 1989, *Proc. IAU Symp. 135*, eds. L. J. Allamandola & A.G.G.M. Tielens, Kluwer, Dordrecht, p357.

Mathis, J.S. 1990, In: "The Evolution of the Interstellar Medium", ASP Conf. Ser., **12**, ed. L. Blitz, (BookCrafters Inc.).

Mathis, J.S., Rumpl, W. and Nordsieck, K.H. 1977, *Ap. J.*, **217**, 425.

Mathis, J.S. and Whiffen, G. 1989, *Ap. J.*, **341**, 808.

Mattila, K., Lemke, D., Haikala, L.K., Laureijs, R.J., Léger, A., Lehtinen, K., Leinert, Ch. and Mezger, P.G. 1996, *Astron. Astrophys.*, **315**, L353.

McKenzie, D.R., McPhedran, R.C. and Savvides, N. 1983, *Thin Solid Films*, **108**, 247.

Mendoza-Gómez, C.X., de Groot, M.S. and Greenberg, J.M. 1995, *Astron. Astrophys.*, **295**, 479.

Mennella, V., Colangeli, L., Blanco, A., Bussoletti, E., Fonti, S., Palumbo, P. and Mertins, H.C. 1995, *Ap. J.*, **444**, 288.

Mennella, V., Colangeli, L., Palumbo, P., Rotundi, A., Schutte, W. and Bussoletti, E. 1996, *Ap. J.*, **464**, L191.

Mennella, V., Baratta, G.A., Colangeli, L., Palumbo, P., Rotundi, A., Bussoletti, E. and Strazzulla, G. 1997, *Ap. J.*, **481**, 545.

Metcalfe, L., Steel, S.J., Barr, P., Clavel, J., Delaney, M., Gallais, P., Laureijs, R.J., Leech, K., McBreen, B., Ott, S., Smith, N. and Hanlon, L. 1996, *Astron. Astrophys.*, **315**, L105..

Millar, T.J. 1992, *Mon. Not. R. Astron. Soc.*, **259**, 35p.

de Muizon, M.J., d'Hendecourt, L.B. and Geballe, T.R. 1990, *Astron. Astrophys.*, **235**, 367.

de Muizion, M.J., Geballe, T.R., d'Hendecourt, L.B. and Baas, F. 1986, *Ap. J.*, **307**, L105.

Nagata, T., Tokunaga, A.T., Sellgren, K., Smith, R.G., Onaka, T., Nakada, Y. and Sakata, A. 1988, *Ap. J.*, **326**, 157.

Nir, D. 1984, *Thin Solid Films*. **112**, 41.

Nitsan, U., & Shankland, T. J. 1976, *Geophys. J.*, **45**, 59.

Ogmen, M. and Duley, W.W. 1988, *Ap. J.*, **334**, L117.

Olnon, F.M. and Raimond, E., (Eds.). 1986, *Astron. Astrophys. Supp.*, **65**, 607.

Ossenkopf, V. 1993, *Astron. Astrophys.*, **280**, 617.

Papoular, R., and Pégourié, B. 1983, *Astron. Astrophys.*, **128**, 335.

Papoular, R., Conard, J., Guiliano, M., Kister, J. and Mille, G. 1988, In: "Infrared Spectroscopy in Astronomy: Proceedings of the 22nd Eslab Symposium held in Salamanca, Spain 7-9 Dec. 1988", ed. B.H. Kaldeich, (ESA Pub.: Paris), 207.

Papoular, R., Breton, J., Gensterblum, G., Nenner, I., Papoular, R.J. and Pireaux, J.J. 1993, *Astron. Astrophys.*, **270**, L5.

Parisel, O., Berthier, G. and Ellinger, Y. 1992, *Astron. Astrophys.*, **266**, L1.

Pauzat, F., Talbi, D. and Ellinger, Y. 1997, *Astron. Astrophys.*, **319**, 318.

Pégourié, B., and Papoular, R. 1985, *Astron. Astrophys.*, **142**, 451.

Pendleton, Y. 1994, In: "The First Symposium on the Infrared Cirrus and Diffuse Interstellar Clouds", eds. P.M. Curri & W.B. Lauer, *ASP Conf. Ser.*, **58**, 255.

Pendleton, Y., Sandford, S.A., Allamandola, L.J., Tielens, A.G.G.M. and Sellgren, K. 1994, *Ap. J.*, **437**, 683.

Penman, J. M. 1976, *Mon. Not. R. Astron. Soc.*, **175**, 149.

Pinho, G.P. and Duley, W.W. 1993, unpublished.

Pinho, G.P. and Duley, W.W. 1995, *Ap. J.*, **442**, L41.

Pirronello, V., Lie, C., Shen, L. and Vidali, G. 1997a, *Ap. J.*, **475**, L69.

Pirronello, V., Biham, O., Liu, C., Shen, L. and Vidali, G. 1997b, *Ap. J.*, **483**, L131.

Platt, J.R. 1956, *Ap. J.*, **123**, 486.

Pulker, H.K. 1982, *SPIE*, **325**, 84.

Rappoport, Z. 1967, "Handbook of tables for Organic Compound Identification", (The Chemical Rubber Co.).

Robertson, J. and O'Reilly, E.P. 1987, *Phys. Rev.*, **B35**, 2946.

Robinson, M.S., Beegle, L.W. and Wdowiak, T.J. 1997, *Ap. J.*, **474**, 474.

Roche, P.F., Lucas, P.W. and Geballe, T.R. 1996, *Mon. Not. R. Astron. Soc.*, **281**, L25.

Roche, P.F., Lucas, P.W., Hoare, M.G., Aitken, D.K. and Smith, C.H. 1996, *Mon. Not. R. Astron. Soc.*, **280**, 924.

Roche, P.F. 1988, In: "Infrared Spectroscopy in Astronomy: Proceedings of the 22nd Eslab Symposium held in Salamanca, Spain 7-9 Dec. 1988", ed. B.H. Kaldeich, (ESA Pub.: Paris), 79.

Rosenberg, H.M. 1988, "The Solid State", 3rd ed., (Oxford), 295.

Ross, R.C. and Messier, R. 1981, *J. Appl. Phys.*, **52** (8), 329.

Rössler, K. 1986, In: "Polycyclic Aromatic Hydrocarbons and Astrophysics", eds. A. Léger, L. d'Hendecourt & N. Boccara, (Reidel Publishing Co.: Dordrecht), 173.

Rouleau, F. and Martin, P.G. 1991, *Ap. J.*, **377**, 526.

Rye, R.R. 1977, *Surface Sci.*, **69**, 653.

Sakata, A., Wada, S., Onaka, T., Tokunaga, A.T. 1990, *Ap J.*, **353**, 543.

Salama, F., Bakes, E.L.O., Allamandola, L.J. and Tielens, A.G.G.M. 1996, *Ap. J.*, **458**, 621.

Salem, L. 1966, "Molecular Orbital Theory of Conjugated Polymers", (Benjamin: New York).

Salisbury, D.W., Allen, J.E. Jr., Donn, B., Khanna, R.K. and Moore, W.J. 1988, In: "Experiments on Cosmic Dust Analogues", eds. E. Bussoletti, C. Fusco & G. Longo, (Kluwer: Dordrecht), 129.

Sandford, S.A., Allamandola, L.J., Tielens, A.G.G.M., Sellgren, K., Tapia, M. and Pendleton, Y. 1991, *Ap. J.*, **371**, 607.

Sandford, S.A., Pendleton, Y.J. and Allamandola, L.J. 1995, *Ap. J.*, **440**, 697.

Savage, B.D. and Mathis, D. 1979, *Ann. Rev. Astr. Astrophys.*, **17**, 73.

Saxena, S.K. and Eriksson, G. 1983, *Earth and Planetary Sci. Lett.*, **65**, 7.

Schnaiter, M., Mutschke, H. and Henning, Th. 1996, *Ap. J.*, **464**, L187.

Schenk, A., Biener, J., Winter, C., Lutterloh, C., Schubert, U.A. and Kuppers, J. 1992, *Appl. Phys. Lett.*, **61**, 2415.

Schutte, W.A., Tielens, A.G.G.M., Allamandola, L.J., Cohen, M. and Wooden, D.H. 1990, *Ap. J.*, **360**, 577.

Scott, A. and Duley, W.W. 1996, *Ap. J. (Suppl.)*, **105**, 401.

Scott, A. and Duley, W.W. 1996, *Ap. J.*, **472**, L123.

Scott, A.D., Duley, W.W. and Jahani, H.R. 1997a, *Ap. J.*, in press.

Scott, A., Duley, W.W. and Pinho, G. 1997b, *Ap. J.*, in press.

Seab, C.G. 1988, In: "Dust in the Universe", eds. M.E. Bailey & D.A. Williams, (Cambridge University Press).

Sears, F.W., Zemansky , M.W. and Young, H.D. 1986, "University Physics 7th ed." (Addison-Wesley Pub. Co.: USA).

Sellgren, K. 1984, *Ap. J.*, **277**, 623.

Sellgren, K. 1989, In: "Dusty Objects in the Universe", eds. E. Bussoletti & A.A. Vittone, (Kluwer: Dordrecht).

Sellgren, K., Allamandola, L.J., Bregman, J.D., Werner, M.W. and Wooden, D.H. 1985, *Ap. J.*, **299**, 416.

Sellgren, K., Smith, R.G. and Brooke, T.Y. 1994, *Ap. J.*, **433**, 179.

Sellgren, K., Werner, M.W. and Dinerstein, H.L. 1983, *Ap. J.*, **271**, L13.

Shen, M., Wang, H., Ning, Z., Chao-Ye and Ren, Z. 1996, *J. Phys.: Condens. Matter*, **8**, 8953.

Shen, M., Wang, H., Ning, Z., Chao-Ye and Ren, Z. 1997, *J. Phys.: Condens. Matter*, **9**, 2981.

Sloan, G.C., Bregman, J.D., Geballe, T.R., Allamandola, L.J. and Woodward, C.E. 1997, *Ap. J.*, **474**, 735.

Smith, F. W. 1984, *J. Appl. Phys.*, **55** (3), 764.

Snow, T.P. and Witt, A.N. 1995, *Science*, **270**, 1455.

Snow, T.P. and Witt, A.N. 1996, *Ap. J.*, **468**, L65.

Sofia, U.J., Cardelli, J.A., Guerin, K.P. and Meyer, D.M. 1997, *Ap. J.*, **482**, L105.

Sorrell, W.H. 1990, *Mon. Not. R. Astron. Soc.*, **243**, 570.

Sorrell, W.H. 1991, *Mon. Not. R. Astron. Soc.*, **248**, 439.

Suess, H.E. 1964, in:"Isotopic and Cosmic Chemistry." ed. H. Craig, North-Holland Publ., Chap. 25.

Swab, P., Krishnaswamy, S.V. and Messier, R. 1980, *J. Vac. Sci. Technol.*, **17** (1), 362.

Talbi, D., Pauzat, F. and Ellinger, Y. 1993, *Astron. Astrophys.*, **268**, 805.

Tauc, J. 1973, "Amorphous Semiconductors" ed. M.H. Brodsky, (Plenum Press: New York).

Taylor, S.D. and Williams, D.A. 1993, *Mon. Not. R. Astron. Soc.*, **260**, 280.

Tokunaga, A.T. 1996, Paper presented at the meeting, "Diffuse Infrared Radiation and the IRTS", Inst. of Space and Astronautical Sciences, Tokyo, Japan.

Tokunaga, A.T., Nagata, T., Sellgren, K., Smith, R.G., Onaka, T., Nakada, Y., Sakata, A. and Wada, S. 1988, *Ap. J.*, **328**, 709.

Tomkin, J., Woolf, V.M. and Lambert, D.L. 1995, *A. J.*, **109**, 2204.

Trumpler, R.J. 1930, *Pub. Astron. Soc. Pacific.*, **42**, 214.

Trumpler, R.J. 1930, *Pub. Astron. Soc. Pacific.*, **100**, 297. (reprint)

Ugarte, D. 1994, *MRS Bulletin*, November, p. 39.

van de Hulst, H.C. 1957, "Light Scattering in Small Particles", (Wiley: New York).

van de Hulst, H.C. 1964, *Pub. Roy. Obs. Edinburgh*, **4**, 35.

van der Zwet, G.P. and Allamandola, L.J. 1985, *Astron. Astrophys.*, **146**, 76.

Verstraete, L. and Léger, A. 1992, *Astron. Astrophys.*, **266**, 513.

Verstraete, L., Puget, J.L., Falgarone, E., Drapatz, S., Wright, C.M. and Timmermann, R. 1996, *Astron. Astrophys.*, **315**, L337.

Vidal-Madjar, C., Gonnord, M.F. and Guichon, G. 1975, *J. Coll. Inter. Sci.*, **52**, 102.

Voevodin, A.A., Walck, S.D., Solomon, J.S., John, P.J., Ingram, D.C., Donley, M.S. and Zabinski, J.S. 1996, *J. Vac. Sci. Technol. A*, **14(3)**, 1927.

Wang, C.Z., Ho, K.M. and Chan C.T. 1993, *Phys. Rev. Lett.*, **70(5)**, 611.

Wdowiak, T.J. 1986, *B.A.A.S.*, **18**, 1030.

Webster, A. 1992, *Mon. Not. R. Astron. Soc.*, **255**, 41p.

Whittet, D.C.B., Bode, M.F., Longmore, A.J., Adamson, A.J., McFadzean, A.D., Aitken, D.K. and Roche, P.F. 1988, *Mon. Not. R. Astron. Soc.*, **233**, 321.

Whittet, D.C.B., Duley, W.W. and Martin, P.G. 1990, *Mon. Not. R. Astron. Soc.*, **244**, 427.

Whittet, D.C.B. 1992, "The Graduate Series in Astronomy: Dust in the Galactic Environment", eds. R.J. Tayler & R.E. White, (IOP: Bristol).

Whittet, D.C.B., Smith, R.G., Adamson, A.J., Aitken, D.K., Chiar, J.E., Kerr, T.H., Roche, P.F., Smith, C.H. and Wright, C.M. 1996, *Ap. J.*, **458**, 363.

Wild, Ch. and Koidl, P. 1987, *Appl. Phys. Lett.*, **51**(19), 1506.

Willacy, K. and Williams, D.A. 1993, *Mon. Not. R. Astron. Soc.*, **260**, 635.

Williams, D. A. 1989, *Proc. IAU Symp. 135*, eds., L.J. Allamandola & A.G.G.M. Tielens, Kluwer, Dordrecht, p367.

Williams, R.M. and Leone, S.T. 1995, *Ap. J.*, **443**, 675.

Williams, P.M., van der Hucht, K.A. and Thé, P.S. 1987, *Astron. Astrophys.*, **182**, 91.

Willner, S. P., Gillet, F.C., Herter, T.L., Jones, B., Krassner, J., Merrill, K.M., Pipher, J.L., Puetter, R.C., Rudy, R.J., Russell, R.W., Soifer, B.T. 1982, *Ap. J.*, **253**, 174.

Witt, A.N. and Boroson, T.A. 1990, *Ap. J.*, **355**, 182.

Witt, A.N., Petersohn, J.K., Bohlin, R.C., O'Connell, R.W., Roberts, M.S., Smith, A.M and Stecher, T.P. 1992, *Ap. J.*, **395**, L5.

Woodsworth, A.W., Kwok, S. and Chan, S.J. 1990, *Astron. Astrophys.*, **228**, 503.

Zaikowski, A., and Knacke, R. F. 1975, *Astrophys. Sp. Sci.*, **37**, 3.

10. GLOSSARY OF ACRONYMS

aC	amorphous carbon
AGB	asymptotic giant branch
DIB	diffuse interstellar band
FTIR	fourier transform infrared
HAC	hydrogenated amorphous carbon
IR	infrared
IRAS	infrared astronomical satellite
ISO	infrared space observatory
LIMS	laser ionization mass spectroscopy
LRS	low resolution spectrometer
MCT	mercury cadmium telluride
N-HAC	nitrogenated HAC
PAH	polycyclic aromatic hydrocarbon
PNe	planetary nebulae
SEM	scanning electron microscope
STM	scanning tunnelling microscope
TEM	transmission electron microscope
UIR	unidentified infrared
UV	ultraviolet
VUV	vacuum ultraviolet

11. INDEX

2

217.5nm feature 6, 25, 29, 31, 34, 166

A

absorption

atomic 6

infrared 8, 37, 47, 68, 105, 114, 143, 150, 168, 172, 176, 181

interstellar 41

measured 82

ultraviolet 40, 95

amorphous carbon ..... iv, 8, 11, 12, 95, 174

annealing ..... iv, 9, 29, 36, 42, 94, 108, 114, 120, 123, 126, 142, 150, 153, 156, 159, 182, 183

C

colour excess 1

column density 2

comets 149

D

dehydrogenation ..... iv, 20

depletion 3, 11

diamond 12, 71, 84, 85, 89, 90, 93, 94

DIBs 41, 166

E

emission

atomic 6

infrared 4, 8, 11, 20, 21, 42, 43, 47, 118, 120, 123, 126, 146, 149, 150, 153, 156, 161, 182
interstellar 40
equivalent width 2
ERE 11, 41, 43
extinction 31
interstellar 1, 4, 8, 29, 174, 178
ultraviolet 6, 8, 25, 34, 176

F

fragmentation 18, 21, 22, 23, 24, 131, 135, 140, 151, 164, 183
fullerenes ..... iv, 33, 132, 140, 141, 164, 165, 166, 176, 183

G

graphite 6, 12, 15, 16, 68, 84, 85, 89, 90, 93, 94, 151, 165, 167, 178

K

Kramers-Kronig relations 97, 102

M

magnitude 1

P

PAHs ..... iv, 9, 18, 23, 24, 33, 40, 41, 42, 43, 49, 135, 140, 146, 150, 161, 165, 166, 182, 183
planetary nebulae 11, 46, 47, 146, 149, 159
polarization 6, 8, 174, 176
proto-planetary nebula 149, 159
protostars 146, 172, 173, 181

R

reflection nebulae 9, 43, 146, 153, 159, 166

S

shocks 9, 12, 20, 164, 165, 183, 184

silicates ..... iv, 6, 8, 10, 172, 176, 181

T

thermal spiking 20, 30, 42, 108, 164, 183

U

UIR ..... iv, 8, 37, 39, 42, 45, 47, 48, 146, 150, 153, 154, 155, 161, 162, 166, 182, 183, 184

V

VSGs 132, 140, 141, 164, 167, 183